



International Committee for Future Accelerators

Sponsored by the Particles and Fields Commission of IUPAP

Beam Dynamics Newsletter

No. 52

**Issue Editor:
W. Fischer**

**Editor in Chief:
W. Chou**

August 2010

Contents

1	FOREWORD.....	9
1.1	FROM THE CHAIR	9
1.2	FROM THE EDITOR	10
2	INTERNATIONAL LINEAR COLLIDER (ILC).....	11
2.1	STUDENTS ADMITTED TO THE FIFTH INTERNATIONAL ACCELERATOR SCHOOL FOR LINEAR COLLIDERS.....	11
3	THEME SECTION: CURRENT BEAM-BEAM PROBLEMS.....	14
3.1	OBSERVATIONS AND OPEN QUESTIONS IN BEAM-BEAM INTERACTIONS.....	14
3.1.1	Introduction	14
3.1.2	Beam-Beam Limits in Different Colliders	15
3.1.2.1	<i>Hadron Colliders.....</i>	<i>15</i>
3.1.2.2	<i>e^+e^- Colliders</i>	<i>18</i>
3.1.3	Scaling Laws	20
3.1.3.1	<i>Tevatron: Losses at Injection</i>	<i>20</i>
3.1.3.2	<i>Tevatron: Anti-Proton Losses during Stores.....</i>	<i>21</i>
3.1.3.3	<i>SPS Study of Proton Losses.....</i>	<i>21</i>
3.1.3.4	<i>Tevatron: Proton Losses due to Head-on Collisions</i>	<i>22</i>
3.1.4	Influence of Machine Optics on Beam-Beam Phenomena.....	23
3.1.4.1	<i>Local and Beam-Beam Chromaticity</i>	<i>23</i>
3.1.4.2	<i>Local Coupling and Dispersion</i>	<i>25</i>
3.1.4.3	<i>Matching Beam Sizes.....</i>	<i>26</i>
3.1.5	Orbit Vibrations at the IP	26
3.1.6	Coherent Phenomena.....	27
3.1.7	Compensation of Head-on Interactions with an Electron Lens.....	28
3.1.8	Compensation of Long-Range Interactions with Wires	29
3.1.9	Future Developments Related to the LHC	29
3.1.10	References	30
3.2	REVIEW OF CRAB CROSSING IN KEKB	33
3.2.1	Introduction	33
3.2.2	Motivation for the Crab Crossing.....	33
3.2.2.1	<i>Beam-Beam Limit with or without Crossing Angle in Simulations</i>	<i>33</i>
3.2.3	Operation with Crab Cavity.....	34
3.2.3.1	<i>KEKB Performance before Installation of the Crab Cavities.....</i>	<i>34</i>
3.2.3.2	<i>Correction of x-y Coupling at IP.....</i>	<i>36</i>
3.2.3.3	<i>Chromatic Coupling at IP.....</i>	<i>38</i>
3.2.3.4	<i>Luminosity Degradation due to Beam Noise.....</i>	<i>39</i>
3.2.3.5	<i>Beam Life Time Issue Related to the Collision.....</i>	<i>40</i>
3.2.3.6	<i>Other Possibilities for Luminosity Degradation</i>	<i>41</i>
3.2.4	Summary.....	41

3.2.5	References.....	42
3.3	BEAM-BEAM SIMULATIONS FOR CRABBED BUNCHES	42
3.3.1	Introduction.....	42
3.3.2	Crabbed Beam Distribution	43
3.3.3	Requirements on the Grid Sizes.....	44
3.3.4	Nonrectangular and Non-uniform Grids.....	45
3.3.4.1	<i>Integration</i>	47
3.3.4.2	<i>Interpolation</i>	48
3.3.5	Testing the Grids.....	49
3.3.5.1	<i>Interpolation</i>	49
3.3.5.1	<i>Integration</i>	51
3.3.6	Crabbed Beams	53
3.3.7	Conclusions.....	54
3.3.8	Acknowledgements.....	54
3.3.9	References.....	54
3.4	BEAM-BEAM INTERACTION AT THE PEP-II e^+e^- COLLIDER	55
3.4.1	Introduction.....	55
3.4.2	General PEP-II Parameters	55
3.4.3	Interaction Region	57
3.4.4	Operations	57
3.4.5	Best Betatron Tune Location	60
3.4.6	Beam-Beam Observations	60
3.4.7	Acknowledgements.....	66
3.4.8	References.....	66
3.5	BEAM-BEAM EXPERIENCE IN RHIC	67
3.5.1	Introduction.....	67
3.5.2	Achieved Beam-Beam Parameters in RHIC.....	67
3.5.3	Luminosity Lifetimes at Different β^*	68
3.5.4	Strong-Strong Effects	69
3.5.5	Unequal RF Frequencies.....	69
3.5.6	Future Improvements.....	70
3.5.7	References.....	70
3.6	BEAM DYNAMICS STUDY FOR THE LHC PHASE I LUMINOSITY UPGRADE INCLUDING BEAM-BEAM	71
3.6.1	Introduction.....	71
3.6.2	Simulation Setup.....	71
3.6.3	Analysis of Particle Motion	73
3.6.4	Effect of Rounding Errors.....	76
3.6.5	Volunteer Computing with LHC@HOME.....	77
3.6.6	Simulation Results	77
3.6.7	Conclusions and Outlook.....	80
3.6.8	References.....	80
3.7	LONG-RANGE BEAM-BEAM COMPENSATION IN THE LHC	81
3.7.1	Introduction.....	81

3.7.2	The Long-Range Beam-Beam Effect in the LHC	82
3.7.3	The Compensation Strategy	83
3.7.4	Compensation in Numerical Simulations	85
3.7.5	Compensation in Experiments and Operations	89
3.7.6	SPS Compensation Experiments	89
3.7.7	Application in DAΦNE	93
3.7.8	Conclusions	94
3.7.9	Acknowledgement	94
3.7.10	References	94
3.8	LONG-RANGE EXPERIMENTS IN RHIC	95
3.8.1	Introduction	95
3.8.2	RHIC Experiments	95
3.8.3	DC Wires in the RHIC	96
3.8.4	Long-Range Experiments	97
3.8.4.1	<i>Single Long-Range Measurements</i>	97
3.8.4.2	<i>Wire Scans on Single Beams</i>	98
3.8.4.3	<i>Long-Range Effect with Head-on Collisions and Compensation</i>	99
3.8.5	Summary	101
3.8.6	References	101
3.9	HEAD-ON BEAM-BEAM COMPENSATION IN RHIC	102
3.9.1	Introduction	102
3.9.2	Design Considerations	102
3.9.3	Summary	106
3.9.4	Acknowledgments	106
3.9.5	References	107
3.10	WEAK-STRONG BEAM-BEAM SIMULATIONS FOR HEAD-ON BEAM-BEAM COMPENSATION IN THE RHIC	107
3.10.1	Introduction	107
3.10.2	Frequency Map Analysis	109
3.10.3	Dynamic Aperture Calculation	110
3.10.4	Beam Lifetime Calculation	112
3.10.5	Summary	114
3.10.6	Acknowledgments	115
3.10.7	References	115
3.11	BEAM-BEAM SIMULATION	115
3.11.1	Introduction	115
3.11.2	Computational Model	116
3.11.3	Applications	119
3.11.4	Acknowledgements	122
3.11.5	References	122
3.12	SPACE-CHARGE LIMITATIONS IN A COLLIDER	123
3.12.1	Introduction	123
3.12.2	Space-Charge Effects	123
3.12.3	Beam-Beam Effects	124

3.12.4	Space-Charge and Beam-Beam Limits in a Collider.....	125
3.12.5	RHIC Experience.....	126
3.12.6	References	128
3.13	BEAM-BEAM ISSUES IN ERHIC	128
3.13.1	Introduction	128
3.13.2	Electron Beam Disruption Effect	130
3.13.2.1	<i>Linear Approximation</i>	131
3.13.2.2	<i>Nonlinear Effects</i>	133
3.13.3	Kink Instability	139
3.13.4	Electron Beam Random Errors.....	143
3.13.5	References	144
3.14	BEAM-BEAM ISSUES IN ELIC.....	144
3.14.1	Introduction	144
3.14.2	Simulation Model, Code and Scope	145
3.14.3	Simulation Results.....	146
3.14.3.1	<i>Luminosity Trends for Normal Design Parameters</i>	146
3.14.3.2	<i>Luminosity Dependence on Beam Current</i>	147
3.14.3.3	<i>Coherent Beam-Beam Instability</i>	147
3.14.3.4	<i>Multiple Interaction Points</i>	147
3.14.3.5	<i>Locating Optimal Working Point Using an Evolutionary Algorithm</i>	147
3.14.4	Discussion and Outlook.....	148
3.14.5	References	148
3.15	BEAM-BEAM ISSUES IN THE ILC AND IN CLIC	149
3.15.1	Introduction	149
3.15.2	ILC Optimization.....	149
3.15.2.1	<i>Luminosity</i>	150
3.15.2.2	<i>Beamstrahlung</i>	151
3.15.2.3	<i>Disruption and Travelling Focus</i>	151
3.15.3	CLIC Optimization at 3 TeV	155
3.15.4	Final Focus Design Issues and ATF2.....	157
3.15.4.1	<i>Final Focus System Tuning</i>	159
3.15.4.2	<i>Background Optimization</i>	160
3.15.5	Luminosity Operation at Lower than Nominal Energies.....	160
3.15.5.1	<i>ILC</i>	160
3.15.5.2	<i>CLIC</i>	160
3.15.6	Beam-Beam Background.....	161
3.15.6.1	<i>Coherent Pair Creation</i>	162
3.15.6.2	<i>Incoherent Pair Creation</i>	163
3.15.6.3	<i>Hadronic Background</i>	163
3.15.6.4	<i>Luminosity Spectrum Reconstruction</i>	164
3.15.7	Code Development and Benchmarking	164
3.15.8	References	165
3.16	BEAM-BEAM EFFECTS IN MUON COLLIDERS	166
3.16.1	Introduction	166

3.16.2	Incoherent Beam-Beam Effect	166
3.16.2.1	<i>Dynamic Aperture</i>	167
3.16.2.2	<i>Dynamic Beta Effect</i>	167
3.16.3	Coherent Beam-Beam Oscillations	168
3.16.4	References	169
4	WORKSHOP AND CONFERENCE REPORTS	169
4.1	LASER APPLICATIONS FOR FUTURE HIGH-ENERGY AND HIGH-INTENSITY ACCELERATORS	169
4.1.1	Introduction	169
4.1.2	1-10 TeV e^+e^- Colliders Based on Laser Plasma Acceleration	171
4.1.3	10 TeV e^+e^- Colliders Based on Direct Laser Acceleration	176
4.1.4	200 GeV $\gamma\gamma$ Colliders	179
4.1.5	Laser Stripping of H^- Particles in High-Intensity Proton Accelerators.....	182
4.1.5.1	<i>Laser Stripping of H^- Particles for SNS</i>	182
4.1.5.2	<i>Laser Stripping of H^- Particles for Project</i>	185
4.1.5.2.1	Direct Laser Ionization.....	186
4.1.5.2.1	Three-Step Stripping	187
4.1.6	Acknowledgements	187
4.1.7	References	187
5	RECENT DOCTORAL THESES	189
5.1	ATF2 OPTICS SYSTEM OPTIMIZATION AND EXPERIMENT STUDY	189
5.2	SIMULATION AND EXPERIMENTAL RESEARCH ON LASER WAKEFIELD ELECTRON ACCELERATORS	190
5.3	RESEARCHES ON ELECTRON INJECTION AND PLASMA DENSITY DIAGNOSTICS IN LASER PLASMA WAKEFIELD ACCELERATION	191
6	FORTHCOMING BEAM DYNAMICS EVENTS	193
6.1	ICFA ADVANCED BEAM DYNAMICS MINI-WORKSHOP: X-BAND RF STRUCTURES, BEAM DYNAMICS AND SOURCES (XB10)	193
7	ANNOUNCEMENTS OF THE BEAM DYNAMICS PANEL.....	193
7.1	ICFA BEAM DYNAMICS NEWSLETTER.....	193
7.1.1	Aim of the Newsletter.....	193
7.1.2	How to Prepare a Manuscript	194
7.1.3	Distribution.....	195
7.1.4	Regular Correspondents	195
7.2	ICFA BEAM DYNAMICS PANEL MEMBERS	196

1 Foreword

1.1 From the Chair

Weiren Chou, Fermilab
Mail to: chou@fnal.gov

The International Committee for Future Accelerators (ICFA) met on July 24, 2010 at the Palais des Congrès de Paris during ICHEP2010. Atsuto Suzuki, Director General of KEK and Chair of ICFA, chaired this meeting.

Jonathan Bagger, Chair of the ILCSC, presented a summary report of the ILCSC meeting, which had taken place earlier on the same day. The GDE is on track for producing a Technical Design Report (TDR) by the end of 2012. The Research Director will produce a Baseline Design for two detectors for the TDR. There was an extended discussion on post-2012 ILC activities. The consensus was that there would be a transitional stage after 2012, overseen by a multi-laboratory collaboration; the ILC effort would be a “virtual” lab (like the current GDE) becoming more real as time progresses. This model is general, and so could also cover CLIC or a muon collider in the future if either of these becomes the preferred lepton collider. A technical committee will be needed to evaluate the readiness of possible successor machines to the LHC, once the required energy is known; this committee could be organized by ICFA, in a way similar to the ITRP (International Technical Recommendation Panel) which compared superconducting and room-temperature linear colliders in 2004.

ICFA formed a steering committee to draft a document describing worldwide particle physics opportunities in a coherent and compelling manner. This committee is chaired by Pier Oddone, Fermilab Director. A first draft is expected in February 2011, with a final version to be presented at the ICFA Seminar in October 2011.

Toshiki Tajima, Chair of the International Committee for Ultra Intense Lasers (ICUIL), was invited to the meeting and gave a report on joint activities between ICFA and ICUIL. A joint task force has been created, and a first joint workshop was held at GSI in April 2010. (A brief report of this workshop can be found on p. 239 of issue no. 51 of this newsletter. It also appears in the June 2010 issue of *CERN Courier*.) Possible laser use has been considered in 1-10 TeV e^+e^- colliders, 200 GeV $\gamma\gamma$ colliders (based on either ILC or CLIC), light sources (Compton inverse scattering sources and FEL), hadron therapy machines, and H^- stripping in high-intensity proton accelerators. The laser requirements and key technical bottlenecks for each have been identified, and a technical report is in progress. The major laser challenges are: high average power, high efficiency, and high repetition rate; the operating electricity cost will also be significant. The challenges are large, but no showstoppers have been found. The promising laser technologies include thin disk, slab and fiber lasers.

The ICFA Beam Dynamics Panel plays an active role in the ICFA-ICUIL collaboration. A number of accelerator physicists from major accelerator laboratories (CERN, DESY, SLAC, KEK, Fermilab, GSI, PSI, LBNL, LANL, SNS, etc.) attended the joint workshop. A report entitled “*Laser applications for future high-energy and high-intensity accelerators*” has been written and is published in Section 4.1. It will be

combined with several other reports (light sources, medical accelerators and laser technologies) to form a complete technical report.

Junji Urakawa, a senior scientist from KEK, has served on this panel for a number of years and made numerous valuable contributions, including editing no. 50 of this newsletter and helping organize the international linear collider school. Due to his new appointment, he decided to step down from the Beam Dynamics Panel. He will be replaced by Toshiyuki Okugi, an accelerator scientist also from KEK. ICFA has approved this membership change. On behalf of the panel, I want to thank Junji for his excellent service in the past years and wish him success in his new endeavor. I also welcome Toshiyuki on board and look forward to working with him in the coming years.

The student selection for *The Fifth International Accelerator School for Linear Colliders*, which will be held from October 25 – November 5, 2010 at Villars-sur-Ollon, Switzerland, is complete. Barry Barish, Director of the ILC GDE, wrote an article on the school in Section 2.1, which also appears in the *Director's Corner* of the August 5, 2010 issue of the weekly online journal *ILC Newslines*. The school web address is <http://www.linearcollider.org/school/2010/>.

The editor of this issue is Dr. Wolfram Fischer, a panel member and an accelerator scientist at Brookhaven National Laboratory, USA. Wolfram collected 16 well-written articles in the theme section “*Current Beam-Beam Problems*.” These articles give a comprehensive review of this important and challenging beam dynamics problem. In this issue there are also three recent doctoral theses abstracts (Sha Bai, Da Zhang Li and An He, all from the Institute of High Energy Physics in China) and an ICFA mini-workshop announcement (XB10). I thank Wolfram for editing and producing a newsletter of great value to our accelerator community.

1.2 From the Editor

Wolfram Fischer, Brookhaven National Laboratory, Upton, New York

Mail to: Wolfram.Fischer@bnl.gov

Beam-beam effects became a subject of study as soon as there were colliders beginning with the first e^+e^- collider AdA in Frascati that started operating in 1960, and the first pp collider ISR at CERN that started operating in 1971. Over the years the research focus has shifted as old problems were better understood, and new problems emerged. Current research topics include beam-beam in conjunction with electron cloud effects in B-factories, crab crossing, collision with crab waist, collisions with round and flat beams, beam-beam in conjunction with other nonlinear effects, long-range and head-on compensation, beam-beam with space charge effects, beam disruption in linear colliders, kink instabilities in electron-ion colliders, dynamic aperture and beam lifetime simulations for both lepton and hadron colliders, and more. In general, beam-beam problems are now almost always defined in the context of one or more other phenomena.

Previous ICFA Beam Dynamics Newsletters have discussed some aspects of beam-beam problems: [No. 30](#) (April 2003, “Electron-Ion Colliders”), [No. 31](#) (August 2003, “High-Luminosity e^+e^- Colliders”), [No. 34](#) (August 2004, “Beam-beam Interactions”), [No. 48](#) (April 2009, “ e^+e^- Colliders: Past and Present Experiences and Future Frontiers”). This Newsletter is a little heavy on the side of hadron colliders, and for

more information on lepton colliders we refer readers to the relatively recent Newsletter [No. 48](#) (April 2009), edited by M. E. Biagini.

I would like to thank all contributors to this edition of the ICFA Beam Dynamics Newsletter for providing the excellent articles that allow the wider community to get an overview of current beam-beam problems.

2 International Linear Collider (ILC)

2.1 Students Admitted to the Fifth International Accelerator School for Linear Colliders

Barry Barish, ILC GDE
Mail to: barish@ligo.caltech.edu

This year we have again had a very big demand and many qualified applicants for the [Fifth International Accelerator School for Linear Colliders](#). This year's school will be held from 25 October to 5 November 2010 in Villars-sur-Ollon, Switzerland, continuing the tradition of cycling the school between Europe, Asia and the Americas. The focus of the school will be on accelerator science related to the next-generation TeV-scale colliders, including the International Linear Collider (ILC), the Compact Linear Collider (CLIC) and the muon collider.

We have selected 70 highly qualified students from an increased pool of 276 applications for the 2010 school. We received applicants from 44 countries, of which 72% were from countries having programmes in high-energy physics. The country distribution of the accepted students includes 19 from Asia and Oceania, 31 from Europe and 20 from North and South America. These students will be divided into two classes: Class A (44) for accelerator physics and Class B (26) for radiofrequency (RF) technology. Dividing the class, following introductory common lectures into two tracks was introduced last year and enables a more in-depth school and opens the possibility of accepting some returning students, of which we will have five this year.

The organisation of the Linear Collider accelerator school is done jointly by the Global Design Effort (GDE), the Compact Linear Collider (CLIC) Study and the International Committee for Future Accelerators (ICFA) Beam Dynamics Panel. The continuing popularity and success of the school clearly indicates the important need for providing advanced training in accelerator science for the high-energy physics community. There are very good opportunities in this field, even in these difficult financial times, as was highlighted in a recent article "[A Field where Jobs Go Begging](#)" in Symmetry magazine. Particle physics has been responsible for much of the development of particle accelerator science because of our own need for new accelerators for our research and therefore our investment in advanced accelerator R&D.

The attendees at the LC school are graduate students, postdoctoral fellows and junior researchers from around the world, including physicists who are considering a career change from experimental physics to accelerator physics. The subjects from accelerator dynamics to superconducting RF are forward-looking subjects in the field with many possible applications beyond the next-generation Terascale lepton colliders.

The curriculum will contain an overview of the different future collider options and a lecture on linac basics, followed by a choice of two in-depth tracks: one on electron and positron sources, damping rings, linacs and beam delivery system; and one on superconducting and warm radiofrequency technology, low-level RF and high-power RF.

We are set to have another very successful LC accelerator school this year. We have excellent lecturers, well-qualified students, an in-depth curriculum and a beautiful site for the school. I am happy to be able to once again be able to personally participate. I will be giving both the introductory lecture on high energy physics and the lecture on the International Linear Collider.

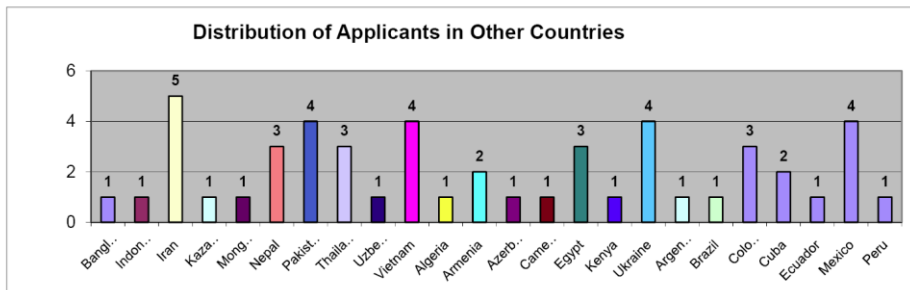
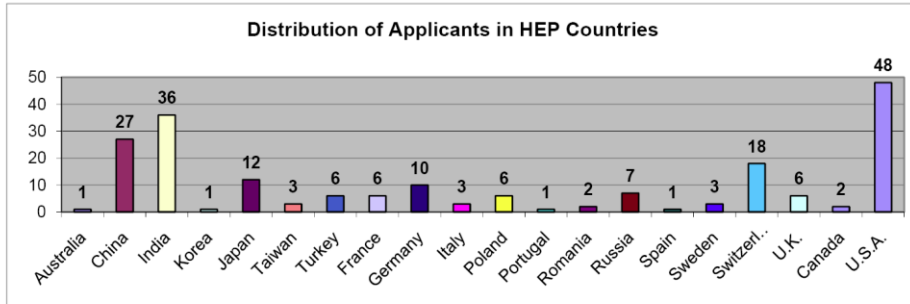
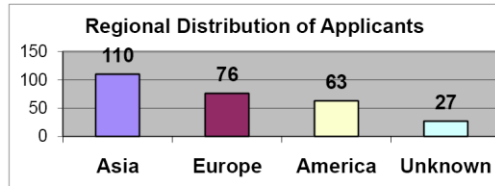
Lecturers of the 2010 LC Accelerator School

Lecture	Topic	Lecturer
I1	Introduction	Barry Barish (Caltech)
I2	ILC	Barry Barish (Caltech)
I3	CLIC	Frank Tecker (CERN)
I4	Muon collider	Bob Palmer (BNL)
A1	Linacs	Daniel Schulte (CERN)
A2	Sources	Masao Kuriki (Hiroshima U.)
A3	Damping rings	Mark Palmer (Cornell U.)
A4	Beam delivery & beam-beam	Andrei Seryi (John Adams Inst.)
B1	Room temperature RF	Walter Wuensch (CERN) Erk Jensen (CERN) Alexej Grudiev (CERN)
B2	Superconducting RF	Jean Delayne (ODU-CAS)
B3	LLRF & high power RF	Stefan Simrock (ITER)

2010 LC Accelerator School – Applicants Distribution

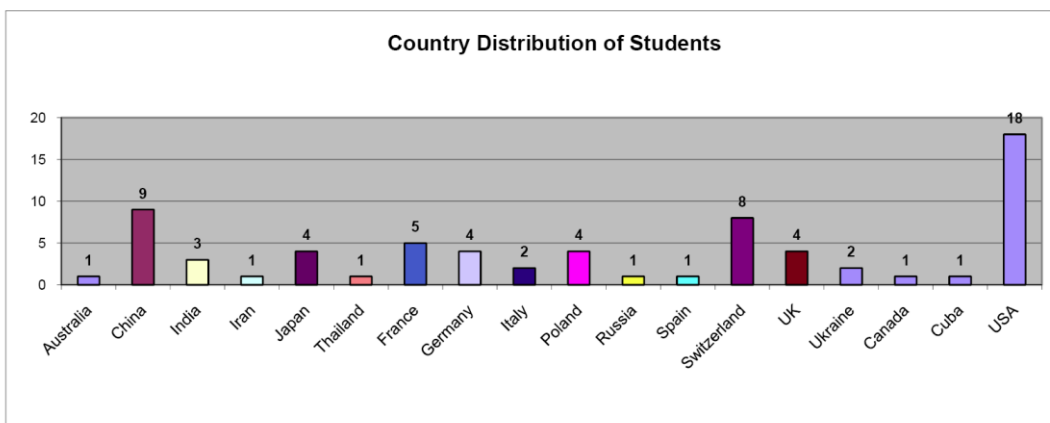
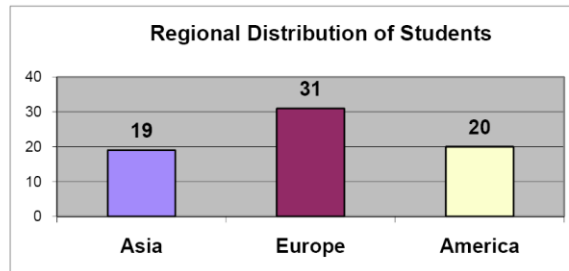
276 applicants from 44 countries

- 72% from 20 HEP countries
- 18% from 24 other countries
- 10% unknown



2010 LC Accelerator School – Students Distribution

- 70 students selected from 18 countries
- 93% from 14 HEP countries
- 7% from 4 other countries



3 Theme Section: Current Beam-Beam Problems

3.1 Observations and Open Questions in Beam-Beam Interactions

Tanaji Sen, Accelerator Physics Center, FNAL, Batavia, IL 60510, USA

Mail to: tsen@fnal.gov

3.1.1 Introduction

The first of the hadron colliders, ISR, started operation in 1970. In the following years, the hadron colliders to follow were the SPS (started 1980), the Tevatron (started 1987 first as a fixed target machine), RHIC (started 2000) and most recently the LHC, which started in 2008. HERA was a hybrid that collided electrons and protons. All of these accelerators had or have their performance limited by the effects of the beam-beam interactions. That has also been true for the electron-positron colliders such as LEP, CESR, KEKB and PEP-II. In this article I will discuss how the beam-beam limitations arose in some of these machines. The discussion will be focused on common themes that span the different colliders. I will mostly discuss the hadron colliders but sometimes discuss the lepton colliders where relevant. Only a handful of common accelerator physics topics are chosen here, the list is not meant to be exhaustive. A comparative review of beam-beam performance in the ISR, SPS and Tevatron (ca 1989) can be found in reference [1]. Table 1 shows the relevant parameters of colliders (excluding the LHC), which have accelerated protons.

Table 1: Basic parameters of past and present fully commissioned hadron colliders.

	ISR	SPS	Tevatron	HERA p	RHIC
Circumference [m]	943	6911	6283	6336	3834
Energy [GeV]	31	315	980	920	250 / 100
Peak Luminosity [$\times 10^{32} \text{ cm}^{-2} \text{ s}^{-1}$]	1.3	0.06	4.0	0.5	0.85
Lumi lifetime [hrs]	?	9	6	?	6
#of head-on collisions	8	3	2	2	2
Number of parasitics	0	9	70	0	4
Total bm-bm spread	0.008	0.015	0.025	0.003	0.013/0.011
β_x^* , β_y^* [m]	30, 0.3	0.6, 0.15	0.28, 0.28	2.45, 0.18	0.7 / 0.7
ϵ_x , ϵ_y [rms, $\pi \mu\text{m}$]		2.75, 2.75 3, 2.5 (a)	2.9, 3.3 1.6, 1.4(a)	3.7, 3.7	3.3, 3.3
Bunch intensity [$\times 10^{11}$]	-	1.3(p) 0.7(a)	3.1 (p) 1(a)	0.9	1.1/1.35
Number of bunches	N/A	6	36	180	110
Bunch spacing [nsec]	N/A	1150	396	96	108
Bunch length [m]	N/A	0.72	0.6	0.30	0.6 / 0.8

Notation: a = anti-protons

Luminosity lifetime in the table refers to the initial luminosity lifetime at the start of stores. ISR also collided protons-antiprotons but peak luminosities were reached with protons in both beams. HERA was an e-p collider but is included here.

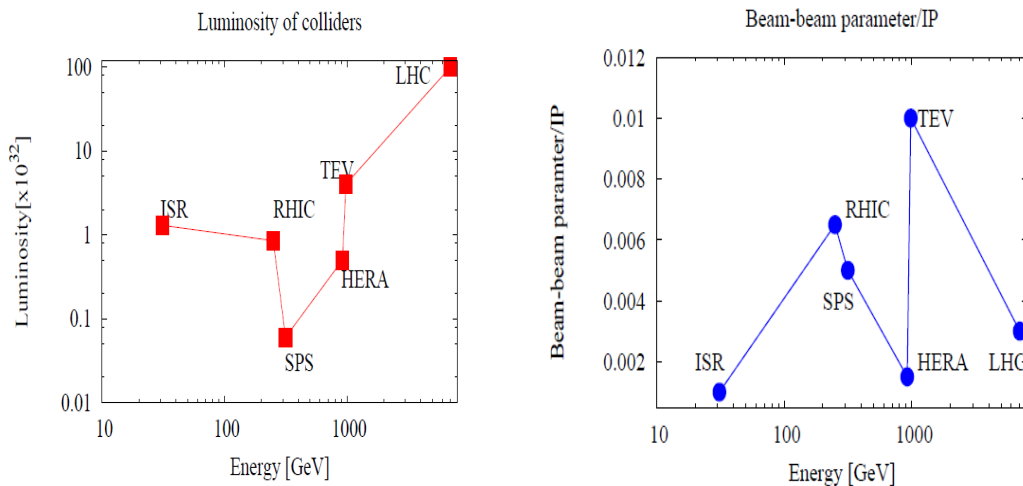


Figure 1: Left plot shows the luminosity in $\text{cm}^{-2}\text{s}^{-1}$ vs. beam energy. Right plot shows the beam-beam parameter per IP vs. beam energy. For SPS and the Tevatron, the beam-beam parameter for the anti-protons is shown. Also shown are the parameters for the LHC at its design energy and luminosity.

Figure 1 shows the luminosity and beam-beam parameter/IP ξ for the different colliders. While the SPS had the lowest luminosity (because of the fewest number of bunches), it had small emittance bunches and had the highest specific luminosity so far.

Tune space: In the Tevatron, the working points lie above the half integer between the 5th and 7th order resonances with an available tune space of 0.028 which is comparable to the total beam-beam tune spread. In RHIC, the working points also above the half integer lie between 3rd and 10th order resonances with an available tune space of 0.03. The maximum tune spread is about half this value. The SPS also operated within these resonances. In HERA-p, tunes were below the half integer but placed between 7th and 10th order resonances with an available tune space of 0.014, several times the beam-beam induced tune spread for protons. In most of these colliders, the tunes have to be controlled to within 0.002 for optimal operation. This is not always easy, e.g. in the Tevatron the proton tune spread is determined by the anti-proton bunch intensity which can vary significantly from bunch to bunch.

3.1.2 Beam-Beam Limits in Different Colliders

Limits imposed by the beam-beam interactions can manifest in several different ways. Here we briefly review how the limits arise/arose in different colliders.

3.1.2.1 Hadron Colliders

Tevatron

Beam-beam interactions impose limits at all stages of the operation cycle and in different ways. At injection, the limits are imposed by the long-range interactions when the two beams with 36 bunches each circulate on their helical orbits and each bunch suffers 72 long-range interactions around the ring. Both beams suffer losses proportional to the intensity of the other beam. At collision with 2 head-on interactions and 70 long-range interactions, the limiting processes are different for the two beams. The long-range interactions contribute a tune spread of about 0.008, equal to from each

of the main collisions. In current operations, both species have about the same beam-beam tune spread and are effectively in the strong-strong regime. Early in Run II, anti-protons suffered large losses during the beta squeeze and stores due to the long-range interactions, particularly the 4 interactions with smallest separations on either side of the 2 IPs. In 2006, additional separators were installed to increase the beam separations from about 5.4σ to about 6σ [2] at these locations. Beginning in 2005 electron cooling of anti-protons in the Recycler was made operational which made their emittance much smaller than those of protons [3]. Consequently the anti-protons effectively experience only the linear part of the head-on beam-beam force and do not suffer much from it. Since 2006, anti-proton losses due to beam-beam interactions during stores have been small, provided the tunes are well controlled. Protons on the other hand have tunes closer to 12th order resonances and are transversely larger than the anti-protons. Consequently during head-on collisions, they experience the non-linear beam-beam force enhanced by chromatic effects and suffer beam loss and emittance growth. Long-range interactions have affected protons occasionally during the beta squeeze when separations can drop to low values.

Earlier reports on beam-beam phenomena early in Run II can be found in several references, e.g. [4-6]. A review of beam-beam observations in Run I can be found in [1]. In 2010 the Tevatron achieved a peak luminosity of $4 \times 10^{32} \text{ cm}^{-2} \text{ s}^{-1}$, about three times the peak value obtained with the ISR. Summaries of recent improvements made to the Tevatron complex can be found in [3-4].

RHIC

RHIC has collided many species including proton-proton, gold-gold, gold-deuteron and copper-copper. I will discuss here some of the limits observed with proton-proton collisions. The beams in the Blue and Yellow rings have nearly the same intensity and emittances, so RHIC operates in the strong-strong regime, as does the LHC. During injections and acceleration, the beams have a large enough vertical separation that long-range interactions at 6 locations do not lead to any losses. At collision most bunches suffers 2 head-on collisions. During recent runs, the beam-beam parameter ξ per IP has approached 0.009, close to the value in the Tevatron [8]. Dominant sources of beam lifetime limitations, not due to luminosity burn up, include beam-beam effects, IR multipole errors and parametric modulations due to mechanical vibrations of the triplets [9]. RHIC operates between the 3rd and 10th order resonances. When the tunes get too close to the 10th order resonances, both luminosity lifetime and proton polarization (which may be affected by beam-beam) suffer. During the latest runs, β^* values became comparable to the bunch length and the hourglass effect became significant enough to reduce the luminosity [10]. At intensities beyond 2×10^{11} /bunch, the beam-beam tune spread will exceed the resonance free space. There are plans to use electron lenses to compensate the effects of these head-on interactions.

HERA

The beam-beam parameter for HERA-p was almost a factor of 10 lower than in the Tevatron. Also, as remarked above, the resonance free space was about 4-5 times the beam tune spread. Nevertheless the head-on interactions did induce beam losses.

During the early commissioning stage, proton transverse beam sizes were about 3-4 times the electron beam sizes and their lifetime during stores was very low, around 0.5 hours. As the proton beam size was reduced to match the electron size, the lifetime

improved to about 100 hours or more [11]. During 2003 and 2004, proton beams were observed to be driven by coherent oscillations of the lepton beam when the tunes of the two beams approached resonances too closely. Under extreme conditions, the proton beam emittance grew by a factor of 2-4 [12]. This growth was avoided by careful choice of the tunes and by bringing the beams into collision sequentially at the two IPs. In the final years of operation, increasing beam-beam forces on the protons increased diffusion into the beam halo and background rates and thus led to a “soft limit” rather than a hard limit [13]. However orbit vibrations at the IP due to mechanical vibrations of the triplet by more than a few microns were considered intolerable.

The lepton beam-beam limit in HERA was primarily due to operation close to the integer tune in order to maximize polarization. When the beam-beam tune spread overlapped low order synchro-betatron resonances, coherent oscillations and emittance growth of the lepton beam resulted. Careful control of the tunes was necessary to avoid these resonances [13].

SPS

Prior to 1988 the SPS operated with 3 proton bunches and 3 anti-proton bunches circulating in the same vacuum chamber. The protons had an emittance about 4 times larger than that of the anti-protons. During the start of stores, the proton loss rate was high with an initial lifetime of around 10 hours and the background rates were unacceptably large [14]. Protons in the transverse tails were sensitive to very high order resonances such as the 16th order and were lost. The losses were controlled by a controlled increase of the anti-proton emittance at the start of the stores – similar to what is done now in the Tevatron. Along with other upgrades in 1988, the proton to anti-proton emittance ratio was reduced to 12/7 and the number of bunches in each beam was increased to 6. During injection and acceleration, the beams were horizontally separated with electrostatic separators. At injection, the beam separations at the 12 parasitic interactions varied between 1.3 to 7.9 units of the anti-proton beam size [14]. Beam losses due to 7th order resonances were associated with these interactions during injection and acceleration. At top energy each bunch had 3 head-on collisions, two at the experiments and one in between them. During stores with more equal beam sizes, the protons were now sensitive to lower order resonances such as 10th order but background rates were acceptable and the initial proton lifetime had increased to about 50 hours. A comparative review of SPS and Tevatron performance up to 1989 can be found in [15].

ISR

This machine had two interleaved rings in which first unbunched beams of protons and later antiprotons and other particles were brought into collision. There were 8 crossing points of which 5-6 were used for experiments [16,17]. Another feature of the ISR was that it had a working line, shown in Figure 2, rather than a working point.

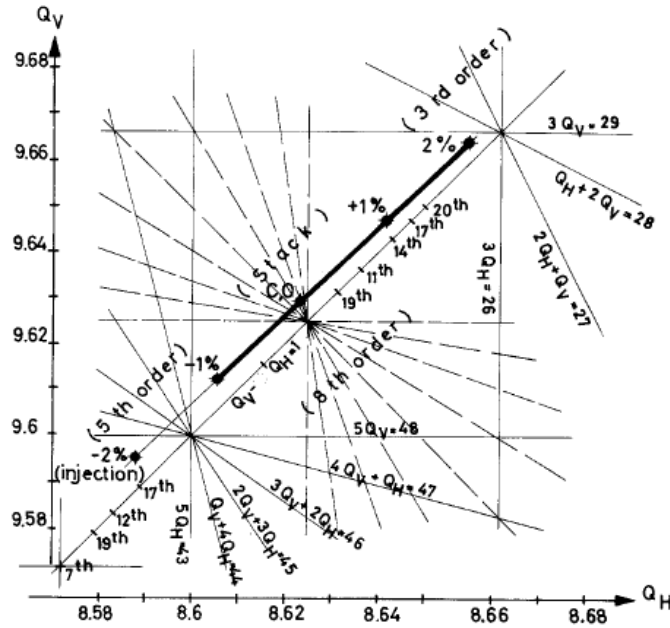


Figure 2: One of the working lines in the ISR (named 8C) between 3rd and 5th order resonances and straddling 8th order resonances (taken from [18]).

This large tune spread was required for stability against the transverse resistive wall instability. As a consequence, the beams crossed some low order betatron resonances which led to particle loss. Synchro-betatron resonances were not an issue. During collisions beam-beam effects also led to particle loss, often from coherent effects. This will be discussed further below. Beam currents in the range of 30–40 Amps were stored during high luminosity runs with lifetimes in the tens of hours. Overviews of the accelerator physics issues in the ISR can be found in [19, 20].

3.1.2.2 e^+e^- Colliders

KEKB

Prior to 2007, beams in KEKB had a crossing angle of 22 mrad at the IP. Crab cavities were introduced in 2007, one in each ring, to have effective head-on collisions and recover the geometric loss of luminosity. However when the bunch currents were raised beyond values circulated without the crab cavities, beam lifetimes dropped. The lifetimes could be improved by introducing horizontal offsets in the crab cavities, the amount of offset depended on the bunch current. In 2008 it was understood to be due to the dynamic beta beating from the beam-beam interaction and operation close to a half integer [21]. The horizontal beam sizes of the beams were large at the crab cavities that did not have sufficient aperture. The optics was changed to reduce β_x at the cavities, β^* was raised to 0.15m to improve lifetime. The most important improvements came from the installation of skew sextupoles around the IR to reduce chromatic coupling at the IP. These alone raised the luminosity by 15% and led to a peak luminosity of $2.1 \times 10^{34} \text{ cm}^{-2} \text{ s}^{-1}$ in 2009 [22, 23].

PEP-II

During 2008, its last year of operation, PEP-II operated with 1732 bunches in each ring and achieved a peak luminosity of $1.21 \times 10^{34} \text{ cm}^{-2} \text{ s}^{-1}$ [24]. At the highest bunch

currents, the performance was limited by the head-on beam-beam interactions. For example, the low energy ring (LER) currents were limited by the losses and backgrounds from the beam in the high energy ring (HER). Additionally increasing the beam current in the LER also increased its own beam size, which was not understood [24]. The maximum beam-beam parameter achieved was 0.113 in the horizontal plane of the HER.

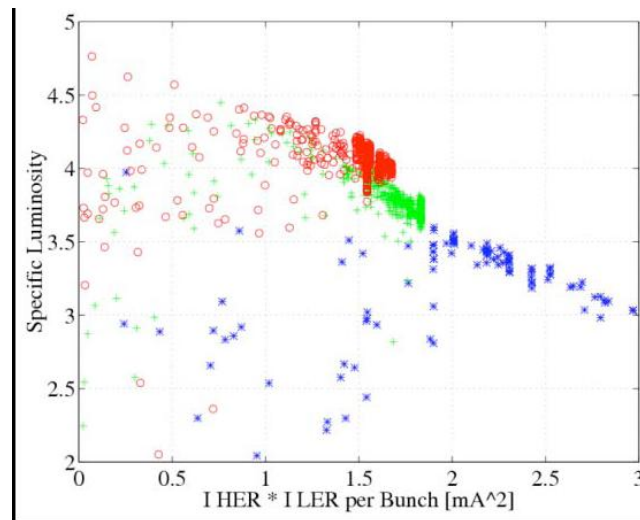


Figure 3: The specific luminosity vs. the product of the bunch currents in the two rings in PEP-II (taken from reference [24]). At low currents the dynamic beta effect increased the luminosity by decreasing beam sizes at the IP but at higher currents, losses due to the beam-beam interactions reduced the specific luminosity.

The effect of the parasitic collisions on the luminosity was reduced to a few percent, after correcting for the tune shift and coupling generated by the vertical separation of the beams at these locations. In the early years of operation, electron cloud effects in the LER had to be mitigated by solenoidal fields in the straight sections, addition of antechamber, photon stops and TiN coatings in the arcs. A complete list of improvements made to PEP-II over the years can be found in reference [24].

CESR

Until 2001 CESR operated as a symmetric energy collider at 5 GeV with electrons and positrons circulating in the same beam pipe. In 2001 there were nine bunch trains in each beam with 4 bunches per train for a total of 71 long-range interactions and 1 head-on collision. The beams were horizontally separated into pretzel orbits by electrostatic separators. The beam separations appear to have ranged from 4 to 7 σ [25]. The bunch currents were limited by the parasitic interactions. When a 5th bunch was added to each train, the specific luminosity and the beam lifetimes suffered [25]. Attempts to increase the bunch current beyond 7.5 mA with 4 bunches in each train also led to lower lifetimes. The average beam-beam tune shift in the vertical plane saturated at 0.07. In 2001 CESR became CESR-c to study the bound states of charmed quarks and the energy was lowered to 2 GeV. During 2006 it operated with 8 trains of 3 bunches each, so each bunch suffered 47 long-range interactions and 1 head-on collision. Beam-beam effects were more severe at the lower energy. After local compensation of the phase

advance shifts and beta-beats due to the long-range interactions, bunch currents could be raised to 3 mA from 2.5 mA before the compensation [26].

3.1.3 Scaling Laws

Scaling laws which relate how beam loss rates or luminosity lifetimes relate to beam parameters can be useful for predicting the changes when beam parameters change in a given machine, for example after an upgrade. However these laws depend on the details of the machine and can usually not be applied across different accelerators. Furthermore even in a single machine, it is hard to measure beam loss rates or emittance growth against a single variable (such as bunch intensity of the opposing beam) over a wide enough range and with enough statistics, keeping all other factors constant. This is usually due to the lack of dedicated study time. Typically the loss rates or beam growth are measured at different points in time when other machine parameters (such as orbits, tune, chromaticities etc) may have also changed. With these caveats in mind, we now take a look at some scaling laws, some of which were obtained from data taken during machine experiments.

3.1.3.1 Tevatron: Losses at Injection

At injection, the long-range interactions are responsible for losses. In 2005, the losses of anti-protons and protons were fitted to some key parameters. Figure 4 shows the proton loss rate dependence on the horizontal chromaticity.

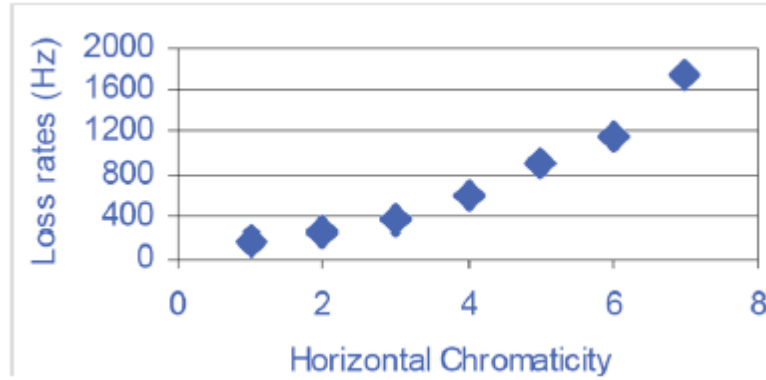


Figure 4: Dependence of proton loss rates in the Tevatron on horizontal chromaticity at injection.

The empirical law relating proton and anti-proton losses to key parameters (adapted from [27]) was found to be

$$\frac{\Delta N_{a,p}}{N_{a,p}} \propto \sqrt{t} N_{p,a} \varepsilon_{a,p}^2 Q_{a,p}^2 \mid \Rightarrow (Q_{x,y}, d_{a-p}, \varepsilon_L, D_{apert} : const) \quad (1)$$

Here t is the time spent at injection, N_p , N_a are the proton and anti-proton bunch intensities, ε_p , ε_a are the proton and anti-proton transverse emittances, Q' is the chromaticity. The above dependencies hold only if the variables in parentheses are held

constant. Q_a, Q_p the tunes, d_{a-p} , the separation between the beams, ε_L the longitudinal emittance and D_{apert} is the distance to the physical aperture. The functional dependencies on these parameters (N, ε, Q') can be completely different if any of the variables held constant, e.g. the tunes, change. The \sqrt{t} dependence can be explained as the initial time dependence of a normal diffusion process [28], which at long times progresses to the more familiar $\exp(-t)$ decay for the intensity. It would be desirable to develop a theoretical model that explains the linear dependence on the opposing beam intensity and the quadratic dependence on its emittance and chromaticity but such a detailed understanding has not yet been developed.

3.1.3.2 *Tevatron: Anti-Proton Losses during Stores*

Anti-proton loss rates are determined mostly by the long-range interactions. Data taken during 2004-2005 could be empirically fit to the law [27]

$$\frac{1}{\tau_a} = \frac{1}{N_a} \frac{dN_a}{dt} \propto N_p \frac{\varepsilon_a^2}{d_{a-p}^3} \mid \Rightarrow (Q_{x,y}, Q'_{x,y}, \varepsilon_p, \varepsilon_L, M, D_{apert} : const) \quad (2)$$

where M is the bunch number in the train and d_{a-p} is an average distance between the beams or more precisely the scale of the helix size compared to a nominal helix. The dependence on the beam separation was measured by changing the size of the helix everywhere in the ring by a scale factor. It is worth noting that changing the helix also changes tunes, coupling and chromaticities so their effects on beam loss may also be present. As at injection, the losses depended linearly on the opposing beam intensity and quadratically on its own transverse emittance. It is possible that these dependencies on (N, ε) are nearly universal for a well tuned machine away from harmful resonances. One machine where this could be tested is the LHC which also has several long-range interactions per turn.

3.1.3.3 *SPS Study of Proton Losses*

It is very likely that the inverse cube power law dependence on the beam separation is not universal but depends on the details of the beam and machine parameters. One example in the SPS is drawn from a study done with a single proton bunch interacting with two anti-proton bunches [29]. At two points the beams collided head-on, at two other points they were separated by $6-7\sigma$ of the anti-proton beam size. The loss rate and background rates were measured during two horizontal tune scans, one with full separation and the other with half their separations at the parasitic interaction locations. Figure 5 shows the decay rate on the left vertical scale and the background rate on the right vertical scale. There was a jump in the rates (by a factor of 2 – 3) for the halved separation only at the 13th and 16th order resonances, but not at the 10th order resonance.

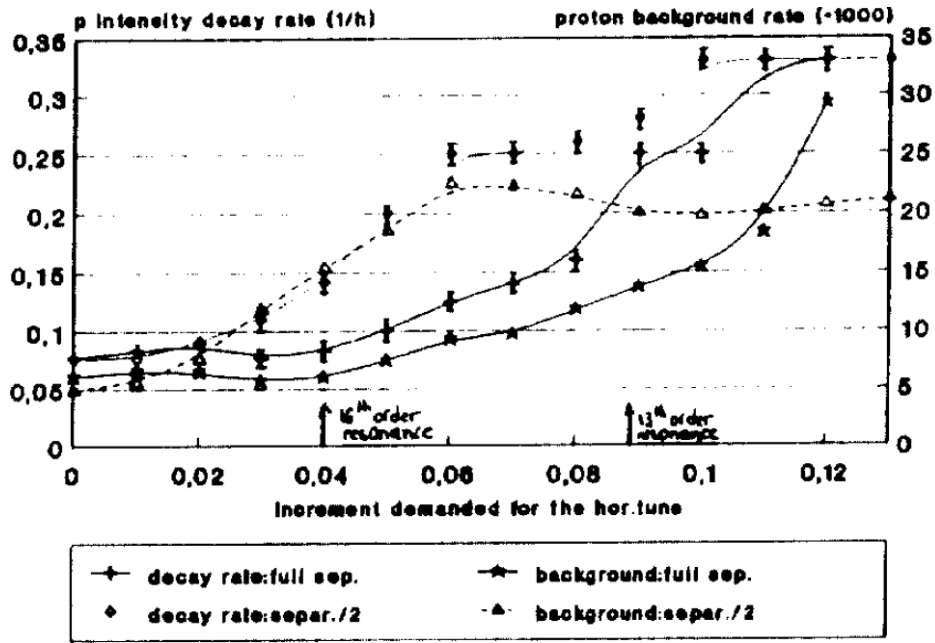


Figure 5: Proton intensity decay rate and proton background rate as a function of the horizontal tune at two separations (taken from [29]).

The power law dependence on the separation is weaker in this measurement compared to the Tevatron data and it is tune dependent. The jump in rates at the 16th order resonance suggests that it was driven by the parasitic interactions but the 10th order resonance was not.

3.1.3.4 *Tevatron: Proton Losses due to Head-on Collisions*

Proton loss rates during the first two hours of stores in 2008 are plotted against the product of the anti-proton bunch intensity and the ratio of emittances in Figure 6 below.

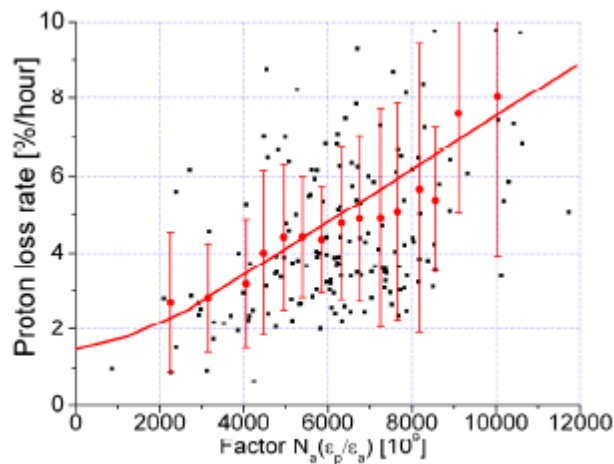


Figure 6: Proton loss rates vs. $N_a \left(\frac{\epsilon_p}{\epsilon_a} \right)$ during stores in 2008 (taken from Ref [4]).

This shows a nearly linear dependence of proton losses on this product. This suggests an empirical law

$$\frac{1}{\tau_p} = \frac{1}{N_p} \frac{dN_p}{dt} = N_a \left(\frac{\varepsilon_p}{\varepsilon_a} \right) \mid \Rightarrow (Q, Q', \beta^*, \varepsilon_L : \text{const}) \quad (3)$$

However note that the error bars on the data are fairly large. Also, there was not much variation in the proton emittance in this data.

The only models that exist to describe particle transport and beam loss in the absence of external noise are based on diffusion due to the overlapping of resonances. The diffusion coefficient is determined by the change in action which when dominated by beam-beam effects is proportional to the beam-beam parameter, hence

$$D(J) \sim \Delta J^2 \sim \xi^2 \quad (4)$$

Diffusion models therefore lead to diffusion coefficients that depend quadratically on the beam-beam parameter. In general extracting the lifetime from the diffusion coefficients requires solving a diffusion equation. In some cases the lifetime or loss rate can be extracted more directly. For example, the loss rate in the case of isotropic diffusion can be expressed in terms of the diffusion coefficients as [30]

$$\frac{1}{\tau} = N_D \left(\int \frac{J_r dJ_r}{D(J_r)} \right)^{-1} \quad (5)$$

where N_D is the number of dimensions (= 2 or 3 if longitudinal effects are included), J_r is the radial action and $D(J_r)$ is the radial isotropic diffusion coefficient. Thus the loss rate should also depend quadratically on the beam-beam parameter. The empirical fit above in Equation (3) shows a linear dependence on the beam-beam parameter. Reconciling theoretical models to the empirical fits remains a challenge.

3.1.4 Influence of Machine Optics on Beam-Beam Phenomena

In all colliders global orbits, tunes, coupling, chromaticities etc have to be well controlled for optimum integrated luminosity. Here I will discuss some recent examples of how local optics parameters in the interaction regions and beam-beam interactions have influenced performance.

3.1.4.1 Local and Beam-Beam Chromaticity

Experience at the Tevatron

Beam-beam effects can directly contribute to chromaticity. The head-on interactions can do so for bunches with lengths comparable to β^* or for short bunches if the beams are not exactly round at the IP so that the beam-beam tune shift does depend on the β^* values. Alternatively collisions at a crossing angle can also contribute to chromaticity. However these are usually relatively small contributions. Long-range interactions on the other hand have sextupole components in their multipole expansion and if these interactions occur at regions of non-zero dispersion can contribute significantly to the chromaticity. This is the case in the Tevatron where the contributions also differ bunch by bunch since each bunch has its own distribution of long-range separations and locations. The left plot in Figure 7 shows the theoretically calculated chromaticities at top energy due to the long-range interactions only, taken from [31].

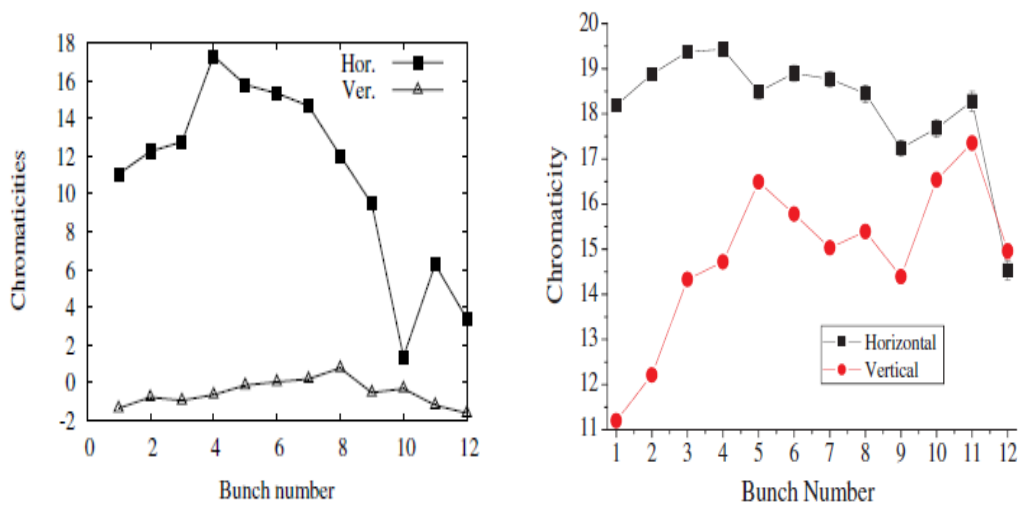


Figure 7: Left: Theoretical estimate of bunch-by-bunch chromaticity due to long-range interactions only. The right plot shows the measured bunch-by-bunch chromaticity that includes machine chromaticity and the effects of coupling as well.

In this theoretical calculation, the contributions to the vertical chromaticity are fairly small because the vertical dispersion is also small around the ring. However this does not take into account coupling between the two planes. The machine chromaticity, which would shift all the chromaticities by constant amounts, was not included. The measured bunch by bunch chromaticity in the Tevatron shown in the right plot of Figure 7, taken from [27], demonstrates (a) similar variation in chromaticity between the bunches and (b) that coupling tends to equalize the horizontal and vertical chromaticities.

It is worth noting that just like the tunes, the chromaticities also depend on the transverse amplitudes and chromaticity footprints exist which are also different for each bunch [32]. As with the beam-beam tune footprints, these footprints are hard to observe directly with measurements. However they can have observable consequences. If particles have chromatic tunes that lie near resonances, then their momentum deviation, their transverse amplitude and the specific bunch will determine which particles are lost due to these resonances.

The level of machine chromaticity also influences the effects of the long-range interactions. Prior to December 2008, the machine chromaticity in the Tevatron during the squeeze was kept between 12-14 units to stabilize the protons against the head-tail instability. However during two stages of the squeeze when the beam separations were low, there were significant proton losses that were accompanied by a reduction in their bunch length. Particles with large momentum deviations were likely hitting synchro-betatron resonances and getting lost. Lowering the chromaticity to about 5 units still provided enough tune spread for stability but also lowered the proton losses and removed the longitudinal shaving [33].

A better-known phenomenon is the contribution of the interaction region to the chromaticity. At collision optics, the triplet quadrupoles contribute large linear and non-linear chromaticity as well as strong chromatic beta beats. The linear chromaticity is corrected to the desired value but the nonlinear chromatic effects, if not corrected, can lead to beam loss due to beam-beam or lattice driven synchro-betatron resonances. This

was the experience in the Tevatron until 2006 when a second order chromaticity correction was put into effect [34]. This reduced the quadratic chromaticity by about a factor of five and decreased proton losses during stores.

Experience at KEKB with Chromatic Coupling

An interesting case of the combined effects of chromaticity and coupling has been recently reported from KEKB after the installation of crab cavities in 2007 in each ring. Coupling was found to be stronger for off-momentum particles both in measurements and simulations with their model lattice. Sources of this chromatic coupling were thought to be the misaligned sextupoles, higher order multiples in the final focus quadrupoles, special magnets and other lattice errors. Weak-strong and strong-strong beam-beam simulations showed that the luminosity was not sensitive to the chromatic coupling without the crab cavities but in their presence, the luminosity could drop as much as 10% due to chromatic effects [35].

KEKB operates close to the 1st order synchro-betatron resonance near the diagonal in tune space $q_x - q_y + q_s = N$, and various sources could be driving this resonance. Installation of skew sextupoles to control the chromatic coupling resulted in about 15% increase in luminosity [22]. Measurements showed that these skew sextupoles were effective in increasing the luminosity with the crab cavities turned off as well [23]. The maximum vertical beam-beam parameter achieved is 0.09 in the higher energy ring as opposed to a predicted value of 0.15 by beam-beam simulations. The reasons for the discrepancy and the limitations on achieving higher luminosity were under active study as of June 2010 [23] and are discussed in the article by K. Ohmi below.

It is an interesting question why KEKB was so susceptible to this chromatic coupling and not other accelerators such as PEP II, since rotational misalignments of sextupoles are not uncommon. It could simply be that KEKB operated closest to the linear synchro-betatron resonances. The tunes in PEP II appear to have been closest to the higher order resonance $q_x - q_y + 2 q_s = N$ in both rings [36] and may have therefore not been affected.

3.1.4.2 *Local Coupling and Dispersion*

In the Tevatron, global coupling is controlled to a minimum tune split of 0.002. Both in the Tevatron and in RHIC local decoupling in the IRs has been operational to correct for rotational misalignments of triplet quadrupoles (in some cases by several mrad) in order to optimize luminosity. Local dispersion is measured and corrected to within a few cm at the IPs in the Tevatron.

In lepton colliders there are direct geometrical effects since the coupling controls the vertical emittance and hence the vertical beam sizes at the IPs. KEKB finds it essential to correct both the local coupling and the dispersion at the IP during their luminosity optimisation. They use anti-solenoids and skew quadrupoles to correct the local coupling sources and dipole correctors to correct the dispersions in both planes at the IP. In PEPII reducing the coupling in the interaction region of the low energy ring was found to be essential to increasing the luminosity. This was done by installing several permanent magnet skew quadrupoles in the IR [24]. It seems to be generally accepted that the dynamical effects of uncorrected coupling and dispersion have a greater impact on the luminosity than the purely geometrical effects in lepton colliders.

3.1.4.3 *Matching Beam Sizes*

SPS had reported that when proton emittances were 4 times larger than anti-proton emittances, protons could be lost due to high order resonances such as 13th and 16th order. From 1988 onwards, the emittance ratio was reduced to <2 , proton losses dropped as long as resonances of lower order such as the 10th were avoided. Dedicated studies were done to measure the impact of unequal emittances [29]. One proton (rms normalized emittance $\sim 5.5 \pi$ mm-mrad) and one anti-proton bunch (rms normalized emittance $\sim 7.5 \pi$ mm-mrad) were injected into the SPS and each collided twice with the other bunch per turn. The tunes were changed and proton background rates and lifetimes were measured first with the initial anti-proton emittances and then the anti-proton bunch was scraped to reduce its emittance to nearly equal the proton emittance and the loss rates measured again. In the first case with the larger and more intense anti-proton bunch, the proton bunch was not sensitive to 13th and 16th order resonances. In the second case with the smaller and less intense anti-proton bunch, the proton bunch was sensitive to these resonances even though the beam-beam parameter was about 40% lower. A scaling law such as the one in Equation (3) would not explain this dependence. A quantitative theoretical model to explain these observations has not yet been developed.

Observations in the Tevatron have been similar. When electron cooling of anti-protons in the Recycler made their emittance about 5-6 times smaller than those of protons, the latter suffered large losses [2]. A noise source was introduced to increase the anti-proton emittance and reduce the emittance ratio to about 3. This reduced the losses to acceptable levels.

HERA also had to control the mismatch but in their case, the beam sizes had to be matched to within 20% for tolerable beam losses [13]. This stringent tolerance is at first glance harder to understand given that the beam-beam parameter was about 0.001 compared to 0.005 in the SPS and about 0.008 in the Tevatron. One can speculate about possible reasons, e.g. the lower beam-beam spread allowed the proton tunes to lie closer to resonances but made them more susceptible to small perturbations such as an increased non-linear field from the smaller opposing beam.

3.1.5 **Orbit Vibrations at the IP**

Orbit vibrations at the IP modulate the offset between the colliding beams and are thought to lead to an emittance increase depending on the frequencies of modulation. Random orbit fluctuations at the IP have been theoretically shown to lead to diffusion and emittance growth [37].

Triplet vibrations in the frequency range from 4 to a few hundred Hz have been measured at the Tevatron and these frequencies have also been seen in the orbit spectrum [38]. Vibrations in this range are attributed to the liquid helium pumps, ground vibrations due to passing vehicles etc. An orbit feedback system installed in 2005 reduced the orbit drift during stores by a factor of eight and may have also helped to keep the bunches better centred at the IPs [39].

In RHIC orbit modulations such as those resulting from the 10 Hz vibrations of the triplet quadrupoles have long been thought to limit proton beam lifetime during stores [9]. Recent measurements showed that modulations of the betatron tunes and orbits could be well correlated with these vibrations [40]. It was suggested that the orbit

modulation could manifest itself as a modulated crossing angle at the IPs and may explain the relative large proton losses at the start of stores in recent years.

In HERA, closed orbit oscillations of the electron beams were measured at the IPs with largest amplitudes at frequencies in the range 2-15 Hz. The sources were traced to vibrations of the electron triplet quadrupoles in the two IRs due to ground motion. These oscillations of the electron orbit led to increased proton background rates as the beams were brought into collision. A feedback system using BPMs upstream and downstream of the IPs was installed to control these oscillations [41].

3.1.6 Coherent Phenomena

Coherent instabilities have long been observed in lepton colliders that operate with nearly equal intensities in both beams, see e.g. reference [42]. Observations of coherent beam-beam effects have been less frequent in hadron colliders. Beam loss due to coherent beam oscillations was reported in the ISR [17]. This usually occurred when the vertical separation between the beams was gradually reduced to initiate collisions. The losses started when the separations reached about 1σ and the beam-beam tune shift was about 0.001 per interaction region. The losses were reduced by a combination of reducing the separation at one interaction region at a time, improving the vertical feedback system and increasing the tune spread to increase Landau damping. SPS does not appear to have suffered from beam loss due to coherent oscillations, possibly due to the large difference in anti-proton and proton intensities.

In the Tevatron coherent instabilities do not cause beam loss during regular operation. There have been sporadic reports of multi-bunch coherent instabilities, usually when the chromaticity was too low [7]. However coherent dipole modes have been observed in recent dedicated studies [43]. The observed modes were in rough agreement with the coupled bunch mode spectrum calculated from a matrix analysis using 3 bunches per beam interacting only via the head-on interactions. However there were some observed frequencies that were unexpected.

RHIC reported the first observation of coherent modes in a hadron collider [44]. Both the sigma mode and the pi mode were observed during operation with protons beams with four head-on collisions per turn and a beam-beam parameter/IP of 0.0015. These modes, shown in Figure 8, appeared when the bunches were colliding and disappeared when the bunches were separated.

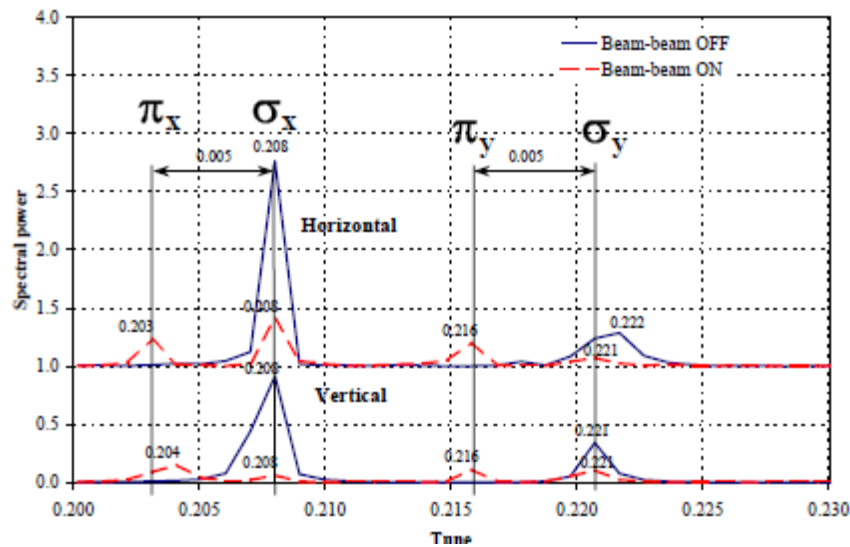


Figure 8: First observation of coherent beam-beam dipole modes in RHIC (taken from [44]).

They were also observed in a dedicated experiment with 1 collision per turn and beam-beam parameter = 0.003. These modes could be well reproduced in simulations [45]. More recent BTF measurements in 2009 have shown the appearance of sigma and pi modes in the vertical plane of both beams but not in the horizontal plane during regular operation [46]. No instability was associated with the appearance of these modes, especially the pi mode, which is outside the incoherent beam-beam spectrum. This runs counter to theoretical expectations that the pi mode being undamped and would therefore, in the presence of machine impedance for example, initiate instabilities [47]. This needs to be better understood especially for the LHC where much effort has been put into understanding possible mechanisms for damping this mode, e.g. [48].

3.1.7 Compensation of Head-on Interactions with an Electron Lens

Compensation with an electron lens is covered elsewhere in this issue, so the discussion here will be brief. Operation with a Gaussian electron lens in the Tevatron has shown that it produces the expected tune shift and tune spread when acting on an anti-proton bunch [49]. Compensation of the head-on interactions has not yet been observed but simulations of the compensation in RHIC and the LHC has been done by three different codes with similar results [50-52]. They find the following:

- The compensation works at higher values of the bunch intensity than at present used in operation in RHIC or the design value in LHC respectively. RHIC already suffers emittance growth and beam loss at present intensities. Even though the head-on collisions cause losses, the electron lens compensation does not become effective until higher intensities. What determines the critical bunch intensity above which the electron lens is useful?
- The electron lens intensity should not compensate more than half the tune spread due to the head-on interaction. At higher electron lens intensities and larger reduction of the tune spread, the proton beam lifetime suffers. Coherent

instability due to a small tune spread is not the cause of this result since these were weak-strong simulations

- The electron transverse density should be uniform with a width larger than that of the proton bunch that is being compensated. With a wider lens, the proton bunch does not experience the sharp nonlinear fields at the edges of the electron beam and effectively sees mostly the linear part of the force from the electron lens. However the effect of the electron lens is more beneficial than a simple tune shift.

These numerical predictions need to be tested with measurements. These will happen after electron lenses are installed in RHIC. If these predictions are borne out, then there is more to understand about the electron lens compensation.

3.1.8 Compensation of Long-Range Interactions with Wires

The principle of long-range compensation with a wire was partially tested in the SPS, DAΦNE, and RHIC in 2009. In RHIC the measurements were done in a single study where a single long-range interaction was created at a very small phase difference from the wire location [53]. Measurements of loss rates and bunch intensities showed that the wire reduced the losses for the beam in the Yellow ring but not for the beam in the Blue ring. Simulations seem to suggest that the separations between the beams (3.1σ) may not have been large enough for the wire compensation to be effective [54]. We recall the field due to the long-range interaction approaches the $1/r$ dependence of the field of a wire when the separations are significantly greater than 3σ . The wires have been removed from RHIC so further measurements may have to wait until wires are installed in the LHC during an upgrade. In earlier studies at RHIC, the effect of a wire on a beam was studied as a function of the beam-wire separation with different particle species at injection and collision [55]. Extensive simulations of the beam-wire interactions showed satisfactory agreement with the measurements [56]. The beam-wire distance at which the loss rates spiked found by simulations agreed to within 0.5σ with measurements at injection and collision and the higher loss rates observed with deuteron beams compared to gold beams were also reproduced in simulations.

3.1.9 Future Developments Related to the LHC

Crab cavities: Following the success with crab cavities in KEKB, there are plans to test the concept for implementation in the LHC during a future upgrade [57]. Two schemes are envisaged: a global scheme with a single cavity per ring or a local scheme with pairs of crab cavities around the high luminosity IRs. Some of the beam dynamics issues were examined in reference [58]. Some issues require detailed studies such as the sensitivity of the beam to phase noise in the cavities, synchro-betatron resonances driven by dispersion in these cavities and perhaps others.

Crab waist: The crab waist concept [59] has been demonstrated to work in DAΦNE [60]. The concept works for flat beams by placing sextupoles at appropriate phase advances in the IR such that the vertical phase advance in the IR becomes independent of horizontal betatron oscillations. This effectively suppresses some resonances driven

by the beam-beam interactions. It is not immediately obvious that the same scheme will also work in hadron colliders with round beams where resonances with modulations of the horizontal phase are strong. Are there modifications of this scheme that can be successfully applied to hadron colliders?

Flat bunches and large Piwinski angles: One of the possible paths to higher luminosity at the LHC is the so-called large Piwinski angle (LPA) scheme in which bunches collide at an angle with a large Piwinski parameter ($\phi \sim 2$) and large bunch intensity keeping the beam-beam parameter at the same value as in other schemes [61]. The luminosity increases with the bunch intensity. The number of bunches is reduced to keep the beam current, hence the heat load, down. An additional 40% gain in luminosity is obtained if a longitudinally flat profile rather than a Gaussian profile is used. These bunch profiles have lower peak fields and hence lower electron cloud effects. Preliminary studies of beam-beam effects showed lower transverse diffusion than with Gaussian bunches [62]. This needs to be checked with more detailed studies. If these results are confirmed, this scheme with longitudinally flat profiles may be attractive even without large Piwinski parameters and high bunch intensities.

Beam-beam limit at high energies: There are plans to operate the LHC at more than double the design energy of 7 TeV. At such energies, effects of synchrotron radiation become much more important with the radiation damping time being of the order of an hour. Will the beam-beam limit be set by the saturation of a beam-beam parameter due to emittance growth (1st beam-beam limit in lepton colliders) or by the creation of tails and beam loss? This issue is already under study [20].

A general list of the beam-beam related issues in the LHC were discussed in reference [63]. Besides the effects discussed in this reference and those listed above, there are likely to be other manifestations of beam-beam effects at the LHC, some anticipated and some perhaps not. The multiple physics aspects of this effect will remain interesting in any circumstance.

3.1.10 References

1. S. Saritepe, G. Goderre, and S. Peggs, "Observations of the Beam-Beam Interaction in Hadron Colliders", in "Frontiers of Particle Beams: Intensity Limitations", Springer-Verlag, Lecture Notes in Physics (1991).
2. A. Valishev, [Simulation of Beam-beam Effects and Tevatron Experience](#), Proceedings of EPAC08, pg 2937
3. K. Gollwitzer, [Run II Luminosity Progress](#), PAC07, pg 1922
4. V. Shiltsev, [High Luminosity Operation, Beam-Beam Effects and Their Compensation in TEVATRON](#), Proceedings of EPAC08, pg 951
5. T. Sen, [New Aspects of Beam-Beam Interactions in Hadron Colliders](#), Proceedings of PAC03, pg
6. T. Sen., [Beam-beam phenomena in the Tevatron](#), ICFA Beam Dynamics Newsletter No. 34, pg 45 (2004)
7. Y. Alexahin, [Theory and Reality of Beam-Beam Effects at Hadron Colliders](#), Proceedings of PAC05, pg 544
8. W. Fischer, [RHIC Luminosity Upgrade Program](#), Proceedings of EPAC10, pg 1227
9. W. Fischer et al, [RHIC Proton Beam Lifetime Increase with 10- and 12-pole Correctors](#), Proceedings of IPAC10, pg 4752

10. C. Montag et al, [RHIC Performance as a 100 GeV Polarized Proton Collider in Run-9](#), Proceedings of IPAC10, pg 531
11. M. Bieler, [Recent and past experience with beam-beam effects at HERA](#), Proceedings of LHC Beam-beam workshop (1999)
12. M. Minty, [HERA Performance Upgrade: Achievements and Plans for the Future](#), Proceedings of EPAC04, pg
13. F. Willeke, [Experiences With The Hera Lepton-Proton Collider](#), Proceedings of APAC07, pg 843
14. L. Evans et al, [Beam-Beam Effects in the Strong-Strong Regime at the CERN-SPS](#) , Proceedings of PAC89
15. M. Harrison and R. Schmidt, [The Performance of Proton Antiproton Colliders](#), Proceedings of EPAC 90, pg 55
16. C. Fischer et al, [Performance of the CERN ISR at 31.4 GeV](#), Proceedings of PAC79, pg 3155
17. J.Y. Hemery et al, [Investigation of the Coherent Beam-Beam Effects in the ISR](#), Proceedings of PAC81, pg 249
18. B. Zotter, [Low-beta configurations for all eight intersections of the ISR](#), CERN-ISR/TH/80-04
19. K. Johnsen, “The ISR and Accelerator Physics”, Part Acc, Vol 18, pg 167 (1986)
20. S. Myers, [Four Decades of Colliders \(from the ISR to LEP to the LHC\)](#) , Proceedings of IPAC10, pg 3663
21. Y. Funakoshi et al, [Recent Progress of KEKB](#), Proceedings of PAC09
22. Y. Ohnishi et al., [Measurement of chromatic x-y coupling](#), Phys. Rev. ST Accel. Beams **12**, 091002(2009).
23. Y. Funakoshi et al, [Recent Progress of KEKB](#)., Proceedings of IPAC10, pg 2372
24. J. Seeman, [Last Year of PEP-II B-Factory Operation](#), Proceedings of EPAC08, pg 946
25. D. Rubin et al, [CESR Status and Performance](#), Proceedings of PAC01, pg 3520
26. J. Crittenden, [Compensation Strategy for Optical Distortions Arising from the Beam-Beam Interaction at CESR](#), Proceedings of PAC07, pg 1778
27. V. Shiltsev et al, [Beam-beam effects in the Tevatron](#), Phys. Rev. ST Accel. Beams **8**, 101001 (2005)
28. T. Sen et al, [Beam Losses at Injection Energy and during Acceleration in the Tevatron](#) , Proceedings of PAC03, pg 1754
29. K. Cornelis et al, [The Beam-Beam Effect in the SPS Proton Antiproton Collider for Beams with Unequal Emittances](#), Proceedings of EPAC90, pg 1670
30. C. W. Gardiner, “Handbook of Stochastic Methods: for Physics, Chemistry and the Natural Sciences”, Springer (2004)
31. T. Sen et al, [Beam-beam effects at the Fermilab Tevatron: Theory](#), , Phys. Rev. ST Accel. Beams **7**, 041001 (2004)
32. B. Erdelyi and T. Sen, [Analytic studies of the long range beam-beam tune shifts and chromaticities](#), FERMILAB-TM-2171, (2002)
33. A. Valishev et al, [Recent Tevatron Operational Experience](#), Proceedings of PAC09
34. A. Valishev et al, [Observations and Modeling of Beam-Beam Effects at the Tevatron Collider](#), Proceedings of PAC07, pg 925
35. D. Zhou et al, [Simulations of beam-beam effect in the presence of general chromaticity](#), Phys. Rev. ST Accel. Beams **13**, 021001 (2010)
36. Y. Cai et al, [Luminosity Improvement at PEP-II Based on Optics Model and Beam-beam Simulation](#), Proceedings of EPAC06, pg 661
37. T. Sen and J. Ellison, [Diffusion due to Beam-Beam Interaction and Fluctuating Fields in Hadron Colliders](#), Phys. Rev. Lett. **77**, 1051 (1996)
38. V. Shiltsev et al, Tevatron magnets and orbit vibrations, ICFA Advanced Beam Dynamics Workshop on Nanometer Size Colliding Beams (Nanobeam 2002)
39. V. Ranjbar. [Stabilizing Low Frequency Beam Motion in the Tevatron](#), Proceedings of

- PAC05, pg 1353
40. M. Minty, [Effect of Triplet Vibrations on RHIC Performance with High Energy Protons](#), Proceedings of IPAC10, pg 528
 41. J. Keil et al, [Design of a Local IP Orbit Feedback at HERA-e](#), Proceedings of EPAC06, pg 2988
 42. S. Krishnagopal, [Luminosity-Limiting Coherent Phenomena in Electron-Positron Colliders](#), Phys. Rev. Lett. **76**, 235 (1996)
 43. A. Valishev et al, [Observation of Coherent Oscillations of Colliding Bunches at the Tevatron](#), Proceedings of EPAC08, pg 3158
 44. W. Fischer et al, [Observation of Strong-Strong and Other Beam-Beam Effects in RHIC](#), Proceedings of PAC03, pg 135
 45. M. Vogt et al, [Simulations of Coherent Beam-Beam Modes at RHIC](#), Proceedings of EPAC02, pg 1428
 46. M. Minty et al, [High Precision Tune and Coupling Feedback and Beam Transfer Function Measurements in RHIC](#), Proceedings of IPAC10, pg 522
 47. Y. Alexahin, "On the Landau Damping and Decoherence of Transverse Dipole Oscillations in Colliding Beams", Part. Accel. **59**, pg 43 (1998)
 48. T. Pieloni and W. Herr, Coherent Beam-Beam Modes in the CERN Large Hadron Collider (LHC) for Multiple Bunches, Different Collisions Schemes and Machine Symmetries, PAC05, pg 4030
 49. A. Valishev et al, [Progress with Tevatron Electron Lens Head-on Beam-Beam Compensation](#), Proceedings of IPAC10, pg 2084
 50. H. J. Kim and T. Sen, [Electron Lens in RHIC](#), Proceedings of IPAC10, pg 2074
 51. Y. Luo & W. Fischer [6-D Weak-strong Simulation of Head-on Beam-beam Compensation in the RHIC](#), Proceedings of IPAC10, pg 4758
 52. A. Valishev, [Simulations of Head-on Beam-Beam Compensation at RHIC and LHC](#), Proceedings of IPAC10 pg 2081
 53. R. Calaga et al, [RHIC BBLR Measurements in 2009](#), Proceedings of IPAC10, pg 510
 54. H.J. Kim & T. Sen, [Long-Range Beam-Beam Compensation in RHIC](#), Proceedings of IPAC10, pg 2072
 55. W. Fischer et al, [Experiments with a DC Wire in RHIC](#), Proceedings of PAC07, pg 1859
 56. H.J. Kim et al, [Simulations of beam-beam and beam-wire interactions in RHIC](#), PRSTAB, Vol 12, 031001 (2009)
 57. P. Raimondi, "Status of the SuperB effort", 2nd Workshop on Super B-Factory, Frascati, March 2006
 58. M. Zobov et al, [Test of "Crab-Waist" Collisions at the DAΦNE Φ Factory](#), Phys. Rev. Lett. 104, 174801 (2010)
 59. R. Calaga et al, [LHC Crab-cavity Aspects and Strategy](#), Proceedings of IPAC10, pg 1240
 60. Y. Sun et al, [Beam dynamics aspects of crab cavities in the CERN Large Hadron Collider](#), Phys. Rev. ST Accel. Beams **12**, 101002 (2009)
 61. F. Ruggiero & F. Zimmermann, [Luminosity optimization near the beam-beam limit by increasing bunch length or crossing angle](#), Phys. Rev. ST Accel. Beams, 5,061001 (2002)
 62. F. Ruggiero et al, [Beam-Beam Interaction, Electron Cloud, and Intrabeam Scattering for Proton Super-Bunches](#), Proceedings of PAC 2003, pg 123
 63. F. Zimmermann, "[Beam-beam effects in the Large Hadron Collider](#)", ICFA Newsletter No. 34, pg 26 (2004)

3.2 Review of Crab Crossing in KEKB

K. Ohmi for KEKB Commissioning Group, KEK, 1-1 Oho, Tsukuba, Japan
Mail to: ohmi@post.kek.jp

3.2.1 Introduction

KEKB had been operated with collision scheme with a finite crossing angle of 11×2 mrad. The peak luminosity was $1.76 \times 10^{34} \text{ cm}^{-2} \text{ s}^{-1}$ at 1340 mA and 1660 mA for electron and positron current. Crab cavities were introduced to compensate the crossing angle effectively and to realize the head-on collision in 2007. Head-on collision gave a high beam-beam performance in a beam-beam simulation [1]. We targeted a high beam-beam parameter larger than 0.1. The operation using the crab cavities has been done since February 2007. The maximum luminosity achieved was $2.11 \times 10^{34} \text{ cm}^{-2} \text{ s}^{-1}$. The chromatic coupling was corrected to achieve the luminosity [2]. Machine parameters for the peak luminosity without and with crab cavity is summarized in Table 2. The crab crossing in KEKB is reviewed in this part.

Table 2: Machine parameters to achieve the peak luminosity without and with crab cavities.

<i>Parameter</i>	<i>Unit</i>	<i>w/o crab</i>	<i>w crab</i>
Circumference, C	m	3016	3016
Emittances, ε_x (HER/LER)	10^{-9} m	24/18	24/18
bunch population, N_{\pm} (HER/LER)	10^{10}	6.3/7.8	4.7/6.5
hor. beta function at IP, β_x	cm	55/6	120/120
ver. beta function at IP, β_y	cm	10	0.59/0.59
Number of bunch, N_b	...	1335	1584
Total current, I_{\pm}	A	1.34/1.66	1.19/1.64
Luminosity, L	$10^{34} \text{ cm}^{-2} \text{ s}^{-1}$	1.76	2.11

3.2.2 Motivation for the Crab Crossing

3.2.2.1 *Beam-Beam Limit with or without Crossing Angle in Simulations*

Collision with a finite crossing angle ($11 \text{ mrad} \times 2$) had been adopted in KEKB to manage IR design for multi-bunch collision. The collision performance toward the luminosity $1 \times 10^{34} \text{ cm}^{-2} \text{ s}^{-1}$ was studied by using beam-beam simulations, while crab cavities had been developed to be a back up for troubles in the collision with the crossing angle. The luminosity was achieved to be $1.7 \times 10^{34} \text{ cm}^{-2} \text{ s}^{-1}$ without crab cavities. The luminosity was achieved at a high bunch current; therefore a burden on vacuum components was very heavy.

The crab cavity was in the limelight to upgrade KEKB again. Beam-beam simulations showed very high performance with crab cavity. The luminosity with or without crab cavity is simulated using weak-strong and strong-strong code, named BBWS and BBSS, respectively [1]. **Figure 8** shows the beam-beam parameter (ξ) estimated by the simulated luminosity as follows,

$$\xi_{\pm} = \frac{2r_e\beta_y}{N_{\pm}\gamma_{\pm}f}L$$

where r_e , γ , and f are the classical electron radius, relativistic factor and the collision repletion, respectively.

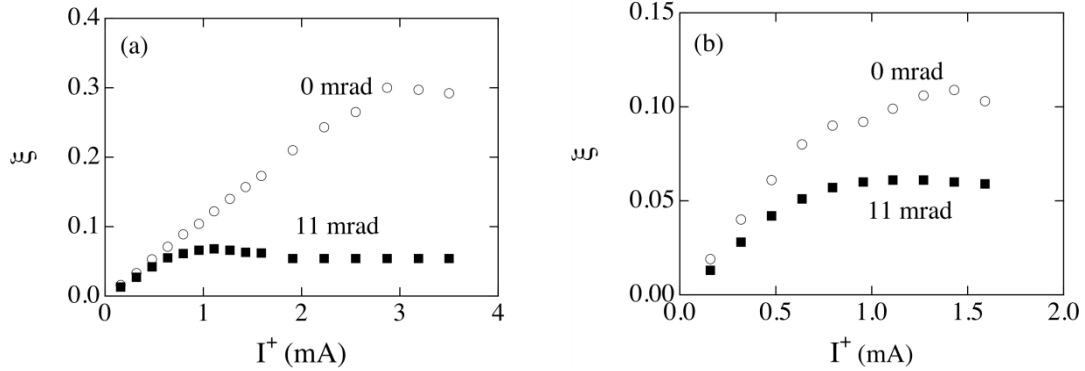


Figure 8: Beam-beam parameter as functions of positron current. Electron current is changed with the same ratio. Plots (a) and (b) are obtained by beam-beam simulation codes with the weak-strong (BBWS) and strong-strong (BBSS) model, respectively.

Another key point for the high luminosity is the tune-operating point. The horizontal tune is very close to a half integer in CESR and KEKB. The luminosity increases for approaching the half integer. Simulations also showed very high performance especially with crab cavity at the operating tune.

3.2.3 Operation with Crab Cavity

3.2.3.1 *KEKB Performance before Installation of the Crab Cavities*

The operation started with crab cavities at February 2007. One crab cavity was installed in each ring to save the budget. The beam tilts in x-z plane in all the position (s) of the ring. The tilt angle is characterized by a kind of dispersion dependent of z, $x = \zeta_x z$. $\Delta\zeta_x$, which is induced by the crab cavity, follows to linear transverse equation of motion and is satisfied to the periodic boundary condition. The dispersion ζ_x and its derivative ζ_x' are matched to the half crossing angle and zero at the collision point for the both rings. In the beam-beam simulation, tolerance for the crab angle was tight, especially in the strong-strong simulation as shown in Figure 9. The crab angle depends on the crab cavity voltage, and the horizontal beta functions at IP and the crab cavity. The crab cavity gives a transverse kick to the beam, when the rf phase is deviated from zero. The valance of the crab cavity voltages of the two rings was determined by whether the relative position of two beam at IP do not change for change of crab phase. The crab voltages are scanned with keeping the valance. Typical voltages are 0.97 MV and 1.45 MV for LER and HER rings, respectively, where β_x 's are 51 m and 122 m at the crab cavities.

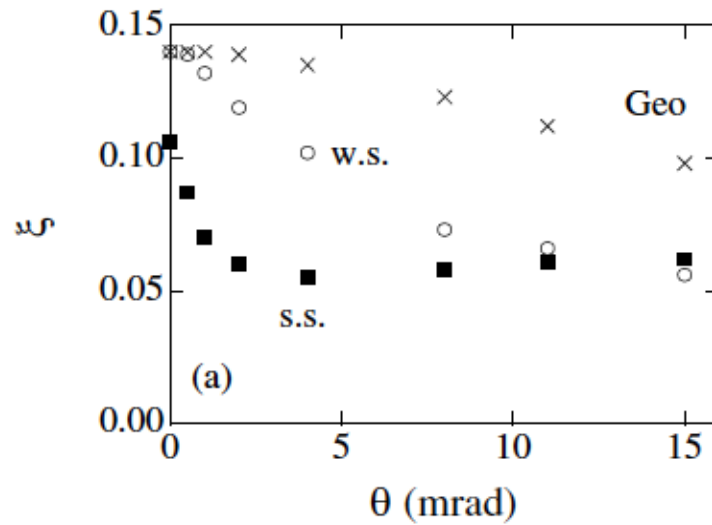


Figure 9: Beam-beam parameter for crossing angle. . Three kinds of dots are given by geometrical luminosity (Geo) and simulated luminosity using weak-strong (w.s) and strong-strong (s.s) model.

The luminosity tuning has been done every day since the start of 2007. Figure 10 shows the achieved specific luminosity. The luminosity given by the simulation is plotted, where two lines, Simulations I and II, are given for $\beta_x^* = 0.8$ m and 1.5 m, respectively, using the strong-strong simulation (BBSS). Black and blue dots depict measured luminosity with and without crab cavity. The luminosity was measured at the operation with 100 bunches (49 bucket spacing) to avoid high current issues, for example electron cloud or heating of vacuum components. The luminosity increased (the specific luminosity decreased) with keeping the beam-beam parameter in the measurement. The beam-beam parameters with and without crab cavity were 0.09 and 0.07, respectively. The gain of the crab cavity was about 20%. While the simulations showed higher luminosity and beam-beam parameter, especially at higher current product.

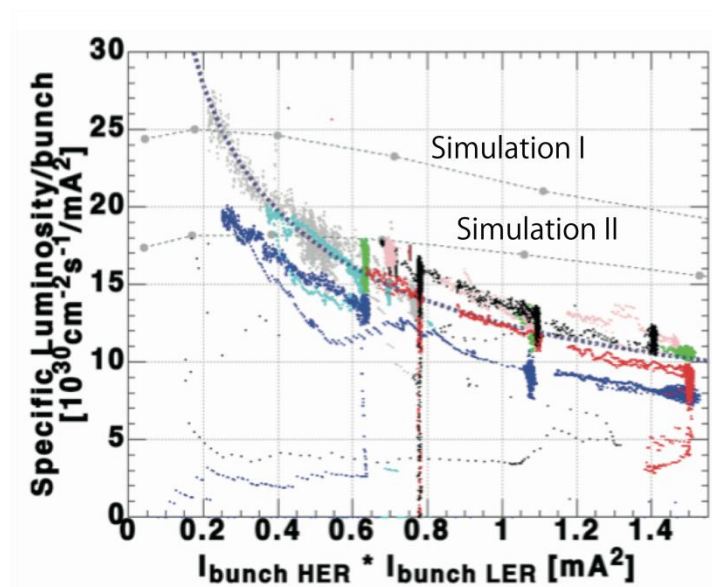


Figure 10: Specific luminosity as function of current product of two beams.

3.2.3.2 Correction of x-y Coupling at IP

Luminosity performance strongly depends on the machine condition. Main tuning knobs are collision offset [3], x-y coupling and vertical dispersion at IP in KEKB. The number of parameters for the collision offset is three, horizontal and vertical offset and vertical crossing angle. The number is six for x-y coupling and vertical dispersion for each ring, thus the total is twelve. These parameters are scanned one or two times in a day. Vertical waist position, horizontal dispersion and chromaticity at IP were also scanned a few times in a week. The crab voltage was scanned a few times in a month. The luminosity was 60-70% of the peak at the early stage of recovering after a long shutdown. It took a couple of month to reach the peak level of luminosity.

We are not sure whether our luminosity is really at the limit. It is only true that we spent three years to get the current peak luminosity. In 2009, we realized chromatic coupling limited the luminosity. The luminosity increased 25 % due to scanning the chromatic coupling. We had actually believed the luminosity before the chromatic coupling correction had been a rigid limit.

Luminosity tuning using the downhill simplex optimization has been done for the twelve coupling and dispersion parameters. The luminosity was saturated at the peak level in 4-8 hours in the optimization. The optimization process was also reproduced by the beam-beam simulation. Errors for the parameters, which were several unit of tuning knob in the operation, were applied, and then optimized values, which should be zero, were searched using the simplex method. Figure 11 shows the luminosity evolution for the simplex iterations. The achieved luminosity should be $2.5 \times 10^{31} \text{ cm}^{-2} \text{ s}^{-1} / \text{bunch}$, but saturated at $1.4\text{-}1.5 \times 10^{31} \text{ cm}^{-2} \text{ s}^{-1} / \text{bunch}$; 60% of the target value. The degradation is consistent with the measured value.

The knob scan process for each parameter was also examined using the beam-beam simulation. The optimized luminosity was again around 60 % of the target value. These facts show the complex of multi-parameter optimization.

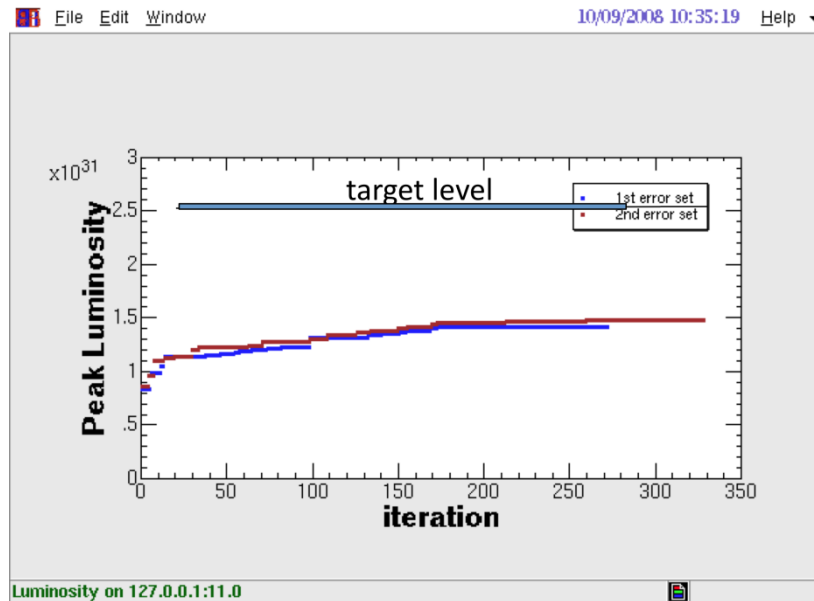


Figure 11: Luminosity optimization in the beam-beam simulation (BBSS, by M. Tawada).

X-y coupling and dispersion at IP were ambiguous as absolute values, though they are scanned every day. Efforts to measure the absolute values have been done. They were measured by turn by turn monitors near the IP [4,5]. We used two sets of monitors for the measurement. First set, named QCS monitor, is two monitors outside of final quadrupole magnets named QCS. Second set, named OctoPos monitor, is two monitors inside of QCS monitors. The two sets are not synchronized with each other. Several results given by OctoPos monitors are presented here. Figure 12 shows the phase space plot characterizing x-y coupling. X-y coupling is characterized by 4 parameters, R1 [rad], R2 [m], R3 [m^{-1}], R4 [rad], which are related to correlation of x-y, p_x -y, x- p_y , p_x - p_y , respectively. R1 and R2, which are related to y, are sensitive to the luminosity, while R3 and R4, which are related to p_y , are less sensitive. The parameters were scanned as is discussed before. Figure 13 shows R4 variation for R4 knob scan. R4 linearly changes and the gradient is 0.88. This fact showed the knob scan change the R parameters correctly. The absolute value was still ambiguous. Table 3 shows the coupling parameters measured April and May 2009. In this period, machine was well tuned, while the coupling parameters were finite values. R2 of LER was around 0.01. We doubted R2 because luminosity is lower than simulations. Figure 14 shows the luminosity as a function of R2 given by the beam-beam simulation. This strong dependence on R2 has been observed in measurements. Considering the luminosity, R2 does not deviate so large. R2 is sensitive for the measurement because it is related to y not p_y . Ambiguity on rotation of monitors was not clear. R3 and R4 were deviated from zero. The monitor has enough sensitivity for R3 and R4 in this range. Luminosity seems better for finite R3 and R4. We did not have clear answer how coupling corrected yet.

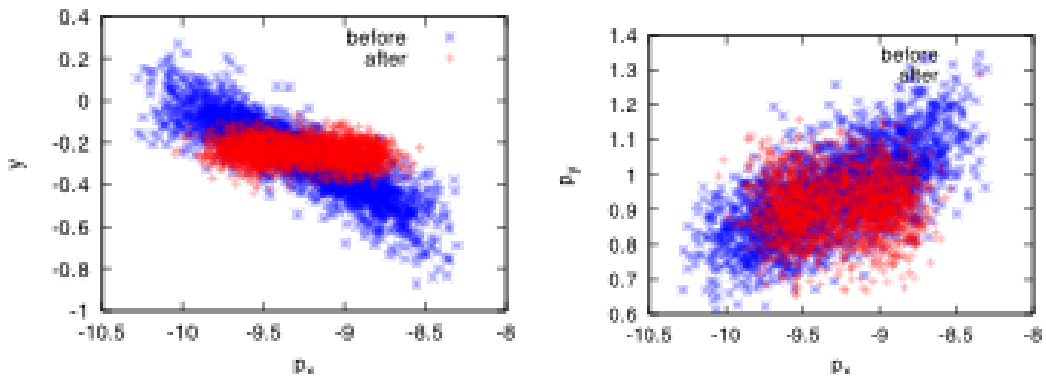


Figure 12: Phase space at IP measured by nearby turn-by-turn monitors (OctoPos).

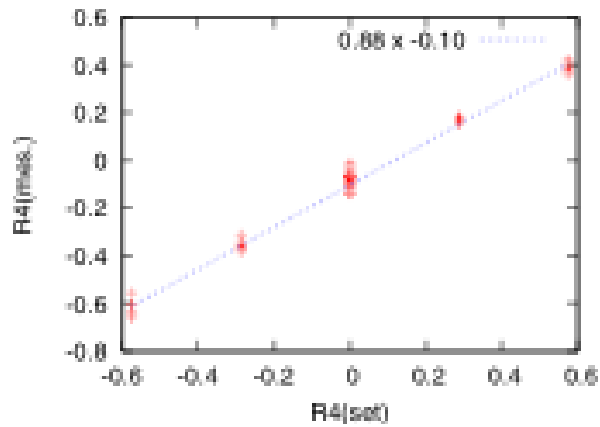


Figure 13: R4 Variation for the Knob scan.

Table 3: Measurements of the coupling parameters in 2009. The units are R1 [rad], R2 [m], R3 [m^{-1}], R4 [rad].

		4/30	5/13	5/26
HER	r1	0.0112	0.0142	0.00974
	r2	0.00163	0.00139	0.00169
	r3	0.0616	0.111	0.0618
	r4	-0.0547	-0.0926	0.0245
LER	r1	0.0104	0.0085	0.00961
	r2	0.0137	0.0137	0.0131
	r3	0.673	0.189	0.221
	r4	-0.144	0.0277	-0.061

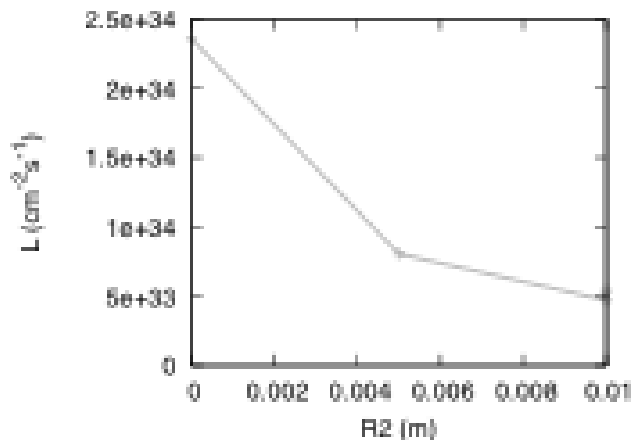


Figure 14: Luminosity as a function of R2 in a beam-beam simulation (BBSS).

3.2.3.3 Chromatic Coupling at IP

Correction of the chromatic coupling was very efficient. The source of the chromaticity is complex IR magnets configuration, solenoid, compensation solenoids and final superconducting quadrupoles (QCS). The existence of the chromaticity was

suggested by a beam size measurement in tune space [6]. The chromatic coupling was measured by off-momentum vertical orbit change for horizontal orbit distortion [7]. The effect of the chromatic coupling for the beam-beam performance was studied by the beam-beam simulations [2]. Figure 15 shows the beam size measurement in the tune space and chromaticity for R4. Coupling and their synchrotron sideband peaks are seen in the figure. The sideband peak is induced by the chromatic coupling. The chromaticity was not negligible for the beam-beam performance, because it spread 0.1-0.2 for $\pm\sigma_{\Delta p/p}$ in HER as shown in the figure. The beam-beam simulation showed that 15-20% of luminosity increase was expected. Skew sextupoles are installed in 2009 spring. The operation with the skew sextupole started at April 2009, and exceeds $2 \times 10^{34} \text{ cm}^{-2} \text{ s}^{-1}$ [8].

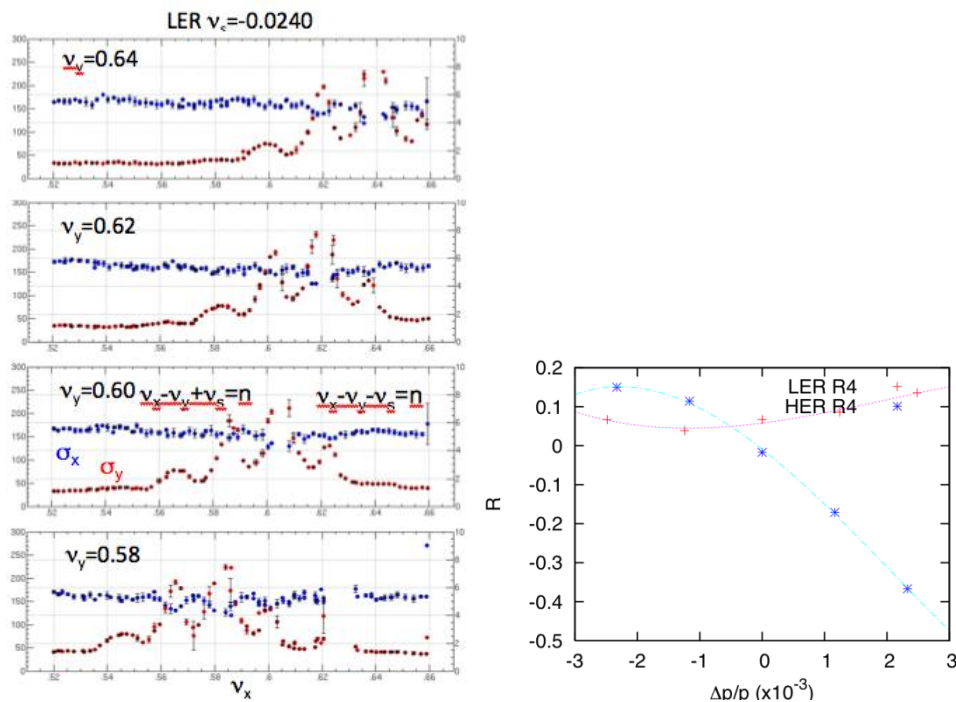


Figure 15: Measurement of the beam size in tune space and of chromaticity for R4 (by Y. Ohnishi & K. Ohmi).

3.2.3.4 Luminosity Degradation due to Beam Noise

A static offset between two colliding beams degrades luminosity due to less geometrical overlap and effect of an asymmetric beam-beam force. Turn by turn offset makes worse the luminosity performance sensitively in strong nonlinear system. For very flat beam (aspect ratio of the beam size at IP is 1/100), the vertical noise is more sensitive than horizontal. We doubted the first noise as a source of luminosity degradation. Figure 16 shows the luminosity degradation for the turn by turn noise given by simulation and measurement. In the simulation, noise of 5% amplitude of the vertical beam size degrades the luminosity from 2.6 to $1.6 \times 10^{34} \text{ cm}^{-2} \text{ s}^{-1}$, i.e. by 60%. The quantum excitation due to the synchrotron radiation is 2% of the beam size. The noise of less than 2% is not effective, because it is hidden in the quantum excitation. In the figure, 10% of degradation is seen for the noise of 2% beam size.

A feedback kicker driven by a noise generator applied a noise into the beam. The noise level of the bunch oscillation was measured by turn by turn position monitors.

The luminosity as a function of the noise amplitude is plotted in the right picture of Figure 16. The measurement showed less sensitivity to noise than the simulation. The measured luminosity is lower than simulated one. The luminosity for 5% or 10% amplitude roughly agrees with measured one. Unknown noise, x-y coupling or other optics issue may disturb to go to the very high peak.

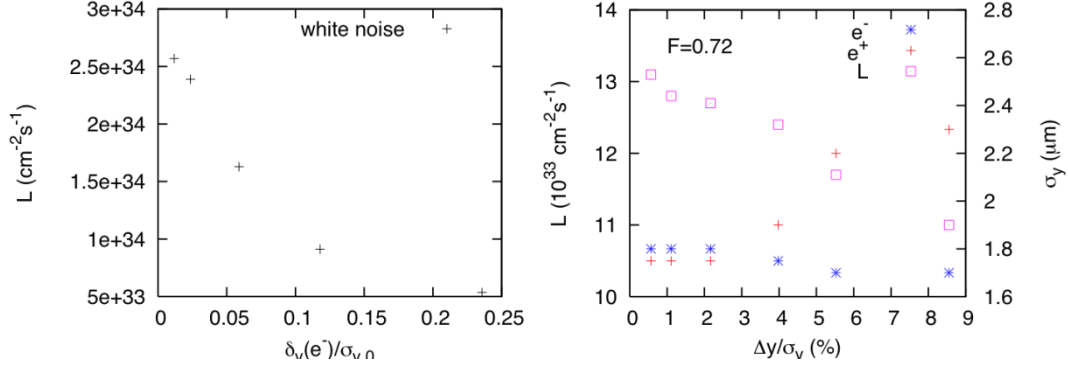


Figure 16: Luminosity for the vertical beam fluctuation amplitude. Left and right plots are given for the simulation and measurement (by M. Tobiyama & K. Ohmi).

3.2.3.5 *Beam Life Time Issue Related to the Collision*

In an early stage of crab operation, beam lifetime issue at collision was very serious. The beam-beam simulation showed better performance for the beam lifetime as is shown in Figure 17. Horizontal offset, in which positron beam is outside of the electron beam at IP, gave a harmfully short lifetime: that is, lifetime was asymmetric for the horizontal collision offset. The lifetime issue was cleared for changing the closed orbit at the crab cavity and relaxation of the horizontal beta function at the crab cavity and IP. A quadrupole magnet near the crab cavity limited the aperture. The beta function in the crab cavity was chosen to be high to reduce the crab cavity voltage. The voltage of LER crab cavity was limited to around 10 MV. To get designed crab angle, beta function at crab cavity was enlarged to 0.8-0.9 m.

Dynamic beta and emittance enhance the aperture limitation, especially the dynamic beta was very strong because the operating point with horizontal tune 0.505 very close to the half integer. The beta functions are 0.9 m and 198 m at IP and at the quadrupole near the crab cavity without collision, while 0.2 m and 1100 m with collision. The horizontal beta function at IP was limited to be 1.2 m for that without crab cavity of 0.55 m [9].

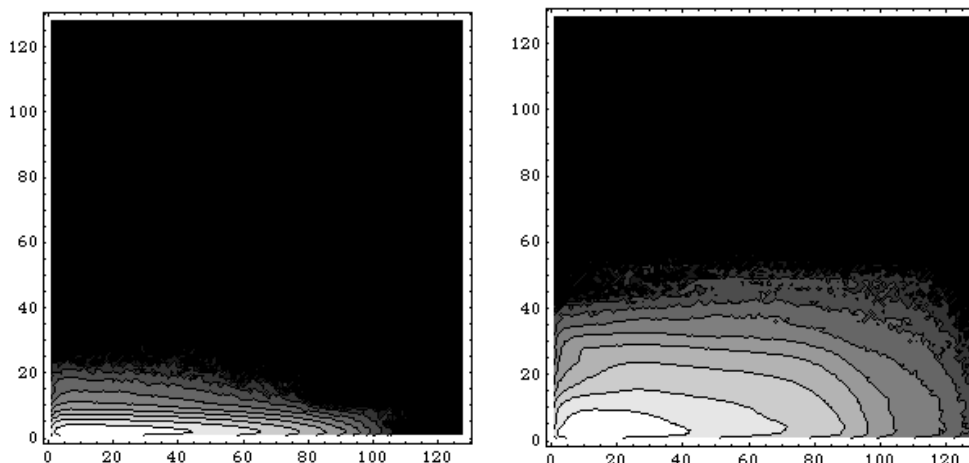


Figure 17: Beam distribution in the transverse space with (left) and without (right) crab cavity given the beam-beam simulation (BBWS). The full scale of the pictures is 0-12.8 σ_x , 0-64 σ_y for horizontal and vertical, respectively.

3.2.3.6 Other Possibilities for Luminosity Degradation

The design or zero current bunch length is 5 mm for the both ring. The bunch lengthening should be weak in impedance estimation [10]. The bunch length was measured by a streak camera [11], and beam spectrum [12]. Energy spread was estimated by hadron event ratio in Belle detector. The impedance, which was consistent with the bunch lengthening and energy spreading, was empirically represented by a resonator model with $L = 106$ nH, $R = 22.9$ k Ω , $C = 0.22$ fF and $L = 109$ nH, $R = 12.5$ k Ω , $C = 0.69$ fF for LER and HER, respectively. The effect of bunch lengthening to the luminosity performance was not dominant for the degradation [13].

The beam is tilted in whole the ring, because one crab cavity is installed in a ring. Tail part of a bunch is kicked by the transverse wake field, thus the bunch shape is distorted like a banana shape. The distortion was estimated for the wake field, $W_x = 1.7 \times 10^6$ m⁻², which was given by the current dependent tune shift in horizontal, $dv_x/dI = 4$ A⁻¹. The distortion and other effects were negligible.

3.2.4 Summary

Crab cavity has been operated to target a very high beam-beam performance of the head-on collision in KEKB. Maximum luminosity 2.11×10^{34} cm⁻²s⁻¹ was achieved by crab cavity and chromatic coupling correction. Luminosity gain due to the crab cavity was about 20%, though 2 times gain was expected. Several reasons of the luminosity degradation were discussed. They are x-y coupling and their chromatic aberration, fast beam noise, aperture related to dynamic beta and beam lifetime, bunch lengthening, and wake effect for the tilt beam. The very high luminosity area was narrow structure in several kind of the parameter scan. The luminosity is obtained by a kind of singular property for the operating point very close to the half integer, so called literally cutting-edge. It may be necessary to overcome further difficulties.

Some regret points, large horizontal beta, one crab cavity per ring etc., remained, though they may not be essential obstacles to achieve the target luminosity.

We acknowledge members of Machine advisory committee for KEKB. We thank contributors on the crab commissioning, Y. Cai, D. Shatilov, F. Zimmermann, M. Zobov.

3.2.5 References

1. K. Ohmi, M. Tawada, Y. Cai, S. Kamada, K. Oide, J. Qiang, “Luminosity limit due to the beam-beam interactions with or without crossing angle”, *Physical Review ST-AB* 7, 104401 (2004).
2. D. M. Zhou, K. Ohmi, Y. Seimiya, Y. Ohnishi, A. Morita, H. Koiso, “Simulations of beam-beam effect in the presence of general chromaticity”, *Physical Review ST-AB* 13, 021001 (2010).
3. Y. Funakoshi, M. Masuzawa, K. Oide, J. Flanagan, M. Tawada, T. Ieiri, M. Tejima, M. Tobiyama, K. Ohmi, H. Koiso, “Orbit feedback system for maintaining an optimum beam collision”, *Physical Review ST-AB* 10, 101001 (2007).
4. Y. Ohnishi, K. Ohmi, H. Koiso, M. Masuzawa, A. Morita, K. Mori, K. Oide, Y. Seimiya, D. Zhou, “Measurement of chromatic x-y coupling”, *Physical Review ST-AB* 12, 091002 (2009).
5. K. Ohmi et al., proceedings of IPAC10.
6. K. Ohmi et al., proceedings of EPAC09.
7. A. Morita, H. Koiso, Y. Ohnishi, K. Oide, “Measurement and correction of on- and off-momentum beta functions at KEKB”, *Physical Review ST-AB* 10, 072801 (2007).
8. Y. Funakoshi et al., to be published.
9. Y. Funakoshi et al., proceedings of IPAC10.
10. D. Zhou et al., proceedings of IPAC10.
11. H. Ikeda et al., proceedings of e+e-in the 1-2 GeV range: Physics and Accelerator Prospects, 10-13 Sep. 2003, Alghero, Italy.
12. T. Ieiri and H. Koiso, proceedings of Accelerator Science and Technology, KEK, 2003, p. 443.
13. Y. Cai, J. Flanagan, H. Fukuma, Y. Funakoshi, T. Ieiri, K. Ohmi, K. Oide, Y. Suetsugu, J. Rorie, “Potential-well distortion, microwave instability and their effects with colliding beam at KEKB”, *Physical Review ST-AB* 12, 061002 (2009).

3.3 Beam-Beam Simulations for Crabbed Bunches

Dmitry Shatilov, BINP, Novosibirsk, Russia

Mail to: Shatilov@inp.nsk.su

3.3.1 Introduction

Weak-strong model is known to be very efficient for beam-beam simulations until we are restrained from considering coherent effects. Indeed, as normally our goal is not investigating in details the “bad” working points where the beams are considerably disturbed, but finding the “good” ones, we can assume the opposite bunch has almost unperturbed density distribution, that is Gaussian in all three dimensions. For such distributions there are well-known formulae [1, 2] to calculate the 3D kicks, which a test particle experiences due to interaction with the opposite bunch.

Unfortunately, such an approach cannot be applied to a novel Crab Waist collision scheme, since the crabbed beams are essentially non-Gaussian even without any beam-beam perturbations. In fact, in the early Crab Waist simulations by LIFETRAC [3, 4]

the opposite (strong) bunch was considered as Gaussian and only the weak bunch was crabbed. Since the main positive effect of Crab Waist (strong suppression of betatron coupling resonances) comes from crabbing of the weak beam, such a simplification was acceptable, but only as a temporary solution. More correct treatment of crabbed beams can be obtained in strong-strong models (see e.g. in [5]), but they have their own restrictions: limited grid sizes and problems at the grid borders, huge computing resources (CPU time) required, and the absence of some important features, which LIFETRAC has – e.g. simulation of beam tails.

Recently a new feature was added to the LIFETRAC tracking code, which allows calculating the beam-beam kicks from the opposite bunch with arbitrary (including the crabbed) distributions. This technique can also be used in future for quasi-strong-strong simulations, which seem to be very promising. In this paper we describe the technique, its accuracy and limitations, and give some numerical examples.

3.3.2 Crabbed Beam Distribution

In the Crab Waist collision scheme [3, 6, 7] there are two strong “crab” sextupoles in the Interaction Region. Betatron phase advances between sextupole and IP must comply with the following relations:

$$\begin{aligned}\Delta\mu_x &= k \cdot \pi \\ \Delta\mu_y &= (2m + 1) \cdot \frac{\pi}{2}\end{aligned}\tag{1}$$

where k, m are integers (to fix the idea, hereinbelow we assume $k = m = 2$). Provided that crab sextupoles have equal strengths, but of the opposite signs, they exactly compensate each other. It means that the beam density distribution at the entrance of the first sextupole will be exactly the same as in the case without crabbing. Now let us find the density distribution function $\rho(x, x', y, y', z)$ for a thin slice of crabbed bunch at arbitrary azimuth z , on conditions that $z = 0$ at IP and transformation from z to IP is a drift. In what follows, a superscript $*$ denotes α and β at IP *without crabbing*, while the other values correspond to the crab sextupole location. Of course, $\alpha_x^* = \alpha_y^* = 0$ due to the symmetry, and also for simplicity we assume there is no dispersion at IP. Taking into account (1), the horizontal and the vertical transport matrixes from sextupole to IP can be written as follows:

$$M_x = \begin{bmatrix} \sqrt{\frac{\beta_x^*}{\beta_x}} & 0 \\ \frac{\alpha_x}{\sqrt{\beta_x^* \beta_x}} & \sqrt{\frac{\beta_x}{\beta_x^*}} \end{bmatrix} \quad M_y = \begin{bmatrix} \alpha_y \sqrt{\frac{\beta_y^*}{\beta_y}} & \sqrt{\beta_y^* \beta_y} \\ \frac{-1}{\sqrt{\beta_y^* \beta_y}} & 0 \end{bmatrix}\tag{2}$$

In the crab sextupole (which is assumed to be thin) a particle experiences a nonlinear kick:

$$\begin{aligned}\Delta x' &= -\frac{\kappa}{2}(x^2 - y^2) \\ \Delta y' &= \kappa \cdot xy\end{aligned} \quad \kappa = \frac{\sqrt{\beta_x^* / \beta_x}}{\theta \cdot \beta_y^* \beta_y}\tag{3}$$

where κ is the integrated sextupole strength, θ is the crossing angle. By some reasons it is convenient to start from the nominal (without crabbing) transverse distribution at IP:

$$\rho^*(x_0, x'_0, y_0, y'_0) = \rho_0 \cdot \exp\left(-\frac{x_0^2}{2\sigma_x^2} - \frac{x'_0{}^2}{2\sigma_{x'}^2} - \frac{y_0^2}{2\sigma_y^2} - \frac{y'_0{}^2}{2\sigma_{y'}^2}\right) \quad (4)$$

where $\sigma_m^2 = \varepsilon_m \beta_m^*$, $\sigma_{m'}^2 = \varepsilon_m / \beta_m^*$, $m = x, y$, and ρ_0 is the density at the center of the given slice. Then, the transformation to azimuth z can be represented as a sequence of 4 steps:

- 1) Back transformation from IP to the first sextupole (matrixes \mathbf{M}_x^{-1} and \mathbf{M}_y^{-1}).
- 2) Nonlinear kick (3) at the sextupole.
- 3) Direct transformation (2) from sextupole to IP (matrixes \mathbf{M}_x and \mathbf{M}_y).
- 4) Drift transformation from IP to z .

Finally, we obtain the relations between the coordinates of the particle at point z and the coordinates *it would have at IP without crabbing* (denoted by a subscript 0):

$$\begin{aligned} x_0 &= x - z \cdot x' \\ x'_0 &= x' + \frac{1}{2\theta} \cdot \left(\frac{\beta_x \cdot (x - z \cdot x')^2}{\beta_y \beta_x^* \beta_y^*} - y'^2 \right) \\ y_0 &= y - z \cdot y' + \frac{(x - z \cdot x') \cdot y'}{\theta} \\ y'_0 &= y' \end{aligned} \quad (5)$$

Note that dependence on α_x and α_y disappeared. Since Jacobian of transformations (5) equals to 1, $\rho(x, x', y, y', z)$ can be expressed simply by formula (4) with the coordinates (x_0, x'_0, y_0, y'_0) substituted from (5). The integrals of $\rho(x, x', y, y', z)$ over x', y' cannot be taken analytically, so a numerical integration is needed even to get the crabbed beam density $\rho(x, y, z)$. And of course, the 3D kick from a slice with such specific distribution can be obtained only numerically, using some special *grids*.

3.3.3 Requirements on the Grid Sizes

We work in a laboratory (stationary) coordinate system with the longitudinal axis Z oriented along the “strong” bunch trajectory at the IP. In ultra-relativistic case electromagnetic field of charged particle shrinks to a $1/\gamma$ cone perpendicular to its velocity, so representation of the strong bunch as a number of slices looks quite appropriate. The slices must be located in X-Y plane. When a test particle from the opposite beam crosses the plane of slice, it experiences a 3D kick (change of momentum). Thus, interaction with the opposite bunch is represented as a sequence of kicks from all the slices the strong bunch is divided into. And the problem comes to finding the kick from a thin slice at the arbitrary azimuth z .

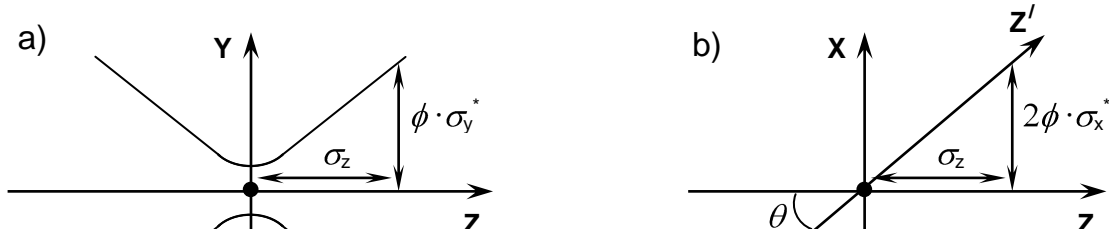


Figure 18: Collision scheme with large Piwinski angle and micro- β_y^* : vertical beam size (a) and horizontal separation (b) versus the longitudinal shift from IP.

In Crab Waist collisions we usually have $\sigma_z \approx \phi \cdot \beta_y^*$, where $\phi \gg 1$ is the Piwinski angle (for instance, in the SuperB project $\phi \sim 20$). It results in a huge hour-glass effect when shifting longitudinally by a distance comparable with σ_z (see Figure 18 a) and must be taken into account when building the grid. On the one hand, the vertical size of grid cell must be small enough (of the order of $\sigma_y^*/10$) to represent the bunch distribution at IP correctly. On the other hand, the grid should extend to large vertical amplitudes (at least $20 \sigma_y$) in the whole area of about $1\sigma_z$ around IP.

In the horizontal dimension the hour-glass effect is small, but separation between bunches in units of σ_x becomes large when shifting from IP longitudinally (see Figure 18 b), thus imposing requirements on the minimum grid width. One more requirement is that the longitudinal distance between grid nodes at IP must be much less than β_y^* , while the longitudinal grid size should be of the order of σ_z .

Apparently, a uniform rectangular 3D grid, which meets the above requirements, would have enormous number of cells. Even though it can be built, such a grid would require a huge memory size to store and huge amount of CPU time to calculate. One of the possible ways to simplify the vertical hour-glass problem is to build nonrectangular grid: the vertical distance between nodes should be, say, $1/10$ of the vertical sigma *at that azimuth*. As we are considering interaction with a thin slice in its own plane, such an approach seems to be rather adequate. However, the problem is not purely two-dimensional since there will be a longitudinal component of the kick due to $\partial p/\partial z \neq 0$.

In order to reduce the number of grid cells, in [5] it was proposed to restrict the horizontal grid size by $5 \sigma_x$ and use the Bassetti-Erskine formulae (as for the Gaussian distribution) for larger horizontal amplitudes. The problem, however, is that at the grid border not only the derivatives but the function itself will be noncontiguous, that can result in serious perturbations in the particle's motion. Note that the grid is linked to the strong bunch's coordinate system (though it does not move). So, the particles from the opposite beam have a rather high probability to find themselves at 5 or even $10 \sigma_x$ in this system when the Collision Point (CP) is shifted longitudinally from IP, see Figure 18 b.

To sum up, the standard approach of solving differential equations for electromagnetic field (or electrical potential) on 3D grids has a number of serious difficulties, especially for collision schemes with large Piwinski angle and $\sigma_z \gg \beta_y^*$.

3.3.4 Nonrectangular and Non-uniform Grids

In order to significantly reduce the number of grid nodes, we decided to build nonrectangular and nonuniform grids. Of course, it would be difficult to utilize such a

grid for solving differential equations, but we refused this method as well. Instead, we perform a direct integration to calculate the 3D kicks at the grid nodes and apply a 3rd order interpolation to find the corresponding values between the nodes.

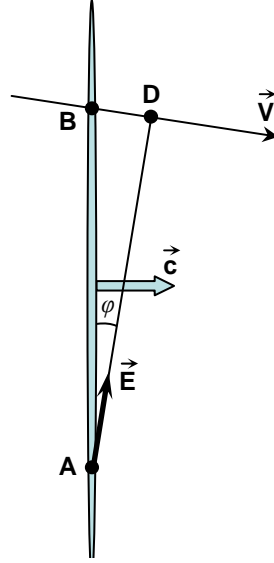


Figure 19: Kick from a single particle.

First of all, let us consider the kick produced at point **A** (a grid node) by a single particle, see Figure 19. The particle belongs to a slice which moves from left to right, and the kick normally should occur at the moment when the slice crosses point **A** (i.e. particle at point **B**). However, the particle can have a small transverse component of velocity, so that perpendicular to vector **V** crosses point **A** when the particle is at point **D**. In ultra-relativistic case the electric field is perpendicular to the particle velocity (vector **E** in Figure 19), so the kick actually originates from point **D** and does not lie in the slice's plane. The range of angle φ can be estimated as $\sigma_{x'}$, and the longitudinal shift from **B** to **D** – as $\sigma_x \cdot \sigma_{x'}$. For SuperB e.g. these values are very small: about 0.3 mrad and 0.002 microns, respectively. Thus we may assume that the kick comes from point **B** but the electric field has the longitudinal component, which is proportional to $E \cdot \varphi$ (this term exactly corresponds to **g** from [2]). The components of the kick emerging due to the electric field can be found in the following way:

$$\begin{aligned}
 U &= \frac{e\gamma}{\sqrt{x^2 + y^2 + \gamma^2 z^2}} \\
 E_x &= \frac{\partial U}{\partial x} = \frac{e\gamma \cdot x}{(x^2 + y^2 + \gamma^2 z^2)^{3/2}} \\
 F_x &= \int_{-\infty}^{\infty} E_x dz = \frac{2e \cdot x}{x^2 + y^2} \\
 F_z &= -F_x \cdot x' - F_y \cdot y'
 \end{aligned} \tag{6}$$

Here x and y are the differences in the corresponding coordinates of points **A** and **B**. Actually, the momentum change, which a test particle experiences at point **A**, has also the magnetic part, but the total kick can be expressed through the components of vector **F** and the test particle velocity, see e.g. in [8].

Thereby, to calculate the three-dimensional kick produced by any slice at the given azimuth z , we only need the four-dimensional distribution $\rho(x, x', y, y', z)$ at that azimuth. Since the others z does not matter, the grid transverse sizes at the different azimuths can be independent. However, for the further interpolation at the points between the grid nodes, it is desirable to have the grid of 3D rectangular shape. The solution is that we build a rectangular grid in the space of $(x/\sigma_x, y/\sigma_y, z)$, where σ_x and σ_y depend on z , of course. So, in the physical space of (x, y, z) the grid follows the hour-glass shape: it is rectangular in X-Y cross-section and nonrectangular in X-Z and, especially, in Y-Z planes. But interpolation will be performed in another space, where it is rectangular in all three dimensions.

One more feature that can be utilized to reduce the number of grid nodes is that the kick's dependence on transverse coordinates becomes weak at large amplitudes. This allows us to increase the distance between nodes at large amplitudes without loss of accuracy. Thus, we come to *nonuniform* grids, where the coordinate of the i -th node (accounted from the center and can be negative as well) is calculated as follows:

$$\begin{aligned} x_i &= i \cdot S_c / N_c & \text{for } |i| \leq N_c \\ |x_i| &= S_c \cdot \exp(|i| / N_c - 1) & \text{for } |i| \geq N_c \end{aligned} \quad (7)$$

Here S_c is the “core” grid size (usually 2 sigma), and the number of cells in this region equals to $2 \cdot N_c + 1$. The same trick can be also applied to the longitudinal direction. Indeed, in the vicinity of IP the longitudinal distance between grid nodes must be small (much less than β_y^*), but when shifting by more than $2 \beta_y^*$, the step can be increased. In practice we use the same formulae (7) for all three dimensions, but S_c and N_c can be different, of course. So, the grid cross-sections in all three planes: $(x/\sigma_x, y/\sigma_y)$, $(z, x/\sigma_x)$ and $(z, y/\sigma_y)$, look like as it is shown in Figure 20.

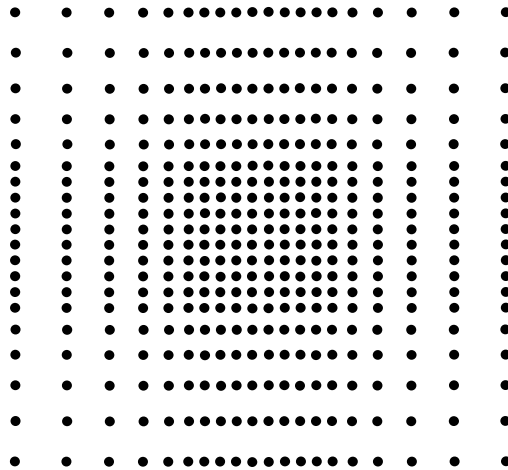


Figure 20: Grid cross section (schematic view).

3.3.4.1 *Integration*

In each grid node we need to store four numbers: the distribution density ρ (it will be used later in tracking to calculate the luminosity) and three components of vector \mathbf{F} . The integration is two-dimensional and consists of two steps:

- 1) Obtaining the ρ and mean angles $\langle x' \rangle$, $\langle y' \rangle$ at each node (integration of $\rho(x, x', y, y', z)$ over x', y').
- 2) Calculating the components of vector \mathbf{F} at each node.

In these calculations the longitudinal grid slices are completely independent and often are processed on different CPUs in parallel. So, herein below we consider a two-dimensional sub-grid: nodes with the same azimuth z . The contribution of node k to the components of vector \mathbf{F} at node m can be written as follows:

$$\begin{aligned}
 F_x^{km} &\propto \iint \frac{\rho_k \cdot (x_k - x_m + x)}{(x_k - x_m + x)^2 + (y_k - y_m + y)^2} \\
 F_y^{km} &\propto \iint \frac{\rho_k \cdot (y_k - y_m + y)}{(x_k - x_m + x)^2 + (y_k - y_m + y)^2} \\
 F_z^{km} &= -F_x^{km} \cdot \langle x' \rangle - F_y^{km} \cdot \langle y' \rangle
 \end{aligned} \tag{8}$$

The integration is performed on the k -th grid cell (x and y vary within \pm half cell size), and we assume the value of ρ_k is constant within this small area. The integrals (8) can be taken analytically and expressed through logarithms and arctangents. Then we have to sum the contributions from all the nodes (sum over k) to get the final value of \mathbf{F}^m at the m -th node. And of course, this procedure must be performed for all the nodes (loop for m).

3.3.4.2 Interpolation

To get the values between the grid nodes we perform a 3D interpolation of the 3rd order. For that we need $4^3=64$ nodes around the given point: the ones with the indexes from $i-1$ to $i+2$ in each dimension, provided that the point's coordinate lies between the i -th and the $(i+1)$ -th nodes. Actually, we simply need to sum up the values from all these nodes with the different weights:

$$V(x, y, z) = \sum_{p=i-1}^{i+2} W_x^p \cdot \sum_{q=j-1}^{j+2} W_y^q \cdot \sum_{r=k-1}^{k+2} W_z^r \cdot V_{pqr} \tag{9}$$

The weights depend on the coordinate differences between the given point and the corresponding nodes. For example, let the x -coordinate of the i -th node be zero, and coordinates of the $(i-1)$ -th, $(i+1)$ -th and $(i+2)$ -th nodes equal to a , b and c , respectively ($a < 0$). Note that for nonuniform grids the relations between a , b and c can be arbitrary. For $0 \leq x \leq b$ the interpolation gives the following weights in the horizontal dimension:

$$\begin{aligned}
W_x^{i-1} &= \frac{x \cdot (x^2 - x(b+c) + b \cdot c)}{a(a-b)(a-c)} \\
W_x^{i+1} &= \frac{x \cdot (x^2 - x(a+c) + a \cdot c)}{b(b-a)(b-c)} \\
W_x^{i+2} &= \frac{x \cdot (x^2 - x(a+b) + a \cdot b)}{c(c-a)(c-b)} \\
W_x^i &= 1 - W_x^{i-1} - W_x^{i+1} - W_x^{i+2}
\end{aligned} \tag{10}$$

For the other two dimensions the calculations are performed in exactly the same way. It is interesting that the CPU time required for all these computations is comparable with that of Bassetti-Erskine formulae, where the most time-consuming part is the complex error functions calculation.

3.3.5 Testing the Grids

In order to test the grids and estimate the accuracies they can provide, it was very useful to build the grids for the normal Gaussian distributions (simply set the crab sextupole strength to zero) and compare them to the analytical formulae. We developed a special dedicated code with GUI for the grids testing, which helped us a lot in improving the calculation algorithms and optimizing the grid parameters. Actually, all the figures in this section were produced by that code.

3.3.5.1 Interpolation

First of all, we can test the interpolation procedure and define the necessary grid resolution (cell sizes) in all three dimensions. For this purpose the values at the grid nodes were calculated analytically (without numerical integrations), so generation of such grids took only a few seconds. We will not discuss here the intermediate results and present only the grid with the final parameters, which then will be used for beam-beam simulations.

The main grid parameters correspond to the LER design of SuperB as of March 2010: $\varepsilon_x = 2.46 \cdot 10^{-7} \text{cm}$, $\varepsilon_y = 6.15 \cdot 10^{-10} \text{cm}$, $\beta_x^* = 3.2 \text{cm}$, $\beta_y^* = 0.0205 \text{cm}$, $\sigma_z = 0.5 \text{cm}$. The core region of the grid was chosen to be as $2\sigma_x \times 2\sigma_y \times 0.05 \text{cm}$, with the cell size of $0.05\sigma_x \times 0.1\sigma_y \times 0.005 \text{cm}$. Thereby, the total number of nodes in the core region is: $(2 \cdot 40 + 1) \times (2 \cdot 20 + 1) \times (2 \cdot 10 + 1) = 69741$. The total grid sizes, of course, must be much larger, in our case: $20\sigma_x \times 40\sigma_y \times 0.5 \text{cm}$. Thus, the uniform grid with the same cells would have 2000 times more nodes. But our nonuniform grid has only $269 \times 163 \times 71 = 3113137$ nodes: factor of 44.64 larger than in the core region, and factor of 44.8 better than the uniform grid! It is worth mentioning that such a grid occupies only about 50MB of memory. Note also that the longitudinal grid slices (71) have no relation to the strong beam slicing – these things are completely different!

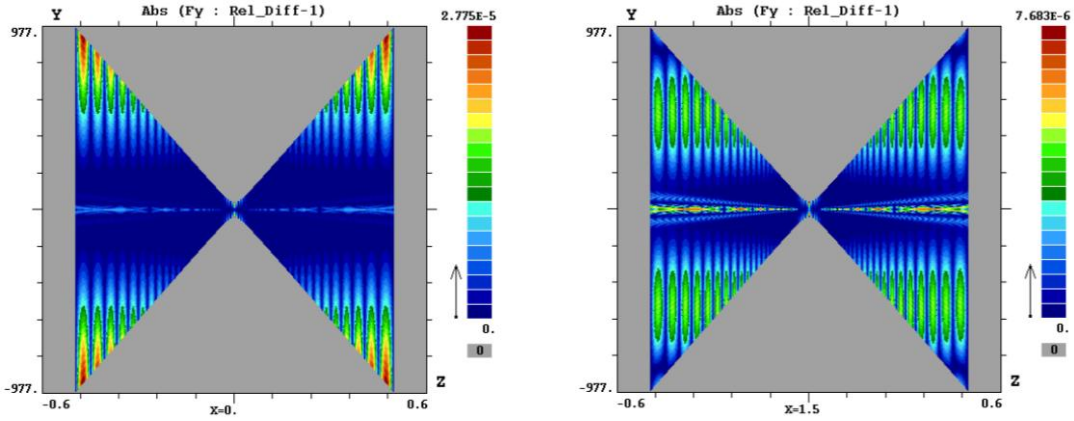


Figure 21: Grid cross-sections in Y-Z plane at $x = 0$ (left) and $x = 1.5\sigma_x$ (right). The units for Y are σ_y^* , for Z – centimetres. The colors correspond to the relative errors of \mathbf{F}_y .

Now we have to make sure that our grid provides a good accuracy though. In Figure 21 the relative errors for \mathbf{F}_y are shown in two vertical planes. Outside the grid all the values are calculated as for the Gaussian distribution – these areas are colored in grey (corresponds to the exact zero). So, the real shape of the grid can be clearly seen, and the vertical size of $977\sigma_y^*$ just corresponds to $40\sigma_y$ at $z = 0.5\text{cm}$.

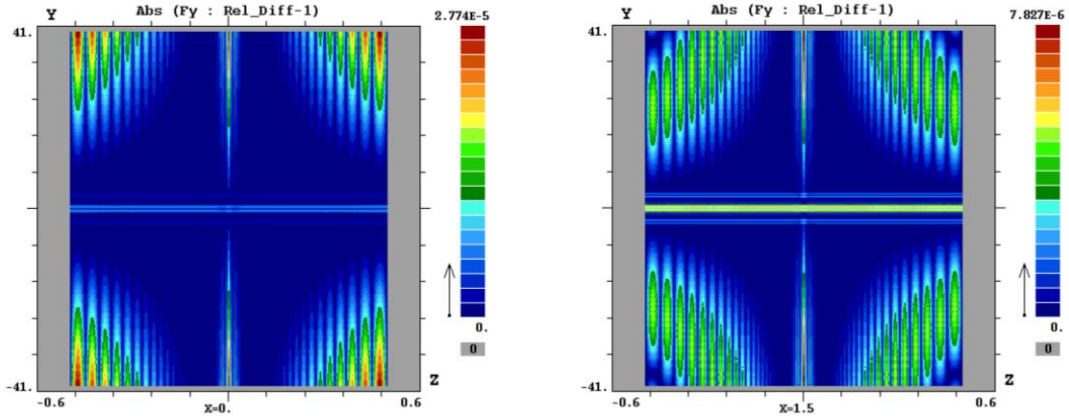


Figure 22: The same plots as in Figure 21, but the units for Y are $\sigma_y(z)$.

In Figure 22 the same plots are presented in normalized units, so the grid is rectangular. These units will be used also in all the following plots. As we see, the maximum errors (dark brown color) are of the order of $3 \cdot 10^{-5}$ only. The cross-sections in X-Y plane are shown below, see Figure 23, but the errors everywhere are well within 10^{-4} .

Besides, it is interesting to check how the accuracy of computation depends on the order of interpolation. For that purpose we performed the comparisons in a small region (to be able to recognize the cell structure of the grid), see Figure 24.

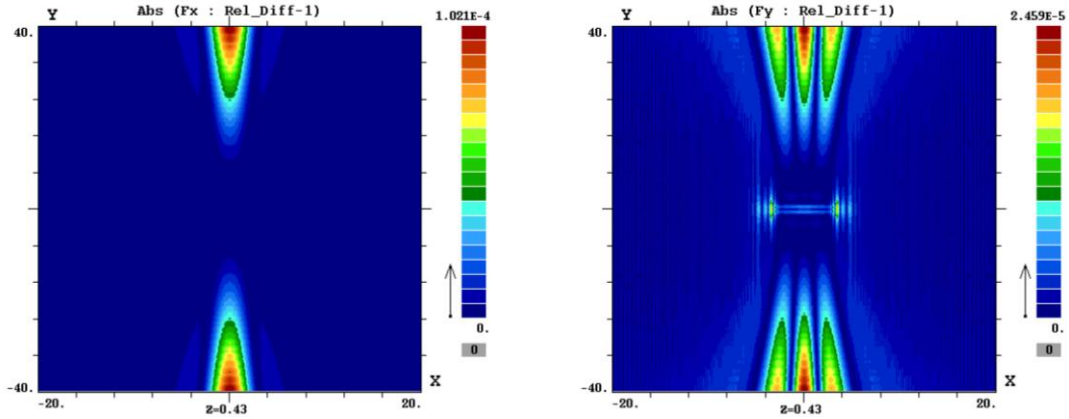


Figure 23: The relative errors for \mathbf{F}_x (left) and \mathbf{F}_y (right) in X-Y plane at the azimuth $z = 0.43\text{cm}$.

To sum up, the 3rd order of interpolation provides the accuracy of 10^{-4} at the whole grid region. Actually, this is even more than enough, as the main errors will come from numerical integration.

3.3.5.1 *Integration*

Numerical integrations (8) performed for the Gaussian distribution must be conformable to the Bassetti-Erskine formulae and the longitudinal kick described in [2]. This was the subject of the next tests, see Figure 25 and Figure 26.

The longitudinal kick \mathbf{F}_z equals to zero at IP due to the symmetry. So, in Figure 26 it is shown at the same azimuth $z = 0.43\text{ cm}$ as the transverse kicks in Figure 25. However, we restricted the X-Y region to avoid the line where \mathbf{F}_z reverses the sign. In vicinity of that line (it is located to the left) the relative errors are too large and affect the color palette. Note also that the maximum relative errors in Figure 26 correspond to the region where the value of \mathbf{F}_z is small.

Finally, we got the accuracy of about 10^{-3} for all the values. In our opinion it is quite enough. Indeed, we know many of the real machine parameters with a worse accuracy. For example, if the real beta-functions, or emittances, or something else, will differ from the design values by 1% (that is very likely), the beam-beam force will be slightly different too, but most probably we will get actually the same (or very similar) equilibrium distribution. Instead, one of the most important requirements on the grids is their *smoothness* in the whole area and especially at the border. In our case the smoothness is provided by interpolation and the border problems disappear since the grid sizes are large and can be made even larger – equal to the aperture.

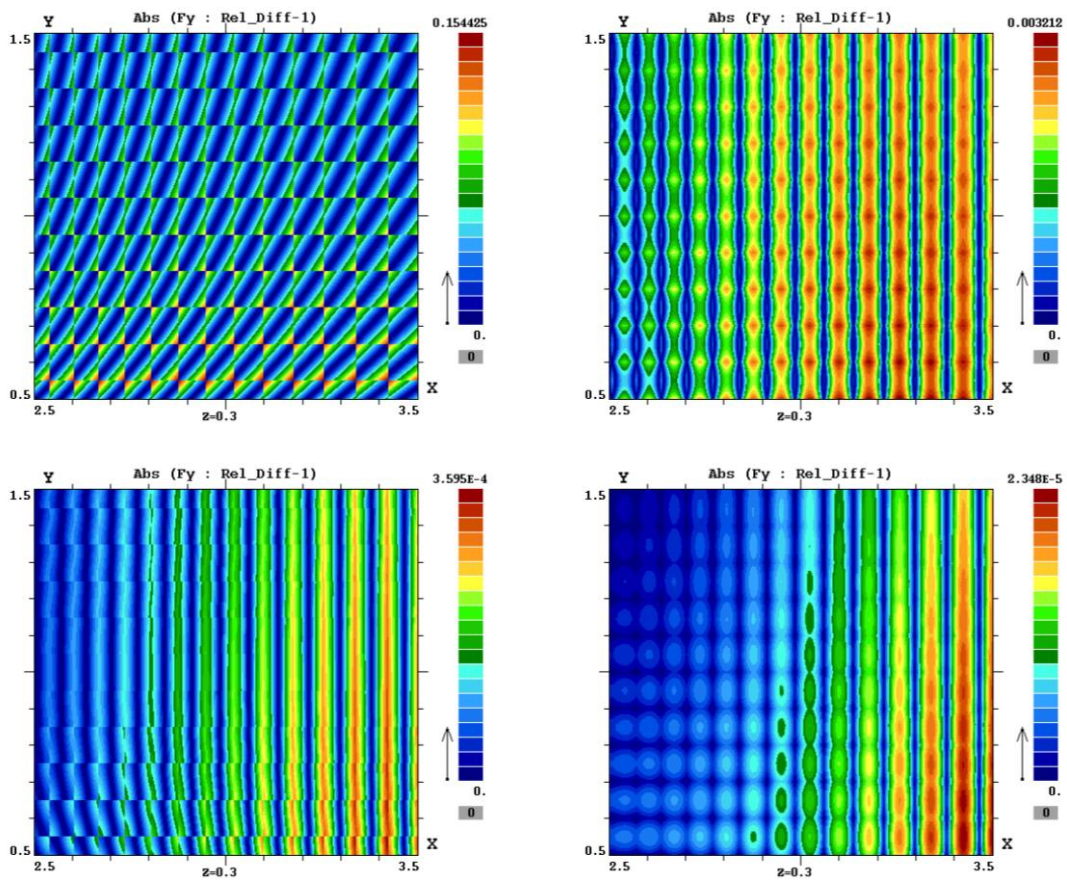


Figure 24: The relative errors for F_y versus the order of interpolation: from 0 (top left) to 3 (bottom right).

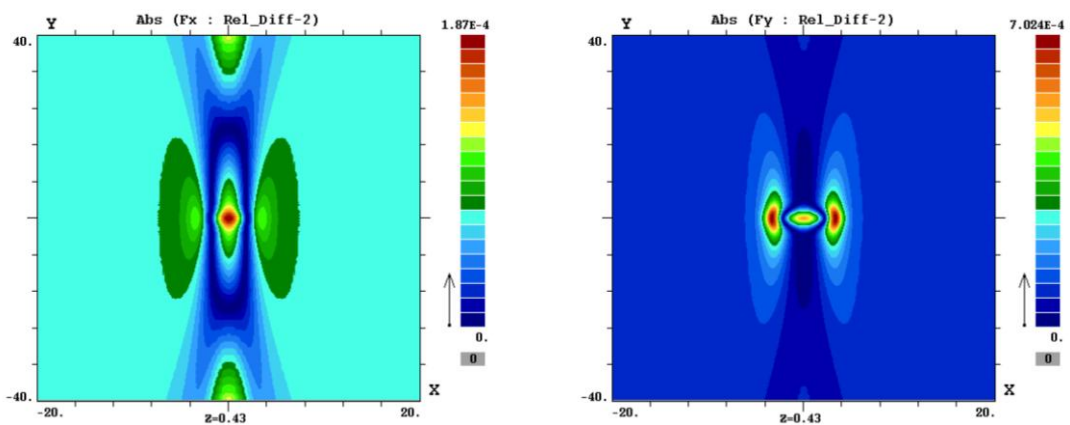


Figure 25: The same plots as in Figure 23, but F_x (left) and F_y (right) at the grid nodes were calculated by numerical integration.

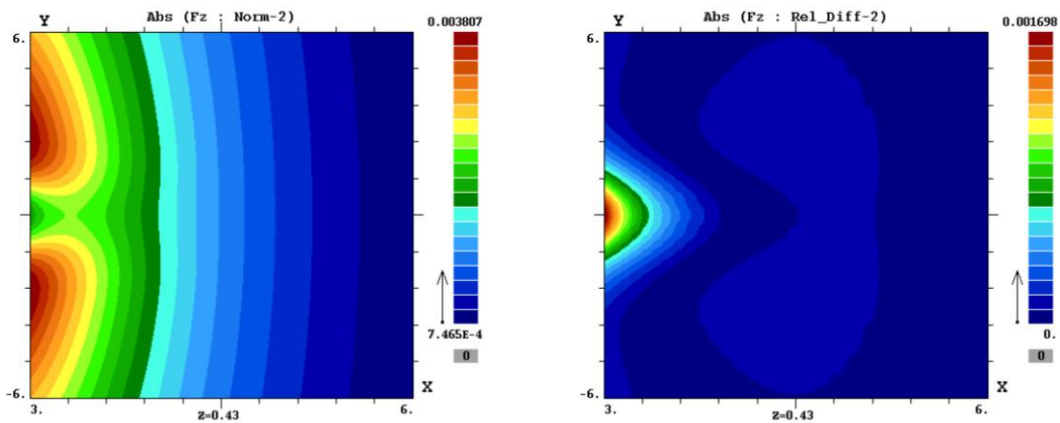


Figure 26: The longitudinal kick F_z (left) and accuracy of its computation (right) versus the transverse coordinates.

3.3.6 Crabbed Beams

For the crabbed distributions we have no analytical formulae to compare with, but there is one more way of testing. Namely, we can build a grid with the higher resolution (more cells and more memory) and use it as the “model”. However, in the most cases the accuracy should be of the same order as for the Gaussian distribution.

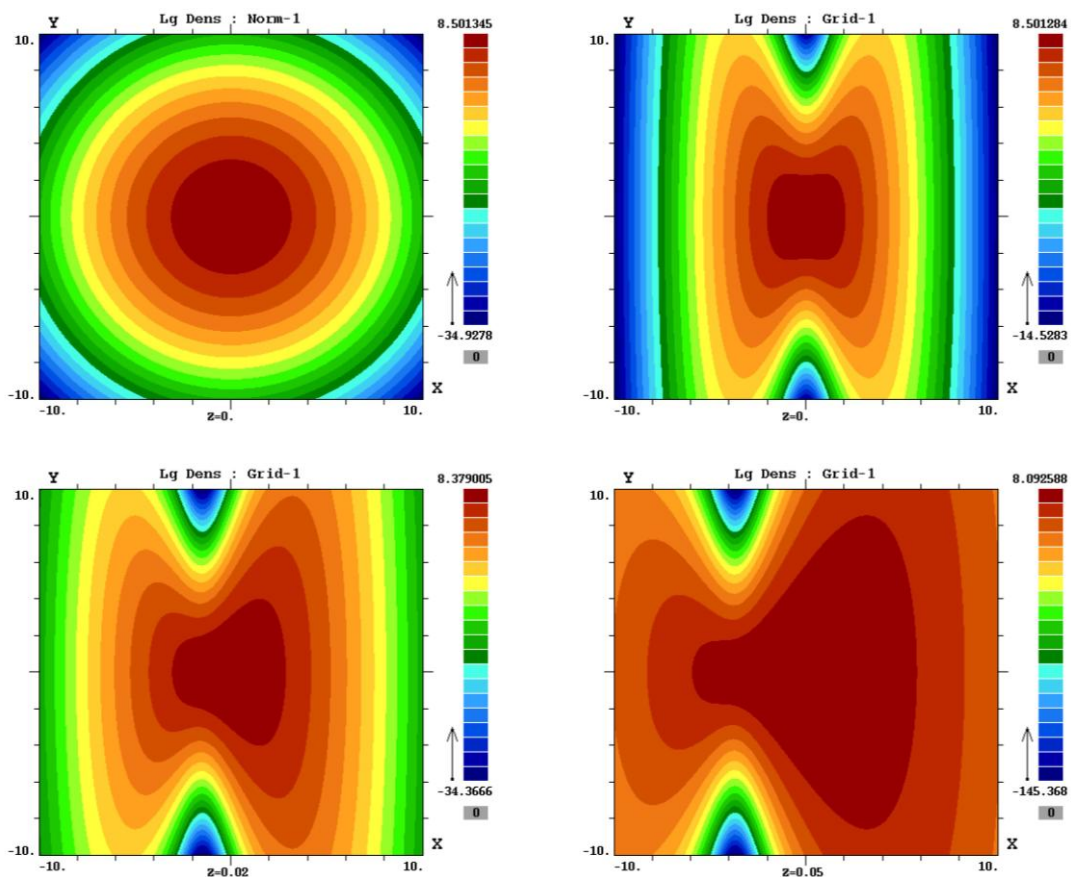


Figure 27: Logarithm of the distribution density for the Gaussian beam (top left) and the crabbed beam at different azimuths: 0.0, 0.02 and 0.05cm.

As it is seen in Figure 27, indeed, the beam distribution is strongly affected by the crab sextupoles. The waist rotation and some asymmetry in the vertical kick arising due to the beams crabbing are shown in Figure 28.

The first beam-beam simulations with the crabbed strong beams represented by grids were performed in the second half of 2009. At first we used the technique in simulations for DAΦNE, and obtained a very good agreement with the experimental data – much better than in the early simulations with the Gaussian strong beam [9]. The recent beam-beam simulations for SuperB also were performed using the new technique.

One more thing, which has to be mentioned, is the CPU time required for the grid calculation. It takes about 25 minutes when computed on a 48-node cluster, that is quite acceptable as the grids are stored in files and can be used in future for many simulations.

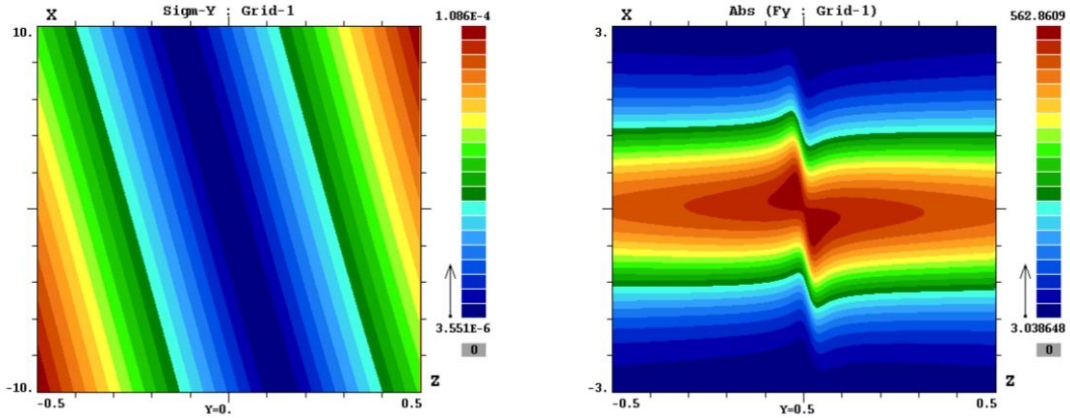


Figure 28: The vertical beam size in X-Z plane (left) and the vertical kick F_y in X-Z plane raised by $0.5\sigma_y$ vertically (right).

3.3.7 Conclusions

We developed a method of calculating the beam-beam interaction force for bunches with arbitrary distribution density. The corresponding grids have relatively small number of nodes and provide a good accuracy, which can be easily tested. The technique was used in beam-beam simulations for Crab Waist collision schemes and showed good results. In future it is planned its implementation for the quasi-strong-strong simulations.

3.3.8 Acknowledgements

The author would like to thank Mikhail Zobov for encouraging me to speed up the fulfillment of this work and for many useful discussions.

3.3.9 References

1. M. Bassetti and G. Erskine, CERN ISR TH /80-06 (1980).
2. K. Hirata, H. Moshhammer, F. Ruggiero, “A Symplectic Beam-Beam Interaction with

- Energy Change”, KEK Preprint 92-117, September 1992.
3. P. Raimondi, M. Zobov, D. Shatilov, “Suppression of beam-beam resonances in crab waist collisions”, Proc. of EPAC’08, Genoa, Italy, 23-27 Jun. 2008.
 4. D. Shatilov, P. Piminov, M. Zobov, “Beam-beam simulations for Super B-factory with asymmetrical LER and HER lattice parameters”, SB-NOTE-ACC-2008-002, December 2008.
 5. K. Ohmi, “Strong-strong Simulations for Super B Factories”, Proc. of IPAC’10, Kyoto, Japan, 23-28 May 2010.
 6. P. Raimondi, “Status of the SuperB Effort”, presented at the 2nd Workshop on Super B-Factory, LNF-INFN, Frascati, Mar. 2006.
 7. P. Raimondi, D. Shatilov, M. Zobov, “Beam-Beam Issues for Colliding Schemes with Large Piwinski Angle and Crabbed Waist”, LNF-07-003-IR, Feb. 2007, e-Print: physics/0702033.
 8. D. Shatilov, M. Zobov, “Beam-Beam Collisions with an Arbitrary Crossing Angle: analytical tune shifts, tracking algorithm without Lorentz boost, Crab-Crossing”, ICFA Beam Dyn. Newslett. 37, p.99 (2005).
 9. M. Zobov, “Beam-Beam Interaction in Novel, Very High Luminosity Parameter Regimes”, Proc. Of IPAC’10, Kyoto, Japan, 23-28 May 2010.

3.4 Beam-Beam Interaction at the PEP-II e^+e^- Collider

J. Seeman and M. Sullivan, for the PEP-II Team, SLAC

Mail to: seeman@slac.stanford.edu, sullivan@slac.stanford.edu

3.4.1 Introduction

The PEP-II B-Factory [1] at SLAC (3.1 GeV e^+ \times 9.0 GeV e^-) operated from 1999 to 2008, delivering luminosity to the BaBar experiment. The design luminosity was reached after one and a half years of operation. PEP-II ultimately surpassed by four times its design luminosity reaching 1.21×10^{34} cm⁻² s⁻¹. It also set world records for stored beam currents of 2.1 A e^- and 3.2 A e^+ . Continuous injection was implemented with BaBar taking data. The total delivered luminosity to the BaBar detector was 557.4 fb⁻¹ spanning five upsilon resonances. PEP-II was constructed by SLAC, LBNL, and LLNL with help from BINP, IHEP, the BaBar collaboration, and the US DOE OHEP.

In order to reach four times the design luminosity the PEP-II accelerator had to manage higher beam currents, lower β_y^* s, more bunches, and increased beam-beam tune shifts. In this note the effects of these changes on the beam-beam interaction are discussed.

3.4.2 General PEP-II Parameters

In PEP-II the Low Energy Ring (LER) is mounted 0.89 m above the High Energy Ring (HER) in the 2.2 km tunnel as shown in Figure 29. The interaction region is shown in Figure 30 where the beams collide head-on. A Be vacuum chamber is located at the IP inside the detector with permanent magnet dipoles on either side. The interface cone angle at the IR between BaBar and PEP-II was at 300 mrad. To bring the beams into collision, the LER is brought down 0.89 m to the HER level and then with horizontal deviation for both rings are made to collide. Since both rings have the same circumference, each bunch in each ring collides with the same bunch in the other ring.

There are small parasitic collision effects from the fact that the bunches experience a near miss as they separate near the interaction point but this effect at full currents only reduced the luminosity by a few percent.

The luminosity in a flat beam collider is given by

$$L = 2.17 \times 10^{34} \frac{n \xi_y E I_b}{\beta_y^*}$$

where n is the number of bunches, ξ_y is the vertical beam-beam parameter limit, E is the beam energy (GeV), I_b is the bunch current (A), and β_y^* is the vertical beta function value at the collision point (cm). This equation holds for each beam separately. These parameters for PEP-II are shown in Table 4 indicating the best values during beam-beam collisions. PEP-II exceeded all design parameters, specifically the luminosity by a factor of 4 to $1.2 \times 10^{34}/\text{cm}^2/\text{s}$ and the integrated luminosity per day by a factor of 7 to 911 pb^{-1} per day [2,3]. The vertical emittances of about 1.25 nm-rad arose from two factors: ~ 0.7 from the IR2 (colliding straight) two vertical doglegs of 0.89 m and ~ 0.6 from mis-steering and coupling in the collider arcs.



Figure 29: The PEP-II collider. The low-energy beam line is mounted above the high-energy beam line. The LER is lowered to the HER elevation in the interaction region.

Table 4: PEP-II beam parameters during collisions.

<i>Parameter</i>	<i>Unit</i>	<i>HER (e-)</i>	<i>LER (e+)</i>
Beam energies	GeV	9.1	3.0
Maximum colliding beam currents	mA	1875	2900
Number of bunches	—	1732	1732
Bunch length	mm	11	10
Ion gap	%	1.5	1.5
Vertical tunes	—	23.62	36.56
Horizontal tunes	—	24.52	38.52
Emittance (horiz.)	nm-rad	52	35
Emittance (vert.)	nm-rad	1.1	1.3
β_y^*	mm	10	8
β_x^*	cm	48	44
ξ_x (beam-beam parameter)	—	0.060	0.064
ξ_y (beam-beam parameter)	—	0.049	0.056
Luminosity	$\times 10^{34}/\text{cm}^2/\text{s}$	1.21	

3.4.3 Interaction Region

The PEP-II interaction region is shown in Fig. 2. The beams meet head on at the collision point. The QD1 and B1 magnets are permanent quadrupole and dipole magnets, respectively. The B1 magnets initiate the beam separation because of the different beam energies. The beam separation is completed by placing the magnetic center of the QD1 magnet close to the beam trajectory of the HER thereby making the LER trajectory off-axis in QD1. This bends the LER beam enough to enable the QF2 magnet to be a horizontal focusing septum magnet that completes the final focus of the LER. The QD4 and QF5 magnets complete the final focus for the HER. The synchrotron radiation photons which are emitted by the entering and exiting beams are masked from the interaction point to minimize backgrounds.

3.4.4 Operations

PEP-II ran with 1732 bunches out of a total possible of 1746. The total number of RF buckets was 3492. The collider was unable to use smaller bunch spacing than every other bucket ($1.26 \text{ m} = 4.2 \text{ ns}$) because of the head-on collision and the fact the beam separation at the IP did not start until the beams entered the B1 magnet 21 cm from the IP. The beams were separated sufficiently at 63 cm from the IP so that the parasitic collision effects were small.

During the start up phase of the accelerator, after a protracted (>1 month) down time in which some of the vacuum system was vented, the HER experienced a significant increase in ion trapping. This was attributed to vacuum processing. It was found that running the accelerator using mini-trains of beam bunches, we were able to store more bunches and deliver more luminosity while the vacuum processed. Over a period of a couple of weeks the small gaps between mini-trains could be gradually filled in with more bunches as the vacuum improved. Figure 31 is a picture of a mini-train configuration.

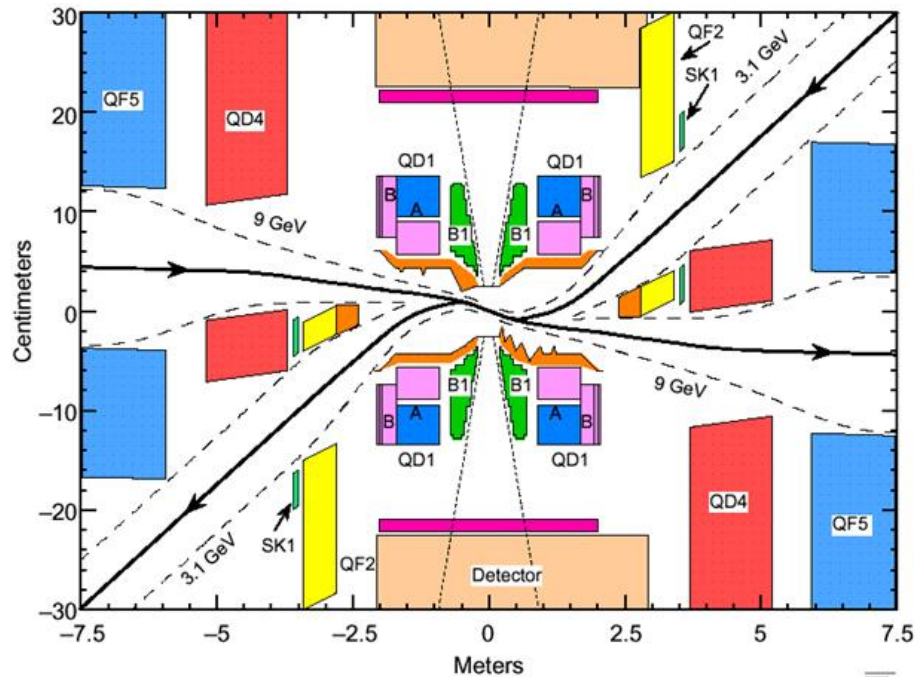


Figure 30: Plan view of the PEP-II Interaction Region (IR) with head-on collisions. Note the exaggerated horizontal scale on the left. There are four permanent magnets within the BaBar 1.5 T solenoidal field covering ± 2.5 m. The dashed lines are the beam-stay-clear envelope. The dotted lines in the middle indicate the detector physics acceptance boundaries of 300 mrad on either side the IP.

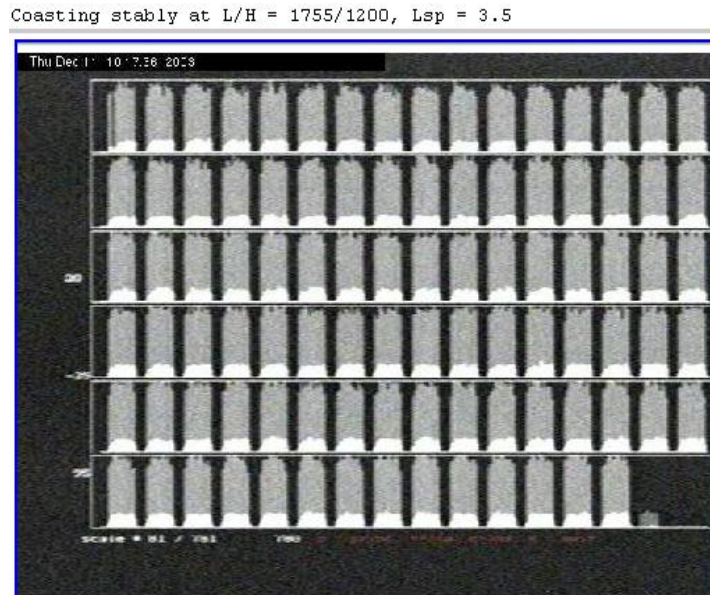


Figure 31: Picture of the luminosity of every bunch in PEP-II while using mini-trains. This also shows that PEP-II had negligible problems with electron clouds in the LER after installing solenoids, TiN coatings, and antechambers.

Initially, the PEP-II accelerator refilled the beam currents approximately hourly and then delivered the colliding beams to the detector. The detector was ramped down during injection. In 2004-2005 accelerator studies concentrated on getting continuous

injection to work. Success was achieved in fall 2005. The improvement in average machine performance was dramatic. The overall average efficiency increased by over 50% which was directly reflected in an increase in integrated luminosity delivered to the detector [4]. The continuous injection rate was about 7 Hz for the LER and 2 Hz for the HER, the HER having the longer lifetime of about 300 min. This use of continuous injection with the detector taking data was the first ever used in the world by a colliding beam accelerator.

To maximize the collision rate, studies found that adjusting the beam orbit in the sextupole magnets around the ring gave strong control of the beta functions, vertical dispersion and the local coupling. A series of software knobs were generated to exercise closed orbit bumps around most of the sextupole magnets in each ring [5,6]. These knobs were used to optimize the machine performance by increasing the lifetime (improving the dynamic aperture) or by directly increasing the luminosity.

The luminosity was measured using a detector placed at the zero degree line from the head-on collision. The B1 dipole magnets shifted the beams away from this line making it possible to install a detector for the zero degree γ -rays generated by radiative bhabhas. There is a synchrotron radiation fan of energy from the B1 magnets that also starts along the zero degree axis; so the beam pipe where the γ -rays exit was water-cooled. A Tungsten pre-radiator was installed just outside of the beam pipe. The primary detector was a quartz block which developed Cherenkov radiation that was picked up by a fast phototube. The γ -ray rate per collision was about one and this rate increased to about three at the highest luminosity. The signal from the detector was better than 1% with an update rate of 1 Hz. The detector signal was also split off and separated into luminosity per bunch with an update rate of about 0.3 Hz [7]. Figure 31 is an example of the bunch-by-bunch luminosity signal.

The beams were held in collision by maximizing the luminosity signal. The high-energy beam (HEB) orbit was adjusted to follow the orbit of the low-energy beam (LEB) at the IP. This was done by dithering the HEB orbit (shifting the orbit $\pm 10\%$ of a beam sigma in x, y and y') and observing the luminosity changes. This was enough to get about a 1% drop in the luminosity signal which enabled us to perform a quadratic fit to the data and then move the HEB to the maximum point in the calculation [8]. The update rate of this feedback system was about 9 sec. We succeeded in upgrading this feedback with a system of air coils that could dither the beam at frequencies of about 100 Hz. This allowed the feedback system to drive each dimension with a different frequency and then use lock-in amplifiers to separate the signals from the three dither dimensions [9]. This new technique permitted an update frequency of at least 1 Hz, limited by the speed of changing the corrector magnets.

In addition to the sextupole orbit bump knobs mentioned above, several other knobs were used for optimizing the accelerator performance. First of all there were the tune trombone knobs which allowed adjustments of the x and y tunes of each ring. Four global skew quads in each ring permitted control of the global coupling and six skew quads on either side of the detector for each ring (a total 24 magnets) to control the local coupling at the IP. Four fixed collimators about 300 m upstream of the IP in each ring helped control injection backgrounds and general beam tail backgrounds. These were one-sided collimators. Closed bumps were used to move the beam closer or farther away from the collimators.

3.4.5 Best Betatron Tune Location

The best location in the tune plane was chosen by the best beam-beam performance. The best location was obtained with the horizontal tune just above the half integer (~ 0.508) and the vertical tune just above (0.572). In Figure 32 are shown simulated luminosity contours on the x-y tune plane indicating optimal performance near the observed best location [10]. Considerable work was needed to correct horizontal beta beat errors at these tunes.

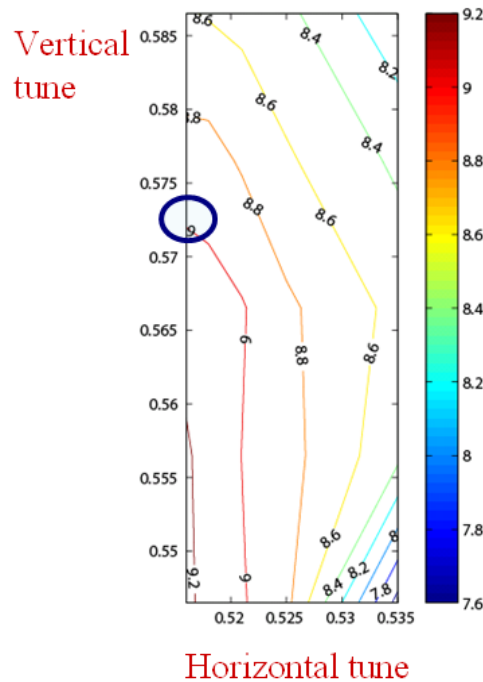


Figure 32: Contours of simulated luminosity in the tune plan. The best fractional tunes in operation were 0.508 horizontally and 0.574 vertically agreeing with experiment.

3.4.6 Beam-Beam Observations

The measured luminosity versus the product of the bunch currents is shown in Figure 33 and the specific luminosity in Figure 34. The resulting maximum vertical beam-beam parameters in the two rings were 0.05 to 0.065. At low currents the luminosity follows the product of the beam currents and is just geometrical in nature. At higher currents the luminosity falls below the product of the currents as the beam-beam parameter(s) start to saturate and one or more of the beam sizes at the IP start to increase with currents. At the highest currents the HER current was limited by the LER lifetime and the LER current by HER generated IR backgrounds in the detector.

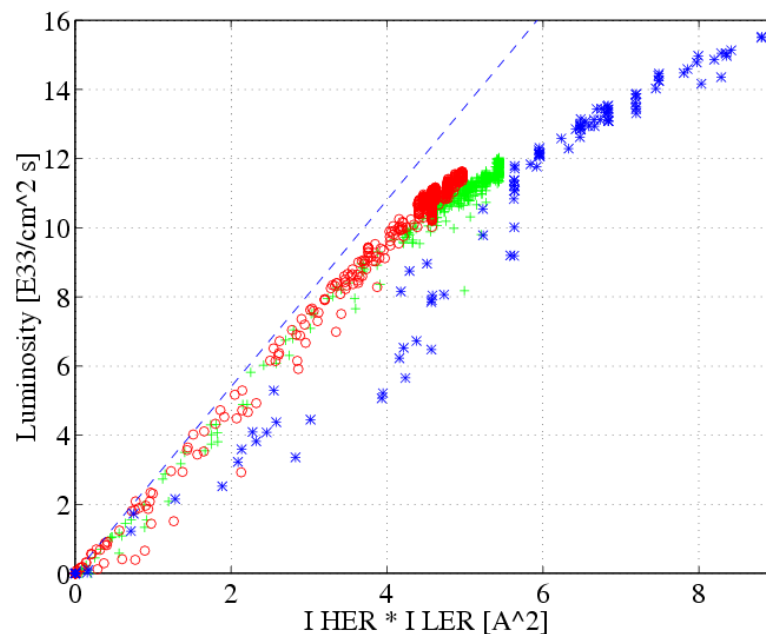


Figure 33: Luminosity versus the product of the bunch charges. The red and green curves show luminosity in the by-2 pattern (4 nsec) bunch spacing during operation achieving a luminosity of 1.2×10^{34} . The blue curve shows the by-4 bunch pattern (8 nsec) scaled to a by-4 bunch pattern, indicating increased luminosity may have been possible in PEP-II with by2.

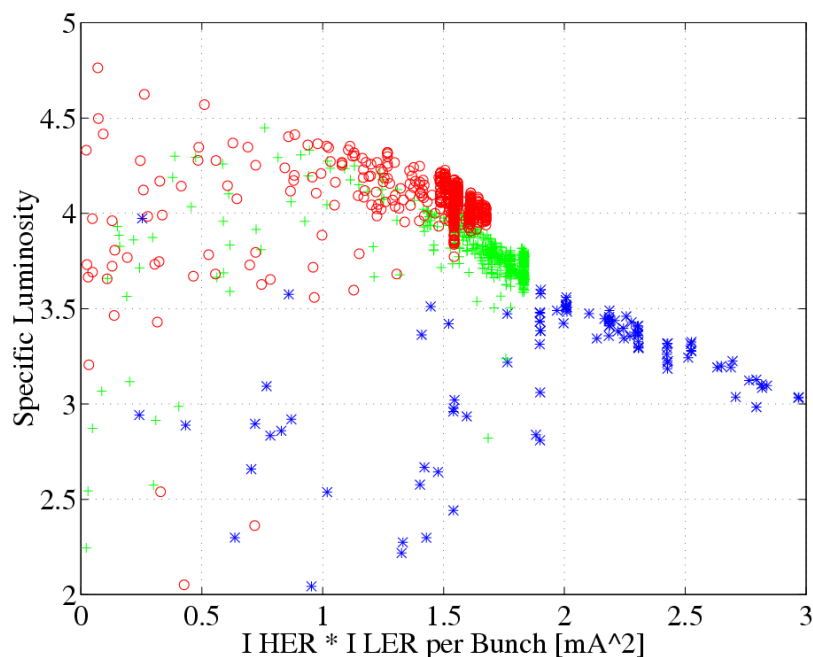


Figure 34: Specific luminosity versus the product of the bunch charges. The specific initially rises because of dynamic beta effects and then falls due to beam-beam interaction both primary and parasitic collisions. The parasitic beam-beam effect was only a few percent.

The vertical beta functions in both rings of PEP-II were lowered to increase the luminosity, as suggested in Equation 1. There is a limit to this process when the vertical beta is just a little smaller ($\sim 10\%$) than the bunch lengths. A calculation of this “hourglass effect” is shown in Figure 35. PEP-II ultimately operated with a β_y^* of about 9-10 mm with a bunch lengths of 10-11 mm. A lower β_y^* can also increase the

background in the detector by increasing the beam sizes in the final doublets, which affect the HER more than the LER.

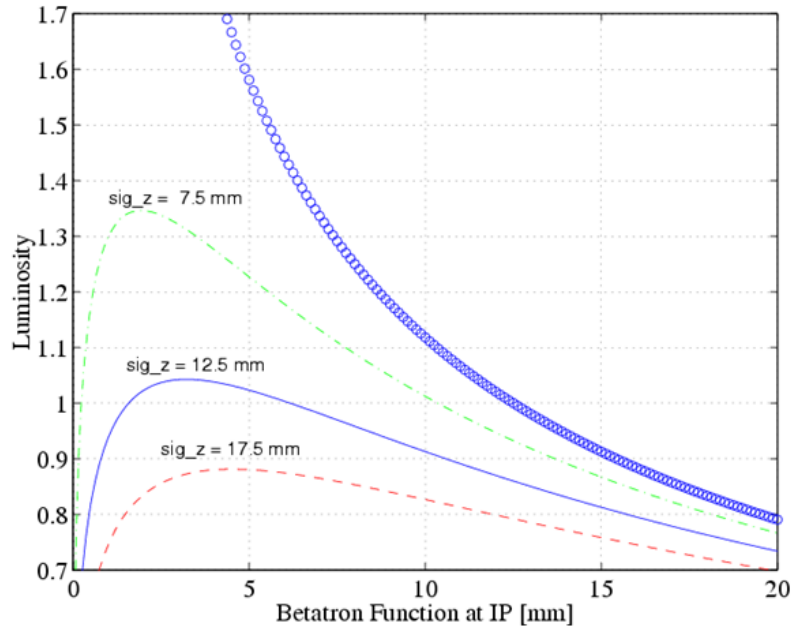


Figure 35: Hour glass effect on relative geometrical luminosity for different bunch lengths. The nominal bunch length for these calculations is 7.5 mm. In operation the bunch lengths were about 10 mm.

A study of the dynamic beta-beat effects is shown in the observations in Figure 36 where the beam sizes away from the interaction region were observed as the beam currents were raised. The beam-beam forces act as a lens and can change the effective beta functions throughout both rings. These changes can be observed by looking at beam size monitors away from the IR at two locations which are in betatron phase and out of betatron phase with respect to the IP. In Figure 36 the x-ray beam size monitor and the synchrotron (visible light) monitor were used in the LER beam to measure horizontal beam changes. The vertical sizes were too small to measure accurately. Significant beam size changes in PEP-II LER were observed when the HER current was raised. This indicates that the strong beta beating of the beam occurs at the core of the beams affected by the beam-beam forces.

A study of the luminosity versus the number of bunches in the two bucket spacing, shown in Figure 31 and Figure 37, indicate that there are no long range effects observed. The measurements were made by observing the luminosity while adding bunches in the 2-bucket pattern with a fixed number of mini-trains but adding bunches to each mini-train (seen in Figure 31). This means that the cures for the electron cloud effects in LER, solenoids in the straight sections and TiN coating and antechambers in the ARCs, were successful. If the cures were turned off or down, the luminosity was reduced at the end of each mini-train and also at the end of the overall bunch pattern just ahead of the large ion gap. The electron cloud in LER enlarged the beam size in this case.

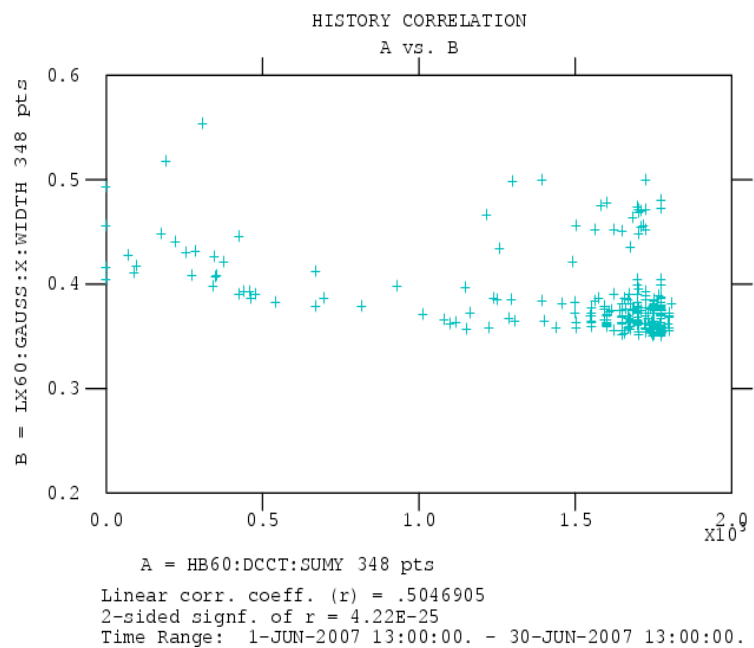
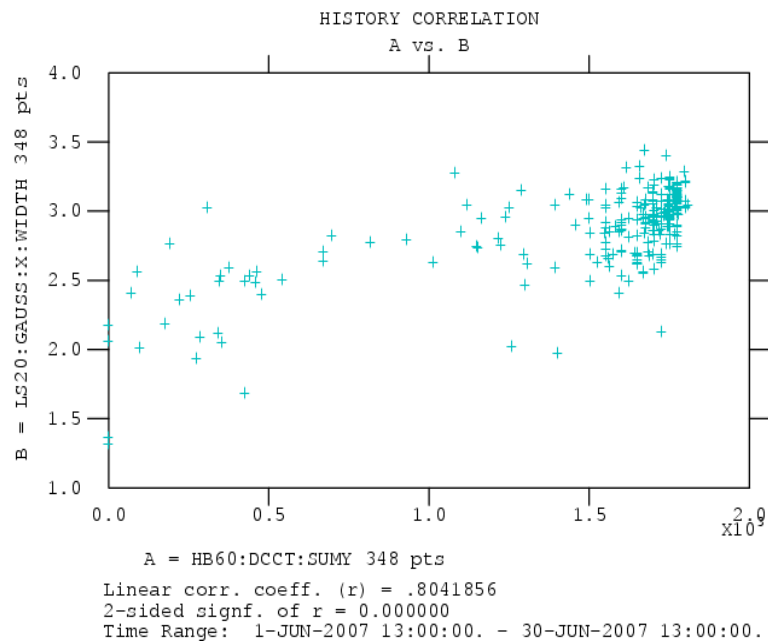


Figure 36: Horizontal dynamic beta effect seen in LER beta beating and observed in the LER beam sizes by the x-ray monitor (lower) in betatron phase (~ 20 deg) with respect to the IR and synchrotron light (upper) out of phase (~ 90 deg) with the IR. The beam sizes changed about 30% indicating a beta function change of about 70%. The LER beam current was held fixed while the HER beam current was increased and the beam sizes observed.

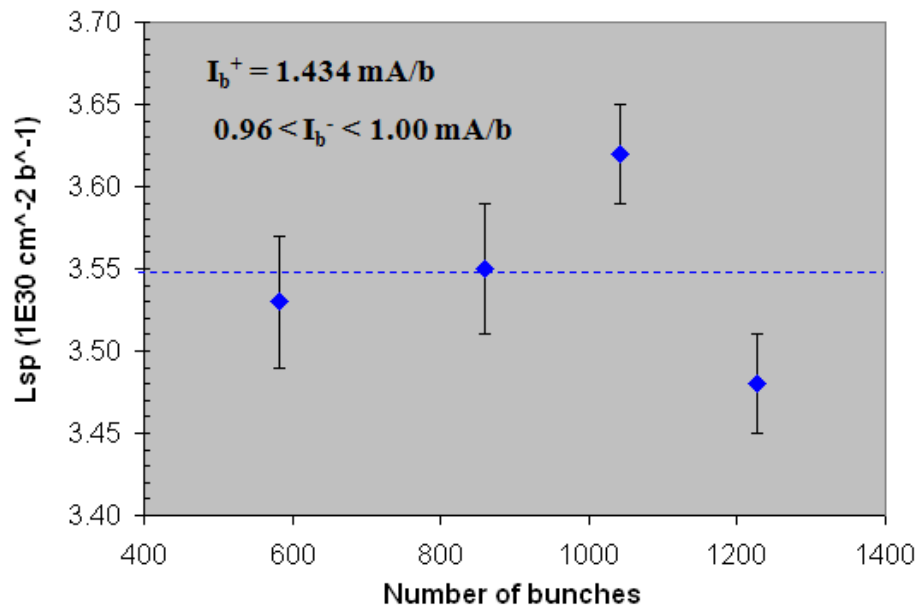


Figure 37: Specific luminosity versus number of bunches with two bucket spacing. The bunch train pattern is shown in Figure 31.

A study of the effect of horizontal beam offsets at the IP was done and the results are shown in Figure 38. The measurements were made by using IR closed steering bumps to move the beams horizontally and observing the luminosity. The results were that at low currents the measurements match the simulations, i.e. the geometrical overlaps explained the entire effect. However, at high bunch currents the beam-beam forces make the effective horizontal beam size much smaller. This effect reduced strongly how robust the beams were to orbit shifts. The source of this reduction is the beam-beam effect but the exact mechanism is not known at this time [11].

A study of the effect of collision crossing angles was done and the results are shown in Figure 39. The measurements were made by using IR closed angle bumps to move the beams horizontally at an angle relative to each other and observing the luminosity. The results were that at low currents the measurements match the simulations, i.e. the geometrical overlaps explained the entire effect. However, at higher bunch currents the beam-beam forces make the beam more sensitive which reduces how robust the beams and luminosity are to angle shifts. The crossing angle perturbations affect the beam over a range that is narrower than predicted [11].

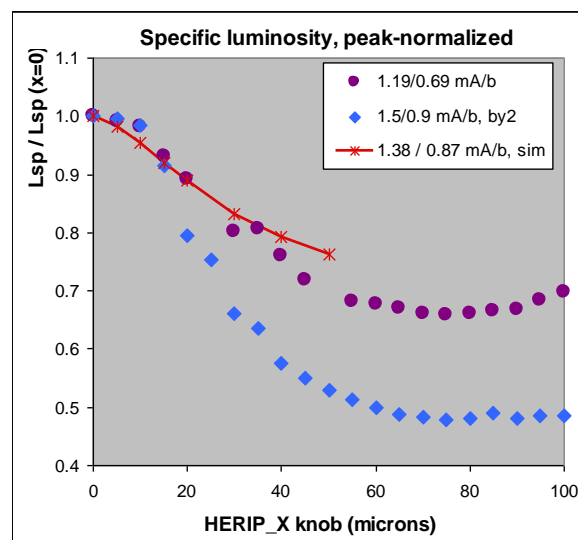
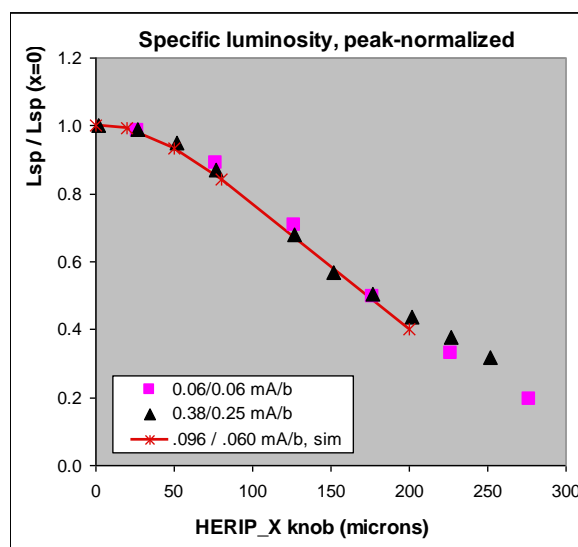
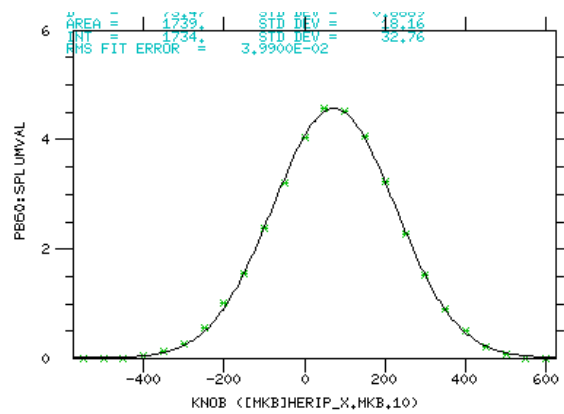


Figure 38: Luminosity versus horizontal offsets. The top plot is a normal scan with a Gaussian fit. The middle plot is for low bunch currents which fits simulations well. The lower plot is at high currents where the effective horizontal beam size becomes much smaller, presumably due to the effects of the horizontal beam-beam effect.

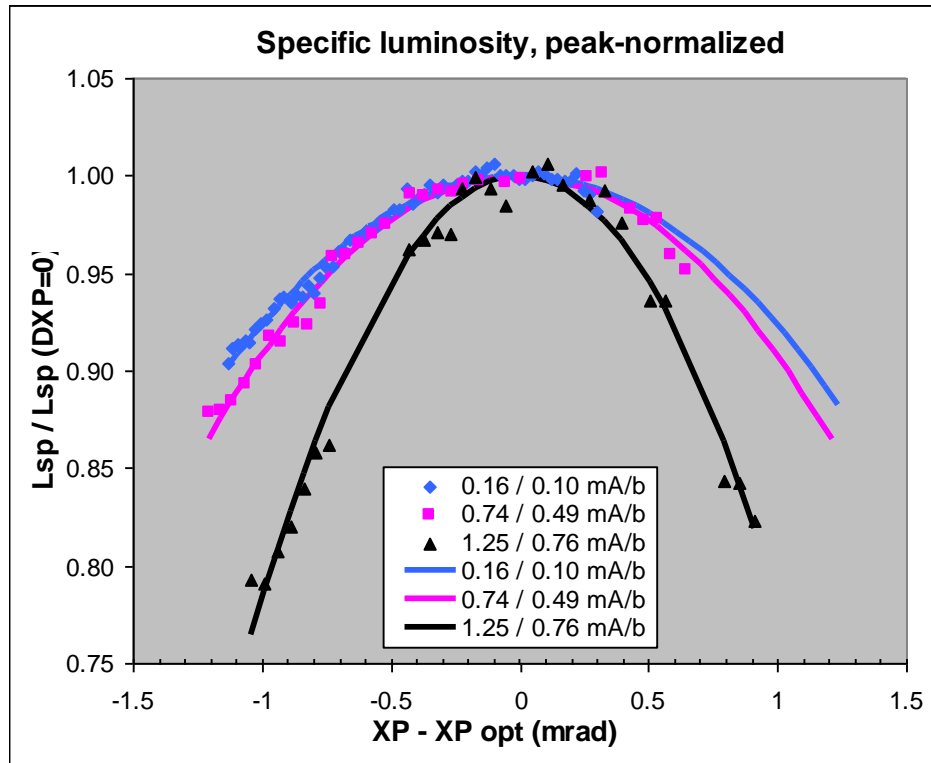


Figure 39: Specific luminosity versus horizontal crossing angle. The specific luminosity becomes more sensitive at higher bunch currents. Higher currents reduce the tolerance to crossing angle changes.

3.4.7 Acknowledgements

The authors wish to thank the PEP-II accelerator, operations, and support staff for making PEP-II such a productive machine. Many people contributed to the study of the beam-beam interaction. We wish to thank specifically Y. Cai, F.-J. Decker, W. Kozanecki, A. Kulikov, M. Placidi, U. Wienands, and Y. Yan.

3.4.8 References

1. "PEP-II an Asymmetric B Factory", Conceptual Design Report, CALT-68-1869, LBL-PUB-5379, SLAC-418, UCRL-ID-114055, UC-IIRPA-93-01, June 1993.
2. M. Sullivan, "PEP-II Status", Proceedings of the 40th ICFA ABDW 2008 (e+e-Factories '08), Novosibirsk, Apr. 14-16, 2008, p. 13.
3. J. Seeman, "Last Year of PEP-II Operation", EPAC 2008, Genoa, pg 947.
4. U. Wienands, "Lepton Collider Operation with Constant Currents", PAC 2005, pg 151.
5. F.-J. Decker *et al.*, "Orbit Distortions and Bumps in the PEP-II Ring", EPAC 2002, Paris, p. 389
6. F.-J. Decker *et al.*, "Lattice Effects Due to High Currents in PEP-II", EPAC 2004, Lucerne, p. 836.
7. W.R. Nelson, *et al.*, "EGS4 Calculations for a PEP-II Luminosity Monitor" SLAC-PUB-7621, Aug. 1997.
8. L. Hendrickson *et al.*, "Slow Feedback Systems for PEP-II", EPAC 2000, Vienna, pg 1897.

9. A. Fisher *et al.*, “Commissioning the Fast Luminosity Dither for PEP-II”, PAC 2007, Albuquerque, pg 4165.
10. Y. Cai, *et al.*, “Simulations and Experiments of the Beam-beam Effects in e+e- Storage Rings,” PAC 2005, pg. 520.
11. W. Kozanecki, *et al.*, “Experimental Study of Crossing Angle and Parasitic Crossing Effects at the PEP-II e+e- Collider,” PAC 2005, pg. 1875.

3.5 Beam-Beam Experience in RHIC

Christoph Montag, Brookhaven National Laboratory, Upton, NY 11973, USA
 Mail to: montag@bnl.gov

3.5.1 Introduction

The Relativistic Heavy Ion Collider RHIC consists of two superconducting storage rings that intersect at six locations around the ring circumference. Two of these interaction regions are currently equipped with experiment detectors, namely STAR at the “6 o’clock” interaction point (IP), and PHENIX at “8 o’clock”. The two beams collide only at these two interaction regions, while they are vertically separated by typically 6-10mm at the other IPs. Together with the separator dipoles located at roughly 10m from the IP, and a distance between bunches of 30m, this avoids any parasitic beam-beam collisions. RHIC is capable of colliding any ion species at magnetic rigidities up to $(B\rho) = 830\text{Tm}$, corresponding to 250 GeV for proton beams, or 100 GeV/nucleon for fully stripped gold ions.

3.5.2 Achieved Beam-Beam Parameters in RHIC

The beam-beam parameter for two identical ion beams can be written as

$$\xi_1 = \frac{Z_1 N_2 Z_2 r_p \beta_1^*}{A_1 4\pi\gamma_1 \sigma_2^2},$$

where the subscripts “1” and “2” refer to the “weak” and the “strong” beam, respectively. Z and A denote the charge state and number of nucleons of the ions, N the number of ions per bunch, and r_p the classical proton radius. β^* and γ are the β -function at the interaction point and the relativistic Lorentz factor, while σ denotes the rms beam radius. With the total bunch charge in RHIC limited to about $Z \cdot N = 2 \cdot 10^{11}$ proton charges regardless of ion species, the highest beam-beam parameters are reached during collisions of (polarized) proton beams. Not surprisingly, performance limitations due to the beam-beam effect were encountered during polarized proton operations only, while for all other ion species the luminosity was limited by other effects. As Table 5 shows, a maximum total beam-beam parameter of 0.018, or 0.009 per interaction point, has been achieved with polarized proton beams at RHIC. The corresponding number for gold-gold collisions, 0.0025, is about a factor 3 smaller than for protons.

Table 5: Latest machine parameters relevant to beam-beam interactions, for Au-Au and p-p collisions.

<i>Parameter</i>	<i>Unit</i>	<i>Au-Au</i>	<i>p-p</i>
relativistic γ , injection	...	10.5	25.9
relativistic γ , store	...	107.4	106.6
no of bunches, n_b	...	111	111
ions per bunch, N_b	10^9	1.3	170
Number of nucleons, A	...	197	1
Charge state, Z	...	79	1
β -function at IP, β^*	m	0.7	0.7
emittance $\varepsilon_{N,x,y,95\%}$	mm-mrad	10	15
chromaticities (ξ_x, ξ_y)	...	(+2, +2)	
harmonic no h , store	...	7×360	360
Number of IPs	...	2	2
Avg. beam-beam parameter per IP	...	0.002	0.0075
Max. beam-beam parameter per IP	...	0.0025	0.009

3.5.3 Luminosity Lifetimes at Different β^*

While the proton bunch intensities have been practically equal for several years, the β -function at the IP has been decreased from 1.0 m in Run-8 to 0.7 m in Run-9 to increase the luminosity. This resulted in the expected peak luminosity increase, but the luminosity lifetime suffered considerably, as illustrated in Figure 40. During the course of Run-9, several attempts were made at understanding and improving this situation [1]. After re-loading the Run-8 lattice configuration restored the luminosity lifetime, it finally became clear that the luminosity lifetime reduction was related to the lower beta-star value of 0.7 m in conjunction with the beam-beam effect.

Tracking studies with a 4-D beam-beam model and all known lattice nonlinearities have shown that the dynamic aperture drops from 4.9σ at $\beta^* = 0.9$ m to 4.1σ at $\beta^* = 0.7$ m, which is a significant reduction [2]. However, since a 4-D beam-beam model is not realistic in the case of RHIC with its rms bunch length of about 1 m, these dynamic aperture simulations are only valid in a relative sense when two lattice configurations are compared.

It is important to note here that the situation at 250 GeV is expected to be significantly better for several reasons. First of all, the multipole errors in the low- β triplet quadrupoles were minimized during construction for the full RHIC proton energy of 250 GeV. Since the Run-9 experience demonstrates that these multipole errors are the main source of beam lifetime degradation, these smaller errors at the higher energy should result in better beam lifetimes for the same lattice configuration. Furthermore, the transverse beam size at 250 GeV is a factor 1.6 smaller than at 100 GeV due to adiabatic damping. With this smaller size, the beam therefore samples smaller magnetic field nonlinearities in the triplets.

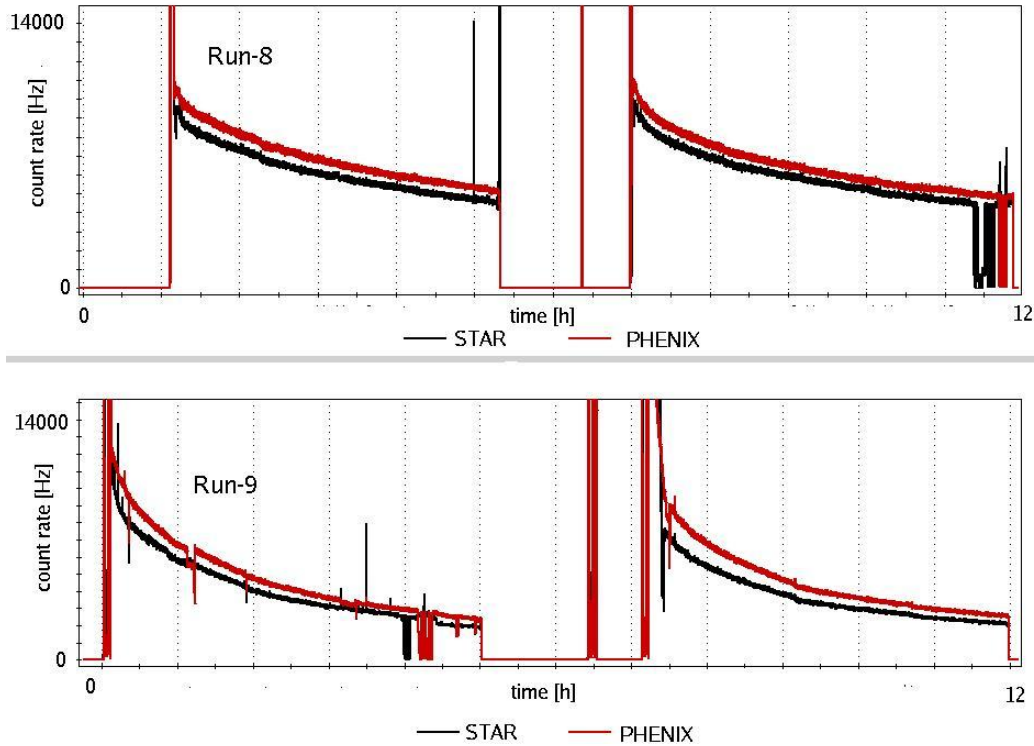


Figure 40: ZDC interaction rates at the two RHIC experiments during Run-8 and Run-9.

3.5.4 Strong-Strong Effects

With the fractional polarized proton tunes of both beams between $2/3$ and $7/10$, and a beam-beam parameter of 0.0075 per IP, coherent beam-beam effects, which in previous years manifested themselves only in dedicated experiments [3], are now observed during regular operations. Since the available tune space between these resonances is not sufficient to suppress these π -modes by means of separating the tunes of the two rings, this effect limits the attainable beam-beam parameter and therefore the luminosity of RHIC. The amplitude of these π -modes may depend on the betatron phase advance between the two beam-beam collision points. Designing a lattice with betatron phase advances of $(2n+1) \cdot \pi$ between IPs 6 and 8 is expected to result in a significant reduction of the π -mode amplitudes, thus allowing for higher beam-beam parameters and therefore resulting in higher luminosity.

3.5.5 Unequal RF Frequencies

When RHIC was providing deuteron-gold collisions during Run-3, the machine was initially set up with equal beam rigidities at injection. The resulting unequal RF frequencies led to pseudo-random beam-beam interactions and in turn to unacceptably short beam lifetimes despite the transverse separation of the beams in the interaction regions [4]. To avoid these detrimental effects, RHIC was subsequently set up with equal relativistic γ , and therefore equal RF frequencies at injection and throughout the entire energy ramp.

3.5.6 Future Improvements

To overcome the present limitations posed by the beam-beam effect, several countermeasures are being studied. A near-integer working point shows improved dynamic aperture in simulations [5]. However, actual operation at tunes close to the integer turned showed intolerably high background levels caused by 10 Hz orbit oscillations whose amplitude is enhanced by roughly a factor five compared to the regular working point near $2/3$ [6]. A fast global orbit feedback system currently under development is expected to eliminate these orbit oscillations, and therefore reduce background levels significantly [7]. 10- and 12-pole correctors in the IRs were shown to improve the beam lifetime under beam-beam conditions [8].

To allow for higher beam-beam parameters, an electron lens will be installed to compensate the nonlinear beam-beam kick of one RHIC interaction point, thus reducing the total beam-beam tunes shift parameter [9]. In turn, bunch intensities can be increased to result in the same total beam-beam parameter as in the present configuration. This is expected to increase the luminosity by a factor up to two.

Systematic experimental studies of the effect of the betatron phase advance between the two interaction points on coherent beam-beam oscillations (π -modes) will be conducted in the near future as part of the head-on beam-beam compensation project. Since the predictive power of dynamic aperture calculations with respect to machine performance is limited, beam lifetime simulations are currently being developed. For realistic results, effects such as intrabeam-scattering, orbit jitter, tune modulations, etc. need to be included in these simulations, which are therefore very challenging in CPU-time intensive.

3.5.7 References

1. C. Montag et al., "RHIC Performance as a 100 GeV Polarized Proton Collider in Run-9", Proc. IPAC 2010
2. Y. Luo, M. Bai, J. Beebe-Wang, W. Fischer, C. Montag, G. Robert-Demolaize, T. Satogata, S. Tepikian, and D. Trbojevic, "Dynamic Aperture Evaluation of the Proposed Lattices for the RHIC 2009 Polarized Proton Run", C-A/AP/349, January 2009
3. W. Fischer, M. Blaskiewicz, J.M. Brennan, P. Cameron, R. Connolly, C. Montag, S. Peggs, F. Pilat, V. Ptitsyn, S. Tepikian, D. Trbojevic, and J. van Zeijts, "Observation of Strong-Strong and Other Beam-Beam Effects in RHIC", proceedings of the 2003 Particle Accelerator Conference, Portland, Oregon (2003).
4. W. Fischer et al., "Tune modulation from beam-beam interaction and unequal radio frequencies in RHIC", BNL C-A/AP/72 (2002)
5. C. Montag et al., "A Near-integer Working Point for Polarized Protons in the Relativistic Heavy Ion Collider", Proc. PAC 2007
6. C. Montag et al., "RHIC Polarized Proton Performance in Run-8", Proc. EPAC 2008
7. M. Minty et al., "Global orbit feedback at RHIC", Proc. IPAC 2010
8. W. Fischer et al., "RHIC proton beam lifetime increase with 10- and 12-pole correctors", Proc. IPAC 2010
9. W. Fischer et al., "Status of the RHIC head-on beam-beam compensation project", Proc. IPAC 2010

3.6 Beam Dynamics Study for the LHC Phase I Luminosity Upgrade including Beam-Beam

E. Laface, S. Fartoukh, and F. Schmidt, CERN, CH-1211 Geneva 23, Switzerland

Mail to: Frank.Schmid@cern.ch

3.6.1 Introduction

The Large Hadron Collider is being commissioned and it is planned to reach the nominal luminosity of $10^{34} \text{ cm}^{-2}\text{s}^{-1}$ in its final configuration.

The Phase I luminosity upgrade is focused on the possibility to reduce the transverse size of the beam at the interaction point, squeezing the β^* from its nominal value of 55 cm, down to 30 cm [1]. This new squeeze is performed replacing the nominal inner triplet with a new longer triplet with a lower gradient and a larger aperture, leaving unchanged the other quadrupoles of the long straight section (the so-called matching section and dispersion suppressors). A consequence of a longer triplet are new parasitic encounters between the beams, with an impact on the stability due to the long-range beam-beam (BB) interaction. In this paper particle stability is studied in terms of Dynamic Aperture (DA) and onset of chaos under the influence of the BB using the scheme of the Phase I Luminosity Upgrade.

The variation of amplitudes due to non-linearities (called "smear") is being investigated, in particular at small amplitudes where it might complicate the collimation procedure.

The unavoidable rounding errors in floating point operations on computers violate the symplectic condition (basically meaning the area preservation of the phase space) in conservative systems like transverse proton oscillations in the LHC. This violation of symplecticity leads to an artificial increase or decrease of the amplitude of the transverse motion. Although, this effect should be very small when the calculations are performed in double precision it should be re-checked for this study since we are dealing with very strong BB non-linearities and due to simulation periods in excess of 1×10^6 turns.

Lastly, we are on the verge of re-activating the volunteer tracking via LHC@HOME which will allow us to do many more systematic checks due to a 100 times larger computing punch.

3.6.2 Simulation Setup

A comparison between the geometry of the new and old interaction region, concerning the lengths of the IR magnets, is reported in Table 6.

Table 6: Length comparison Phase I IR vs. nominal.

Element	nominal	Phase I
Q1	6.37 m	9.135 m
Q2a and Q2b	5.50 m	7.735 m
Q3	6.37 m	9.135 m
IR	119.244 m	149.316 m

Q1, Q2 and Q3 are the three quadrupoles forming the Inner Triplet. IR refers to the length of the interaction region between the left and the right separation dipole “D1”. A relevant parameter to be considered is the number of BB encounters: for the nominal bunch spacing of 25 ns [2] the number of parasitic encounters between the Interaction Point (IP) and the edge of the separation dipole D1 (half interaction region) is 16, for the nominal layout optics and 21 for Phase I. Nevertheless, in the simulations discussed later, the first 5 parasitic encounters after the magnetic entry of D1 are also implemented, till the two beams are fully separated.

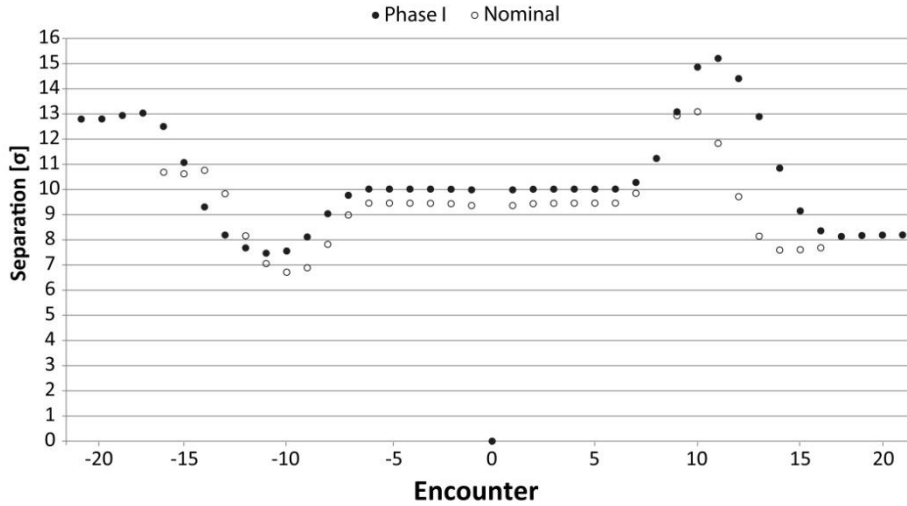


Figure 41: Separation at collision of the BB encounters for the nominal and Phase I optics. This example is the horizontal plane for IP5.

The BB interactions depend critically on the crossing angle of the two beams: it changes both at injection and collision for the new Phase I optics with respect to its nominal value. For the nominal optics the full crossing angle is $340 \mu\text{rad}$ at injection ($\beta^* = 11 \text{ m}$) and $285 \mu\text{rad}$ in collision ($\beta^* = 0.55 \text{ m}$), which corresponds, for collision, to a beam separation of 9.5σ in the drift spaces. For the Phase I optics the crossing angle is kept constant from injection ($\beta^* = 14 \text{ m}$) to collision ($\beta^* = 0.30 \text{ m}$) and at collision it is $410 \mu\text{rad}$ with a beam separation of 10σ which is illustrated along the interaction region in Figure 41.

For the new layout, it is worth noting that out of the 32 first parasitic encounters of either IP only three have a smaller beam separation compared to the nominal layout. The larger beam separation of some 10σ can partially compensate the additional 5+5 parasitic encounters due to the longer triplets.

The head-on BB interaction has a strong impact on the tunes: the fractional part of the tune without BB is the same for the nominal and the Phase I optics (0.31 and 0.32 for the horizontal and vertical plane respectively). Therefore the tune footprint can be directly compared as in Figure 41.

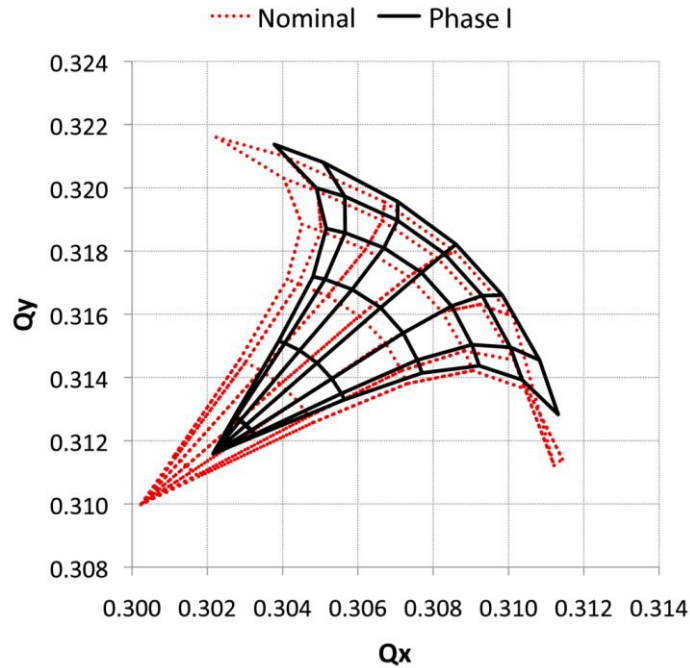


Figure 42: Head-on BB tune shift in the nominal and Phase I optics.

The overall tune footprint, due to the head-on collision, is smaller for the new optics because the crossing angle is larger. To verify the long-term stability of the beam in the presence of the weak-strong BB effect tracking studies are required: the particles are tracked with different configurations based on different initial conditions and 60 different representations of multipolar components, called seeds in the following. The initial conditions are selected considering steps of 15° between 15° and 75° in the x-y plane. For each angle the amplitude is varied in small steps (30 pairs of particles equally spaced over 2σ): at injection the normalized amplitudes of the particles are chosen between 8 and 14σ , and between 4 and 18σ in collision. The magnetic errors are selected according to the study in [3] and the random errors are generated using 60 different seeds. For each configuration of angle, amplitude and seed, the particles are tracked for 10^6 turns. The Dynamic Aperture (DA) is defined as the minimum amplitude that exhibits particle loss. Lastly, the relative momentum deviation is fixed to two thirds of the RF bucket in all tracking runs.

The particles in the LHC will have to survive for some 10^9 turns in collision. However, even very powerful computing facilities like the “volunteer computing”, as described below, do not allow tracking runs for longer than some 10^7 turns. In the next chapter we will check how the 10^5 and 10^6 turn DA compares to the onset of chaos which is a more rigorous bound on particle stability.

3.6.3 Analysis of Particle Motion

First of all it is important to note that all data presented in this chapter represent the minimum over all 60 seeds, i.e. the worst case is inspected here. The results concerning DA will be discussed further down. In this chapter the aim is to compare the DA of 10^5 and 10^6 turns with a more rigorous long-term stability bound, i.e. the chaotic border. It

remains difficult to pin down the exact location of this change of stability behaviour but in practice one finds that the detection of chaos is very sensitive indeed such that those slightly chaotic particles may never get lost.

To avoid a lengthy discussion of how to define the chaotic border two separate curves will be shown: the lower one represents the largest amplitude that is stable and the larger one represents strongly chaotic motion. It goes without saying that within the granularity studied in this context no chaotic behaviour can be found for any amplitude smaller than the lower curve.

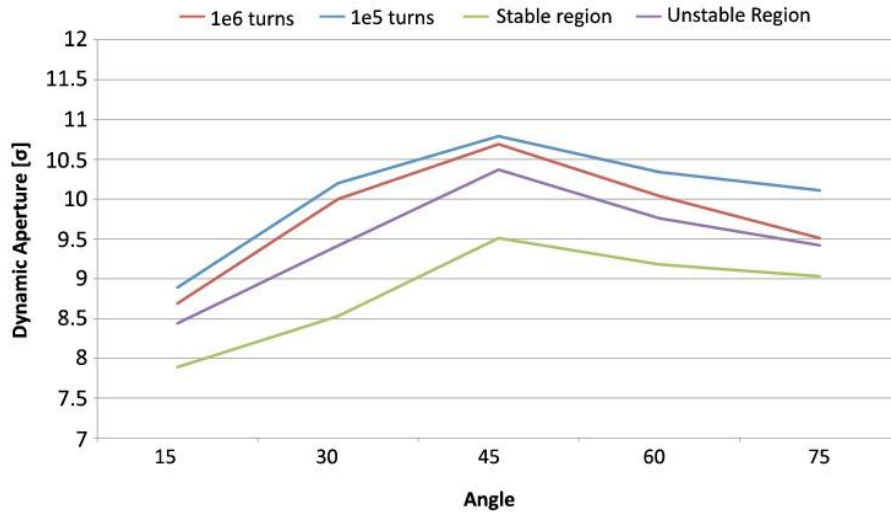


Figure 43: Chaos at injection.

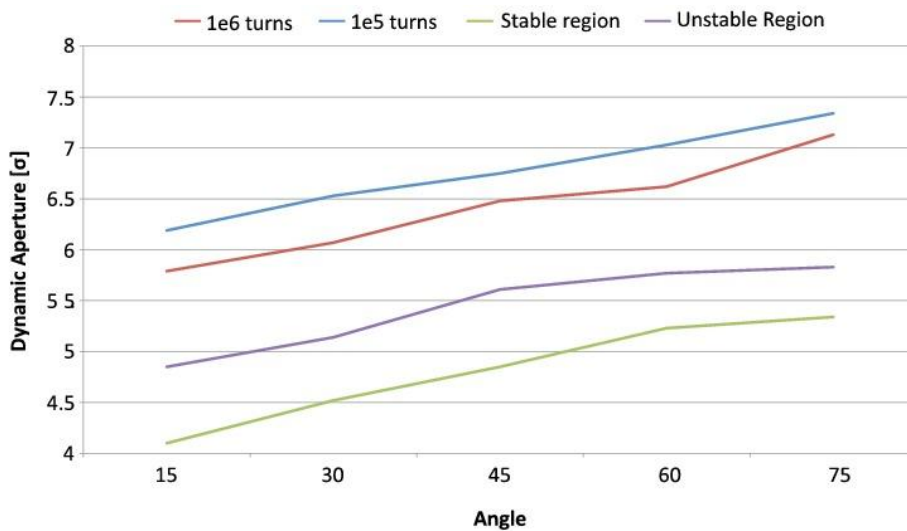


Figure 44: Chaos at collision.

At injection (Figure 43) the DA reduces overall by some 0.25σ when extending the tracking from 10^5 to 10^6 turns except for the large angles where the strong chaotic border is almost reached. With some confidence one can predict that the DA will not go lower than the strong chaotic border for the full injection period that should not exceed 5×10^7 turns.

Figure 44 shows that at collision the long-term stability of the particle motion is much reduced due to the strong head-on and parasitic BB effects. The loss in DA in the 10^6 turn case is about 0.5σ , i.e. considerably higher than at injection. Moreover, the onset of chaos is lower by more than a beam sigma. Since particles have to survive 1000 times longer, compared to what can be simulated, a safe estimate for the 10^9 turn DA is about 5.5σ for the best (vertical) angle. Obviously the long-term DA becomes marginal and this looks like a challenge for the collimation system.

Equally interesting for the collimation is to determine by how much the amplitude is “smeared out” in phase space. This has the consequence that at a certain collimator position particles are scraped off according to this smeared area in the phase space. Figure 45 depicts the phase space smearing for injection and Figure 46 for collision energies respectively.

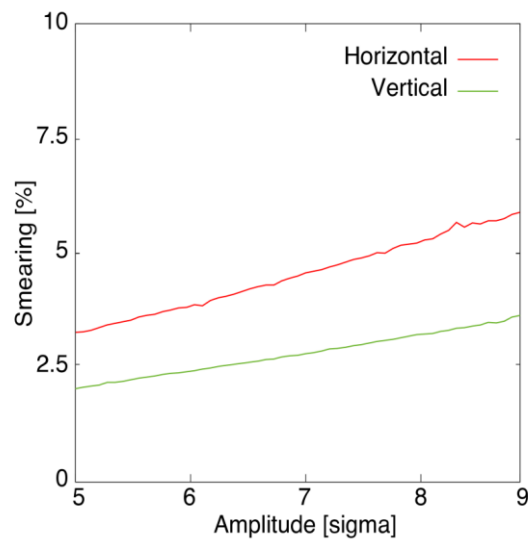


Figure 45: Smear at injection.

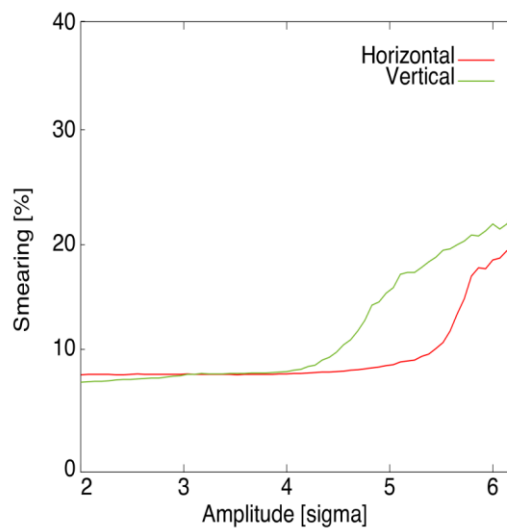


Figure 46: Smear at collision.

One finds that at injection the smear is quite small: even at amplitudes of 9σ it hardly exceeds 5%. However, in collision the smear might reach up to 20% at amplitudes as low as 6σ . One should note however, that the tracking is done with maximum momentum deviation so that these smear values are somewhat pessimistic and this might also explain the peculiar 8% smear levelling in collision. More studies are desirable to clarify this issue further.

3.6.4 Effect of Rounding Errors

The analysis of rounding errors in beam-tracking calculations has first been performed some 25 years ago [5]. There is no reason to believe that these findings are no longer valid today. However, computing hardware has evolved dramatically since then and we are now tracking with the very non-linear beam-beam force. It is therefore worth to re-check by how much relative amplitude loss (or gain) per turn is to be expected due to the inherent loss of symplecticity. In fact, these errors may be larger for the LHC.

In 1985 and performing 6D single particle tracking (without the beam-beam force) for the HERA proton ring [6] the calculations in double precision led to a relative amplitude change per turn of some -2×10^{-13} . As a conclusion the HERA tracking over 10 million turns would still be okay.

For the study presented in this report we have performed a preliminary rounding error analysis of the very worst case, i.e. full BB in collision. To this end we have chosen one seed and did double and four-fold precision tracking over 100,000 turns keeping every single turn. It should be noted that the four-fold precision tracking takes about 100 times longer than the double precision tracking.

Figure 47 shows how on average the simulated particle amplitude is changing as a function of turn number. One finds a linear dependence on the turn number which is in line with the earlier studies. It could also be shown that the rounding errors grow faster for larger amplitudes.

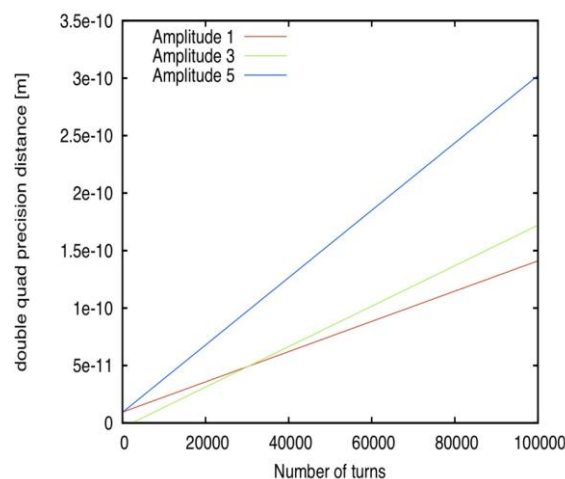


Figure 47: Amplitude change with respect to four-fold precision for small, medium and large regular amplitude, denoted by 1, 3 and 5 respectively.

Table 7 summarizes the results of this preliminary investigation. The relative rounding errors per turn do not follow a simple rule and even may change sign, but this may be expected from IEEE compliant computing machines. What is most worrying is that the rounding errors are larger by a factor 10,000 compared to the old studies. This implies that after only 10^7 turns the amplitude changes by a couple of % which is clearly too large already.

It is therefore mandatory to perform a more systematic study of rounding errors for purely transverse motion or the full 6D phase space, with and without BB and for injection and collision tracking.

Table 7: Amplitude dependent rounding errors.

No.	Amplitude	Relative Rounding Errors per Turn
1	1.6×10^{-7}	9.0×10^{-9}
2	9.8×10^{-7}	-1.7×10^{-9}
3	1.5×10^{-6}	2.0×10^{-9}

3.6.5 Volunteer Computing with LHC@HOME

A decade ago it became apparent that conventional specialized computing facilities and/or PC farms were never large enough or too expensive to perform the systematic tracking studies needed for the LHC in all its configurations. A creative way out of this dilemma has been the screensaver concept to make use of idling PCs either in-house or provided by outside volunteers.

In 2003 [7] a system has been implemented to tap into the several thousand PCs of CERN. An even bigger attempt has been started called LHC@HOME [8] which uses BOINC [9] technology and relies on a large number of volunteers ready to support the LHC. It should be mentioned that using a heterogeneous system of PCs had required special adaptation of the tracking code SixTrack [10] to guarantee bit-by-bit accuracy on any computing platform [11]. As a result it became possible in 2005 [12] to do a systematic BB study with 600,000 jobs over 1×10^6 turns and each job requiring 12 h of computing time.

In the meantime, the performance of BOINC had suffered considerably since it lacked adequate manpower to support this complex system. Therefore BOINC could not be used for such studies as presented here.

Recently, the decision has been made to move BOINC back to CERN and EPFL of Lausanne will manage it. This revived system will not only make systematic BB LHC studies possible again but it will also allow BNL studies with electron lenses which is of mutual interest to both laboratories.

3.6.6 Simulation Results

Three cases are considered both at injection and in collision: the DA without BB effect serves as a reference and is compared to the DA including BB interactions at nominal current (1.15×10^{11}) and ultimate current (1.7×10^{11}) respectively. The tracking for Phase I at injection is shown in Figure 48.

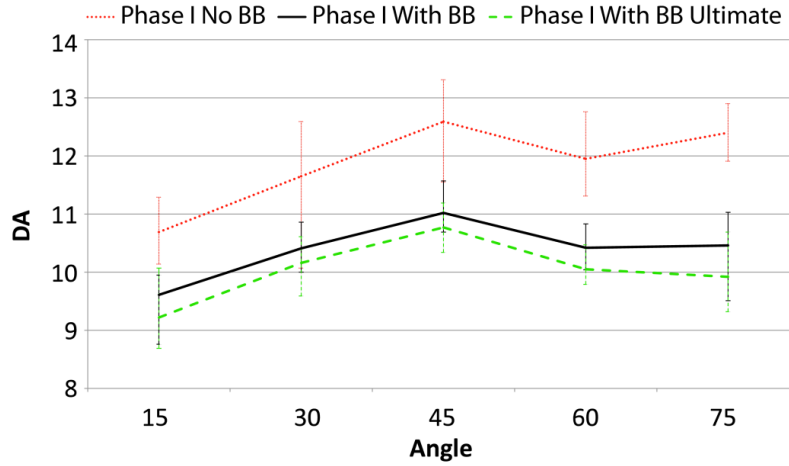


Figure 48: DA at injection.

The three lines represent the average DA over 60 seeds versus the angle for the three cases. The vertical bars give the range between the maximum and the minimum of the 60 seeds. The minimum DA is particularly significant because it is an estimation of the worst possible combinations of errors in the machine. At injection the BB force decreases the average DA by 1.5σ for the nominal current and 2σ for the ultimate current, compatible with the equivalent study which was performed for the nominal LHC.

In collision the effect of the BB force is stronger because of the tune spread induced by the head-on collisions that can push the particles towards the resonance excited by the long-range BB interactions. Consequently the layout and optics of the new insertion, with 21 parasitic encounters and a β^* of 30 cm present some issues to be considered carefully (Figure 49): The average DA with BB at nominal current drops by 6 to 10 σ compared to the case without BB. Moreover, the minimum DA at nominal current is around 6 σ which must be considered as a bare minimum for the stable region of the LHC beam (the primary collimators of LHC in collision are set to 6 σ). The situation is further degraded for ultimate intensity where the minimum DA is, for some seeds, below 6 σ . The average DA of the nominal LHC in collision [2] is around 7 σ and the minimum DA roughly 6 σ , i.e. not far from the results of the tracking obtained for the Phase I upgrade. In essence, however, the DA of the upgrade is barely acceptable and one should aim at improving the situation, in particular for higher current (the ultimate and beyond).

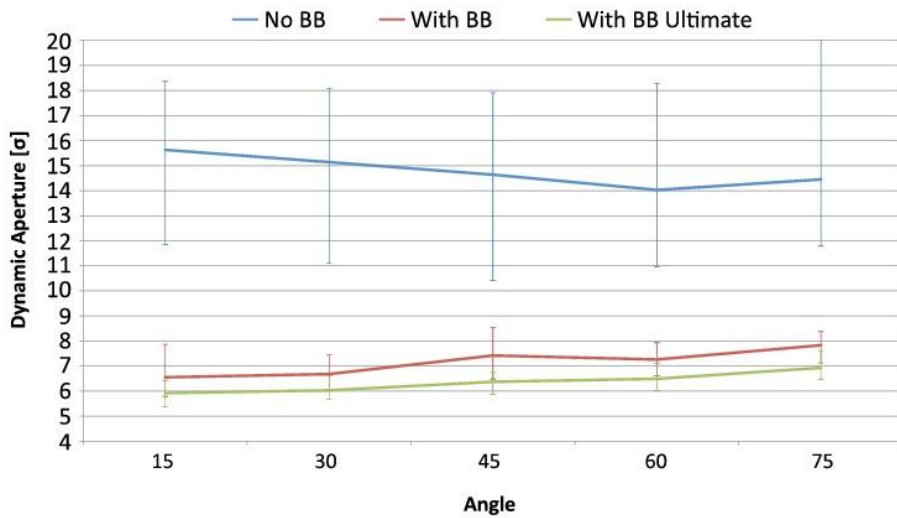


Figure 49: DA in collision with $\beta^*=30$ cm and $\Theta_c=410$ μ rad.

To this end, a back-up collision optics (proposed in [1]) shall be attempted with the intention to reduce the long-range BB effect, with a larger crossing angle. This optics should increase the DA up to the target value of 7.5σ , which corresponds to the reach of the secondary halo in the LHC [2]. This alternative optics is designed to work with the same new inner triplet (IT) imposing to relax β^* in order to preserve the IT aperture in the presence of a larger crossing angle. The new parameters for the back-up solution are: $\beta^*=40$ cm and a crossing angle of 560 μ rad that corresponds to a beam separation of about 16σ . The tracking for this optics is shown in Figure 50.

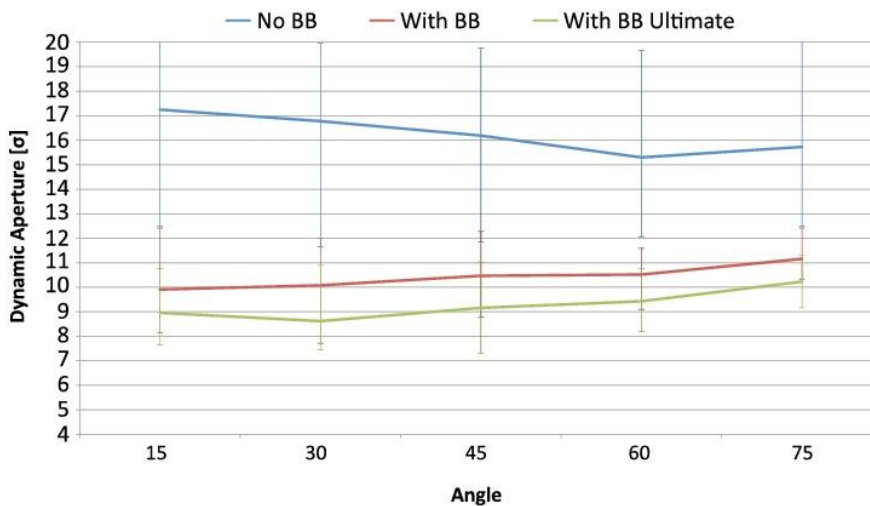


Figure 50: DA in collision with $\beta^*=40$ cm and $\Theta_c=560$ μ rad.

The reduction of the average DA due to the BB effects is still sizable, in between 5 and 7σ but the minimum DA remains above 7.5σ for both nominal and ultimate currents.

The luminosity can be defined as [2]:

$$L \approx \frac{1}{\sqrt{1 + \frac{(\Theta_c \sigma_z)^2}{4\beta^* \varepsilon}}} \frac{n_b N_b^2 f_{\text{rev}}}{4\pi\beta^* \varepsilon},$$

with n_b the number of bunches circulating in the machine, N_b the number of protons per bunch, f_{rev} the revolution frequency of the machine, β^* the β function at the collision point, ε the transverse emittance of the beam, Θ_c the crossing angle and σ_z the RMS bunch length.

The increase of the crossing angle Θ_c and β^* reduces the luminosity for the back-up optics compared to the nominal upgrade optics. However, since the back-up optics allows for higher current (N_b) an overall gain of luminosity might be achievable.

3.6.7 Conclusions and Outlook

As expected, the BB effect in the LHC is one of the most important limiting factors. Any upgrade of the machine will have to face this issue, in particular due to the obvious request for more luminosity. The optics proposed for the Phase I upgrade is close to the limit of the DA acceptable for the LHC, while the back-up collision optics offers more margin. Indeed, thanks to the increased aperture of the new triplet, the normalized crossing angle can be pushed up to about 16σ and the optics still squeezed down to $\beta^* = 40$ cm resulting in a substantially reduced sensitivity of the dynamic aperture with respect to the beam-beam effects. The upgrade optics at 30 cm with a beam separation of 10σ (as in the nominal LHC) seems to push the limits of what can be done in a future LHC upgrade.

In terms of analysis it is not sufficient to look at dynamic aperture over periods accessible to today's computing facilities. For very long time intervals one has to take into account the more rigid limits of where particle motion becomes unstable. On the other hand, non-linearities might even limit the machine performance further in case the smear becomes large at amplitudes that corresponds to the collimator settings.

Future upgrades are foreseen to operate with flat beams and to evaluate if a full 6D treatment of the beam-beam force has further detrimental effects on the stability of particle motion. For systematic studies we are eagerly awaiting to get BOINC back as a tracking facility that will boost our tracking throughput by a factor of 100.

3.6.8 References

1. S. D. Fartoukh, "Layout and Optics Solutions for the LHC Insertion Upgrade Phase I", in the proceedings of IPAC10, Kyoto, 2010.
2. O. S. Brüning *et al.*, *LHC Design Report*, CERN, 2004.
3. B. J. Holzer *et al.*, "Dynamic Aperture Studies and Field Quality Considerations for the LHC Upgrade Optics," in the proceedings of IPAC10, Kyoto, 2010.
4. Y. Luo *et al.*, "Weak-Strong Beam-Beam Tracking for LHC V6.0", BB Workshop Fermilab, 2001.
5. P. Wilhem and E. Lohrmann, "Rounding Errors in Beam-Tracking Calculations", Part. Accel., Vol. 19, pp.99-105 (1986).
6. F. Schmidt, "Untersuchungen zur dynamischen Akzeptanz von Protonenbeschleunigern und ihre Begrenzung durch chaotische Bewegung", DESY HERA 88-02 (1988).

7. E. McIntosh and A. Wagner, "CERN Modular Physics Screensaver or Using Spare CPU Cycles of CERN's Desktop PCs", Computing in High Energy and Nuclear Physics 2004, Interlaken, p. 1055.
8. The official web-site of *LHC@HOME* can be found at: <http://lhathome.cern.ch/athome/history.shtml>.
9. D.P. Anderson, "BOINC: A system for public-resource computing and storage", IEEE/ACM International Workshop on Grid Computing (GRID'04), November 2004, p.4.

3.7 Long-Range Beam-Beam Compensation in the LHC

J.P. Koutchouk, G. Sterbini, and F. Zimmermann, CERN
 Mail to: Jean-Pierre.Koutchouk@cern.ch

3.7.1 Introduction

To maximize the number of bunches and thereby the luminosity in the LHC, the bunch spacing is as small as 7.5 m. This distance is much less than the length of the low-beta insertion of some 120 m. Multiple head-on collisions around each interaction point are prevented by crossing the beams at an angle. For nominal parameters, this angle is chosen to be $285\mu\text{m}$, allowing an average beam separation of 9.5σ for the 18 or 19 long-range beam-beam interactions occurring on either side of the two high-luminosity insertions (Figure 51). Altogether, for the four LHC interaction regions, about 120 long-range interactions occur at a beam separation close to 9.5σ . It was gradually realized from simulations that these interactions are the primary beam dynamics limit of the LHC in collision. This paper reviews a compensation method by wires and the results of investigations obtained so far on numerical and experimental models.

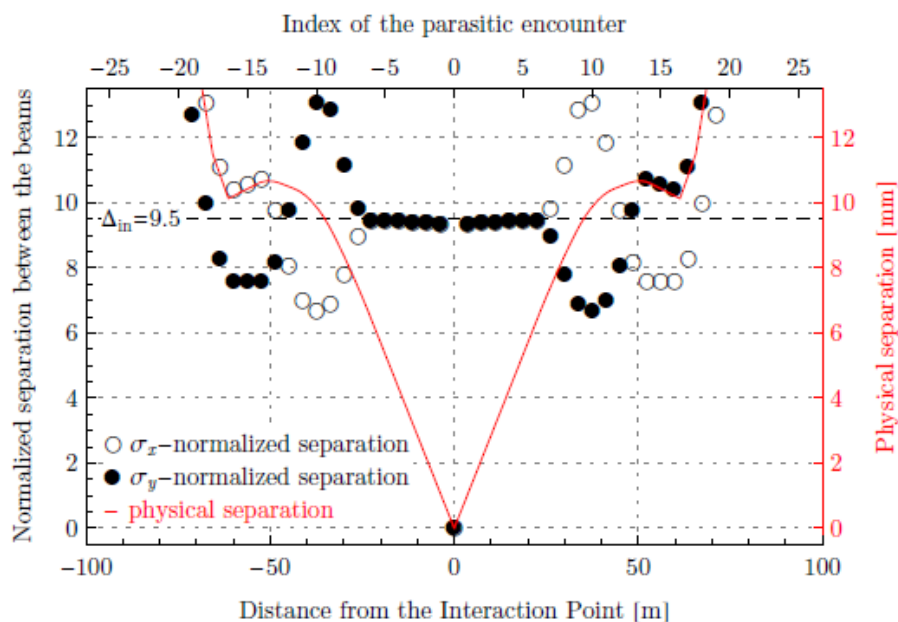


Figure 51: Nominal beam separation at the long-range interaction points in one high-luminosity collision point [1].

3.7.2 The Long-Range Beam-Beam Effect in the LHC

Even though the tune spread caused by the long-range beam-beam effect is significantly smaller than the head-on beam-beam tune spread (Figure 52), the stability limit of the beam motion appears dominated by the former. In simulation, the dynamic aperture is insensitive to the head-on beam-beam effect. Adding the long-range beam-beam effect, however, changes the situation. A decrease of the LHC dynamic aperture is clearly observed when decreasing the crossing angle from its design value (Figure 53) [2].

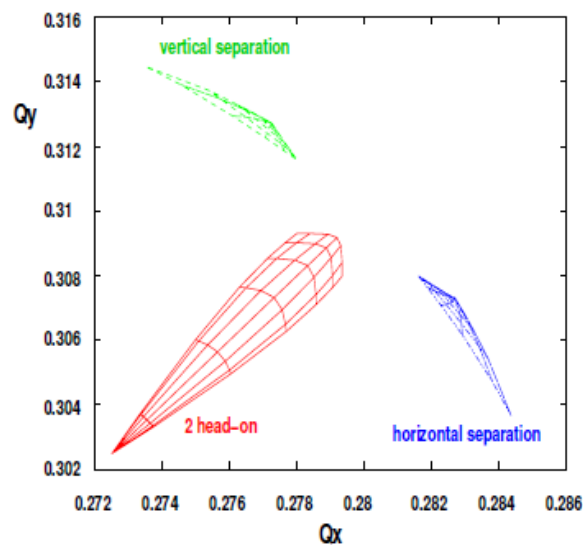


Figure 52: Footprints of head-on and long-range interactions for the nominal LHC (courtesy H. Grote, W. Herr).

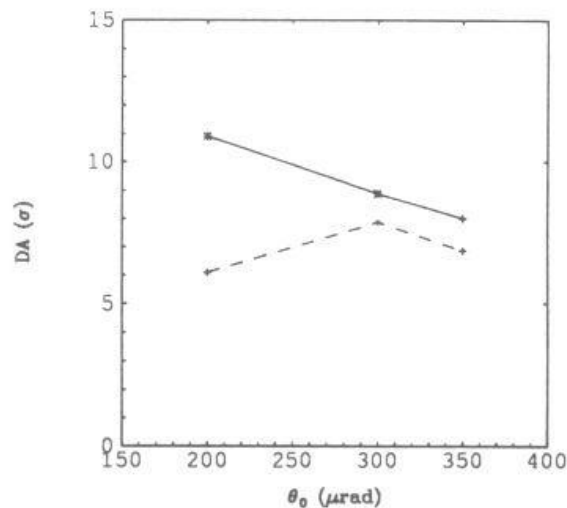


Figure 53: Dynamic aperture versus crossing angle: plain: with magnet errors but without beam-beam, dashed: with both [2].

Similar results have been obtained with other tracking codes [3] (Figure 54 left) or by evaluating a diffusive aperture rather than a dynamic aperture [4] (Figure 54 right).

All these results show consistently that the nominal LHC crossing angle is the minimum required for the nominal bunch intensity and IP beta function. Increasing the angle would have several significant drawbacks though. Primarily, crossing at an angle reduces the luminosity due to the crossing geometry. For nominal parameters this loss is already 16%, and it increases very rapidly with the crossing angle. Another difficulty is related to the synchro-betatron coupling and its impact on the performance. This field is difficult to access: the dense web of resonances excited by synchro-betatron coupling is likely to impact the beam lifetime. The latter is largely out of reach of numerical tracking models. Finally an increased angle requires a larger triplet quadrupole aperture, i.e. a significant investment.

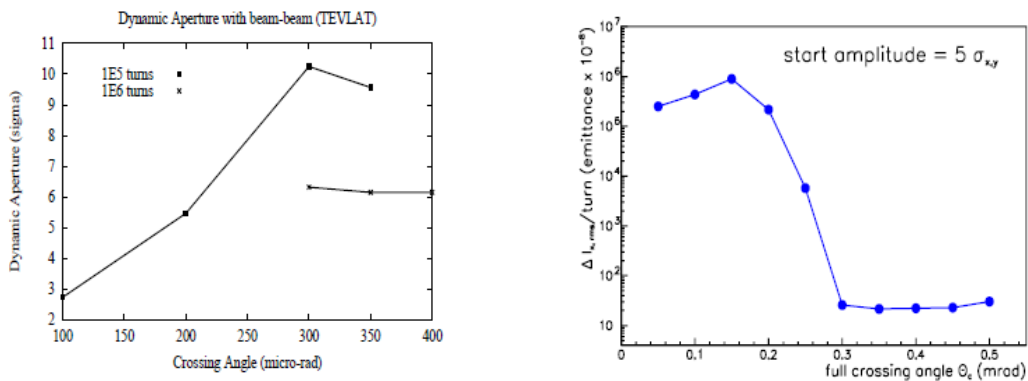


Figure 54: LHC dynamic aperture vs crossing angle with beam-beam and magnetic errors [3] (left); and the diffusive aperture in similar conditions [4] (right).

Given these conflicting requirements, the minimum crossing angle was selected for the nominal LHC, with possible mitigation by increasing β^* . However, both the machine and detectors are designed with the potential of doubling the nominal luminosity by increasing the bunch current by 50%. Later upgrade plans consider much higher beam currents. To solve the long-range beam-beam issue without loss of performance, a long-range beam-beam compensation principle was devised [5]. Thanks to the implementation of wires in RHIC, the importance of the long-range beam-beam effect on beam lifetime could be observed experimentally [6] and used to benchmark simulation codes, giving increased confidence in the conclusion that the long-range beam-beam effect needs compensation.

3.7.3 The Compensation Strategy

Principle

In the common section of the LHC, the nominal beam-beam separation is 9.5σ . The particles contributing to the luminosity have amplitudes lower than 3σ . The particles mostly contributing to the beam lifetime have amplitudes extending to the primary collimation aperture, i.e. 6σ . For those particles and for the round LHC beams, the ratio of the magnetic fields due to a beam of rms size σ_s and that of a compensating current-fed wire, at a distance r from their common centers of gravity, is given by

and shown in Figure 55. It is therefore possible in principle to compensate accurately the long-range beam-beam effect in LHC by compensation wires.

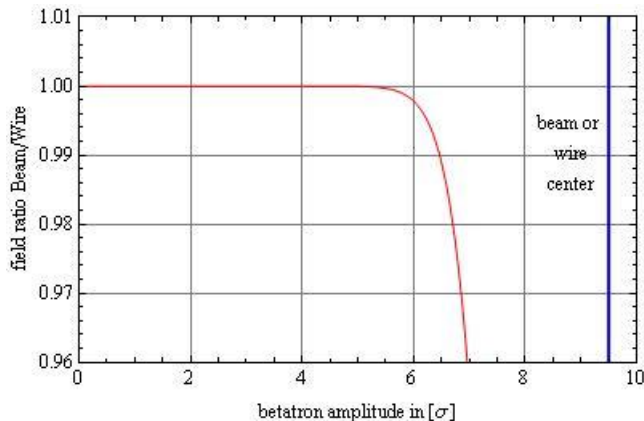


Figure 55: Comparison of the magnetic fields created by a beam or a wire, as a function of the distance to the test particle.

Position of the compensators

It can be easily verified that the required kick from the wire field, of form $1/r$, is independent of the β -function. From this point of view, the compensation can be made anywhere in the machine, provided all distances are implemented in units of local rms beam size (e.g. the beam-wire separation).

The beams have equal transverse sizes in the interaction straight section. In the triplet, the aspect ratio is modulated, but it is not changed on average. In order for the compensation to correctly reproduce the perturbation, the compensation shall be made at a machine azimuth where the β -functions are equal in both transverse planes, whatever their values.

However, the high non-linear content of the long-range beam-beam effect calls for a position of the compensators as close as possible from the perturbation. The large β -function in the LHC triplet (larger than 4 km) has the notable virtue of leaving the betatron phase almost constant over the long-range interaction places on one side of the IP, the triplet and the separation/ recombination section where the beams are brought back to their respective separate channels (Figure 56). This has two consequences: the 18 or 19 long-range interactions on one side of the IP act as if they were lumped; and the optimal position for the compensation is at the crossing of the β -functions in the separation/recombination section, between its two dipoles (positions marked LRC on Figure 56). The betatron phase shift between the lumped perturbation and the compensation is only 2.6 degrees. At this position, the beams are already well separated and the β -functions large enough not to require excessive precision from the compensation equipment (the wire compensator must be transversely mobile and retractable).

Cross-section of the compensating wires

For 50% of the long-range interactions, the beam size aspect ratio is significantly different from one, even if their overall average is close to one. Simulations of the compensation of a single interaction at a beam-size ratio of 2 with a round or elliptic

(same aspect ratio of 2) compensating wire show that a round compensator corrects 90% of the tune footprint in this worst case.

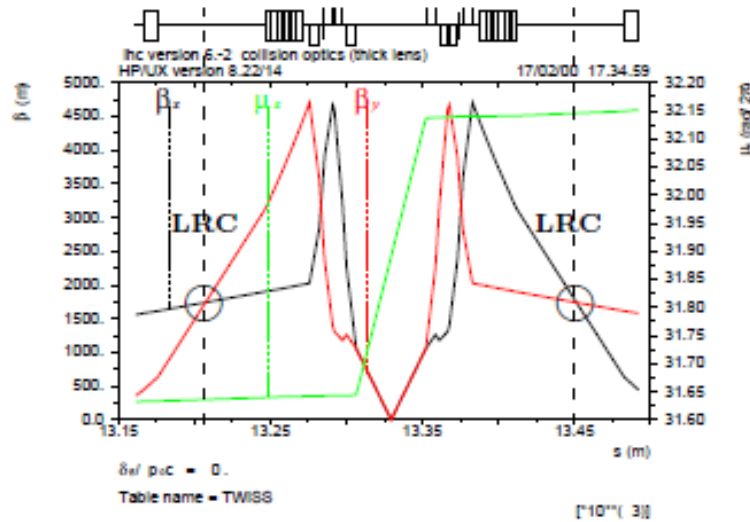


Figure 56: Insertion optics versus azimuth and position of the long-range compensators (LRC's)

Strength of the compensators

To compensate the beam-beam interaction, the wire current integrated along the length of the compensator (counted along the beam propagation axis) shall be equal to the integrated effect of the beam-beam long-range encounters in absolute value and of opposite direction.

3.7.4 Compensation in Numerical Simulations

The efficiency and robustness of the compensation have been studied in detail by several authors in numerical simulations, e.g. [5,7-11], using a number of different codes and criteria.

A first criterion to evaluate the correction efficiency has been the tune footprint [5]; indeed, due to the very low betatron phase advance between perturbation and compensation, this simple non-linear criterion should be sufficiently representative of the non-linear problem. The compensation very efficiently suppresses the orbit deviation in the IP and reduces the tune footprint by a factor 5 (Figure 57). Another reduction of the footprint by factor of 2 can be gained by an empirical 13% overcompensation. It is interesting to note that all other criteria (diffusion, emittance blow-up, discussed later) rather call for a slight under-compensation.

The study by tracking of the diffusive aperture [7] shows a gain of regular motion by 1.5σ in particle amplitude (Figure 58). This gain allows regular motion for all particles inside the physical aperture defined by the LHC collimation system.

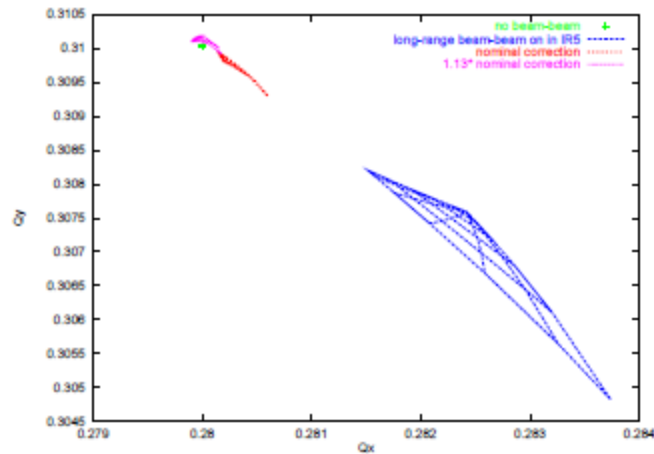


Figure 57: 6σ tune footprint of the LHC beam subject to long-range interactions only, with and without compensation [5].

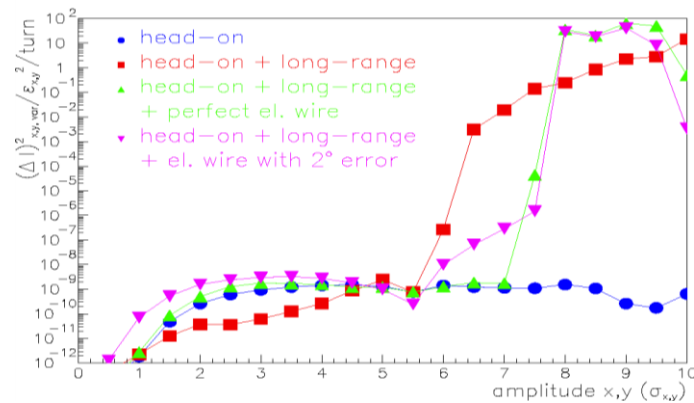


Figure 58: Diffusion rate vs. amplitude in the nominal LHC under several scenarios [7].

Further studies based on the same model show large tolerances with respect to wire parameters (10 degrees in betatron phase shift between perturbation and correction; over 10% and 20% respectively for static excitation current and transverse position). A similar tolerance on the wire transverse position is indeed observed as well in [12]. The only critical tolerance is on the turn-by-turn fluctuations of the wire current that shall remain below 0.1% [7].

In simulations, the long-range beam-beam effect appears to significantly narrow the tune space available for operations [13]. This is identified as well in SPS experiments (see next section). The compensation appears very effective to recover significant freedom in the tune space (Figure 59).

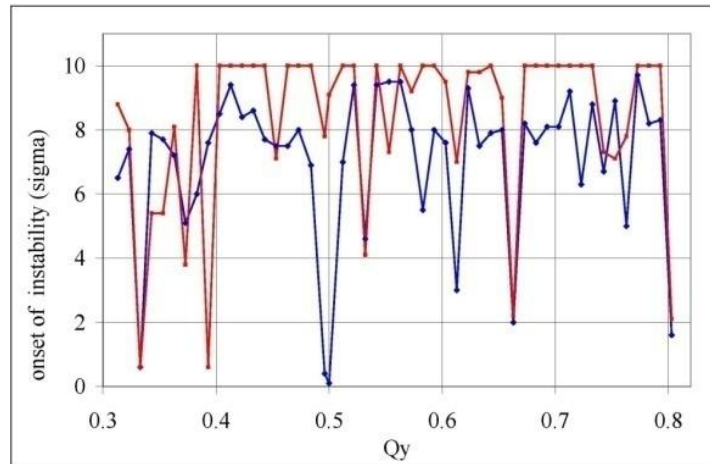


Figure 59: Onset of instability versus tune, without and with compensation [13].

The weak-strong studies mentioned so far were complemented by self-consistent studies of the evolution of the beam size in a strong-strong case using PIC calculation of the beam-beam interaction [10,11]. While weak-strong studies focus on large amplitude dynamics, strong-strong studies give access to the dynamics of particles of lower amplitudes that contribute to the luminosity.

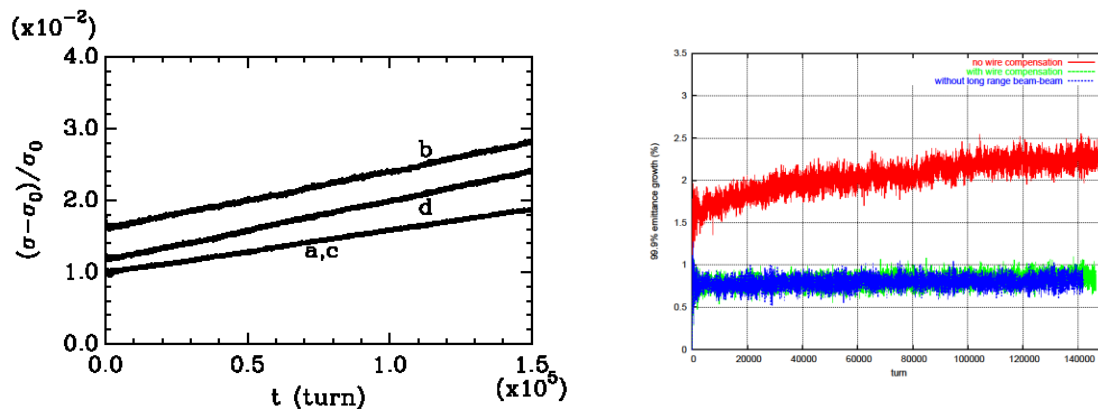


Figure 60: Evolution of the average H and V beam sizes vs turn number; (a) head-on collisions; (c) head-on + long-range compensated; (b) and (d) head-on and long-range without compensation (without/with optical matching) [10] (left). Evolution of emittance with/without compensation [11] (right).

For a beam-beam parameter 5 times above nominal, Figure 60 (left) shows a complete suppression of the emittance blow-up due to the long-range beam-beam effect by the compensation. Identical, but noisier results are obtained for the nominal beam-beam parameter. In addition, this study indicates an even larger tolerance to static wire current errors, from the point of view of emittance growth (Figure 61). This information is of relevance for the compensation of PACMAN bunches.

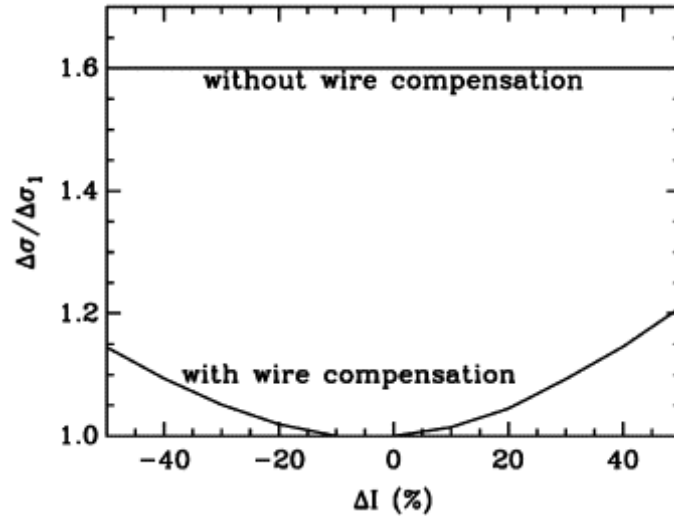


Figure 61: The average horizontal and vertical beam-size growth $\Delta\sigma$ after 10^4 turns vs. the static error of the current ΔI for the wire compensation when $\xi = 0.02$ [10].

The same study confirms the importance of low wire current fluctuations, with a threshold of 0.5% fluctuations, above which emittance blow up is observed. A second later study [11], using a different strong-strong code, observes a very similar evolution of the emittance (the right picture in Figure 60). Once more, the wire compensation perfectly restores the evolution found in the absence of long-range collisions.

While a dc wire excitation is the natural solution for the compensation of nominal bunches, PACMAN bunches, suffering a different and variable number of long-range beam-beam interactions, should require a pulsed compensation. The requirement of very low turn-to-turn jitter identified above has not allowed so far designing a pulsed system, though an interesting proposal of an RF device has been made (F. Caspers), see [8]. However, the large tolerance to wire current errors shown in Figure 61 gives a hint that the compensation of PACMAN bunches might not be a critical issue. Further simulations [14] indeed demonstrate that mitigation of the wire current allows a significant compensation for both types of bunches with a dc compensator (Figure 62).

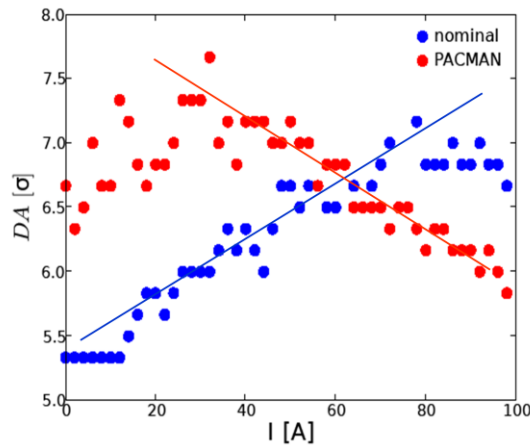


Figure 62: Mitigation of nominal and pacman bunch correction with a dc wire compensator, from [14].

3.7.5 Compensation in Experiments and Operations

Wire compensation has been experimentally investigated over the last decade in three machines: SPS, RHIC and DAFNE. In this paper we review mainly the results obtained in SPS, most relevant to the LHC case. In RHIC, studies mostly concentrated on the long-range beam-beam effect. One compensation experiment was conducted lately. RHIC however only allows a single LR interaction by RF cogging. The weakness of this perturbation requires a reduction of the beam separation to 3σ to enhance the effect, driving the wire compensation system somewhat out of its domain of validity. Evidence of compensation was nevertheless observed, but only in one ring [15]. The DAFNE operations results with a wire are also briefly summarized.

Scaling laws for the long-range beam-beam effect and its compensation

In order to extrapolate the results of experiments, e.g. on the SPS, to the LHC case, the scaling has to be analyzed. It is obtained by imposing that the motion of the particles in the different machines is identical if described in normalized phase space [1,8,16, 17]. We have already referred to the invariance of the problem when distances are expressed in units of rms beam size and to the requirement to correct locally in betatron phase, at a place with identical beam aspect ratio as at the perturbation. Invariance with respect to the ring circumference is naturally obtained by expressing the time in units of turns, and correcting accordingly the lifetime measurements. Invariance with respect to emittance is obtained by scaling the wire current according to:

$$I = I_0 \frac{\varepsilon_N}{\varepsilon_{N0}},$$

with the index 0 denoting nominal LHC values for the wire current and normalized emittance. These prescriptions result in invariance with respect to energy.

3.7.6 SPS Compensation Experiments

Two wire units are installed in the SPS (Figure 63), positioned in the shadow of the vacuum chamber and water cooled. One of them is movable in the vertical plane within the small range of bellow flexibility: a first unit is used to simulate the strong beam by exciting fake beam-beam parasitic encounters. The beam-wire distance is adjusted by moving the beam with a closed orbit bump. The other wire unit, spaced from the first unit by a betatron phase advance equal to the average phase shift with respect to the LR collisions on one side of the IP for the future LHC implementation, i.e. 2.6 degrees, is used as an actual compensator [18].

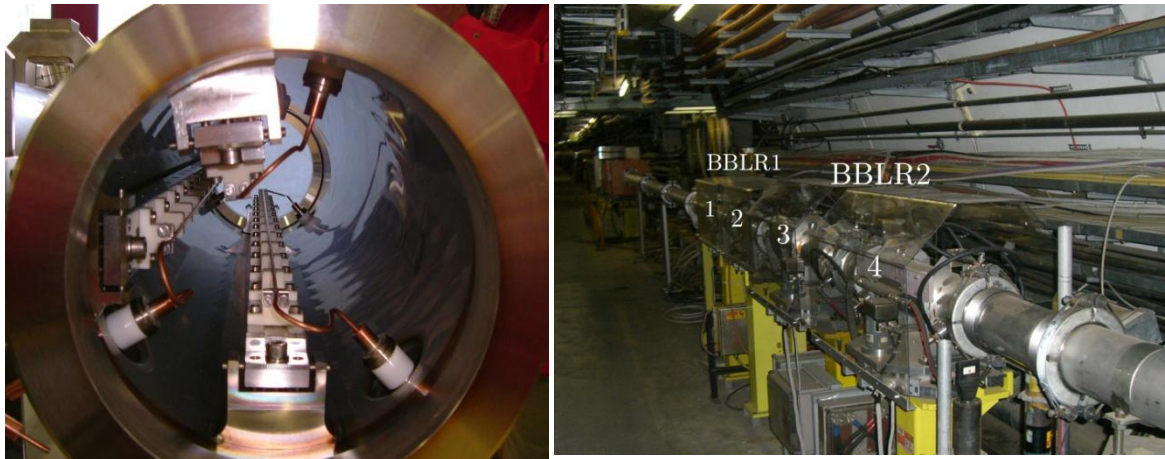


Figure 63: SPS wire units for excitation and compensation. Three wires are installed to study the long-range interactions in different planes and their combinations. Each wire unit consists of two sub-units as indicated on the right.

Each wire is 1.2 m long and can be independently powered up to about 250 A providing an integrated strength of 300 Am. The number of beam-beam parasitic encounters that such integrated strength can simulate, or compensate, assuming equal SPS and LHC beam transverse normalized emittance, is 54, i.e. close to the long-range beam-beam effect created by the two high-luminosity LHC insertions.

To correctly represent the LHC case, the positions of the SPS wires have been chosen to fulfill approximately $\beta_x = \beta_y$, with a phase advance between the two devices of ~ 3 degrees (see section 3.7.5).

The beam losses and the beam lifetime are the main observables of the experiment. They are measured at each of three steps in each experiment, to minimize systematic parasitic effects, namely:

1. WIRES OFF: with wires not excited, the beam-wire separation is varied by moving the beam towards the wires, and all machine parameters are adjusted.
2. EXCITATION ON: the excitation wire is turned on at the appropriate current. The induced orbit and tune perturbations are simultaneously corrected.
3. COMPENSATION ON: the compensation wire is turned on at the desired current. Once more the orbit and tune perturbations are simultaneously corrected.

The parameter space investigated in the experiment is given by the beam energy and emittance, the wire positions and currents, and the machine tunes and chromaticities. Transverse beam profiles have also been measured by wire scans, often revealing a shrinkage of the beam emittance due to a reduced dynamic aperture caused by the effect of the wire (or the equivalent long-range collisions) [18].

In the SPS, compensation experiments were performed at 26, 37 and 120 GeV (single-wire long-range beam-beam experiments also at 55 GeV). The lowest energies are chosen for the better availability of experimental time in shared mode and because the closed orbit correctors used to bump the beam towards the wires have limited strength. 120 GeV is the highest energy that can be contemplated for this experiment, requiring, quite complex bump superpositions to move the beam towards the wires.

Early experiments in pulsed SPS operations:

Figure 64/top shows the first compensation result achieved in the SPS in 2004, reported in [19, 20].

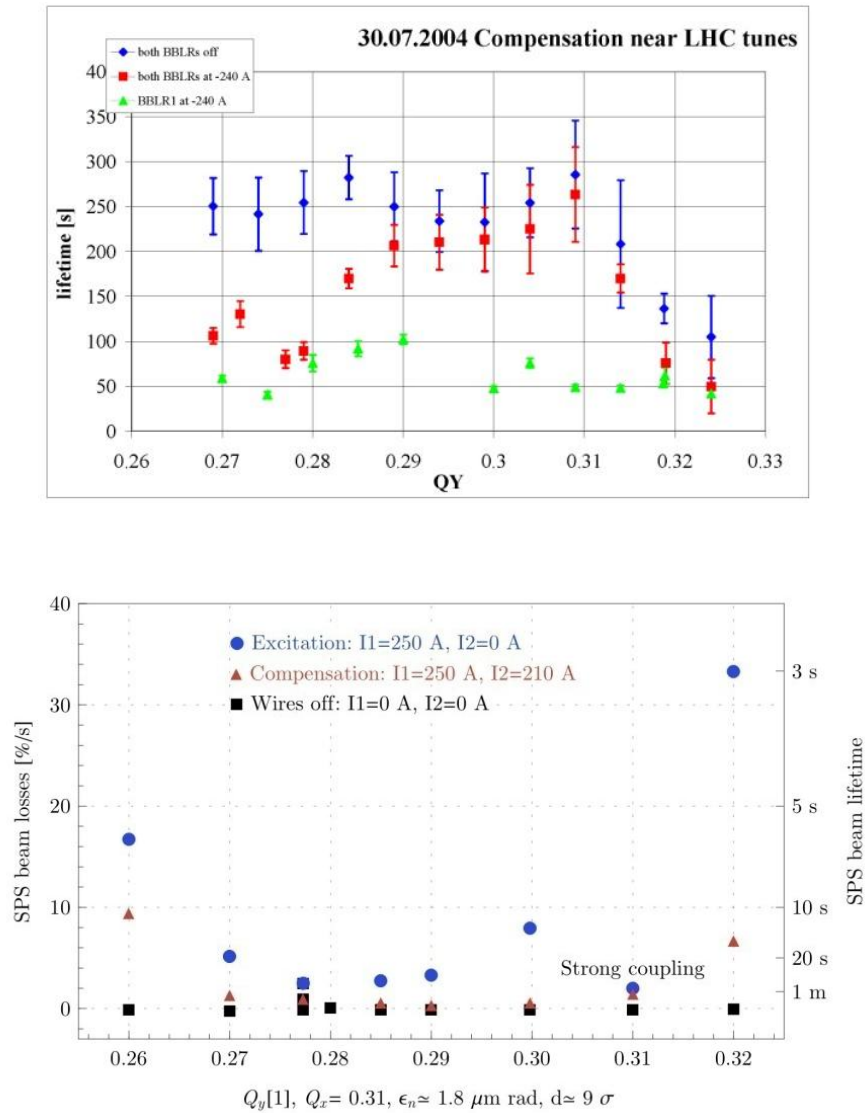


Figure 64: Beam lifetime versus tune for 1) blue: no long-range effect, 2) green: with long-range effect, 3) red: with compensated long-range effect [19, 20] (top). Beam lifetime losses vs. tune for 1) black: no long-range effect, 2) blue: with long-range effect, 3) red: with compensated long-range effect [1] (bottom).

There is a nearly perfect compensation over the interesting tune range; however, compensation unexpectedly partially fails for lower tunes.

Figure 64 shows as well that the nominal tunes 0.31/0.32 found optimal for the head-on beam-beam effect are not optimal for the long-range beam-beam effect. This appears consistent with former SppbarS observations [21]. Similar unexpected tune dependence was observed in 2008 at 37 GeV (Figure 64/bottom): here the best tunes that

minimize the long-range beam-beam effect are around (0.31, 0.28). The compensation is very effective in the range from $Q_v=0.27$ to 0.30 but has only a marginal effect when the tune is close to the third and fourth resonances. With such a local compensation in betatron phase, it is unclear why this significant tune dependence is observed. It might be related to the limitations of the experimental set-up (e.g. the beam aspect ratio differs between the exciting and compensating wires, the alignment of the wires might not be ideal, etc.)

Experiments in coast at 120 GeV/c:

All previous results have been obtained by observing the beam decay for a relative short period (<5s) after which the beam is extracted and a fresh beam is injected for a new measurement. Consequently, a limit of these experimental conditions is the impossibility to distinguish transient beam losses from steady-state ones if the former would be much larger than the latter.

In 2008 a new campaign of wire compensation measurements was undertaken with the goal of increasing the observation time from a few seconds to several minutes by storing a 120 GeV/c beam in SPS. The maximum beam-wire separation that could be reached was 8σ , i.e. close to the nominal 9.5σ beam-beam separation in the LHC. The experimental conditions (wire excitation, beam emittance) correspond to 27 LHC long-range encounters, i.e. about the equivalent of one high-luminosity insertion. Figure 65 shows the beam current and instantaneous losses during a sequence of steps with/without long-range excitation and with/without compensation. All along the experiment, the emittance and machine parameters (orbits, tunes, etc) were monitored and found constant within measurement accuracy (i.e. 0.001 for the tunes).

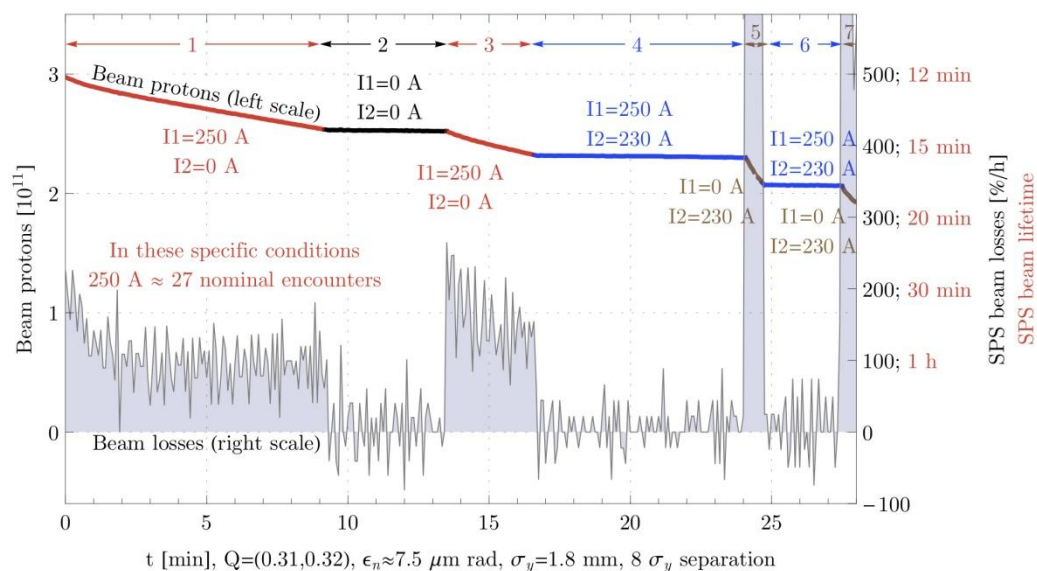


Figure 65: Coast at 120 GeV/c with a beam-wire separation of 8σ : Period 2: no excitation, Periods 1, 3, 5, 7: long-range beam-beam excitation ON; Periods 4, 6: long-range beam-beam excitation and compensation ON, reported in [1].

The results appear clean and reproducible: without excitation (period 2), the beam lifetime is infinite to measurement accuracy. With long-range beam-beam excitation emulated by wire 1 (periods 1 and 3) or wire 2, normally used for compensation

(periods 5 and 7), the SPS beam lifetime drops to 0.5 – 2h (2 – 4 hours in the LHC). With compensation, the beam lifetime is restored to the values observed without excitation (periods 4 and 6). Similar beam decays in periods 1 and 3 suggests that the natural diffusion in the SPS rapidly repopulates the distribution tails, avoiding a bias to the experiment depending on the position in the sequence. During excitation periods, much larger losses are observed when wire 2 is used, carrying a current of opposite polarity to wire 1. This may indicate that, even within measurement accuracy, the tune shift of opposite polarity would have a significant impact. When the long-range simulator is turned on, a large loss occurs over a few seconds before reaching a steady level (not really visible on the time scale of Figure 65). This behaviour underlines the improved accuracy of measurement in coasts, compared to former measurements on the fly, even differential.

This experiment demonstrates the efficiency of the compensation of the long-range beam-beam effect alone. Even if simulations [4] shows that the beam dynamics is dominated by the long-range beam-beam effect, further investigations are planned, using the SPS octupole to induce a tune spread qualitatively similar to the one of the head-on beam-beam effect and to measure its possible impact on the beam lifetime and on the compensation efficiency.

3.7.7 Application in DAΦNE

The first operational application of wire compensation was done in DAΦNE to compensate its long-range beam-beam effect [9]. Contrary to LHC, a local correction was not possible. Hence, only an optimum “global” correction could be found. Figure 66 shows the amplitude plane without/with compensation and for compensation with the opposite (wrong) sign. The improvement with correct compensation is striking.

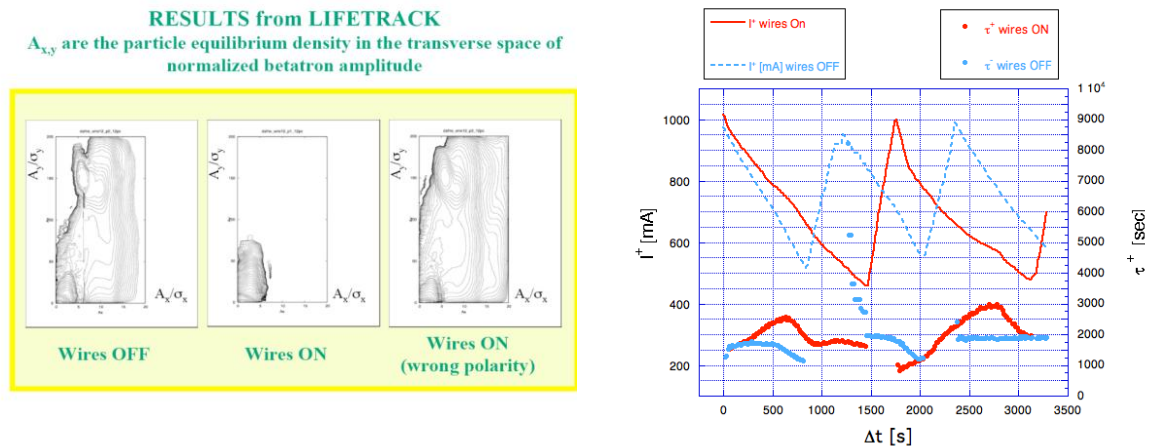


Figure 66: Numerical and experimental results of DAΦNE wire compensation [9].

The observed effect on the beam was a significant increase of lifetime (Figure 66), the suppression of sudden blow-ups and a reduction of background, but no increase in peak luminosity. The wire compensation resulted in a gain in integrated luminosity by 30%.

3.7.8 Conclusions

Numerical and experimental studies by several authors confirm the efficiency and robustness of the wire compensation of the long-range beam-beam effect in the LHC, where the interactions are clustered close to the interaction points. The identified requirement of turn-to-turn stability can be easily met by a dc system. A pulsed system does not appear at this stage absolutely required, but such system would provide an optimal solution if technically feasible. In addition to allowing higher performance, the regularization of the phase space of the beam core is likely to minimize diffusion and thereby to improve running conditions. The physical space has been reserved in the LHC tunnel to install compensators when the need arises. In the meantime, experimental studies will continue on the SPS, using both the existing wires and the wires dismantled from RHIC, which have been kindly donated [22].

3.7.9 Acknowledgement

CARE-HHH and USLARP were instrumental in this collaborative investigation.

3.7.10 References

1. G. Sterbini, An early Separation Scheme for the LHC Luminosity Upgrade, **CERN-THESIS-2009-136 Thèse N. 4574**. - Lausanne: EPFL, 2009.
2. W. Chou & D. Ritson, "Dynamic aperture studies during collisions in the LHC", Proc. PAC 1997, Vancouver and LHC Project Report 123, 1997.
3. T. Sen *et al.*, Effect of the beam-beam interactions on the dynamic aperture and amplitude growth in the LHC, LHC99 beam-beam workshop, CERN-SL-99-039 AP p. 85, 1999.
4. Y. Papaphilippou & F. Zimmermann, Weak-strong beam-beam simulations for the LHC, LHC99 beam-beam workshop, CERN-SL-99-039 AP p. 95, 1999.
5. J. P. Koutchouk, Correction of the long-range beam-beam effect in LHC using electromagnetic lenses, 19th IEEE PAC, Chicago, 18-22 June 2001, p. 1681.
6. W. Fischer *et al.*, Long-range and head-on beam-beam compensation studies in RHIC with lessons for the LHC, HHH2008, CERN, 2008.
7. F. Zimmermann, Weak-strong simulation studies for the LHC long-range beam-beam compensation, Proc. of a workshop on beam-beam effects in circular colliders, Fermilab, June 25-27, 2001, FERMILAB-Conf-01/390T.
8. U. Dorda Compensation of long-range beam-beam interaction at the CERN LHC, PhD Thesis, Technical University Vienna, CERN-THESIS-2008-055.
9. C. Milardi *et al.*, Dafne lifetime optimization with octupoles and compensating wires, CARE-HHH-APD IR07, Frascati, 2007 (arXiv:0803.1544).
10. L. Jin and J. Shi, "Strong-Strong Simulation Study for the Wire Compensation of Long-Range Beam-Beam Effect in LHC", Nucl. Instr. & Meth. A550, 6 (2005).
11. J. Qiang, 3D strong-strong simulations of wire compensation of long-range beam-beam effects at LHC, PAC09, 2009.
12. T. Sen, Beam-beam simulations, CARE-HHH-2004 workshop, CERN, 2004.
13. U. Dorda, LHC with long-range compensation, US-LARP Beam-Beam Workshop, SLAC, 2007.
14. U. Dorda, Beam-beam and emittance growth with wire compensators, CARE-HHH-APD Beam07, CERN, 2007.
15. R. Calaga, W. Fischer & G. Robert-Demolaize, RHIC BBLR measurements in 2009, IPAC'10, Kyoto, Japan, 2010.

16. F. Zimmermann, Diffusive Aperture due to Long-Range Collisions at Injection and Image-Charge Effects, LHC-Project-Note-250 (2001).
17. F. Zimmermann, Scaling of the diffusive aperture with the wire current, 1 July 2003, unpublished, <http://cern-ab-bblr.web.cern.ch/cern-ab-bblr/scaling.pdf>
18. J.-P. Koutchouk et al., Experiments on LHC long-range beam-beam compensation in the SPS, EPAC 2004, Lucerne, Switzerland, 2004.
19. F. Zimmermann et al, Experiments on LHC Long-Range Beam-Beam Compensation and Crossing Schemes at the CERN SPS in 2004, PAC2005 Knoxville (2005).
20. F. Zimmermann, Open issues from the SPS Long-Range Experiment, US-LARP Beam-Beam Workshop, SLAC, 2007.
21. K. Cornelis, SPS experience with reduced distance encounters, CARE-HHH-APD Working meeting on LHC beam-beam effect and compensation, CERN, 2008.
22. W. Fischer, M. Minty, A. Curcio, private communications

3.8 Long-Range Experiments in RHIC

R. Calaga, G. Robert-Demolaize, and W. Fischer, Brookhaven National Laboratory
Mail to: rcalaga@bnl.gov

3.8.1 Introduction

The LHC will experience 32 long-range (LR) encounters at each interaction region (IR) with four IRs and the anticipated bunch spacing of 25 ns. The number of LR encounters is a factor of 5 or larger than colliders of the past and the present. A crossing angle at the interaction point is introduced to separate the beams in the common region by approximately 9σ to help ameliorate some of the LR effects. However, the long-range forces may still pose a significant limitation to the performance of the LHC and the foreseen upgrades in the future. The electromagnetic fields from a DC wire parallel to the beam axis is one proposal to partially compensate the effect of long-range forces [1]. Tests of DC wires have been carried out on high energy circulating beams in the SPS and colliding beams in the RHIC. Brief accounts of the RHIC measurements from 2005-2009 and corresponding observations are discussed in this chapter.

3.8.2 RHIC Experiments

The RHIC accelerator consists of two rings (Blue and Yellow) designed to accelerate and collide heavy ions (for example Au) and also polarized protons. The two beams share six common IRs. Only two of them (IR6 and IR8) are currently in use for high energy and low-beta collisions. Nominally, there exist no LR interactions in the RHIC IRs with the present bunch configuration. Relevant machine parameters for the RHIC accelerator are presented in Table 8.

Table 8: RHIC machine parameters relevant for long-range beam-beam experiments.

<i>Parameter</i>	<i>Unit</i>	<i>Au-Au</i>	<i>p-p</i>
Beam energy	GeV	100	100-250
Rigidity	Tm	831.8	
no of bunches, n_b	...	1-36	
ions per bunch, N_b	10^9	1.1	170
emittance $\epsilon_{N_{x,y} 95\%}$	mm·mrad	10	20
Tune ($Q_{x,y}$)	...	28.23/29.22	28.69/29.68
chromaticities (ξ_x, ξ_y)	...	(+2,+2)	
$\beta_{x,y}$ (blue ring)	m	556/1607	
$\beta_{x,y}$ (yellow ring)	m	1566/576	
Wire current	A	5-50	
Phase advance LR to wire	deg	6	

DC wires have been placed in the RHIC and the SPS with the aim of performing LR experiments [2-4]. Typically observables like lifetime, tune and orbit measurements are used to characterize LR observations. RHIC has the advantage of colliding beams which offers a unique test bed for the LHC.

3.8.3 DC Wires in the RHIC

Two DC wires in the vertical plane were installed in the RHIC accelerator in 2006 (see Figure 67) with the aim of investigating LR beam-beam effects and a potential compensation. The IR6 region was chosen to host the wires which were placed 40.6 m from the IP after the Q3 magnet in the warm region in sector 5. This location has the minimum phase advance (6 deg) between the DX magnet, where a long-range interaction can be setup, and the wire location for compensation. The maximum integrated strength of the wire was designed to be 125 Am which is equivalent to 16 long-range interactions of the nominal LHC and thereby allowed to probe diffusion effects for large amplitude particles similar to the LHC.

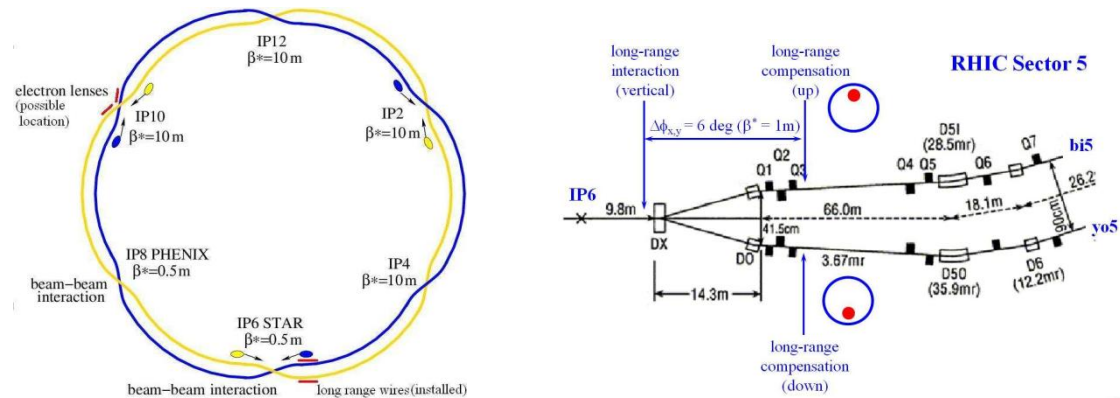


Figure 67: Left: A schematic of the RHIC rings with the DC wires installed in sector 5. Right: A zoom of the sector 5 region to illustrate the interaction region lattice and wire location.

3.8.4 Long-Range Experiments

The measurement of long-range interactions with a DC wire in the RHIC can be broadly categorized into three types:

1. Single long-range effect between the two bunches with proton beams.
2. Effect of the DC wire on a single beam via current and distance scans on proton and gold beams.
3. Effect of long-range interaction either with a wire in the presence of head-on collisions or between the two beams with a simultaneous compensation using the wire.

A summary of all long-range experiments performed in the RHIC accelerator since 2005 are listed with corresponding beam conditions in Table 9 [2]. More than 30 dedicated LR beam-beam experiments were performed at different energies, with different species and various machine configurations to span a variety of long-range conditions and benchmark simulations. Several simulations have been performed for some of the measurements of which some show successful reconstruction of measured lifetimes and onset of losses [5].

Table 9: Summary of long-range beam-beam experiments conducted at RHIC (2005-2009).

Year	Species	Rel. Gamma	No. of bunches	Long-range Condition
2005	Protons	25.963	1	IR4, Blue & Yellow beams
2006	Protons	100	10, 12	IR6, Blue & Yellow beams
2007	Gold	10-100	6, 23, 56	IR6, Blue or Yellow beams with DC wires
2008	Deuterons	100	12	IR6, Blue beam with wire
2009	Protons	100-250	36	IR6, Blue and Yellow beams with head-on and with wire compensation

3.8.4.1 *Single Long-Range Measurements*

LR beam-beam experiments were successfully performed prior to the installation in 2006. The motivation of these experiments was to characterize the effect of one parasitic interaction on beam losses for a future compensation demonstration. The Blue and the Yellow beams were vertically separated in the IR6 region close to the DX magnet with a finite strength in lattice octupoles and a working point close to the 10th order resonance. The marginally stable beam was essential as the effect of the single long-range interaction on the rather stable RHIC beams is subtle. In one such experiment, the effect on the beam losses on both beams as a function of the separation is shown in Figure 68. Note that the Yellow beam was moved while the Blue beam was kept stationary. Therefore, the effect on the Blue beam is of relevance as the losses in the Yellow beam may also be affected by orbit and tunes shifts. A small effect is visible when the beams are approximately 5σ or closer. Compensation of such small effects is difficult as the losses are smaller than the natural reproducibility of the machine for a given beam setup. Therefore, it was important to enhance the loss due to the long-range interactions to clearly demonstrate compensation with a DC wire. Increased

chromaticity and introduction of head-on collisions were utilized to enhance the effect of the LR interaction with the DC wires.

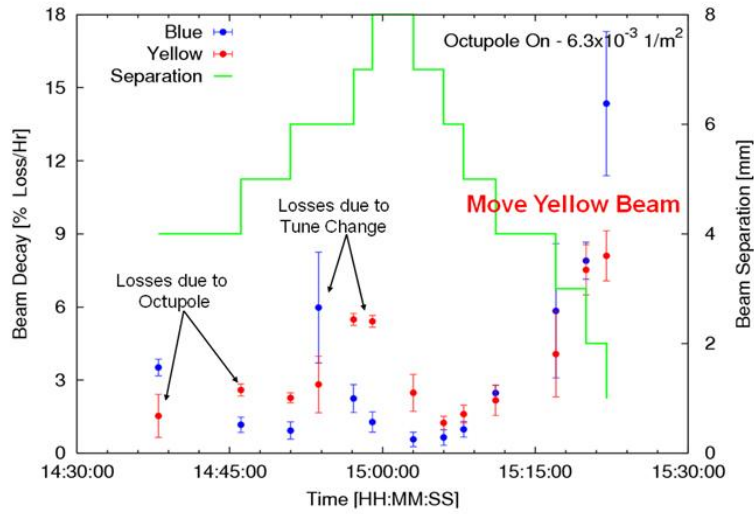


Figure 68: Beam losses due to a single parasitic interaction of the Blue and the Yellow beams. The Yellow beam moved closer to the Blue beam from an initial large separation.

3.8.4.2 Wire Scans on Single Beams

After the installation of the DC wires, several experiments were carried out using the individual wires of the Blue and the Yellow ring to characterize the onset of the losses under certain beam conditions [6,7]. The measurements consisted mainly of distance and current scans and simultaneous measurements of the beam lifetimes, tunes, orbits and transfer functions to benchmark with theory and simulations. One such measurement performed in 2007 is shown in Figure 69 to illustrate the effect of the distance and current scans on the beam loss. The yellow ring shows very weak or no effect with a current scan which is probably due to a previous distance scan resulting in a cleaning of the large amplitude particles. The beam losses are fitted to power law which gives an exponent between 3 and 4 for the different cases as shown in Figure 69. This exponent was speculated to be about 5 for the SPS and about 3 for the Tevatron [2].

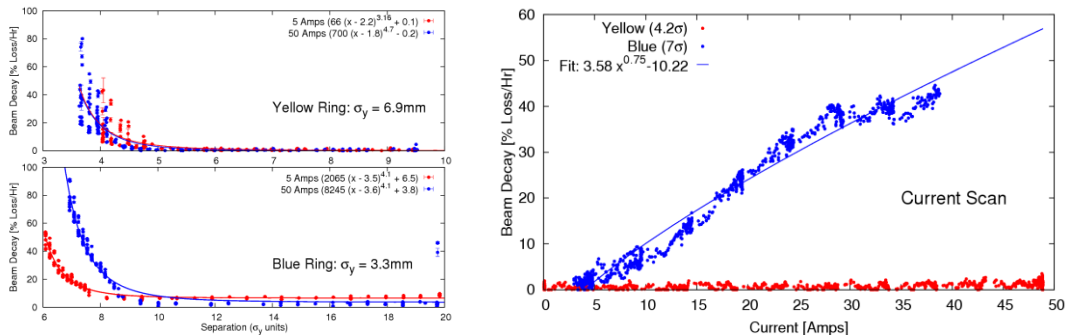


Figure 69: Left: Beam loss as a function of the DC wire separation to the Blue and the Yellow beams at 5 Amps and 50 Amps. Right: Beam loss due to a current scan in the DC wire fixed at a given distance from the beam. Solid lines in all plots show a power law fit to the losses.

The effect on the orbits and tunes were also recorded during each experiment. The orbit deviation due to the dipole kick induced by the DC wire is expressed as ($\Delta y \ll d$)

$$\Delta y = \frac{K\beta_y}{2d} \frac{\cos(\pi Q_y)}{|\sin(\pi Q_y)|} \quad (1)$$

And the tune shift induced is expressed as

$$\Delta Q_{\{x,y\}} = \pm \frac{K\beta_{x,y}}{4\pi} \frac{1}{d_y^2} \quad (2)$$

Figure 70 shows orbit and tune measurements taken during a 2007 experiment (similar to Figure 69) which agree well with analytical predictions.

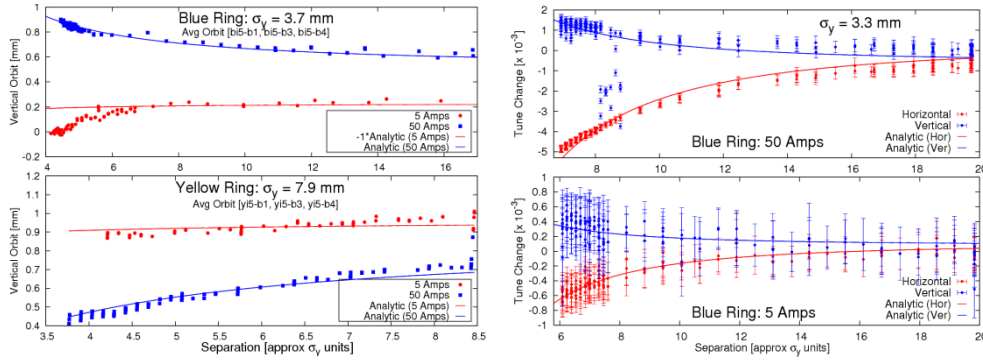


Figure 70: Left: Orbit measurements as a function of the DC wire distance to the beam on the Blue and the Yellow beams at 5 Amps and 50 Amps. Right: Tune measurements as a function of the wire distance to the beam. Solid lines in all plots represent the analytical prediction according to equation 1 and 2.

3.8.4.3 Long-Range Effect with Head-on Collisions and Compensation

Prior to a compensation attempt, a position scan of the wire on each beam was performed with 50 A. Although, some “end of physics” fills were used to test the effect wires on colliding beams (see Table 9), this was the first dedicated attempt. The corresponding beam losses as a function of beam to wire separation on both colliding and non-colliding bunches were measured. The maximum total beam losses were constrained to 100-150% for a very short period to avoid disrupting the beam quality significantly for subsequent measurements. Figure 71 shows the evolution of the intensity between bunches with and without head-on collisions. Bunches with the head-on collisions have a more severe effect from the LR forces of the wire as expected.

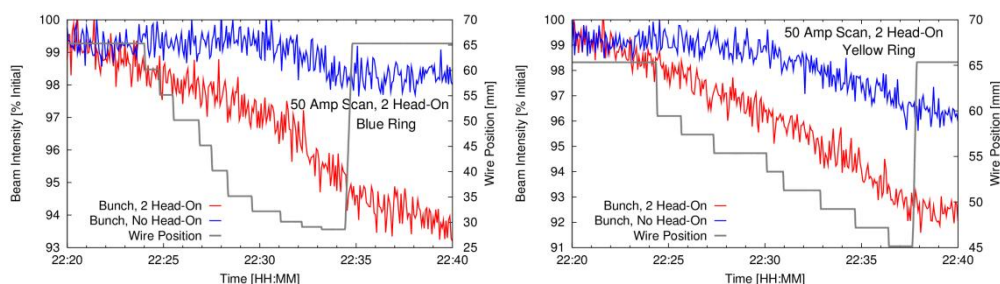


Figure 71: Beam loss of colliding and non-colliding bunches due to the effect of a DC wire on the Blue and the Yellow beams.

The bunch spacing and the interaction region geometry in RHIC does not inherently have LR beam-beam interactions. It is therefore, necessary to shift the collision point towards the DX magnet closest to the DC wires as noted before. This location enables for an artificially induced a LR interaction between the two beams and simultaneously allows for a minimum phase advance between the LR interaction and DC wires (~ 6 deg). Additionally, this location has sufficient aperture for an orbit scan with the range of interest ($3-10\sigma$). The individual bunch intensities and beam losses were recorded during the position scan with the LR compensation.

Figure 72 shows the beam losses as a function of the wire position. In the Blue ring, the losses are always increasing as the wire approaches closer to the beam. Therefore, no evidence of compensation of the LR interaction from the Blue beam is visible. However, in the Yellow ring, the beam lifetime improved as the beam to wire distance approaches 3σ (see Figure 72). Consecutive retractions and restoration of the beam to wire distance to 3σ show similar improvement of the beam lifetime. This indicates a potential compensation of the effect of LR interaction by the DC wire.

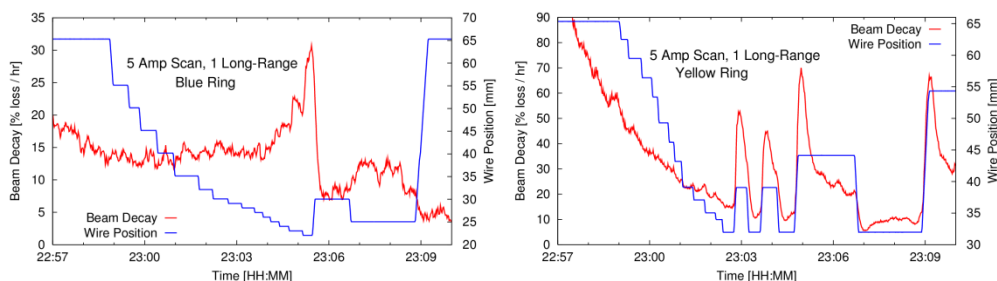


Figure 72: Beam loss comparison between bunches with single long-range and compared to the no long-range interactions as a function of the wire position for Blue and Yellow rings with a current of 5 A.

In addition to beam losses, the individual bunch intensities with and without LR interactions and simultaneous compensation is shown in Figure 73. Note that all 36 bunches experience the effect of the DC wire, but only 30 bunches experience LR interactions. Therefore, only bunches with a LR interaction can experience a compensation. In the Blue ring, the bunch intensity evolution is similar for bunches with and without LR compensation. Hence, only the effect from the wire is visible. The bunches with LR interaction and simultaneous compensation have reduced beam losses as compared to the bunches that only see the wire. This is consistent with the beam loss measurements (see Figure 73).

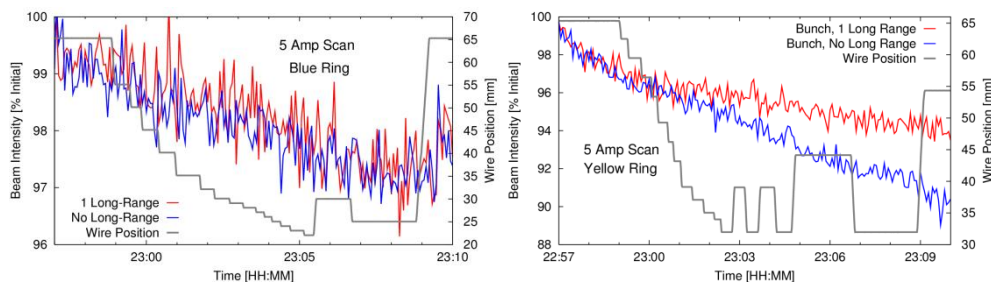


Figure 73: Beam intensity comparison between bunches with single long-range and compared to the no long-range interaction as a function of the wire position for Blue and Yellow rings with a current of 5 A.

3.8.5 Summary

Several long-range experiments were conducted during the period between 2005 and 2009 at the RHIC accelerator. The primary motivation for these experiments was to test the concept of DC wires for compensation of long-range beam-beam effects. The effect of long-range interactions between two proton beams and the effect a DC wire on single colliding and non-colliding beams were studied in detail via beam losses, orbit and tune measurements. Simulations show remarkable agreements to some of the observations. A single attempt to compensate long-range beam-beam interaction via a DC wire shows evidence of compensation.

3.8.6 References

1. J.-P. Koutchouk, “Correction of the long-range beam-beam effect in LHC using electromagnetic lenses”, PAC01.
2. W. Fischer et al., Long-range and head-on beam-beam compensation in RHIC with lessons for the LHC, in the proceedings of the CARE-HHH 2008, Chavannes-de-Bogis, Switzerland.
3. U. Dorda, Ph.D. thesis, Vienna Institute of Technology, Austria, 2008.
4. G. Sterbini, Ph.D. thesis, 2009.
5. H. -J. Kim et al., Phys. Rev. ST Accel. Beams 12, 031001 (2009).
6. R. Calaga et al., Observation of the long-range beam-beam effect in RHIC and plans for compensation, EPAC06, Edinburgh, Scotland, 2006.
7. W. Fischer et al., Experiments with DC wire in RHIC, PAC07, Albuquerque, USA, 2007.

3.9 Head-on Beam-Beam Compensation in RHIC

W. Fischer, Y. Luo, A. Pikin, E. Beebe, D. Bruno, D. Gassner, X. Gu, R. Gupta, J. Hock, A. Jain, R. Lambiase, M. Mapes, W. Meng, C. Montag, B. Oerter, M. Okamura, D. Raparia, Y. Tan, R. Than, J. Tuozzolo, and W. Zhang
Brookhaven National Laboratory, Upton, NY 11973, USA
Mail to: wfischer@bnl.gov

3.9.1 Introduction

Head-on beam-beam compensation with electron lenses had been proposed for the SSC, LHC, and the Tevatron [1,2]. Two electron lenses are installed in the Tevatron [2-4], where they are routinely used as gap cleaner and have been tested in many other configurations. In RHIC there are 2 head-on beam-beam interactions at IP6 and IP8, and 4 long-range beam-beam interactions with large separation (10 mm) at the other IPs.

We consider the partial indirect compensation of the head-on beam-beam effect with one electron lens in each ring. Together with intensity and emittance upgrades [5,6] our goal is to approximately double the luminosity over what can be achieved without these upgrades. A RHIC electron lens consists of: a DC electron gun, an electron beam transport to the main solenoid, the superconducting main solenoid in which the interaction with the hadron beam occurs, an electron beam transport to the collector, and an electron collector. The 2 electron lenses are located in IR10 between the DX beam separation dipoles. The proton beams pass through the main solenoids of both electron lenses, and interact head-on with one of them. The following is a slightly modified version of Ref. [7]. Table 10 shows the main parameters of the proton beam and the electron lenses. References [8-11] present simulations for and discuss beam dynamics problems.

3.9.2 Design Considerations

We aim for a technically feasible and economically viable implementation that comes as close as possible to the ideal compensation scheme: A phase advance of π between p-p and p-e interactions for all betatron amplitudes and the same amplitude dependent beam-beam kick from the p-p and p-e interaction. In addition, the ease of commissioning and operation is a design consideration.

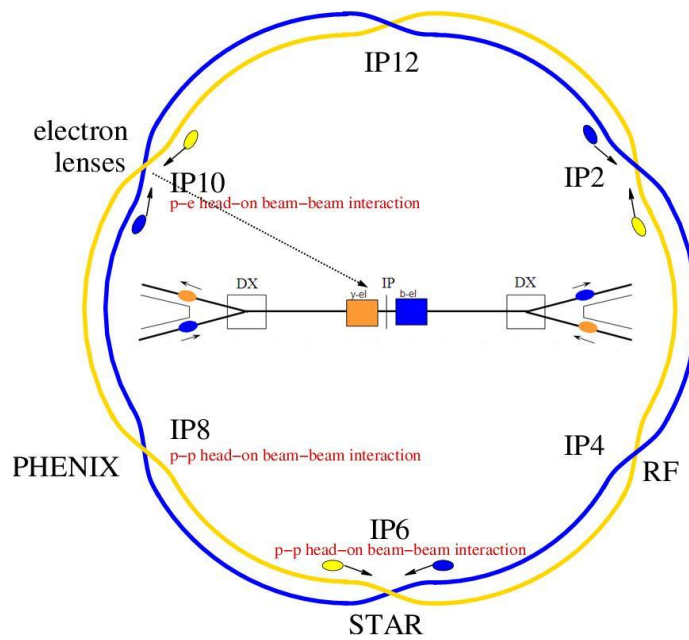


Figure 74: Layout for head-on beam-beam compensation in RHIC. Head-on beam-beam interactions are in IP6 and IP8, compensation near IP10.

Nonlinearities between the p-p and p-e interactions are minimized when these are as close as possible (see Figure 74). Phase advances of π are realized through lattice design and a phase shifter. To obtain the same amplitude dependent forces, the location is limited to the space between the DX magnets, where the dispersion is also small: Since the proton beams are round in the beam-beam interactions, we also require $\beta_x = \beta_y$ at the electron lens and matched transverse proton and electron beam profiles.

The tolerances for the main solenoid field straightness and the tolerances for the relative beam alignment are easier to meet with a larger proton beam. The β -function at IP10 can be as large as 10 m.

The electron beam size in the main solenoid σ_e is given by its size at the cathode σ_{ec} , the solenoid fields at the cathode B_{sc} , and in the main solenoid B_{sm} : $\sigma_e = \sigma_{ec} \times (B_{sc}/B_{sm})^{1/2}$. B_{sm} is limited to about 6 T, and a strong field makes a correction of the field straightness difficult. B_{sc} has to be large enough to suppress space charge effects. With these limits, and a given beam size σ_e the electron beam size and current density at the cathode follow, and must be technically feasible. We use a DC electron beam to minimize the noise in the electron beam.

With both electron lenses in IR10, in a section common to both beams (see Figure 74), the effect of the main solenoids on coupling and spin orientation are locally compensated.

The instrumentation must allow monitoring of the electron beam current and shape, and the relative position and angle of the electron and proton beams. In a diagnostics mode the electron beam current is modulated.

Table 10: Reference case for RHIC beam-beam and beam-lens interactions.

<i>Parameter</i>	<i>Unit</i>	<i>Value</i>
Proton beam parameters		
Total energy E_p	GeV	250
Relativistic factor β_p	...	0.999993
Relativistic factor γ_p	...	266.4
Bunch intensity N_p	10^{11}	2.0
$\beta_{x,y}^*$ at IP6, IP8 (p-p)	M	0.5
$\beta_{x,y}^*$ at IP10 (p-e)	M	10.0
Lattice tunes (Q_x, Q_y)	...	(.695,.685)
Rms emittance ϵ_n , initial	mm mrad	2.5
Rms beam size at IP6, IP8, σ_p^*	μm	70
Rms beam size at IP10, σ_p^*	μm	310
Rms bunch length σ_s	M	0.25
Rms momentum spread $\delta p/p$	10^{-3}	0.30
Hourglass factor F , initial	...	0.88
Beam-beam parameter ξ/IP	...	0.010
Number of beam-beam IPs	...	2+1
Electron lens parameters		
Distance of center from IP	M	2.0
Effective length L_e	M	2.1
Kinetic energy E_e	kV	6.4
Relativistic factor β_e	...	0.16
Relativistic factor γ_e	...	1.013
Electron line density n_e	10^{11}m^{-1}	0.82
Electrons in lens N_{e1}	10^{11}	1.7
Electrons encountered N_{e2}	10^{11}	2.0
Current I_e	A	0.62

Electron gun

The gun has to provide a beam with a transverse profile that is close to Gaussian. Considering the magnetic compression of the electron beam into the main solenoid center with maximum magnetic field of 6 T the a cathode diameter of 7.0 mm gives a Gaussian profile with 2.8 rms beam sizes. The perveance of the gun is $P_{\text{gun}}=0.86 \times 10^{-6} \text{AV}^{-1.5}$. The current density of the electron beam on its radial periphery can be changed with the control electrode voltage while the general shape of the beam profile remains Gaussian. The cathode should be capable of providing an emission current density of 21Acm^{-2} for an electron beam current of 1 A continuously and in a regime of short pulses with a reasonable life time of several thousand hours. Cathodes made of IrCe satisfy these requirements.

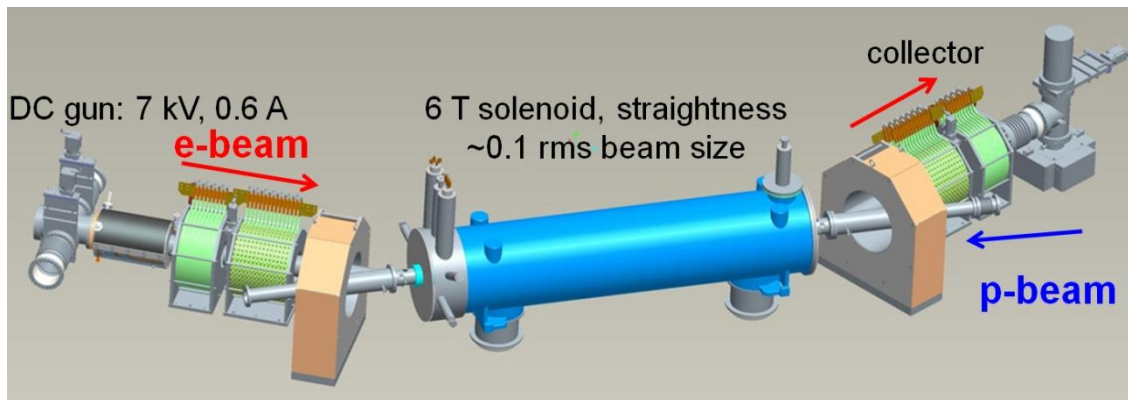


Figure 75: Electron lens layout with gun, electron beam transport, superconducting main solenoid for interaction with the proton beam, and electron collector.

Transport solenoids and steering magnets

The electron beam is transported from the gun to the main solenoid through two solenoids (see Figure 75) which provide focusing. Within the second solenoid horizontal and vertical steering magnets are incorporated that can move the beam by 5 mm in either plane. The power consumption of both electron lenses should be limited to a total of 500 kW in order to avoid upgrades to the electrical and water cooling infrastructure in IR10.

Superconducting main solenoid

The superconducting main solenoid provides the interaction region between the electron and the proton beam. The length and the electron beam current define the interaction strength. The field strength (6 T), together with the solenoid field strength at the gun define the transverse beam size, that must match the proton beam size. The field lines in the solenoid should not deviate from a straight line by more than 10% of an rms beam size (see Table 10). This requires 5 dipole correctors in each plane that will increase the straightness of the cold solenoid by a factor 4-5. A horizontal and vertical angle corrector for the electron beam will also be implemented. All dipole corrector are superconducting magnets, wound on top of the main solenoid, and housed in the same cryostat.

Electron collector

The electron collector has to dissipate the power of the electron beam coming from the interaction region. The nominal current of the electron beam is 0.6 A and the maximum is close to 2 A. The design is dictated primarily by the UHV requirements of RHIC. It allows the separation of the heavily bombarded area from the rest of the electron lens by using a small diaphragm. A magnetic shield leads to fast diverting electrons inside the collector. The reflector has a potential lower than the cathode and pushes electrons outwards to the water-cooled cylindrical surface. Under a load twice as high as expected from a 2 A electron beam the maximum temperature on inner surface of the shell is 102°C. This temperature is acceptable for the material (copper) and for UHV conditions in RHIC. 20 tubes with an ID of 8 mm are brazed to the outside of the cylindrical shell and are connected in parallel for water flow.

Diagnostics

In commissioning mode an electron current modulator is used so that the beam is on only during the abort gap or a few selected RHIC bunches. In compensation mode the electron beam is DC. The goal is to align a small proton beam inside an only slightly larger electron beam within about 10% of an rms beam size. BPMs are used to bring both beams close together, while bremsstrahlung detectors [11] and proton beam diagnostics are used to maximize the overlap of the beams. Due to the large difference in electron (1 μm) and proton beam bunch lengths (5 ns), separate electron and proton beam position monitors are needed. The electron beam needs to be monitored for shape, current, and loss. Multipurpose isolated electrodes will be mounted throughout electron beam transport. The electrodes detect lost beam, and clear ions.

Power supplies

Most of the supplies are referenced to ground; elements in the gun and collector are referenced to the cathode. The gun supplies include the cathode bias supply, the cathode heater, the beam forming supply, and two anode supplies (DC and pulsed). A cathode, focusing, and bending solenoid are powered individually. There are also four sets of dipole windings for each lens. The superconducting solenoid has a power supply that allows slow ramping only. Within the superconducting solenoid, eight drift tubes and twenty trim magnets are powered individually. The collector power supply is rated with 10 kV at 2 A, and will limit the energy deposited in the device should an arc occur. An ion extractor is powered with respect to the cathode potential. A suppressor element is powered with respect to the collector.

Vacuum system

The gun and collector vacuum will be UHV compatible, with a design pressure of 10^{-10} Torr, and interface to the RHIC warm bore with a nominal pressure of 10^{-11} Torr. For this reason all of the components shall be bakable to 250°C. All-metal gate valves separate the gun and collector vacuum. The gun and collector chambers will have a confined gas load by using a conductance limiting aperture, and enough installed pumping speed. All vacuum chambers interfacing with the RHIC warm bore will be made from stainless steel and have NEG coating.

3.9.3 Summary

Partial head-on beam-beam compensation is planned in RHIC with electron lenses. The main solenoid, electron gun and collector, the electron beam transport, and instrumentation are designed and under construction. We expect the completion of the hardware installation at the end of 2012 expect a luminosity gain of up to a factor of two together with a polarized proton source upgrade [5,6] that can deliver higher bunch intensities.

3.9.4 Acknowledgments

We are thankful for discussion and support to many, in particular N. Milas, J. Alessi, M. Anerella, A. Fedotov, G. Ganetis, E. Haug, W. Herr, V. Kamerzhiev, J.-P. Koutchouk, G. Kuznezov, W. Nakel, K. Ohmi, T. Roser, T. Sen, L. Snydstrup, V. Shiltsev, G. Sterbini, P. Thieberger, A. Valishev, and F. Zimmermann.

3.9.5 References

1. E. Tsyganov, R. Meinke, W. Nexsen, A. Zinchenko, “Compensation of the beam-beam effect in proton colliders”, SSCL-PREPRINT-519 (1993).
2. V. Shiltsev, V. Danilov, D. Finley, and A. Sery, “Considerations on compensation of beam-beam effects in the Tevatron with electron beams”, Phys. Rev. ST – Accel. Beams 2, 071001 (1999).
3. V. Shiltsev, Y. Alexahin, K. Bishofberger, V. Kamerdzhev, G. Kuznetsov, and X.-L. Zhang, “Experimental demonstration of colliding-beam-lifetime improvement by electron lenses”, Phys. Rev. Lett. 99, 244801 (2007).
4. V. Shiltsev et al., “Tevatron electron lenses: Design and operation”, Phys. Rev. ST Accel. Beams 11, 103501 (2008).
5. D. Raparia et al., “Results of LEBT/MEBT reconfiguration at BNL 200 MeV LINAC”, PAC’09, submitted to Phys. Rev. ST – Accel. Beams (2009).
6. A. Zelenski, “Review of polarized ion sources”, Rev. Sci. Instrum. **81** 02B308 (2010).
7. W. Fischer et al., “Status of the RHIC head-on beam-beam compensation project”, Proc. IPAC10.
8. W. Fischer, Y. Luo, C. Montag, “Bunch length effects in the beam-beam compensation with an electron”, Proc. IPAC2010
9. C. Montag et al., “Ion bunch length effects on the beam-beam interaction in a high luminosity ring-ring electron-ion collider with head-on beam-beam compensation”, Proc. IPAC2010.
10. Y. Luo and W. Fischer, “6-D weak-strong simulation of head-on beam-beam compensation in RHIC”, Proc. IPAC2010.
11. Y. Luo, “SimTrack: a simple C++ library for particle tracking”, Proc. IPAC2010.
12. C. Montag et al., “Optimizing the beam-beam alignment in an electron lens using bremsstrahlung”, Proc. IPAC2010.

3.10 Weak-Strong Beam-Beam Simulations for Head-on Beam-Beam Compensation in the RHIC

Y. Luo and W. Fischer, Brookhaven National Laboratory, Upton, NY 11973, USA

Mail to: ylo@bnl.gov

3.10.1 Introduction

The simulation studies of head-on beam-beam compensation for the 250 GeV polarized proton run in the Relativistic Heavy Ion Collider (RHIC) can be dated back to 2007 when we found that head-on beam-beam compensation can greatly reduce the large beam-beam tune spread generated by the proton-proton beam-beam interaction at IP6 and IP8. The current working point of the polarized proton runs is constrained between $2/3$ and $7/10$ to achieve good beam-beam lifetime and to maintain the proton polarization. To further increase the proton bunch intensity above 2.0×10^{11} to increase luminosity, there will not be enough tune space between $2/3$ and $7/10$ to hold the beam-beam tune. The idea of head-on beam-beam compensation is to introduce another low energy electron beam into the ring to head-on collide with the proton beam. The device to provide such an electron beam is called electron lens (e-lens). For detail of the design and parameters of head-on beam-beam compensation in the RHIC, please consult the article by W. Fischer in this issue [1].

Single particle tracking

Considering the e-lens is a highly non-linear element, we need to investigate its effect on the proton beam dynamics and the proton beam lifetime. We first studied the stability of single proton motion in the presence of head-on beam-beam compensation [2]. Some indicators, such as tune footprint, tune diffusion, Lyapunov exponent, action diffusion are used. All these indicators show that head-on beam-beam compensation help stabilize the particles in the bunch core since it pulls them away from 2/3 resonance line. However, these indicators also show that head-on beam-beam compensation introduces non-linearity into the proton beam dynamics and destabilizes the particles in the bunch tail. Half head-on beam-beam compensation may be the optimum choice for the 250~GeV polarized proton run in the RHIC.

To better compensate the non-linearity from the proton-proton beam-beam interaction at IP8 with the e-lens which is located around IP10, we adjusted the betatron phase advances between IP8 and the center of e-lens to be multiples of π . From the lattice model, the betatron phase advances between IP8 and the center of e-lens are $(8.5\pi, 11.1\pi)$. After phase advance adjustment, they are $(7\pi, 9\pi)$. We also investigated the effect of second order chromaticity correction on the dynamic aperture. The first order chromaticities are always corrected to (1, 1) before tracking. Before second order chromaticity correction, they are about 2700. After correction, they are below 500.

We calculated and compared the dynamic apertures of proton particles without and with head-on beam-beam compensation [3]. Dynamic aperture is defined as the maximum betatron amplitude within which particles are not lost after a certain number of tracking turns. The long-term dynamic aperture converges to the boundary between the regular and chaotic motions. In the dynamic aperture study, we scanned the head-on beam-beam compensation strength, the proton bunch intensity, the proton beam's working point and the electron beam's transverse size and so on.

Multi-particle tracking

We also carried out multi-particle tracking to investigate head-on beam-beam compensation's effect on the proton beam's lifetime and emittance growth [4]. Particle loss is well defined in the tracking. The physical aperture is set to 0.1~m all along the ring in the simulation. As we know, the particles with large amplitudes in the bunch tail are likely to be lost in the tracking. Therefore, to overcome the statistical error in the calculated particle loss rate and to better represent the particles in the tail of a 6-d Gaussian bunch, we need a large number of macro-particles and a good Gaussian distribution generator. A large number of macro-particles in the tracking will significantly increase the computing time. Another approach is to track particles with a hollow Gaussian distribution of a proton bunch [5]. This is based on the assumption that the particles in the bunch core are not lost in the tracking turns. To use this method, the boundary between the stable core and the unstable bunch tail needs to be carefully determined.

The emittance evolution of the proton bunch can be calculated through the determinant of beam size matrix or simply from σ^2/β in the simulation. Since the real emittance growth of the proton beam in 10^7 turns is very small, a very high resolution in the emittance calculation is required. Increasing the total number of macro-particles in the simulation and a good algorithm of emittance calculation are helpful. We noticed that particle loss and large amplitude particles affect the value of calculated emittance. To reduce the fluctuation in the calculation of the emittance, the straight-forward way is

to increase the total number of macro-particles in the simulation. However, limited by the CPU time, this is not easily possible. Another approach is to calculate the averaged emittance with the coordinates of all the particles in all turns in each step of 10^5 turns. However, it is still difficult to see that there is a clear trend of the emittance change in 10^7 turn tracking for the RHIC head-on beam-beam compensation. In our simulation, the fluctuation in the calculated emittance is about 0.3% of its average value.

Beam-beam model and code development

In our early simulation studies we modeled the proton-proton beam-beam interaction at IP6 and IP8 as a simple 4-d weak-strong beam-beam kick. The 4-d weak-strong beam-beam kick is based on the equations given by Bassetti-Erskine [6]. However, considering $\beta^*=0.5$ m is comparable to the rms proton bunch length which is about 0.45 m, a 6-d beam-beam treatment is needed. In our simulation, we adopt the 6-d weak-strong synchro-beam map by Hirata [7]. Since the e-lens in the RHIC is working in a DC mode, in the simulation we split it into 8 slices and model each slice as drift-(4-d weak-strong beam-beam kick)-drift. The strong proton beam in another ring and the electron beam are considered rigid and will not be affected by the test particles in the simulation.

The particle motion in the magnetic elements is tracked with the 4th order symplectic integration by R. Ruth [8]. To save the time involved in the numeric tracking, we treat the multipoles as thin lenses. That is, the non-zero length multipoles will be replaced by drift-(multipole kick)-drift. Of course, the tunes and chromaticities will be re-matched to original ones before the dynamic aperture tracking.

To increase the flexibility in the tracking and to benchmark the 6-d beam-beam modeling among different codes, we developed our C++ tracking library called SimTrack [9]. SimTrack is about 6000 lines. It is able to calculate the linear optics. It supplies some versatile functions to manage the elements and lines. The parameters of elements can be easily accessed and adjusted even during tracking. In SimTrack, a new type of element is easy to be created. We benchmarked the 6-d beam-beam treatment in SimTrack with BBSIM [10] and the particle motion through the magnetic elements with Tracy-II [11].

In the following, we first prove that head-on beam-beam compensation is effective to reduce the beam-beam tune spread through frequency map analysis. Then we present some tracking results from the calculations of dynamic aperture and particle loss rate under different beam-beam conditions.

3.10.2 Frequency Map Analysis

Here we calculate and compare the tune footprint and tune diffusion with head-on beam-beam compensation in the RHIC through frequency map analysis. Frequency map analysis has been widely used to study the long-term stability of single particle motion since J. Laskar introduced it into accelerator physics from its application in the solar system studies [12].

As an example, we choose the proton bunch intensity $N_p=2.0\times 10^{11}$. With head-on beam-beam compensation, we set the beam size of electron beam same as the proton's at the e-lens. The non-colliding working point is fixed to (28.685, 29.695) so that there is no particle cross the depolarization resonance line 7/10 before and after beam-beam interaction. The on-momentum particles are tracked. The rf voltage is turned off to

avoid its disturbance to the betatron tune determination. Figure 76 shows the tune footprints together with the tune diffusion in the (Q_x, Q_y) plane.

From the left plot of Figure 76, with proton-proton beam-beam interaction at IP6 and IP8, the particles in the proton bunch core are pushed onto the horizontal third order resonance $3Q_x$. And several yellow curves with tune diffusion between 10^{-4} and 10^{-3} appear from 0 to 5σ . These yellow curves correspond to 8th, 5th, 7th and 9th order resonance lines which cross $(2/3, 2/3)$ in the tune space.

From the right plot of Figure 76, with head-on beam-beam compensation, the tune spreads generated by the proton-proton interaction are effectively reduced. The particles in the bunch core are pulled away from the $2/3$ resonance line. The tune spread with half beam-beam compensation is about half of that without compensation. And the tune spread with full beam-beam compensation is comparable to that from magnetic non-linearity in the lattice. For half head-on beam-beam compensation, the resonance lines less than 10th order are not seen in the footprint up to 4σ .

However, with head-on beam-beam compensation, folding in the tune footprints [13] are visible in the right plot of Figure 76, especially for the case with full beam-beam compensation. With beam-beam interaction only, the tune footprint folding occurs around 5σ . With half beam-beam compensation, it occurs around 4σ . With full beam-beam compensation, the tune footprint folding starts at very small amplitudes in both radial and azimuthal directions. This may hint that head-on beam-beam compensation introduces non-linearity into the proton particle dynamics although it reduces the beam-beam tune spread.

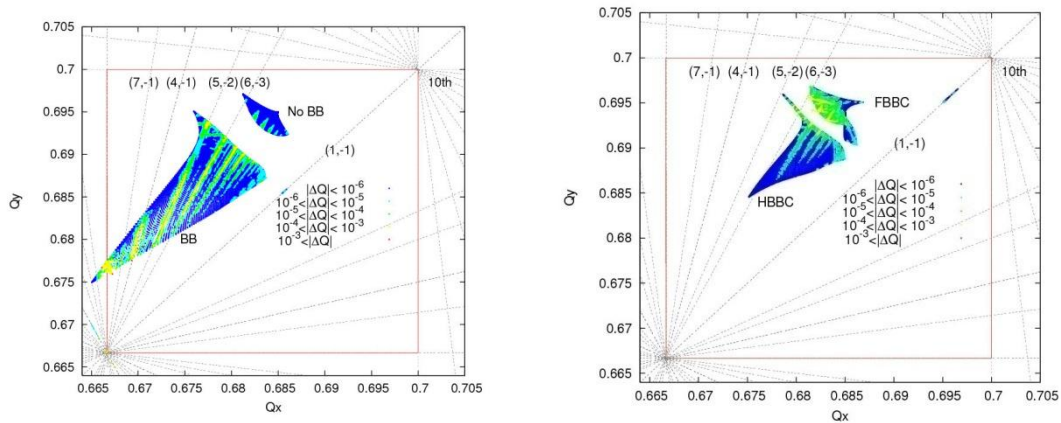


Figure 76: Tune footprints with proton bunch intensity $N_p = 2.0 \times 10^{11}$. Left: without beam-beam interaction (no BB) and with beam-beam interaction (BB). Right: with half beam-beam compensation (HBBC) and with full beam-beam compensation (FBBC).

3.10.3 Dynamic Aperture Calculation

Here we present some results from the dynamic aperture study with head-on beam-beam compensation. The particles are tracked up to 10^6 turns. The particle's initial momentum deviation is $+0.0005$. The dynamic aperture is searched in 5 angles in the first quadrant in the x-y plane. The dynamic aperture is measured in the unit of rms transverse beam size. In the following we only focus on the comparison of the minimum dynamic aperture among these 5 angles. Figure 77 shows the dynamic apertures in the scan of proton bunch intensities from 1.2×10^{11} to 3.0×10^{11} with half head-on beam-beam compensation. From Figure 77, when the proton bunch intensity is

above 2.0×10^{11} , half beam-beam compensation improves the dynamic aperture. On top of half head-on beam-beam compensation, phase advances of $k\pi$ between IP8 and the center of the e-lens increase the dynamic apertures for proton bunch intensity from 2.0×10^{11} to 2.5×10^{11} . The second order chromaticity correction further increases the dynamic apertures when the proton bunch intensity is above 2.0×10^{11} .

Figure 78 shows the dynamic aperture in the scan of the compensation strength. Compensation strength is defined as the electron beam intensity divided by twice the proton bunch intensity. For half and full head-on beam-beam compensation, their compensation strength is 0.5 and 1 respectively. From Figure 78, head-on beam-beam compensation with compensation strength above 0.7 reduces the dynamic aperture for all the three bunch intensities 2.0×10^{11} , 2.5×10^{11} and 3.0×10^{11} . For bunch intensity 2.0×10^{11} , the peak dynamic aperture occurs at compensation strength 0.4-0.5, while for bunch intensities 2.5×10^{11} and 3.0×10^{11} , the peak dynamic aperture occurs at compensation strength around 0.6.

Figure 78 shows the dynamic aperture in the scan of the compensation strength. Compensation strength is defined as the electron beam intensity divided by twice the proton bunch intensity. For half and full head-on beam-beam compensation, their compensation strength is 0.5 and 1 respectively. From Figure 78, head-on beam-beam compensation with compensation strength above 0.7 reduces the dynamic aperture for all the three bunch intensities 2.0×10^{11} , 2.5×10^{11} and 3.0×10^{11} . For bunch intensity 2.0×10^{11} , the peak dynamic aperture occurs at compensation strength 0.4-0.5, while for bunch intensities 2.5×10^{11} and 3.0×10^{11} , the peak dynamic aperture occurs at compensation strength 0.6-0.65.

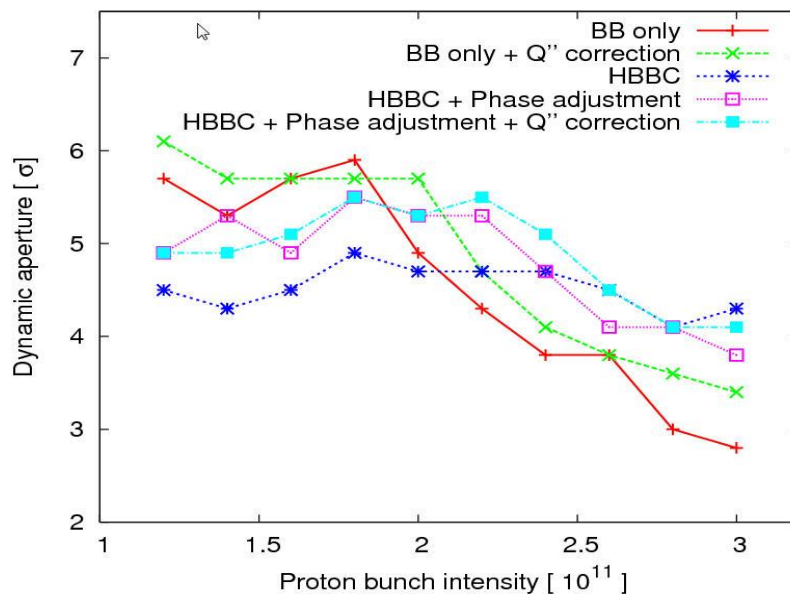


Figure 77: Calculated dynamic aperture with half head-on beam-beam compensation in the scan of proton bunch intensity.

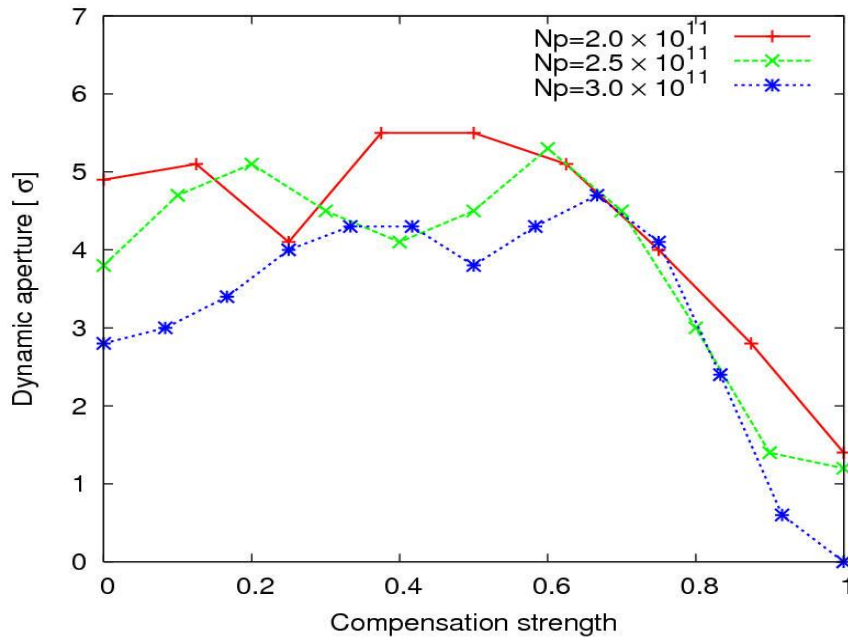


Figure 78: Calculated dynamic aperture versus the head-on beam-beam compensation strength.

3.10.4 Beam Lifetime Calculation

Here we show some results from the calculations of particle loss rate of a proton bunch in the presence of head-on beam-beam compensation. To save the computing time, we track 4800 macro-particles of a hollow 6-d Gaussian distribution up to 2×10^6 turns. The relative beam intensity shown in the following plots is calculated with the number of lost particle among the 4800 tracked macro-particles divided by the total particle number of the 6-d Gaussian bunch they represent.

Figure 79 shows the relative beam intensity without and with half beam-beam compensation in the 2×10^6 turn tracking for the three proton bunch intensities. From Figure 79, half beam-beam compensation reduces proton particle loss for bunch intensities 2.5×10^{11} and 3.0×10^{11} . However, for bunch intensity 2.0×10^{11} , half beam-beam compensation doesn't increase the proton lifetime.

Figure 80 shows the relative proton beam intensity with phase adjustment and second order chromaticity correction. Comparing Figure 79 and Figure 80, the phase advances of $k\pi$ between IP8 and e-lens help increase the proton lifetime with half head-on beam-beam compensation. On top of it, the second order chromaticity correction further improves the proton lifetime for all the three proton intensities.

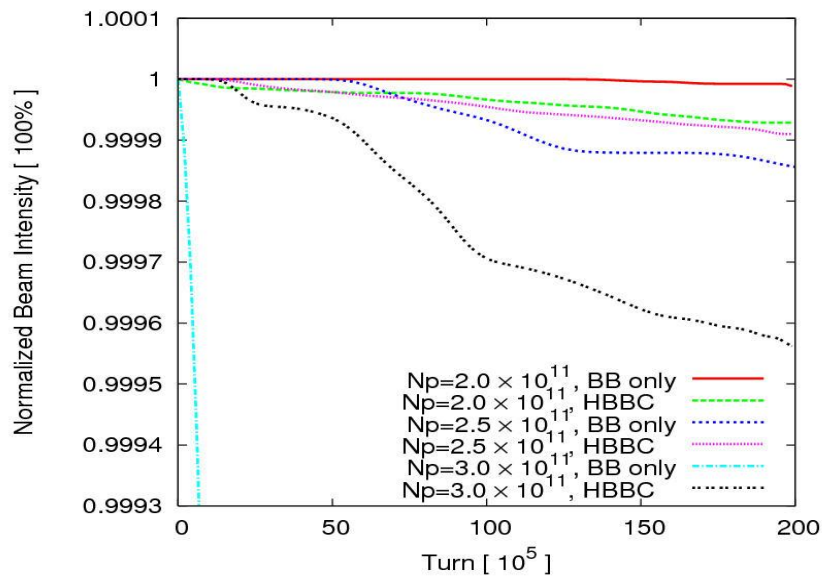


Figure 79: Particle loss without and with half head-on beam-beam compensation.

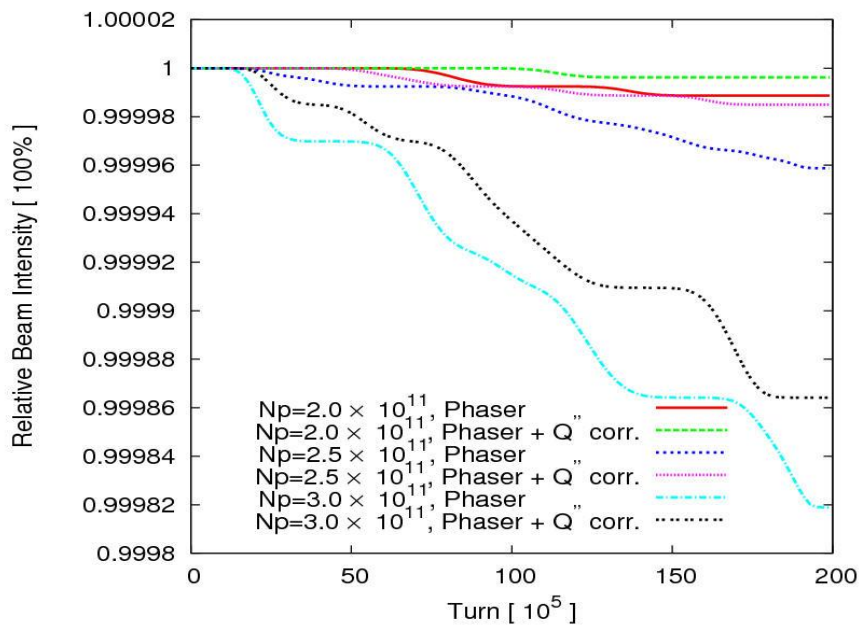


Figure 80: Particle loss with the phase adjustment and second order chromaticity correction.

Figure 81 shows the relative proton beam intensity in the tune scan. In this study, the proton bunch intensity is 2.5×10^{11} and half beam-beam compensation is applied. The working point shown is the tunes of the zero-amplitude particles with beam-beam and its compensation. From Figure 81, the working point (28.675, 29.67) gives the best proton beam lifetime, while the working point (28.685, 29.68) gives the worst beam lifetime. The proton beam lifetime is better with a working point below the diagonal than that above the diagonal with swapped horizontal and vertical tunes.

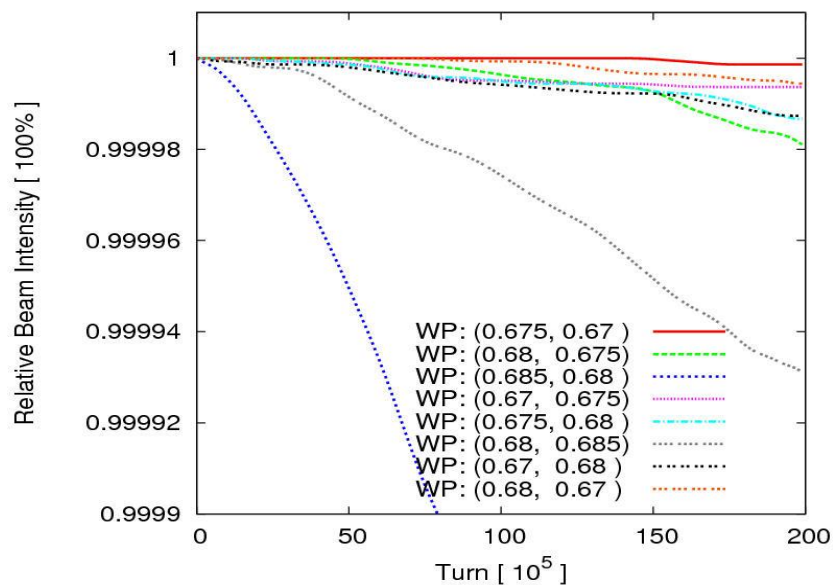


Figure 81: Particle loss in the scan of proton beam's working point.

3.10.5 Summary

We investigated the effects of head-on beam-beam compensation on the proton beam dynamics in the 250 GeV polarized proton operation in the RHIC. We calculated and compared the frequency map, dynamic aperture and particle loss rate under different beam-beam conditions. We confirmed that with the proton bunch intensity above 2.0×10^{11} , there is not enough tune space between $2/3$ and $7/10$ to hold the beam-beam tune spread generated from the beam-beam interaction at IP6 and IP8. Head-on beam-beam compensation is found to be an effective way to reduce the beam-beam tune spread. Head-on beam-beam compensation also gives a possibility to further increase the proton bunch intensity and/or to reduce the proton transverse emittance to increase the luminosity.

From the frequency map analysis, dynamic aperture and particle loss rate calculations, we found that half head-on beam-beam compensation may be the best choice for the head-on beam-beam compensation in the RHIC. Full head-on beam-beam compensation introduces too much non-linearity in the proton beam dynamics so that it reduces the proton beam's dynamic aperture and lifetime. Simulation shows that half head-on beam-beam compensation improves the proton beam lifetime when the bunch intensity is above 2.0×10^{11} . The betatron phase advance adjustment between IP8 and the e-lens and the second order chromaticity correction further improve the proton dynamic aperture and the proton beam lifetime on top of half head-on beam-beam compensation. We did tune scan and found that lower working points gives better proton beam lifetime. And slightly larger electron beam size will benefit the proton beam lifetime. For detailed simulation results, please consult Refs. [2-4].

3.10.6 Acknowledgments

We are thankful for the discussions with Y. Alexahin, J. Beebe-Wang, A. Kabel, H.-J. Kim, C. Montag, T. Roser, F. Schmidt, T. Sen, V. Shiltsev, S. Tepikian, A. Valishev and many others. This work is jointly supported by the US DOE under contract No. DE-AC02-98CH10886 and the US LHC Accelerator Research Program (LARP).

3.10.7 References

1. W. Fischer, et al., "Head-on beam-beam compensation in RHIC", in this issue.
2. Y. Luo, et al., "Stability of single particle motion with head-on beam-beam compensation in the RHIC", BNL C-AD AP Note 310, May 2008.
3. Y. Luo, et al., "Evaluation of dynamic aperture in presence of head-on beam-beam compensation in the RHIC", BNL C-AD AP Note (to be posted), March 2010.
4. Y. Luo, et al., "Lifetime calculation with head-on beam-beam compensation in the RHIC", BNL C-AD AP Note (to be posted), April 2010.
5. Y. Luo, et al., "Multi-particle tracking of head-on beam-beam compensation in the RHIC", Proc. EPAC2008.
6. M. Bassetti and G.A. Erskine, "Closed expression for the electrical field of a two-dimensional Gaussian charge", CERN-ISR-TH/80-06.
7. K. Hirata, H. Moshhammer, F. Ruggiero, "A symplectic beam-beam interaction with energy change", Particle Accel. 40 (1993) 205-228.
8. R.D. Ruth, "A canonical Integration Technique", IEEE Trans. Nucl. Sci., vol. NS-30, PP.2669-2671 (1983).
9. Y. Luo, "SimTrack: a simple C++ library for particle tracking", Proc. IPAC2010.
10. T. Sen and Y.-J. Kim, private communications.
11. J. Bengtsson, private communications.
12. J. Laskar, Physica **67 D**, 257 (1993).
13. J. Laskar, "Frequency map analysis and particle physics", in the Proceedings of 1994 Particle Accelerator Conference, 2003.

3.11 Beam-Beam Simulation

Hyung Jin Kim, Fermilab, MS220, P.O. BOX 500, Batavia, IL 60510
Mail to: hjkim@fnal.gov

3.11.1 Introduction

In high energy storage-ring colliders, the beam-beam interactions are known to cause the emittance growth and the reduction of beam lifetime, and to limit the collider luminosity [1-6]. The long-range beam-beam effects can be mitigated by separating the beams to the extent possible. Increasing the crossing angle is a way of beam separation. It has several undesirable effects, the most important of which is a lower luminosity due to the smaller geometric overlap and the excitation of synchro-betatron resonance. In addition, in order to achieve a high luminosity, it needs to increase the beam intensity and often to focus the beam to smaller sizes at the interaction points. The effects of head-on interactions become even more significant. A tune spread is introduced by the head-on interactions due to a difference of tune shifts between small and large amplitude particles. The combination of beam-beam and machine nonlinearities excites

betatron resonances which diffuse particles into the tail of beam distribution and even beyond the stability boundary.

It is therefore important to mitigate the beam-beam effects. Compensation of long-range beam-beam interactions by applying external electromagnetic forces has been proposed for the LHC [7]. At large beam-beam separation, the electromagnetic force which a beam exerts on individual particles of the other beam is proportional to $1/r$, which can be generated and canceled out by the magnetic field of a current-carrying wire. Direct-current wires were installed in SPS [7-9], DAΦNE [10], and later in RHIC [11] for tests. Low energy electron beam, so called electron lens, has been used in the Tevatron at Fermilab to compensate the tune shift due to the beam-beam interaction [12-14]. The electron lens demonstrated the lifetime improvement of the Tevatron proton bunches. Its application to the mitigation of head-on beam-beam effects has been proposed recently in RHIC [15-16].

In this report we present an overview of computational model for beam-beam simulation, and its applications to both the long-range and head-on interactions in RHIC and LHC.

3.11.2 Computational Model

In the collider simulation, the two beams moving in opposite direction are represented by macroparticles of which the charge to mass ratio is that of each beam. The number of macroparticles is much less than the bunch intensity of the beam because even with modern supercomputers it is too time consuming to track the particle inside the bunch, for example, 10^{11} particles for the number of revolutions of interest. The macroparticles are generated and loaded with an initial distribution for a specific simulation purpose, for example, six-dimensional Gaussian distribution for long-term beam evolution. The transverse and longitudinal motion of particles is calculated by transfer maps which consist of linear and nonlinear maps.

The six-dimensional accelerator coordinates $\vec{x} = (x, x', y, y', z, \delta)^T$ are applied, where x and y are horizontal and vertical coordinates, x' and y' the trajectory slopes of each coordinates, $z = -c\Delta t$ the longitudinal distance from the synchronous particle, and $\delta = \Delta p / p_0$ the momentum deviation from the synchronous energy. Coupling between the transverse planes is included in the transfer map between elements. We adopt the weak-strong model to treat the beam-beam interactions where one beam is strong and is not affected by the other beam while the other beam is weak and experiences a beam-beam force due to the strong beam during the interactions. The density distribution of the strong beam is assumed to be Gaussian.

The bunch length effect needs to be considered in case of (1) the longitudinal bunch length σ_z is comparable to the transverse lengths σ_x and σ_y , (2) the orbit function β_x and β_y are not constant through beam-beam interactions, and (3) the transverse beta functions are small and comparable to σ_z . The finite longitudinal length is considered by dividing the beam into longitudinal slices. We make slices of both beams moving in opposite directions. Each slice is integrated over its longitudinal boundary, and has only transverse charge distribution at the center of its longitudinal boundary. We take into account the collision between a pair of slices: the i^{th} slice of a beam and the j^{th} slice of the other beam. The collision is taken place at collision point which is usually different

from IP. For example, i^{th} the slice of a bunch has the successive collisions with slices of a bunch in the other beam. In addition, electric field energy varies along the bunch due to the inhomogeneity of beam parameters in the longitudinal direction, and couples transverse and longitudinal motions. The coupling can be modeled by the synchrotron map which includes beam-beam interactions due to the longitudinal component of the electric field as well as the transverse components [17].

When there exists a finite crossing angle between colliding two beams at interaction point, the beam-beam force experienced by a test particle will have transverse and longitudinal components. The existence of longitudinal force makes it difficult to apply the result of no crossing angle. A transformation can be used to remedy the difficulty. It transforms a crossing angle collision in the laboratory frame to a head-on collision in the rotated and boosted frame which is called the head-on frame [18-19]. The transformation can be described by a transformation from the accelerator coordinates to Cartesian coordinates, the Lorentz transformation, and again a backward transformation to the accelerator coordinates.

It is well known that for a large separation distance at parasitic crossings, the strength of long-range interactions is inversely proportional to the distance, as shown Figure 82. Its effect on a test beam can be compensated by current carrying wires which create just the $1/r$ field. The advantage of such an approach consists of the simplicity of the method and the possibility to deal with all multipole orders at once. For a finite length of a wire embedded in the middle of a drift length L , the change in slopes of a test beam at the wire is [20]

$$\begin{pmatrix} \Delta x' \\ \Delta y' \end{pmatrix} = \frac{\mu_0}{4\pi} \frac{I_w l_w}{B\rho} \frac{u-v}{x^2+y^2} \begin{pmatrix} x \\ y \end{pmatrix} \quad (1)$$

where I_w is the current of wire, u and v are $\sqrt{(L/2+l_w)^2+x^2+y^2}$ and $\sqrt{(L/2-l_w)^2+x^2+y^2}$ respectively. Taking into account the wire placement including pitch and yaw angles, the transfer map of a wire can be written as

$$M_w = S_{\Delta x, \Delta y} \circ T_{\theta_x, \theta_y}^{-1} \circ D_{L/2} \circ M_k \circ D_{L/2} \circ T_{\theta_x, \theta_y} \quad (2)$$

where T_{θ_x, θ_y} represents the tilt of the coordinate system by horizontal and vertical angles θ_x, θ_y to orient the coordinate system parallel to the wire, $D_{L/2}$ is the drift map with a length $L/2$, M_k is the wire kick integrated over a drift length, and $S_{\Delta x, \Delta y}$ represents a shift of the coordinate axes to make the coordinate systems after and before the wire agree. For cancelling the long-range beam-beam interactions of the round beam with the wire, one can get the desired wire current and length by equating the kicks from the wire and the strong beam at the large amplitude; the integrated strength of the wire compensator should be commensurate with the integrated current of the beam bunch, i.e., $(I_w l_w) = nqc$, where n is the beam intensity, q the beam charge, and c the speed of light.

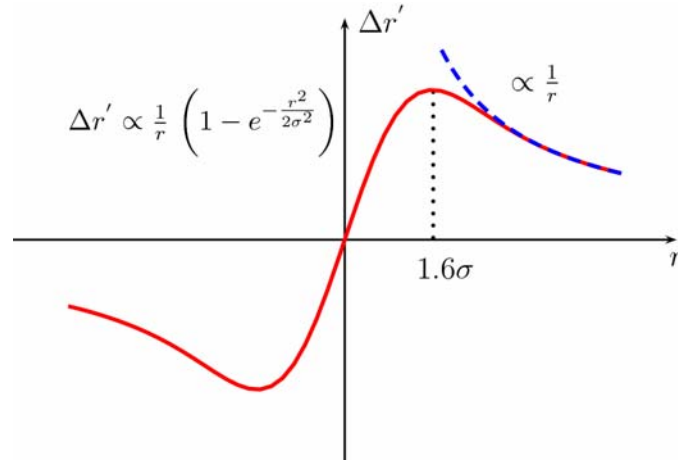


Figure 82: Beam-beam force of round Gaussian beam and a current-carrying wire.

A space charge force of low-energy electron beam is acting as a focusing or defocusing lens depending on the high energy bunch. A proton bunch colliding with a counter-rotating proton bunch experiences a defocusing force which can be canceled out by a counter-rotating electron beam having the same parameters as the counter-rotating proton bunch. The transverse electron beam profile and its beam current are key parameters. The longitudinal electron beam profile is not really important because the betatron phase advance is negligible over the bunch length. Two electron beam distribution functions are commonly considered as shown in Figure 83: (i) Gaussian distribution and (ii) Smooth-edge-flat-top (SEFT) distribution. The transverse kick on the high energy beam from the electron beam is given by

$$\Delta \vec{r}' = \frac{2nr_0}{\gamma} \frac{\vec{r}_\perp}{r_\perp^2} \zeta(r_\perp : \sigma) \quad (3)$$

where n is the number of electrons of the electron beam adjusted by the electron speed, r_0 is the classic proton radius, and γ is the Lorentz factor. The function ζ is given by

- for Gaussian distribution

$$\zeta = 1 - \exp\left(-\frac{r_\perp^2}{2\sigma^2}\right) \quad (4)$$

- for SEFT distribution

$$\zeta = \frac{\sqrt{2}\rho_0}{8} \left[\frac{1}{2} \log\left(\frac{\theta_+^2 + 1}{\theta_-^2 + 1}\right) + \tan^{-1}\theta_+ + \tan^{-1}\theta_- \right] \quad (5)$$

where ρ_0 is a constant, and $\theta_\pm = \sqrt{2}(r/\sigma)^2 \pm 1$.

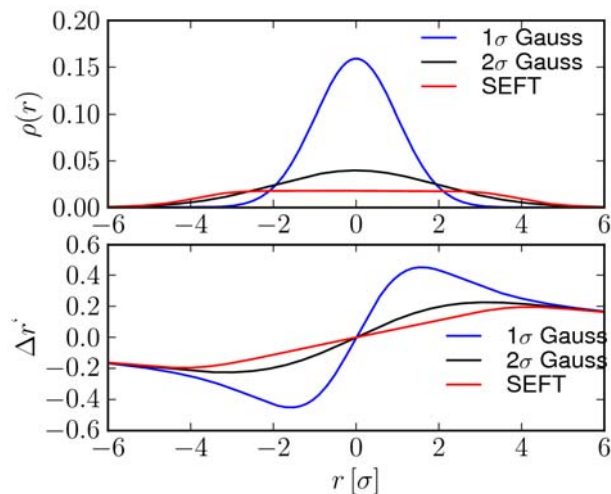


Figure 83: (top) Transverse electron beam distributions: (black) $2\sigma_p$ Gaussian distribution, (blue) $1\sigma_p$ Gaussian distribution, and (red) constant distribution with smooth edge; $\rho(r) \sim 1/(1+(r/4\sigma_p)^8)$. (bottom) Kicks from the electron beam distribution. Note that the number of particles of three distribution is the same.

Following the above physical model, a beam-beam simulation code BBSIMC has been developed at FNAL over the past few years to study the effects of the machine nonlinearities and the beam-beam interactions [21]. If required, time dependent effects such as tune modulation and fluctuation, beam offset modulation and fluctuation, dipole strength fluctuations to mimic rest-gas scattering etc can be included in the model. The code is under continuous development with the emphasis being on including the important details of an accelerator and the ability to reproduce observations in diagnostic devices. At present, the code can be used to calculate tune footprints, dynamic apertures, beam transfer functions, frequency diffusion maps, action diffusion coefficients, emittance growth and beam lifetime. Calculation of the last two quantities over the long time scales of interest is time consuming even with modern computer technology. In order to run efficiently on a multiprocessor system, the resulting model was implemented by using parallel libraries which are inter-processor Message Passing Interface standard [22] and Portable, Extensible Toolkit for Scientific Calculation [23].

3.11.3 Applications

Relativistic Heavy Ion Collider

At store energy the Relativistic Heavy Ion Collider (RHIC) has nominally two head-on beam-beam collisions at IP6 and IP8. There are no long-range interactions. In order to investigate the long-range beam-beam interactions and test the compensation scheme, two current carrying wires, one for each beam, were installed between the magnets Q3 and Q4 of IP6 in the RHIC tunnel [11]. The impact of a wire can be observed by measuring the orbit change, tune shift, the beam transfer function and the loss rates. The tune shift is one of the fundamental observables and it can be directly verified with analytical calculation. However, numerical simulations allow us to calculate other quantities not easily observable but which give valuable insight into the beam dynamics

and can complement the experiments. These numerically calculable quantities include the tune footprint, the frequency diffusion map, the dynamic aperture, and the diffusion coefficients to characterize the diffusion in action. These are discussed in detail in ref. [21]. In this letter we will present the effect of the wire on the beam loss rates as the beam-wire separation is changed. In the simulation, the loss rates are estimated from the asymptotic limit by extrapolating the simulated loss rate because in the beginning of the simulation, the loss rate decreases exponentially rapidly and then approaches a constant rate at later times. The onset of beam losses, seen in Figure 84, is observed at 8σ and 9σ for gold and deuteron beams respectively. In both cases, the threshold separation for the onset of sharp losses observed in the measurements and simulations agree to better than 1σ . It is also significant that the simulated loss rates at 7σ and 8σ separations for the gold beam and 8σ and 9σ for the deuteron beam are very close to the measured loss rates.

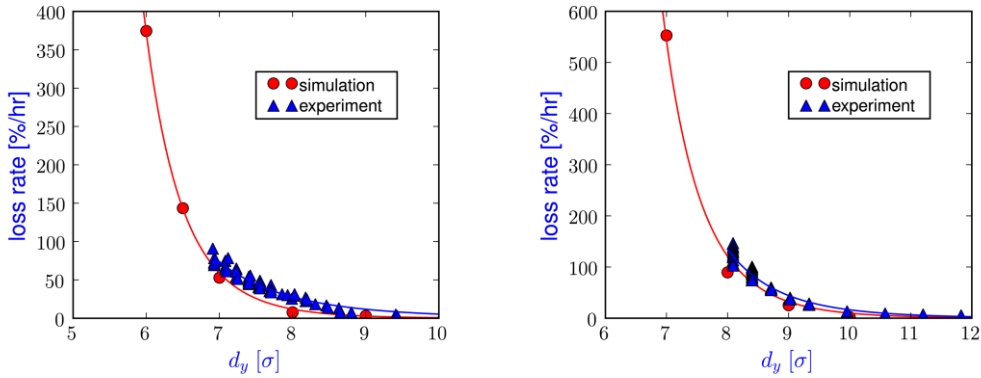


Figure 84: Comparison of the simulated beam loss rates with the measured as a function of separations. (left) gold beam at collision energy, (right) deuteron beam at collision energy. Wire strength is 125 Am.

The electron lens has been proposed in particular for a reduction of the large tune spread of proton beam and emittance growth in RHIC [15, 16]. The tune spread can be fully compressed by the electron lens with an electron beam profile which matches to a proton beam. Simulation studies, however, showed that the electron lens leads to an increase of beam loss when the electron beam profile matches a proton beam at the lens location and its intensity is chosen to fully compress the tune spread [24]. The full compensation of betatron tune is not a necessary and sufficient condition for improving the beam lifetime because the beam stability can get worse from footprint folding. In order to investigate the effects of different electron lens profiles and intensities on the beam dynamics, we calculated dynamic apertures, frequency diffusion maps, and particle loss [25, 26]. We observed a small increase in the dynamic aperture of off-momentum particles at small compensation strength. There is however a significant reduction in beam loss. A wider electron beam profile than the proton beam at the electron lens location is found to increase beam life time. In addition, the tune scan shows that the electron lens reduces the particle loss over the wide range of betatron tune for wide electron beam profile while no increase of beam lifetime is indicated for 1σ Gaussian profile, as shown in Figure 85. This looser tolerance on the allowed variations in electron intensity is likely to be beneficial during experiments.

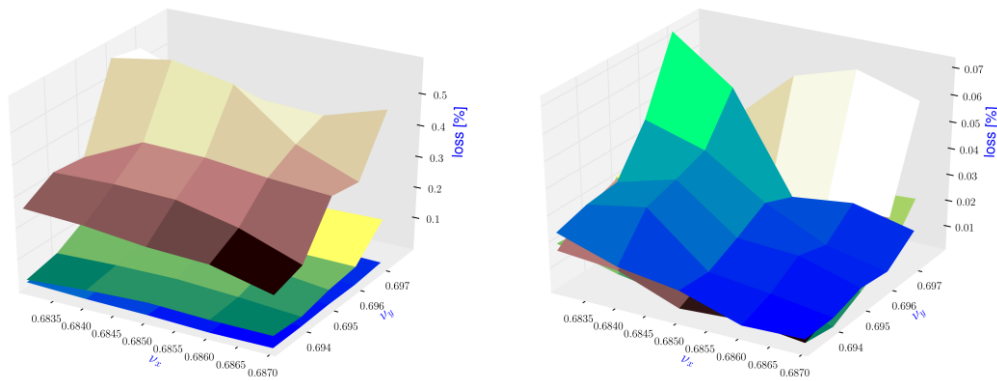


Figure 85: Plot of beam loss relative to the loss of no wire case: (left) 1σ Gaussian and (right) SEFT electron lens.

Large Hadron Collider

The Large Hadron Collider (LHC) has at most four interaction points. Due to the design goal of highest luminosity, the LHC operates with a large number of bunches at high intensities. The beams in the LHC experience a large number of up to 120 long-range interactions on either side of collision points. The long-range interaction is expected to limit the LHC performance. In order to mitigate the nonlinear effect of the long-range collisions, one can employ a current-carrying wire at the location of the long-range encounters. The wire's locations are proposed where the beta functions in both transverse planes are equal [6]. The average phase advance between the location of the wire and the location of the long-range interaction points is about 3° . The integrated current for optimal tune compression is 82.8 Am. At the nominal LHC the beam-beam separation distance normalized by the transverse rms bunch size varies from 6.3σ to 12.6σ and is asymmetric with respect to the interaction points. The resulting beam-beam force is not identical to that generated by a single or multiple wire(s). The wire-beam separation distance is therefore one of major parameters which determine the performance of a wire compensator. Figure 86 shows the results of proton beam loss for different wire-beam separations. The particle loss saturates at large separation while there is a sharp increase of particle loss at small separation. The minimum particle loss is observed between 8σ and 9σ wire-beam separations which are close to the averaged beam-beam separation on each side of the interaction points.

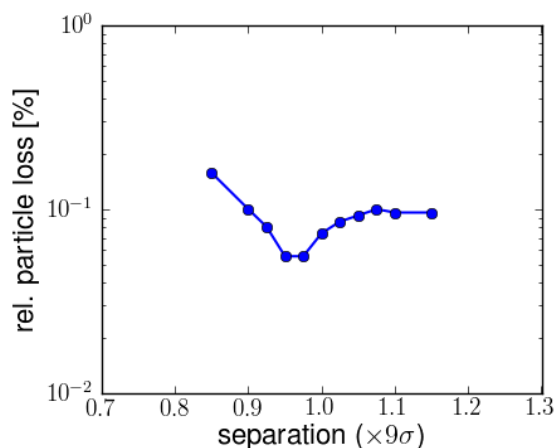


Figure 86: Plot of particle loss according to wire-beam separation distance with wire strength 82.8 Am.

3.11.4 Acknowledgements

Some of the parallel computations were performed at the NERSC facility at LBL and the CARC at UNM. This work was supported by the US-LARP collaboration which is funded by the US Department of Energy.

3.11.5 References

1. T. Sen, B. Erdelyi, M. Xiao, and V. Boochoa, *Phys. Rev. ST Accel. Beams* **7**, 41001 (2004).
2. V. Shiltsev, Y. Alexahin, V. Lebedev, P. Lebrun, R. S. Moore, T. Sen, A. Tollestrup, A. Valishev, and X. L. Zhang, *Phys. Rev. ST Accel. Beams* **8**, 101001 (2005).
3. A. Valishev, *Proceedings of EPAC08*, p. 2937 (2008).
4. V. Ptitsyn et al., *Proceedings EPAC06*, p. 592 (2006).
5. K. Ohmi, *Proceedings of EPAC08*, p. 2593 (2008).
6. J.-P. Koutchouk, *Proceedings of PAC07*, p. 3387 (2007).
7. J. P. Koutchouk, J. Wenninger, and F. Zimmermann, *Proceedings of EPAC04*, p. 1936 (2004).
8. U. Dorda, J. Koutchouk, R. Tomas, J. Wenninger, F. Zimmermann, R. Calaga, and W. Fischer, *Proceedings of EPAC08*, p. 3176 (2008).
9. F. Zimmermann, J.-P. Koutchouk, F. Roncarolo, J. Wenninger, T. Sen, V. Shiltsev, and Y. Papaphilippou, *Proceedings of PAC05*, p. 686 (2005).
10. C. Milardi, D. Alesini, M. A. Preger, P. Raimondi, M. Zobov, and D. Shatilov, *Proceedings of CARE-HHH- APD IR07 Workshop*, p. 92 (2007).
11. W. Fischer et al., *Proceedings of PAC07*, p. 1859 (2007).
12. V. Shiltsev, Y. Alexahin, K. Bishofberger, V. Kamerzhiev, G. Kuznetsov, and X.-L. Zhang, *Physical Review Letters*, **99**, 244801 (2007).
13. V. Kamerzhiev, Yu. Alexahin, V. Shiltsev, A. Valishev, and X. L. Zhang, *Proceedings of PAC07*, p. 1703 (2007).
14. V. Shiltsev et al, *New Journal of Physics*, **10**, 043042 (2008).
15. Y. Luo and W. Fischer, *BNL-CAD/AP/286* (2007).
16. Y. Luo, W. Fischer, and N. Abreu, *BNL C-A/AP/310* (2008).
17. K. Hirata, H. Moshhammer, and F. Ruggiero, *Part. Accel.* **40**, 205 (1993).

18. K. Hirata, SLAC-PUB-637 (1994).
19. L. Leunissen, F. Schmidt, and G. Ripken, Phys. Rev. ST Accel. Beams **3**, 124002 (2000).
20. B. Erdelyi and T. Sen, Fermilab-TM-2268-AD, (2004).
21. H.J. Kim, T. Sen, N. P. Abreu, and W. Fischer, PRST-AB **12**, 031001 (2009).
22. MPI-2: Extensions to the Message-Passing Interface, Message Passing Interface Forum, University of Tennessee (2003).
23. S. Balay, W. D. Gropp, L. C. McInnes, and B. F. Smith, ANL-95/11, Revision 2.3.3 (2008).
24. A. Valishev et al., LARP Mini-Workshop on Electron Lens Simulations at BNL (2008).
25. H.J. Kim and T. Sen, Proceedings of PAC09, WE6PFP032 (2009).
26. H.J. Kim and T. Sen, Proceedings of IPAC10, p. 2075 (2010).

3.12 Space-Charge Limitations in a Collider

Alexei V. Fedotov, Brookhaven National Laboratory, Upton, NY 11973
 Mail to: fedotov@bnl.gov

3.12.1 Introduction

Design of several projects which envision hadron colliders operating at low energies such as NICA at JINR [1] and Electron-Nucleon Collider at FAIR [2] is under way. In Brookhaven National Laboratory (BNL), a new physics program requires operation of Relativistic Heavy Ion Collider (RHIC) with heavy ions at low energies at $\gamma=2.7-10$ [3].

In a collider, maximum achievable luminosity is typically limited by beam-beam effects. For heavy ions significant luminosity degradation, driving bunch length and transverse emittance growth, comes from Intrabeam Scattering (IBS). At these low energies, IBS growth can be effectively counteracted, for example, with cooling techniques. If IBS were the only limitation, one could achieve small hadron beam emittance and bunch length with the help of cooling, resulting in a dramatic luminosity increase. However, as a result of low energies, direct space-charge force from the beam itself is expected to become the dominant limitation. Also, the interplay of both beam-beam and space-charge effects may impose an additional limitation on achievable maximum luminosity. Thus, understanding at what values of space-charge tune shift one can operate in the presence of beam-beam effects in a collider is of great interest for all of the above projects.

Operation of RHIC for Low-Energy physics program started in 2010 which allowed us to have a look at combined impact of beam-beam and space-charge effects on beam lifetime experimentally. Here we briefly discuss expected limitation due to these effects with reference to recent RHIC experience.

3.12.2 Space-Charge Effects

The Coulomb force between the charged particles in a beam in an accelerator creates a self-field which acts on the particles inside the beam. The Lorentz force experienced by the particle in the radial direction consists of repulsive electric force and attractive magnetic forces which almost cancel each other yielding the factor of γ^2 in the denominator for the force expression. As a result, a direct space-charge effect is

nonrelativistic in nature. In general, such space-charge force can change frequencies of oscillations of individual particles (incoherent effect) as well as frequencies of collective beam oscillations. This can lead to rather complex phenomena of space-charge driven resonances, as well as complicates response to the resonances driven by other effects. These effects are mostly of a concern for space-charge dominated beam transport and high-intensity storage rings operated close to the space-charge limit associated with low-order machine resonances. For discussion of these effects see for example Refs. [4-6] and references therein.

A convenient figure of merit for direct space charge effects in circular accelerator is change of the number of betatron oscillations of a single particle per machine turn (tune), which is called incoherent direct space-charge tune shift. In addition, beam surroundings in accelerator result in “indirect” space-charge effects due to image charges, which are omitted from present discussions.

For a beam with non-uniform transverse distribution, the radial force is non-linear which results in amplitude-dependent tune shift. The force can be linearized for small amplitudes near the beam center which provides expression for maximum tune shift. The tune shifts for particles having larger oscillation amplitudes are smaller than those for particles at the center of the beam. As a result, one has to consider the full tune spread introduced by the space charge. In bunched beam, transverse space-charge force is proportional to line charge density, which results in a tune shift being dependent on the longitudinal position within the beam. This causes a tune spread along the bunch as well. For a Gaussian transverse distribution, the maximum incoherent space-charge tune shift can be estimated as:

$$\Delta Q_{sc} = -\frac{Z^2 r_p}{A} \frac{N_i}{4\pi\beta^2\gamma^3\epsilon} \frac{C_r}{\sqrt{2\pi}\sigma_s}, \quad (1)$$

where r_p is the proton classical radius, N_i is the number of ions per bunch, A and Z are the ion atomic and charge numbers, γ , β are relativistic factors, ϵ is the unnormalized RMS emittance, σ_s is the rms bunch length, and C_r is ring circumference. Here we assumed round beam transversely and Gaussian longitudinal profile.

3.12.3 Beam-Beam Effects

Similar space-charge effect occurs in colliding beams. Each time the beams cross each other, the particles in one beam feel the electric and magnetic forces due to the particles of the other beam. The Lorentz force on the test particle linearized for small particle amplitudes gives linear incoherent beam-beam tune shift, which is also referred to as beam-beam parameter. For a round beam, linear incoherent beam-beam tune shift for hadrons is:

$$\xi = -\frac{Z^2 r_p}{A} \frac{N_i}{4\pi\beta^2\gamma\epsilon} \frac{1+\beta^2}{2}, \quad (2)$$

where ϵ is the unnormalized RMS emittance. Here we assumed colliding beams moving with the same velocity. The positive sign of β^2 corresponds to the case of the test particles and the bunch moving in opposite directions. When test particles and bunch

travel in the same direction the sign of β^2 is negative, resulting in the same space-charge cancellation $1/\gamma^2$ as for direct space-charge tune shift. The sign of the incoherent beam-beam force depends on the signs of the charges in the two colliding beams. If the two beams contain particles of the same charge, the force is repulsive which results in negative tune shift similar to direct space-charge tune shift.

The periodicity of beam-beam interaction and the fact that beam-beam force has nonlinear dependence on particle amplitude cause two important effects: an excitation of the nonlinear resonances and tune dependence on particles amplitude. As a result, one has to consider the full tune spread within the beam similar to the tune spread due to direct space-charge. The beam-beam interactions are very complex phenomena and involve both incoherent and coherent effects. It has been the topic of many dedicated workshops and conferences and many excellent reviews on this subject are available.

3.12.4 Space-Charge and Beam-Beam Limits in a Collider

In a collider, when maximum luminosity is limited by beam-beam effects it can be expressed through beam-beam parameter as

$$L = \frac{A}{Z^2 r_p} \frac{N_i c}{\beta^* C_r} \frac{2\gamma\beta^2}{1+\beta^2} f\left(\frac{\sigma_s}{\beta^*}\right) \xi, \quad (3)$$

where β^* is the beta function at the interaction point (IP) and σ_s is the rms value of the longitudinal beam size. The factor $f(\sigma_s/\beta^*)$, which describes the ‘‘hourglass’’ effect, is close to unity when the longitudinal rms beam size is much less than the value of beta function at the IP, and decreases when σ_s is increased.

If the luminosity is limited by the space-charge tune shift value ΔQ_{sc} , then it can be expressed as:

$$L = \frac{A}{Z^2 r_p} \frac{N_i c}{\beta^*} \frac{\sqrt{2\pi}\sigma_s}{C_r^2} \gamma^3 \beta^2 f\left(\frac{\sigma_s}{\beta^*}\right) \Delta Q_{sc}, \quad (4)$$

where no transverse acceptance limitation was taken into account. For typical parameters of low-energy collider with bunch length much smaller than ring circumference and low values of relativistic parameter γ , strongest limitation comes from space charge, while for higher energies beam-beam limitation starts to dominate, as, for example, for low-energy RHIC operation [7].

Ultimate limits on maximum values of space-charge and beam-beam parameters are typically associated with beam instabilities. However, before such limits are reached beam lifetime is strongly influenced by beam response to high-order non-linear resonances.

In hadron colliders, the total achieved tune spread due to beam-beam interactions is much smaller than in electron machines, which is believed to be due to a negligible effect of strong damping mechanism through synchrotron radiation which counteracts beam-beam diffusions in electron machines. The largest total tune spread due to several beam-beam interactions per turn which was achieved in Tevatron is only about 0.03.

Similarly, when space-charge tune spread becomes significant, the beam overlaps many machine imperfection resonances, leading to large beam losses and poor lifetime.

For machines where beam spends only tens of msec in high space-charge regime, and machines where the resonances are compensated, the tolerable space-charge tune shift can be as large as $\Delta Q_{sc}=0.2-0.5$. However the acceptable tune shifts are smaller for longer storage times, with beam lifetimes of several minutes achieved for space-charge tune shifts of about 0.1-0.2 [8]. For a collider when one is interested in even longer beam lifetimes, smaller acceptable space-charge tune spreads can be expected. In dedicated studies of IBS in RHIC, without beam-beam collisions beam lifetime of few hours was measured for space-charge tune spread of about 0.03. although no attempt was made to push space-charge tune shifts any further at that time.

A mostly unexplored effect at this moment is the interplay of direct space-charge and beam-beam effects, which is the case when one wants to collide beams with significant space-charge tune spread. In such a case, in its most simple manifestation beam-beam can excite resonances which will be crossed as a result of space-charge tune spread. We started to explore these effects in RHIC both in dedicated Accelerator Physics Experiments (APEX) and during 2010 physics Run at low energies which is briefly summarized in next section.

3.12.5 RHIC Experience

An experimental investigation of the interplay of beam-beam and space-charge effects in RHIC started with APEX experiments in 2009 using protons beams at $\gamma=25$. In these experiments beam-beam parameter per single interaction was up to $\xi=0.01$ and space-charge tune spread up to $\Delta Q_{sc}=0.03$. Strong excitation of beam-beam resonances was observed, which resulted in peeling of large amplitude particles after beams were put into collisions. This is shown in Figure 87 for transverse beam emittances measured with the Ionization Profile Monitor (IPM). Resulting reduction of beam intensity is shown in Figure 88. Fortunately, for such rather modest space-charge tune spread it was possible to find working point in the machine where effect of beam-beam resonances was minimized. An example of beam lifetime for such better working point is shown in Figure 89.

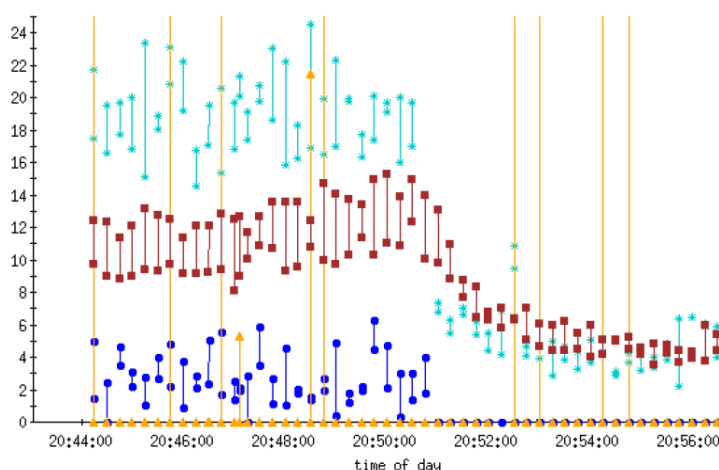


Figure 87: Measurements of transverse beam emittances (95%, normalized, in mm.mrad) during May 2009 RHIC APEX with proton beam at $\gamma=25$ for the working point where strong beam-beam resonances were excited. Brown rectangles show transverse emittance of one colliding beam while light-blue color stars show emittance of another colliding beam. After

beams were put into collisions at about 20:50, dramatic loss of large amplitude particles was observed.

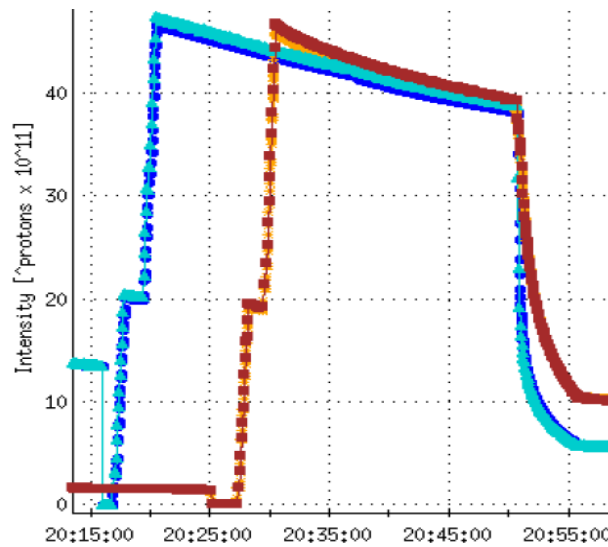


Figure 88: Measurements of total beam intensity loss (corresponding to Figure 87) during May 2009 RHIC APEX for proton beams at $\gamma=25$ before and after beams were put into collisions for the working point where strong beam-beam resonances were excited.

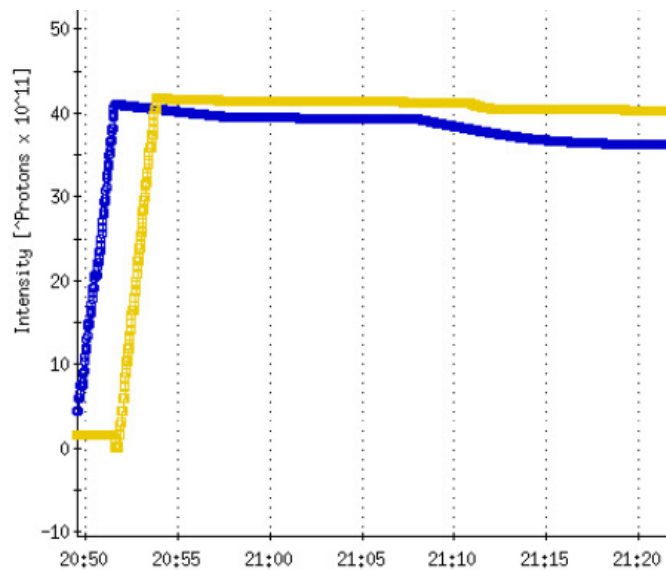


Figure 89: Measurements of total beam intensity loss during June 2009 RHIC APEX for proton beams at $\gamma=25$ before and after beams were put into collisions for a different working point where strong beam-beam resonances were avoided.

Experimental studies continued during RHIC operation with Au ion beams at low energies ($\gamma=4-10$) in 2010. Due to very low energies in this regime of parameters space-charge tune spread was much larger than beam-beam parameter. Thus, it was expected that beam-beam effects should be relatively small and one should be able to accommodate relatively large space-charge tune spreads. In March 2010 APEX experiments, for modest space-charge tune shift of $\Delta Q_{sc}=0.03$, long beam lifetime was

measured with almost no effect from beam-beam. For very large space-charge tune spread it appeared difficult to find sufficient space free from dangerous resonances on the tune diagram to achieve long beam lifetime. Although effects of beam-beam on beam lifetime were clearly observed we were able to provide collisions for physics with space-charge tune shifts up to 0.1. Detailed analysis of measured beam lifetime for various values of space-charge and beam-beam tune spreads are presently under way and will be presented elsewhere [9].

3.12.6 References

1. G. Trubnikov et al., "Project of the Nuclotron-based Ion Collider Facility (NICA) at JINR, Proc. of IPAC10 (Kyoto, Japan, 2010), p. 693.
2. A. Jankowiak et al., "Concept of Electron-Nucleon Collider at FAIR", Proc. of PAC'09 (Vancouver, Canada, 2009), WE6PFP063.
3. T. Satogata et al., "RHIC low-energy challenges and plans", Proc. of 5th International Workshop on Critical Point and Onset of Deconfinement-CPOD09 (BNL, New York, 2009).
4. A.V. Fedotov, "Resonances and beam loss in high intensity rings", Proc. of PAC03 (Portland, OR, 2003), p. 383.
5. A.V. Fedotov, I. Hofmann, R.L. Gluckstern, H. Okamoto, "Parametric collective resonances and space-charge limit in high-intensity rings", Phys. Rev. ST Accel. Beams 6, 094201 (2003).
6. I. Hofmann, "Space charge resonances in high-intensity beams", Proc. of HB2008 Workshop (Nashville, TN, 2008), p. 113.
7. A.V. Fedotov et al., "Beam dynamics limits for low-energy RHIC operation", Proc. of HB2008 Workshop (Nashville, TN, 2008), p. 75.
8. E. Metral and H. Burkhardt, "Achievable space-charge tune shift with long lifetime in the CERN PS and SPS", Proc. of HB2008 Workshop (Nashville, TN, 2008), p. 153.
9. A.V. Fedotov et al., "Interplay of space-charge and beam-beam effects in a collider", Proc. of HB2010 Workshop (Switzerland, 2010), to be presented.

3.13 Beam-Beam Issues in eRHIC

Y. Hao and V. Ptitsyn, Brookhaven National Laboratory, Upton, NY 11973, USA
 Mail to: yhao@bnl.gov, vadimp@bnl.gov

3.13.1 Introduction

eRHIC, a future electron-ion collider developed at BNL, aims to provide electron-ion collisions by adding a new electron accelerator to the existing RHIC ion accelerator rings [1]. To assure that eRHIC will become an invaluable tool, we must ensure that

- the energy of electron beam and nuclei is adjustable over a large range (5-30 GeV for electrons, 50-250 GeV for protons)
- high luminosity (exceeding $10^{33} \text{ cm}^{-2}\text{s}^{-1}$)
- high polarization for both the electron and proton beams

Possible options for accelerating high average current electron beam include an energy-recovery linac (ERL) or a storage ring. Since the proton beam is circulating in

the accelerator ring, corresponding collision schemes are called linac-ring and the ring-ring. The electron accelerator option based on the electron storage ring was studied on earlier stages of the eRHIC design [2]. It was found that the luminosity in this ring-ring scheme was limited by the beam-beam interaction to the level of several units of $10^{32} \text{ cm}^{-2} \text{ s}^{-1}$. Thus, the eRHIC design, using an ERL to accelerate the electron beam, became a preferred one and has been developed in recent years. In ERL-based eRHIC the luminosity can exceed the value of the ring-ring scheme by at least an order-of-magnitude because the electron beam is used only once, and therefore, the opposing proton beam can disrupt it more. The high average current of polarized electrons has to be provided by a polarized electron source, which presents an important R&D item for the ERL-based eRHIC design. The beam-beam effects in the linac-ring scheme have several specific features and challenges. Since there has been no collider operating with the linac-ring collisions, the thorough exploration of the features of the beam-beam interaction in ERL-based eRHIC is required both analytically and by simulations. Several studies of the beam-beam effects in the linac-ring scheme were done in early nineties, when this scheme was considered at the design of B-factories [3].

During the collision the electron beam undergoes a large beam-beam phase advance that entails a considerable mismatch between the beam distribution and the design electron optics. Furthermore, the phase advance exhibits a dependence on the betatron amplitude because of the nonlinearity of the beam-beam force, so causing the distortion of the distribution in the transverse phase space, the so-called ‘disruption effect’. Both the mismatch and the disruption effects must be studied carefully to ensure the proper transportation of the electrons after the collision in the decelerating stage, which is required by the energy-recovery process. Such studies will determine the required apertures of the linacs and the transport paths.

Another key feature of the linac-ring scheme is that a head-tail type of instability may develop in the proton beam, named the “kink instability”. The electron beam deforms during its interaction and transfers information from the head of the proton beam to the tail. Hence, the proton beam experiences a wake field created by its interaction with the electron beam. We must ensure the suppression of this instability if its parameters are beyond the instability threshold.

In addition to the possible coherent instability of the proton beam, it might be degraded by the nonlinearity of the beam-beam force. Nonlinear diffusion is enhanced because the electron beam is focused by the beam-beam interaction to a smaller rms beam size, resulting in considerable enlargement of the beam-beam force acting on the proton beam. This effect, usually referred as the “pinch effect”, must be mitigated to reduce the growth rate of the proton beam transverse emittance.

Table 11: Beam parameters of ERL-based eRHIC.

	High-energy setup	
	p	e
Energy (GeV)	250	10
Bunch intensity ($\times 10^{11}$)	2	1.2
rms emittance (nm)	3.8	5.0
β^* (cm)	26	20
Beam-beam parameter for proton, Disruption parameter for electrons	0.015	5.9
rms bunch length (cm)	20	0.7
Peak Luminosity, $\text{cm}^{-2}\text{s}^{-1}$	2.6×10^{33}	

Another important challenge is related with the random errors in the initial condition of the electron beam. The position jitter of the electron beam becomes a random dipole field error for the proton beam, while the fluctuations of the intensity and beam size of the electron beam create quadrupole errors. While these deviations are inevitable, they can be lowered by improving the stability of the electron source and the electron beam transport.

The effect of the beam-beam interactions on the proton beam is characterized by the beam-beam parameter. The beam-beam parameter limit of 0.015 was accepted for the protons on eRHIC, following the experience with proton-proton collisions in RHIC. For an electron beam, the disruption parameter ($d = \sigma_z / f$) presents a better measure of the beam-beam effects, where σ_z is the proton beam bunch length and f is the focal length of the beam-beam lens. The disruption parameter indicates the number of betatron oscillations the electrons perform inside the proton beam [4].

3.13.2 Electron Beam Disruption Effect

In eRHIC, the effect of beam-beam interaction on the electron beam is much larger than that on the proton beam. The beam-beam force disrupts the electron beam distribution considerably after just one collision with protons; meanwhile, the distribution of the proton beam changes very slowly. To investigate the evolution of the electron beam in one collision process, we can assume that proton beam is rigid. Then, we can distinguish two components in the disruption of the electron beam. First, the nonlinearity of the beam-beam force distorts its distribution, since the phase advance differs at various transverse amplitudes, and increases its transverse emittance. Second, the linear part of the beam-beam interaction (strong focusing) engenders a mismatch between the electron distribution in phase space and the aperture's shape, as defined by the design lattice without collisions. The deformation of the electron beam distribution by the beam-beam interactions must be minimized in order to guarantee successful transport of the electron beam at the deceleration stage of the energy recovery process. Because of that the detailed studies of the electron beam disruption in eRHIC have been done [5].

3.13.2.1 *Linear Approximation*

We start our discussion from the linear approximation in which we treat the beam-beam force as a thick focusing element in both transverse directions, with arbitrary longitudinal profile that is determined by the proton beam longitudinal distribution. We discuss here a uniform distribution, and a Gaussian distribution.

The linearized beam-beam force rotates the electron beam in phase space, causing a mismatch between the electron-beam distribution and the acceptance of the electron lattice downstream. Consequently, the emittance of the electron beam increases if we measure it with the optics functions of the lattice; we name this as “effective emittance”. We distinguish it from the former emittance calculated from the beam distribution that we call the “geometric emittance”.

To mitigate the growth of the effective emittance, we seek a solution for the optics of the electron beam so that, after the beam-beam interaction, its distribution exactly matches the lattice downstream. With this solution, at the position far away from the interaction point one cannot conclude whether there was a beam-beam interaction at all. In the absence of the beam-beam interaction, the interaction region lattice can be characterized by the optics parameters (β^* and s^*), which represents the waist beta-function and its position. If the timing of the collision is perfect, the beam-beam force exercised by the electron beam is symmetric to the IP. Therefore, the perfect matching solution exists only if the lattice design also is symmetric ($s^* = 0$). Thus, the only variable is the beta function at IP.

In Figure 90, we illustrate the evolution of optics functions in the IR at different design β^* . The proton beam has a Gaussian longitudinal distribution, with rms bunch length 0.2 m. Table 11 lists the other relevant proton beam parameters. The electron beam propagates from the right side of the figure to the left. In general, the optics with beam-beam interaction deviates from those without it. At $\beta^* = 1$ m, the beta function after collision is larger with beam-beam effect, while it is smaller when $\beta^* = 0.2$ m. We can calculate the exact matching β^* with a numerical solver. The result is $\beta^* = 0.225$ m. In Figure 91, we show that the optics functions match each other at both the entrance and exit of the collision region; deviation is limited to the region where the proton beam is present.

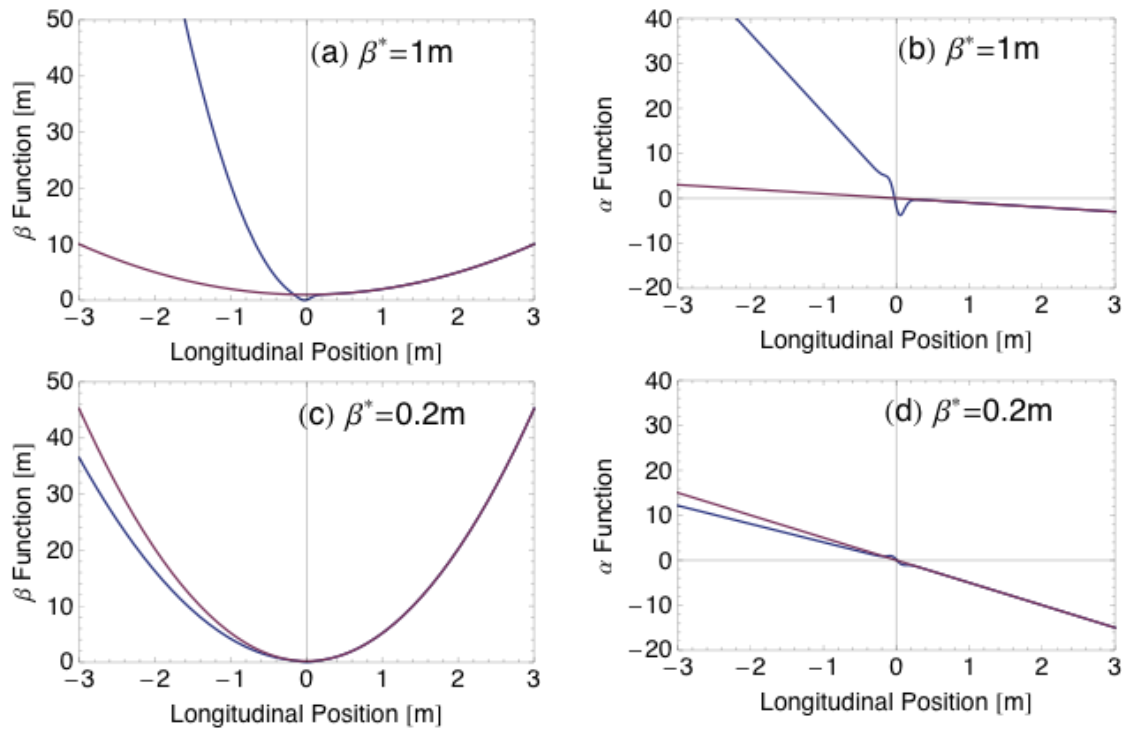


Figure 90: Comparison of the beta function at IR at different beta functions. The red lines are cases without beam-beam interaction (design optics); the blue ones are those with beam-beam interaction.

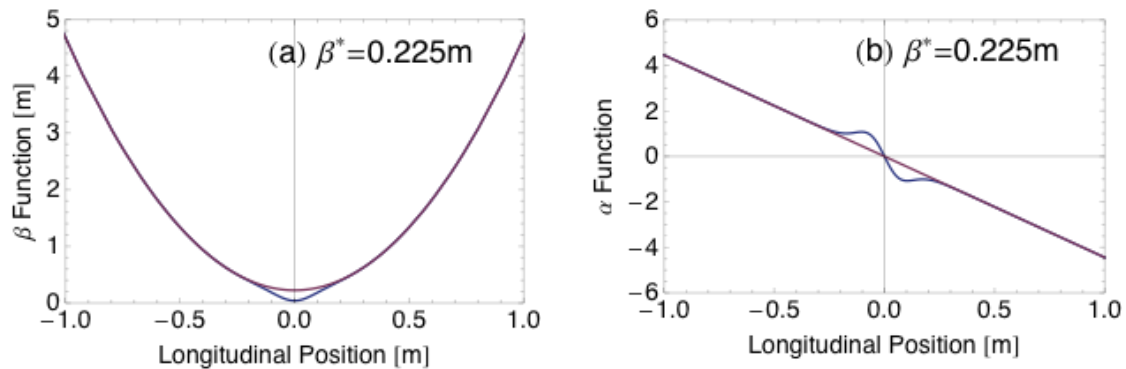


Figure 91: The optics functions of a perfect matching design ($\beta^* = 0.225$ m). The red lines are the cases without beam-beam interaction (design optics); the blue ones are those with beam-beam interaction.

The exact matching solution can be derived analytically [5] if we assume that the proton beam has a uniform longitudinal distribution:

$$\beta^* = \frac{\sqrt{1 - k^2 L^2 + kL [\tan(kL) - \cot(kL)]}}{k}$$

Here, the proton beam has the uniform distribution $[-2L, 2L]$ and the focusing strength is defined as $k = (2f_e L)^{-1/2}$. This relation shows that the matching condition does not

always exist for all parameters, as demonstrated in Figure 92. When kL falls within the region $[0, \pi/2]$, the matching solution always exists. Equivalently, this requires that the disruption parameter D is less than 5.7. For a Gaussian longitudinal distribution, we can similarly determine the requirement for the maximum disruption parameter. In this case, the disruption parameter that assures a matched optics solution should be less than 8.3. As Figure 92 shows there are also another kL ranges, at higher kL values, which allows the exact matching solution.

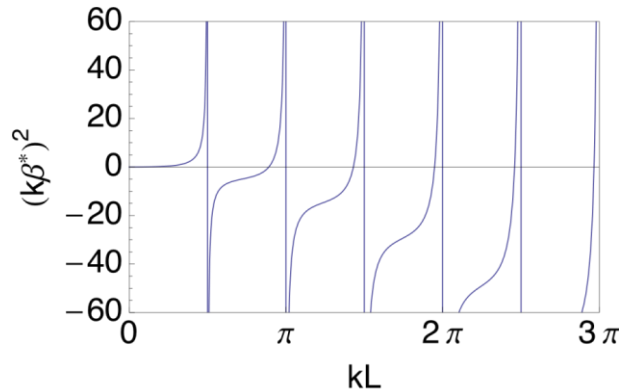


Figure 92: The solution of the design beta-function for the exact matching solution for uniform proton distribution. The real solution exists only when $(k\beta^*)^2$ is positive

3.13.2.2 *Nonlinear Effects*

If we account for nonlinearity, the electrons with various betatron amplitudes have different phase advances. Accordingly, the electron distribution is distorted, especially at large betatron amplitudes, thereby altering the geometric emittance of the electron beam. To explore the resulting deterioration of the beam emittance, we undertook a simulation of its dynamics.

In this simulation, we assumed that the proton beam is rigid (strong beam) and has the parameters listed in Table 11. We ignored the length of the electron beam bunch; therefore, its longitudinal profile is a delta function. The optimized electron beta function from the linear approximation does not necessarily fit well in the nonlinear case. Here, for comparison, the cases of two different electron β^* (0.2 m and 1 m) are illustrated. The transverse emittance of the electron beam is changed correspondingly to match that of the proton beam. In Figure 93 and Figure 95, we depict the evolution of the rms size of the electron beam, its geometric emittance and its effective emittance. The electron beam travels from the right side to the left. The evolution of the electron beam depends strongly on the design electron-beam optics (β^*). The geometric emittance increases as the electron beam moves through the opposing proton beam. This increment ratio for the low β^* is well below than that for the high β^* case. The effective emittance, mainly contributed by the advance in linear phase, exhibits about a 5 times difference between these two examples. The low β^* case certainly is the desirable one since it has a lower emittance after collision.

Figure 94 and Figure 96 show the phase-space distribution after the collision of the electron beam, along with the rms emittance ellipse. We back-traced those distributions to the IP so to compare them with the design optics (β^*). The mismatch between the beam distribution and the design optics is smaller for low β^* .

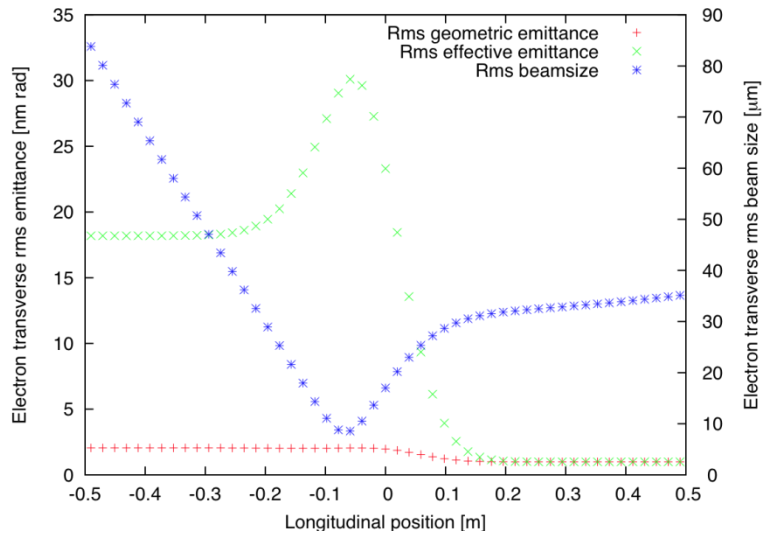


Figure 93: Evolution of beam size and rms emittance (geometric and effective) of the electron beam for $\beta^* = 1\text{ m}$.

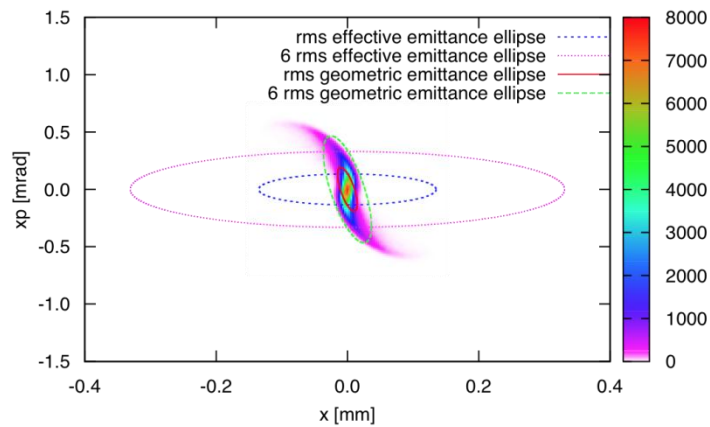


Figure 94: Phase-space distribution of the electron beam after collision for $\beta^* = 1\text{ m}$, back-traced to the IP. The rms and 6 rms ellipses for both the geometric and the effective emittance are plotted.

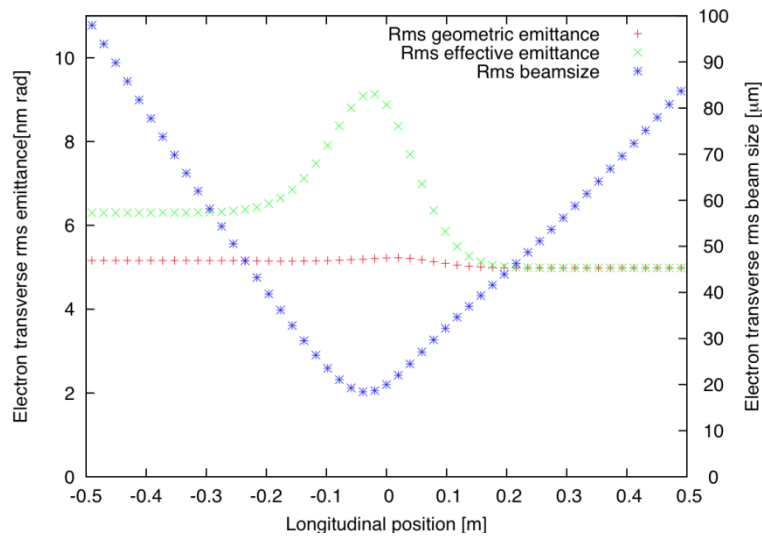


Figure 95: Evolution of the beam size and rms emittance (geometric and effective) of the electron beam for $\beta^* = 0.2$ m.

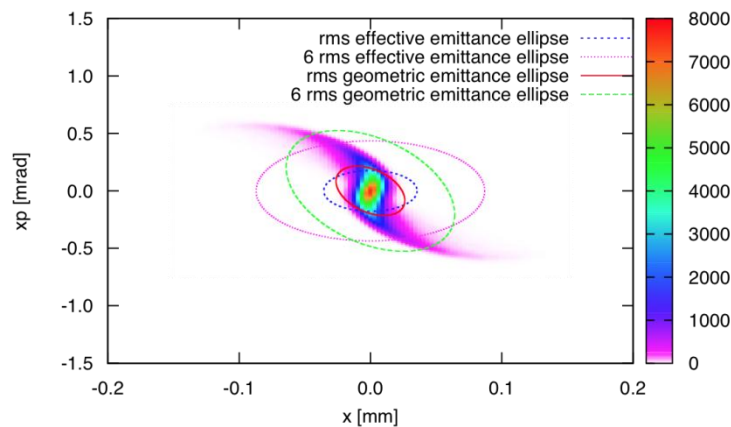


Figure 96: Phase-space distribution of the electron beam after collision for $\beta^* = 0.2$ m, back-traced to IP. The rms and 6 rms ellipses for both the geometric- and effective- emittance are plotted.

Another notable effect is the so-called “pinch effect” whereby the opposing proton beam greatly focuses the electron beam. In both of these above two cases, the minimum size of the rms electron beam, respectively, reaches 8 microns ($\beta^* = 1$ m) and 16 microns ($\beta^* = 0.2$ m). The direct consequence is an enhancement in luminosity because the average size of the rms electron beam shrinks during the beam-beam interaction. Table 12 lists the integrated luminosity from different initial electron optics. The pinch effect augments luminosity, while the hourglass effect degrades it. These two effects countermand each other, so that luminosity is higher than its nominal value when β^* is larger than 0.2 m.

Table 12: Luminosity for different electron beam parameters.

Initial electron beam parameters			Luminosity [$\text{cm}^{-2}\text{s}^{-1}$]
Emittance [nm-rad]	β^* [m]	Waist position [m]	
1	1	0	3.7×10^{33}
4	0.25	0	3.3×10^{33}
5	0.2	0	3.0×10^{33}
10	0.1	0	2.3×10^{33}

However, the intensification of luminosity is not without its drawbacks. The beam-beam parameter for the proton beam becomes too large when the electron beam reaches its minimum rms size. For example, for the design $\beta^* = 1$ m, the minimum beam size is 8 microns, one quarter of the nominal waist size without the collision. There, the maximum focusing strength of the beam-beam force has a value 16 times that of the designed value. Furthermore, the shrinkage of the electron beam size changes its distribution. The histogram, shown in Figure 97, demonstrates the modification of the transverse beam distribution by the beam-beam interaction.

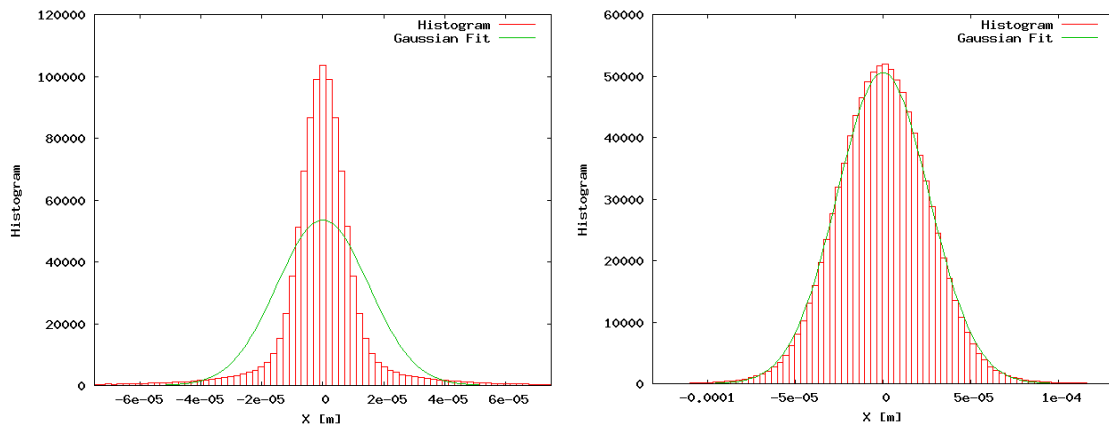


Figure 97: Histogram of the electron transverse positions after beam-beam collision. Left: the initial electron rms emittance is 1 nm-rad and β^* is 1 m at IP. Right: the initial electron rms emittance is 5 nm-rad and β^* is 0.2 m at IP. The green curve corresponds to the Gaussian-function fit based on the electron beam rms size and histogram data.

Figure 97 reveals that, if the initial beta function is large, the electron distribution forms a denser core and longer tail than a Gaussian distribution with same rms size. However, the deformation is almost negligible when beta function is 0.2 m. The pinch effect not only shrinks the electron beam size but also distorts its distribution so to entail an even higher shift in the beam-beam phase for the proton beam. This large, nonlinear phase-shift will impair the quality of the proton beam due to the nonlinear resonance resulting from the large tune-spread.

In summary, multiple goals must be met to achieve the optics design of the electron beam. The machine requires high luminosity, a successful energy-recovery process demands a low electron beam emittance after collision, and the pinch effect needs to be small to assure the stability of the opposing proton beam. As we discussed, our findings demonstrate that for same electron beam waist size, a higher waist beta-function leads

to larger luminosity, but worsens the final emittance by imposing a larger pinch effect, and consequently, a short lifetime for the proton beam. We need to compromise to reach our goals by choosing the proper optics functions.

Figure 98 and Figure 99 show some of the important outcomes of optimizing the parameters. Each point in these figures corresponds to one initial electron-beam parameter and optics; we vary three parameters, viz., the initial electron-emittance, the waist beta-function β^* , and its position s^* .

Table 13: The parameters ranges used at the optimization of the electron IR optics design and the luminosity in eRHIC.

Initial Electron rms Emittance ($\times 10^{-9}$ m-rad)	[1 ; 8]
Electron waist beta function β^* (m)	[0.1 ; 2]
Electron Waist position s^* (m)	[-0.5 ; 0.5]

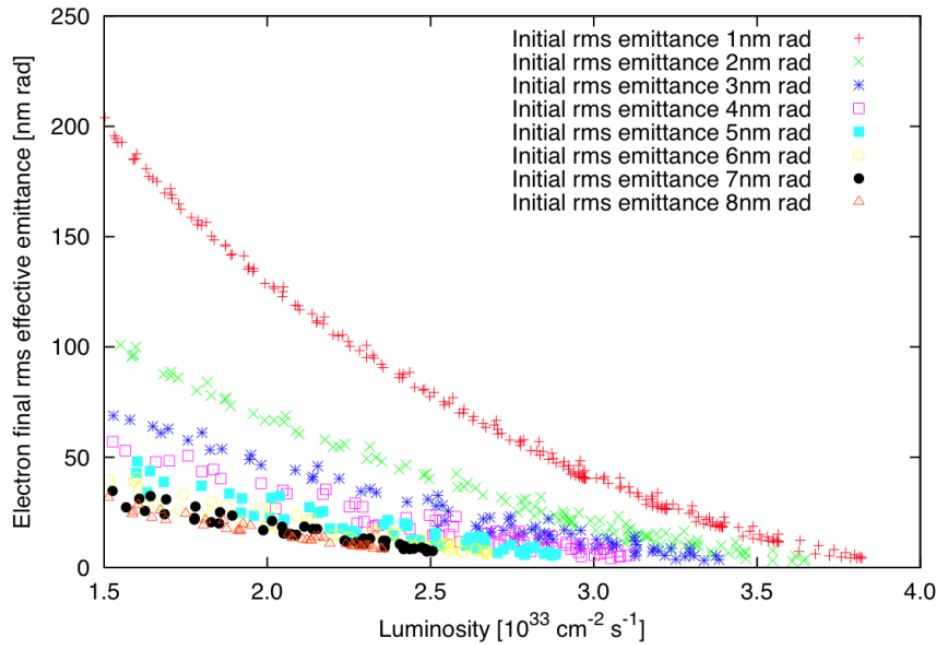


Figure 98: Electron beam rms effective emittance after collision plotted as a function of the resulting luminosity.

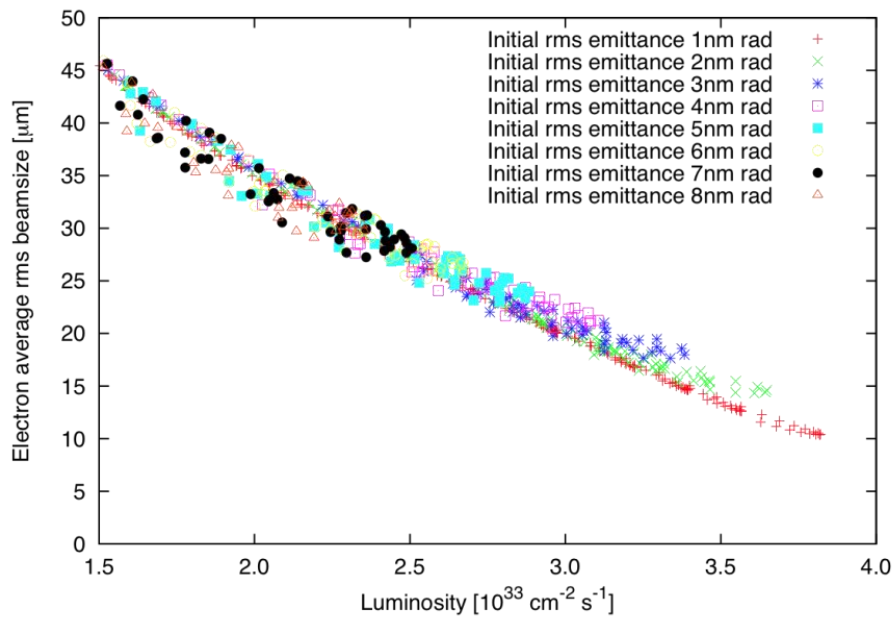


Figure 99: Plots of the rms electron-beam size during collision as a function of the resulting luminosity.

In Figure 98 the final rms effective emittance is plotted as function of the resulting luminosity after considering the pinch and the hourglass effects. An interesting feature is that, for a fixed luminosity, a larger initial rms emittance leads to the lower final emittance. Further, at any given initial rms emittance, if the designed optics produces high luminosity, then, simultaneously, a smaller final rms emittance is obtained. Luminosity and the final rms emittance have a very simple relationship.

However, the pinch effect limits the realizable luminosity. Figure 99 plots the correlation between luminosity and the average size of the electron beam during the collision. A small electron beam enhances the beam-beam force acting on the protons, and causes a slow deterioration of the proton beam emittance. Simulations demonstrate that the limit of the average electron beam size is about 20 microns, corresponding to about $3 \times 10^{33} \text{ cm}^{-2} \text{ s}^{-1}$ luminosity. At smaller beam size the deterioration of the proton beam emittance becomes not acceptable.

On the basis of the results obtained from scanning of the electron beam parameters, we concluded that the initial emittance of 5 nm rad and $\beta^* = 0.2 \text{ m}$ present the optimal choice, which assure both an acceptable electron beam quality after collision and large luminosity. The shift of the electron beta-waist location s^* from the center, towards the electron beam, produces somewhat large luminosity, as shown in Figure 100. The original eRHIC IR design, based on $\beta^* = 1 \text{ m}$, was modified to satisfy the results of this studies, which led to the beam parameter set presented in Table 11.

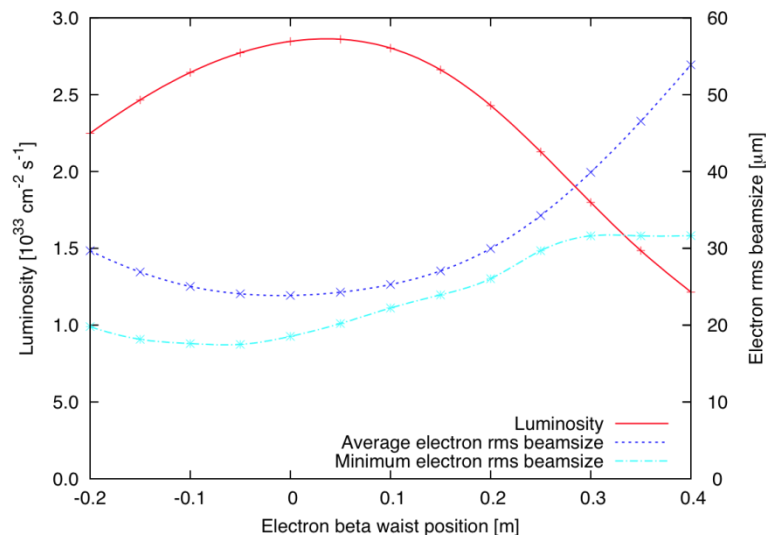


Figure 100: Dependence of luminosity and the electron beam size as function of the waist position of the beta function.

3.13.3 Kink Instability

Kink instability is a head-tail type instability [6,7] that arise from the beam-beam interaction between the two colliding beam. Through the interaction, the imperfection of the hadron beam can pass from the head of the beam to the tail and build up exponentially in the ring and form instability. Usually the dipole moment of the imperfection has the most important effect for the proton beam, since it has the lowest threshold.

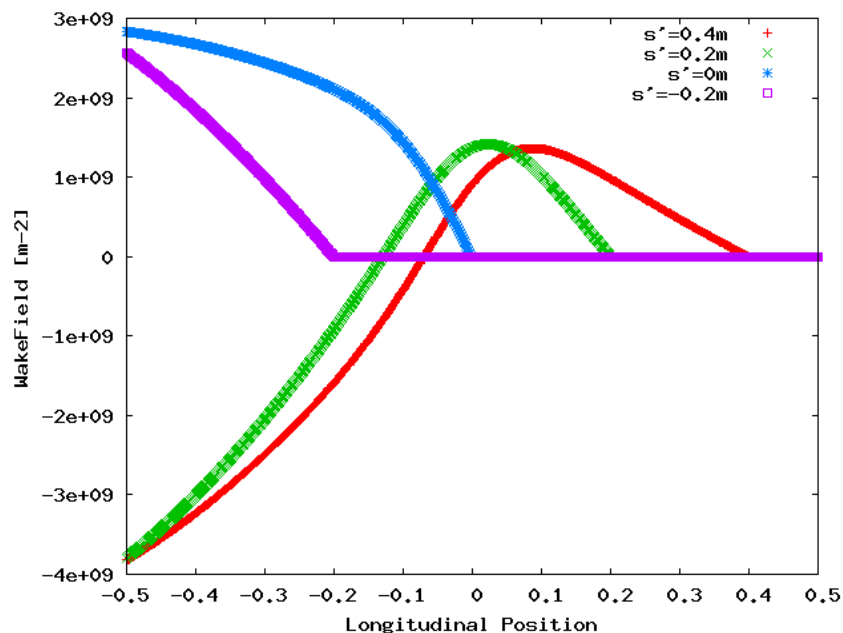


Figure 101: The wake field of a longitudinal Gaussian distribution.

Effectively, the interaction with the electron beam can be deemed as an interaction with a complicated wake field. This wake field depends on the proton beam distribution. For a uniform distribution with length $2L$, the wake field has a simple

sinusoidal form $W(s-s') = \sin k(s-s')H(s'-s)$, where $k = (2f_e L)^{-1/2}$ is the focusing strength of the electron beam, H is the Heaviside step function and s' presents the longitudinal position of the proton. In this special case, the wake field only depends on the longitudinal distance between heading and trailing particles. However, this does not hold for arbitrary proton longitudinal distribution. For a general distribution, the wake field is a function of both longitudinal positions instead of their difference. It can be derived from the simulation of the electron disruption study. Figure 101 reflects the wake field of the proton beam with a longitudinal Gaussian distribution. It has different shapes for various longitudinal position s' .

The threshold of the instability needs to be determined from the wake field. The simplest estimation can be done theoretically. By using a constant wake field and 2 macro-particles to represent the proton beam, the threshold of the kink instability is given approximately by $D_e \xi_p < v_s$ [8], where the disruption parameter of the electron beam, the beam-beam parameter of the proton beam and the proton synchrotron tune are involved. Although it is not a precise one, the estimation does reflect the basic feature of the head-tail instability. When no synchrotron motion is present, the system is always unstable. The faster the synchrotron motion is, the larger beam-beam strength is allowed.

For the real situation, simulation results can anticipate the threshold more precisely than the over-simplified analytical model. The simulation considers the real proton transverse and longitudinal distribution as well as a short electron bunch. Therefore the correct wake field and the nonlinearity of the interaction are taken into account.

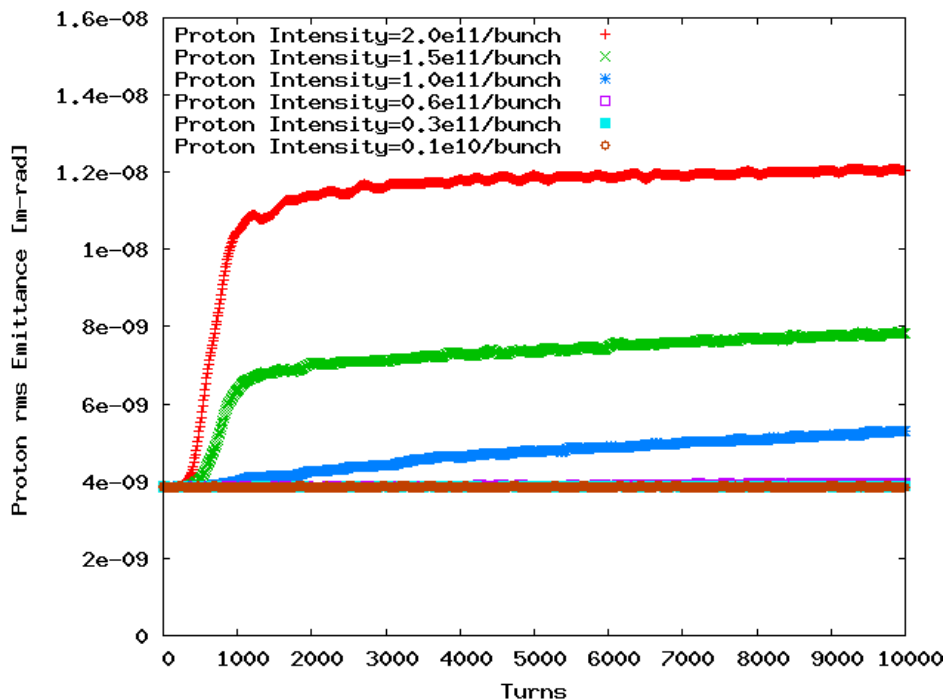


Figure 102: The proton rms emittance growth at different proton beam intensities.

Figure 102 shows the proton rms emittance growth under nonlinear beam-beam force with zero chromaticity for different proton beam intensities. Here the electron and proton parameters follow the nominal design values (Table 11) except proton beam

intensity. The nominal proton beam intensity is 2.0×10^{11} per bunch, which gives fastest emittance growth. The growth rate decreases as the proton intensity drops down. At very low intensity ($< 3.0 \times 10^{10}$ protons per bunch), no emittance growth is observed within calculation time. After rising quickly, the emittance growth in the unstable high intensity cases is suppressed by nonlinearity of the force.

Apparently, the eRHIC parameters exceed the threshold of the kink instability. To stabilize the beam, we can introduce tune spread to increase Landau damping. In reality, many effects, such as the nonlinear field in the lattice magnet elements, space charge effects and energy spread with a non-zero chromaticity, can bring up tune spread. In simulation, one of the easiest ways to generate controllable tune spread is the chromaticity. With a proper chromaticity of correct sign, the emittance growth can be suppressed and the proton beam becomes stable.

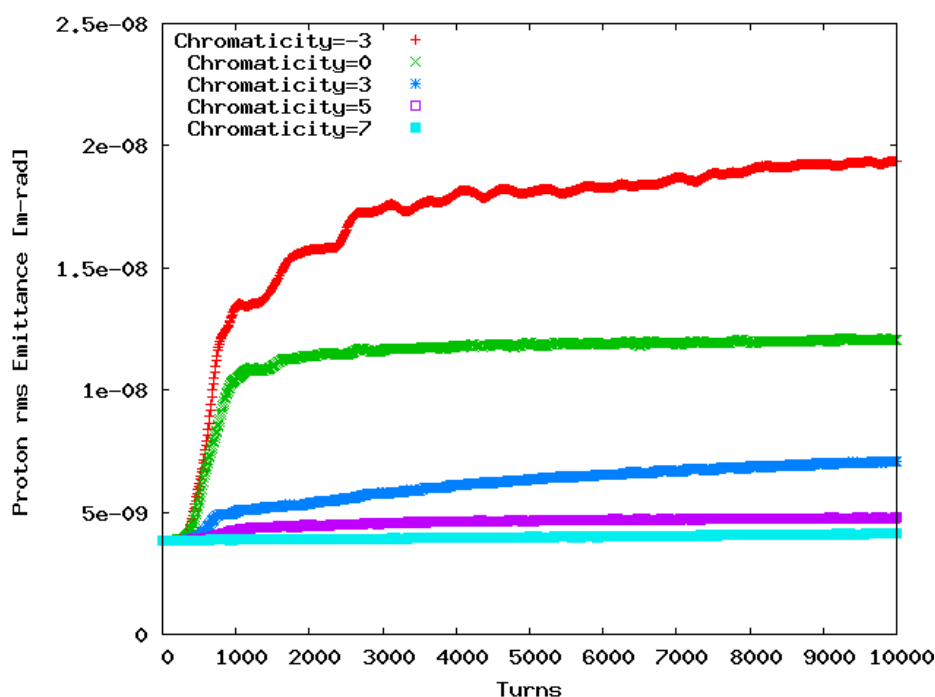


Figure 103: Proton rms emittance growth at different chromaticities with rms energy spread 5×10^{-4} and bunch intensity 2×10^{11} .

Figure 103 shows the effect of the Landau damping, produced by the chromaticity induced tune spread. A negative chromaticity enhances the instability, as we expect for common head-tail instability, while a positive chromaticity does reduce the proton beam emittance growth. The figure indicates that the positive chromaticity of 5-7 can stabilize the proton beam in eRHIC.

In hadron machine operation, the large chromaticity may be unpleasant since the momentum aperture is limited. Even if the large tune spread can be produced by other means, it is always a concern that the nonlinear resonance can slowly deteriorate the beam. To avoid this problem, we consider a feedback system to eliminate the kink instability.

Figure 104 illustrates how the feedback system works. After each collision the orbit offset of the electron beam is measured by a Beam Position Monitor (BPM) and the value of the offset is transferred back to a kicker located before the interaction point.

The next bunch of the electron beam, which collides with the same proton bunch, is kicked by an amount proportional to the measured offset value. The factor, which defines the proportionality, is defined by the strength of the beam-beam interactions, by the location of the BPM and the kicker and by one turn transformation of the proton beam.

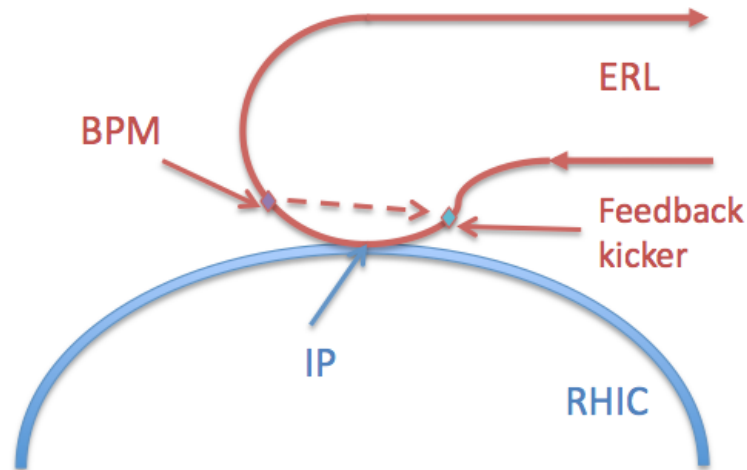


Figure 104: scheme of the feedback system for mitigating the kink instability.

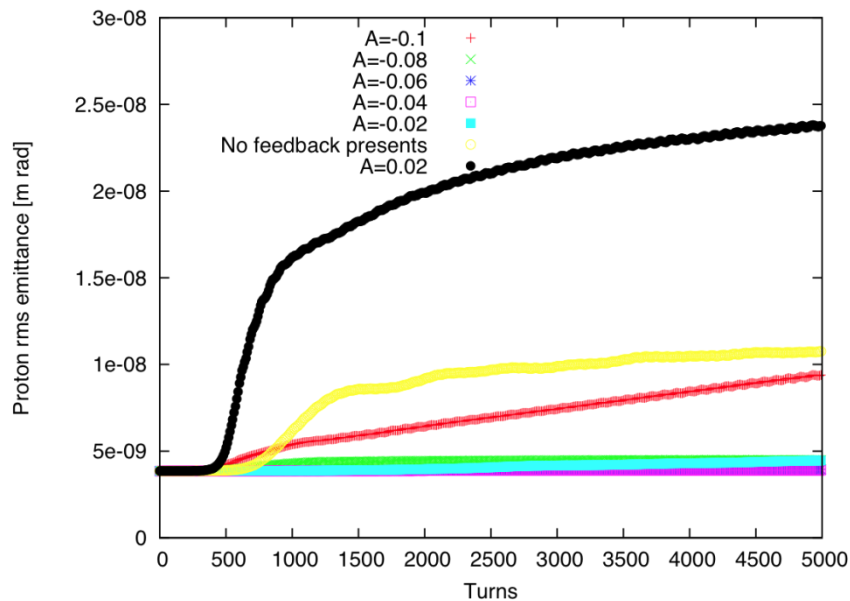


Figure 105: The simulation the kink instability with the state-of-art feedback system.

Figure 105 shows the effect of the described feedback system to damp the kink instability. In the example, an electron bunch initial transverse offset, produced by the kicker, is determined by an offset measured at the BPM, amplified by a predefined factor A . No BPM and kicker errors are assumed to get these results. As expected, the factor A has to be a specific sign (negative in this example). An opposite sign will enhance the instability. The optimum case for stabilizing the beam is $A = -0.04$.

3.13.4 Electron Beam Random Errors

In ERL-based eRHIC, a proton bunch meets millions electron bunches, which have slightly different parameters. The bunch parameter errors, characterizing the deviation of the bunch parameters from mean values, will affect the proton beam via beam-beam interaction [9,10]. Some errors, such as the electron beam intensity error, the rms beam size error affect the beam-beam parameter of the proton beam and can be called quadrupole errors. While other errors, such as the initial transverse position and momentum offsets can be called dipole errors because they lead to an extra kick to the proton beam.

By assuming a white noise spectrum of the electron bunch parameter errors, we can get simple estimation of the random effect on the proton beam. The dipole errors create a random walk motion of protons and ultimately lead to the linear growth of the rms beam size square over time. The growth is proportional to the amplitude of the noise.

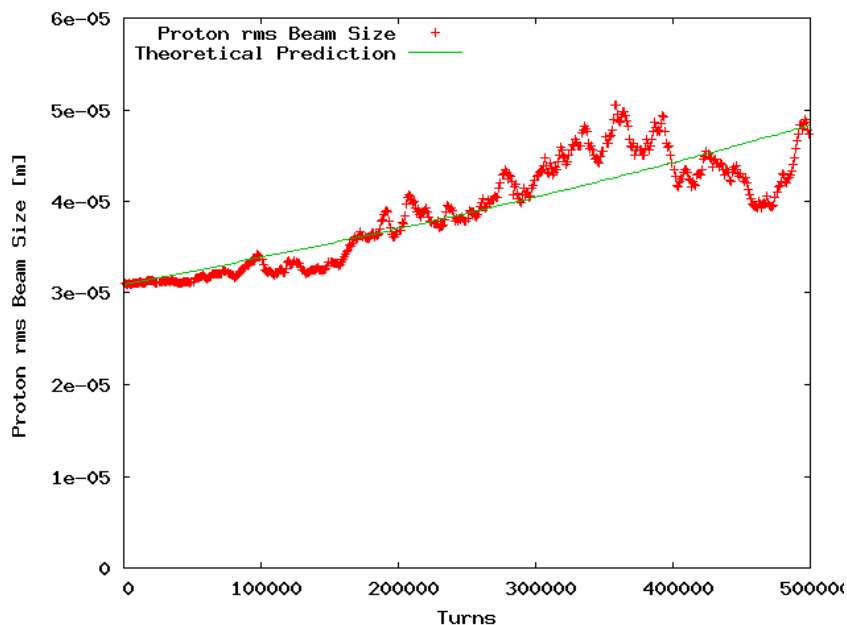


Figure 106: Proton rms beam size evolution at the presence of the electron bunch intensity noise and the comparison with the theoretical anticipation. Each beam size data is the average of 1000 turns.

The effect of quadrupole errors causes the exponential growth of the rms proton beam size. Figure 106 shows an example of simulation done with electron bunch intensity errors. The proton rms size increases exponentially and the result meets the theoretical anticipation. However, the real spectrum won't be a white noise. In general the noise contains more low frequency components. Once the actual frequency spectrum is determined, the detailed simulations will be done to evaluate the effect on the proton beam. The random error studies should provide tolerances on the fluctuations of electron beam parameters at the electron source and on the stability of elements in ERLs and transport lines. The evaluated tolerances and the element stability must be achieved to ensure a reasonable proton beam lifetime.

3.13.5 References

1. V.Ptitsyn, et al., “eRHIC Conceptual Design”, Proceed. of Hadron Beam Workshop, Nashville, WGE01, p.388 (2008).
2. *eRHIC Zeroth-Order Design Report*, M. Farkhondeh and V. Ptitsyn, CA-D Note 142, 2004
3. P. Grosse Wiesmann, Stanford Linear Accelerator Center Report No. SLAC PUB 4545, 1988
4. S. A. Heifets, G. A. Krafft, and M. Fripp, Nuclear Instruments & Methods in Physics Research Section a-Accelerators Spectrometers Detectors and Associated Equipment 295 (1990) 286.
5. Y.Hao, V.Ptitsyn, “Effect of electron disruption in the energy recovery linac based electron ion collider” accepted by PRSTAB (July, 2010)
6. E. A. Perevedentsev and A. A. Valishev, Physical Review Special Topics-Accelerators and Beams 4 (2001)
7. R. Li, et al., in Proceedings of the Particle Accelerator Conference, Chicago, (2001)
8. Y. Hao, et al., in Proceedings of the International Particle Accelerator Conference, Kyoto, Japan (2010)
9. Y. Hao, et al., in Proceedings of the Particle Accelerator Conference, Albuquerque, NM (2007)
10. M. Blaskiewicz, BNL CAD/AP Notes, 363

3.14 Beam-Beam Issues in ELIC

Balša Terzić and Yuhong Zhang, Thomas Jefferson National Accelerator Facility
Mail to: terzic@jlab.org and yzhang@jlab.org

Ji Qiang, Lawrence Berkeley National Laboratory
Mail to: jqiang@jlab.org

3.14.1 Introduction

Over the last decade, Jefferson Lab has been actively pursuing design studies of an electron-ion collider for future nuclear physics research articulated in the most recent Long Range Plan of the DOE/NSF Nuclear Science Advisory Committee [1]. This collider (ELIC), [2], which is based on the existing CEBAF facility, would provide collisions between polarized electrons and polarized light ions or unpolarized heavy ions over a wide CM energy range at multiple interaction points (IP). Recent evolution of science programs and accelerator design iterations guided us toward a staged path, making a low-to-medium energy collider (CM energy up to 51 GeV) an immediate project goal and a high-energy collider (CM energy 100 GeV or higher) a future upgrade option.

The present medium-energy ELIC design features a high luminosity, at the level of $10^{34} \text{ cm}^{-2} \text{ s}^{-1}$ per detector, with the possibility of up to three IPs, by taking full advantage of a high bunch repetition CW electron beam from the upgraded 12 GeV CEBAF recirculated SRF linac, construction of a new ion complex and two new figure-8 shape collider rings. As a design concept, ELIC high luminosity is attained by utilizing high bunch repetition and high average current crab-crossing colliding electron and ion beams with small transverse emittance and short bunch length, and strong final focusing at collision points. Choice of this luminosity concept was motivated by the

remarkable success of two electron-positron colliders – KEK-B and PEP II B-factories – which reached luminosities over $10^{34} \text{ cm}^{-2}\text{s}^{-1}$. In a way, Jefferson Lab is poised to replicate the same success in a collider involving *hadron* beams. The new concept requires the colliding ion beams of ELIC to be very different from all existing or previously operated hadron colliders in terms of bunch charge (very small), bunch length (very short), transverse emittances (very small) and repetition frequency (very high and CW), while, at the same time, it pushes the final focusing parameter β^* to be an order of magnitude smaller than what has been achieved in hadron colliders. To support such a conceptual design, extensive R&D programs have been established at Jefferson Lab, supplemented by several external collaborations.

Since several key parameters of the ELIC ion beam and IR design have been expanded into an unexplored region, in particular, ELIC employs very small (cm or less) β^* to squeeze transverse beam sizes to several μm at collision points, and requiring a moderate (50 to 100 mrad) crab crossing angle due to very high (0.5 to 1.5 GHz) bunch repetition, investigating the beam-beam effect becomes critically important as part of feasibility study of this conceptual design. The sheer complexity of the problem requires us to rely on computer simulations for evaluating this nonlinear collective effect. It is our R&D goal to examine the incoherent and coherent beam-beam effects under the nominal design parameters, to characterize luminosity and operational sensitivities of these parameters as well as to take into account coupling to single particle nonlinear dynamics in the collider rings. In a late phase of this study, we plan further to evaluate beam-beam instability coupled to several other collective beam effects of a similar time scale, such as electron cooling of the colliding ion beam, and, at low ion energy, the space charge. This work is partially supported by a DOE SciDAC grant and as a collaboration with the Accelerator Modeling and Advanced Computing Group of the Center for Beam Physics at LBNL.

3.14.2 Simulation Model, Code and Scope

From the simulation standpoint, a ring-ring beam-beam study can be divided into two naturally distinct parts: tracking of particle collisions at IPs, and transporting beams through collider rings. These two parts are usually modeled differently to address different physics mechanisms and characteristic timescales. At the present stage, our attention is focused on disruption of colliding beams by nonlinear beam-beam kicks and induced luminosity reduction. Tactically, we simplify beam transport in the rings by ideal linear mappings plus synchrotron radiation damping and associated quantum fluctuations of electrons, effectively omitting rich and important single and collective effects in the rings, in order to extract maximum information about the pure beam-beam effect through the most detailed tracking within the current computer capability. This idealized physics model is in a so-called strong-strong regime in which both colliding beams can be disrupted by the beam-beam kicks. On the computational level, colliding bunches are modeled by groups of macroparticles interacting with each other through nonlinear beam-beam kicks calculated using the standard particle-in-cell method.

The simulation code utilized in the present ELIC study is BeamBeam3D, a self-consistent code developed at LBNL which solves the Poisson equation for electromagnetic fields using the shifted integrated Green function method over a 2D mesh for a number of longitudinal slices [3]. The code has been benchmarked against other beam-beam codes and experimental data with reasonable success [4]. A numerical

test indicated that a 64×128 transverse mesh and 20 slices are sufficient to produce converged results with minimum 200,000 macroparticles for each colliding bunch. With these run parameters, a typical production run for tracking two colliding bunches and a single IP over 10,000 turns in the ring (corresponding to roughly 0.1 seconds storing time, and approximately 10 to 12 electron damping times) usually takes about several hours of wall clock time on a 64 CPU cluster of a NERSC supercomputer or the JLab LQCD parallel computer, as a consequence defining the scope of the simulations. It should be acknowledged that while our ELIC simulations should reveal short-term (fractions of a second) dynamics under repeated particle collisions, they could not be used to predict long-term (minutes or longer) beam behaviour.

3.14.3 Simulation Results

We have completed two ELIC beam-beam simulation studies: one for an early ELIC design with a higher CM energy (7 GeV electron to 150 GeV proton), and the other for the present medium-energy (5 GeV electron to 60 GeV proton) version of ELIC. These two studies are very similar in scope, starting with simulations using nominal design parameters with a synch-betatron tune working point selected empirically, followed by a luminosity scan against the current of one of the two colliding beams in order to explore both limits of design parameters and threshold values for the onset of coherent beam-beam instabilities. Both studies also present very similar simulation results. An empirical search for a better working point in the two dimension betatron tune space was also commenced, assisted by examination of the footprints in the tune space. For the first study, in addition to the single IP case, simulations for a system of four collision points and two subsets of 12 bunches were also performed to examine the influence of coupling of multiple bunches through multiple IPs on the beam-beam effect. Details of these two studies were documented in two PAC and IPAC papers [5,6]. Here we only present a brief summary of some of the main results.

3.14.3.1 *Luminosity Trends for Normal Design Parameters*

With a fair working point, ELIC luminosity settles on an equilibrium value of about 50% of the design value (including 25% loss due to the hourglass effect for the case of high energy ELIC) after an initially rapid decay usually within one electron damping time. The saturated luminosity is highly sensitive to choice of the betatron tune working point, as is readily seen from the relative position of the beam footprint in the tune map. The reduction of luminosity, apart from the hourglass effect, is primarily due to large degradation of the vertical emittance of the electron beam, indicating that the flat electron beam (with emittance aspect ratio 25 at 7 GeV) is a relatively weak beam. A troubling observation is that there is a very slow decay of luminosity, indicating an unknown underlying physical process with a time scale on the order of few seconds or longer, which is far beyond scope of this simulation study. It should be noted that planed electron cooling of ion beams in the ELIC design will indeed introduce a damping mechanism with a damping time in order of several seconds, and therefore will very likely, pending further simulation studies, suppress this slow drift of luminosity and deliver stable collider operation.

3.14.3.2 *Luminosity Dependence on Beam Current*

The simulations show that in the region near the ELIC nominal design, luminosity increases almost linearly as the current of each beam is increased, one at a time. For example, as the proton currents are increased, the vertical RMS size of the electron beam also increases, while the horizontal RMS size of the electron beam and both transverse RMS sizes of the proton beam remain the same. When a current is increased far beyond the design values of either proton or electron beams, nonlinear beam-beam interactions start to dominate, causing a notable slowdown of luminosity increase, and eventually breakup of the beams. The fact that the linear region of beam currents is very large, up to a factor of three over the design current (1 A and 2.5 A for proton and electron, respectively, for the high energy ELIC case), does not mean we can immediately take advantage of increasing design beam currents to harvest a much higher luminosity. It is not only that the stored beam currents are limited by other effects in the ring such as allowable total synchrotron radiation power for the electron beam, but also by the fact that our simulations are based on a simplified model which has already excluded nonlinear single particle dynamics in the ring and other coupled collective effects. The main result from these numerical simulations is that the limit of current in ELIC colliding beams due to the *pure* beam-beam effect alone is very large. Including in the simulation the coupling to nonlinear beam dynamics and other collective effects could change the situation significantly; this will be addressed in the next stage of the ELIC beam-beam studies.

3.14.3.3 *Coherent Beam-Beam Instability*

The coherent beam-beam instability – a coherent oscillation of particle distribution of colliding beams – was observed for the high-energy ELIC collider when the electron current is increased to three times its design value. Further increase of the beam current leads to beam blow-up. For the medium-energy ELIC, the coherent beam-beam instability was not observed, even when the electron and proton beam currents were increased four and six times their design value, respectively.

3.14.3.4 *Multiple Interaction Points*

The ELIC design supports collisions at multiple IPs. Attempts have been made to evaluate the additional bunch-to-bunch coupling brought by multiple IPs. Taking advantage of a symmetric layout of the figure-8 shape collider rings and assuming certain integer ratio of the IP-to-IP distance over the ring circumference, the simulated system can be reduced into two coupled sets of small number of bunches, one set from each beam, leading to significant computational savings. For the high-energy ELIC, simulations demonstrate that luminosity in the case of four IP operation behaves very much like the case of the single IP, with equilibrium luminosity per IP nearly identical to the single IP luminosity. We can conclude that multiple bunch and multiple IP couplings do not amplify the old beam-beam instability nor introduce any new coherent instability at least for this set of ELIC design parameters.

3.14.3.5 *Locating Optimal Working Point Using an Evolutionary Algorithm*

It is well known that the beam-beam effect and collider luminosity are sensitive to synchro-betatron resonances of the two colliding beams. Therefore, careful selection of

a tune working point is essential for successful operation of a collider as well as for achieving high luminosity. A systemic method of searching a good working point is certainly preferable to empirical methods, which are traditionally used. A brute-force scan of the 4D (betatron tunes only for the two colliding beams) or 6D (also including synchrotron tunes) parameter space is computationally prohibitive, which is why we turned to other advanced searching algorithms. To that end, we implemented an evolutionary algorithm, similar to what was used in a photoinjector design [7]. The objective function here is the collider's luminosity, computed by the BeamBeam3D code, and subject to constraints of the independent variables – in this case the four betatron tunes. The algorithm traverses only relatively small regions of the parameter space devoid of resonance lines, and has located excellent working points which reach very close to (and sometimes even exceed) the design luminosity [8]. This automation of the search for the working point is a valuable tool for numerical optimization of the collider's performance.

3.14.4 Discussion and Outlook

There are several outstanding issues we would like to address in the future beam-beam simulation studies of ELIC. The first issue is improving the simulation model by including nonlinear dynamics in the collider ring and taking into account such complications as chromatic effect and imperfect magnets, which will require expansion of scope of simulation both in the complexity and execution time. The next issue is examining the effect of several unique features of ELIC IR design on the beam-beam problem, most important among which is a crab crossing of the colliding beams enabled by high integrated-voltage SRF crab cavities. The third issue is assessing the effect of coupling between beam-beam and other collective phenomena. Two of such coupling effects are of particular interest: a damping mechanism associated with electron cooling of ion colliding beams, and, at very low energy, the ion space charge effect. The former effect should help stabilize the ion beam and improve collider performance, while the latter should add coupling between different slices of colliding bunches at and near collision points, thereby presenting a tremendous challenge to the computational algorithm and capability.

On the methodology level, we will consider using both strong-strong and weak-strong simulation regimes to yield answers for questions associated with different time and particle scales. The strong-strong self-consistent code enables the study of the beam-beam physics alone to a high precision, but only limited complexity of the underlying model. At the price of sacrificing the self-consistency of the model, the much-faster strong-weak simulations can enable the study of the long-term beam-beam behavior of ELIC. Ultimately, our goal for beam-beam studies is to ensure the validity of the ELIC conceptual design as well as of the design optimization.

3.14.5 References

1. The Frontiers of Nuclear Science: A Long Range Plan, U.S. Department of Energy and U.S. National Science Foundation (2007).
2. S. A. Bogacz, *et al.*, proceedings of the 2008 European Particle Accelerator Conference, Genoa, Italy, P2632 (2008).
3. J. Qiang, M. A. Furman and R. D. Ryne, Phys. Rev. ST: Accel. Beams, 5, 104402 (2002).

4. E. Stern *et al.*, proceedings of the 2007 Particle Accelerator Conference, Albuquerque (2007).
5. Y. Zhang and J. Qiang, proceedings of the 2009 Particle Accelerator Conference, Vancouver, Canada (2009).
6. B. Terzić and Y. Zhang, proceedings of the 2010 International Particle Accelerator Conference, Kyoto, Japan (2010).
7. I. V. Bazarov and C. Sinclair, Phys. Rev. ST: Accel. Beams, 8, 034202 (2005).
8. B. Terzić, M. Kramer and C. Jarvis, in preparation (2010).

3.15 Beam-Beam Issues in the ILC and in CLIC

D. Schulte and R. Tomas, CERN, CH-1211 Geneva 23, Switzerland

Mail to: Daniel.Schulte@cern.ch

3.15.1 Introduction

In future linear colliders, beam-beam effects are of critical importance. They limit the achievable luminosity and strongly impact the choice of fundamental machine parameters, e.g. the crossing angle at the interaction point or in case of CLIC the design of the accelerating structure. During the beam collisions background particles are produced that impact the design and performance of the detectors.

In this paper we will remind the reader of the relevance of the beam-beam effects for the machine design and show how they impact the optimisation of the specific luminosity in ILC and the parameter choice in CLIC. We will discuss the difficulties in the beam delivery system to achieve and maintain small beam sizes and the importance of ATF2. The need to produce luminosity at lower than nominal energy is an important concern for ILC and CLIC, we will briefly discuss the consequences. Finally we will remind the reader of the beam-beam background and mention some new developments of the simulation codes.

3.15.2 ILC Optimization

The GDE [25] currently attempts to reduce the cost of the International Linear Collider (ILC) to make funding more likely. One of the cost reduction options that have been considered is to reduce the total charge per beam pulse, while the pulse length remains basically unchanged. In this case, the beam will extract only half the RF power from the klystrons. This allows one to reduce the number of klystrons. In order not to compromise the luminosity target, the specific luminosity has been increased. The trade-off between cost reduction and increase in risk is still being debated, we will not comment on this here. However, the increase of specific luminosity is of great interest and one can take advantage of it independent of the RF power chosen. In the following we will briefly discuss the consequences for the machine.

Table 14: ILC parameters under discussion for several energies. Official RDR values existed for 500 GeV, other parameters have been educated guesses from individual experts. The proposed SB2009 values are with travelling focus (TF) and without. The table is copied from [6].

	RDR			SB2009 w/o TF				SB2009 w TF			
CM Energy (GeV)	250	350	500	250.a	250.b	350	500	250.a	250.b	350	500
Ne- (*10 ¹⁰)	2.05	2.05	2.05	2	2	2	2.05	2	2	2	2.05
Ne+ (*10 ¹⁰)	2.05	2.05	2.05	1	2	2	2.05	1	2	2	2.05
Nb	2625	2625	2625	1312	1312	1312	1312	1312	1312	1312	1312
Tsep (nsecs)	370	370	370	740	740	740	740	740	740	740	740
F (Hz)	5	5	5	5	2.5	5	5	5	2.5	5	5
γ _x (*10 ⁻⁶)	10	10	10	10	10	10	10	10	10	10	10
γ _y (*10 ⁻⁸)	4	4	4	3.5	3.5	3.5	3.5	3.5	3.5	3.5	3.5
β _x (mm)	22	22	20	21	21	15	11	21	21	15	11
β _y (mm)	0.5	0.5	0.4	0.48	0.48	0.48	0.48	0.2	0.2	0.2	0.2
σ _z (mm)	0.3	0.3	0.3	0.3	0.3	0.3	0.3	0.3	0.3	0.3	0.3
σ _x eff (*10 ⁻⁹ m)	948	802	639	927	927	662	474	927	927	662	474
σ _y eff (*10 ⁻⁹ m)	10	8.1	5.7	9.5	9.5	7.4	5.8	6.4	6.4	5.0	3.8
L (10 ³⁴ cm ⁻² s ⁻¹)	0.75	1.2	2.0	0.2	0.22	0.7	1.5	0.25	0.27	1.0	2.0

3.15.2.1 Luminosity

In linear colliders the beams need to be focused to very small size at collision in order to obtain high luminosity. The electro-magnetic fields of the bunches therefore become very strong and focus the oncoming bunch during the collision. This focusing is described conveniently with the help of the so-called disruption parameters D_x and D_y , which are the ratio of bunch length to the focal length of the beam for a small beam-beam force.

$$D_{x,y} = \frac{2Nr_e\sigma_z}{\gamma\sigma_{x,y}(\sigma_x + \sigma_y)}$$

Here, N , is the number of particles per bunch, γ is the relativistic factor of the beam, and r_e is the classical electron radius. Usually one chooses $D_x < 1$ and $D_y \gg 1$. For $D \ll 1$ the beam can be treated as a thin lens that kicks the particles of the other beam towards the centre. For $D \gg 1$ the particles of each beam start to oscillate in the field of the oncoming bunch. The luminosity can be expressed as

$$L = H_D \frac{N^2}{4\pi\sigma_x\sigma_y} n_b f_r$$

Here, n_b is the number of bunches per beam pulse and f_r the repetition rate of beam pulses. H_D is the so-called luminosity enhancement factor, which results from the reduction of the beam sizes during collision due to the strong forces. This parameter is typically in between one and two. The luminosity can be written in a form that makes the dependence on specific luminosity and beam current more explicit:

$$L = H_D \frac{N^2}{4\pi\sigma_x\sigma_y} n_b f_r \propto \frac{N}{\sigma_x} \frac{1}{\sigma_y} N n_b f_r$$

In order to increase the luminosity for a given beam power one has to increase either N/σ_x or decrease σ_y . As is well known the first choice changes the quality of the

luminosity delivered while the second option has a strong impact on the beam-beam collision dynamics and tolerances.

3.15.2.2 *Beamstrahlung*

During the collision the two beams will emit beamstrahlung. This will lead to the development of a luminosity spectrum rather than a sharp peak at the nominal centre-of-mass energy. In the classical limit, which is applicable to the ILC, the number of beamstrahlung photons emitted per beam particle can be approximated as

$$n_\gamma \approx 2.1 \cdot \alpha \frac{Nr_e}{\sigma_x + \sigma_y}$$

Here, α is the fine structure constant. The average photon energy can be written as

$$\frac{E_\gamma}{E} \approx 0.385 \frac{N\gamma_e^2}{\alpha(\sigma_x + \sigma_y)\sigma_z}$$

Assuming $\sigma_x \gg \sigma_y$, one can rewrite the luminosity as a function of the beamstrahlung photon number

$$L \propto H_D n_\gamma \frac{1}{\sigma_y} N n_b f_r$$

Decreasing the horizontal beam size at the collision point leads to more luminosity but to a degradation of the luminosity spectrum. Hence, the suggested modification of the horizontal beam size for ILC corresponds to a different choice for the luminosity spectrum quality; some reduction of the quality is the price to be paid for higher luminosity per beam particle. With the SB2009 parameters the number of photons emitted per beam particle will go up from ≈ 1.4 to ≈ 1.9 . The spectra are shown in Figure 107. Also the spectrum for the SB2009 parameters is shown with a reduced bunch length of 200 μm , which leads to the emission of ≈ 1.8 photons.

3.15.2.3 *Disruption and Travelling Focus*

Another possibility to push the specific luminosity is to decrease the vertical beam size, which can be done by either reducing the vertical emittance or beta-function. Smaller emittances are more difficult to generate and for the vertical beta-function an optimum exists. The smaller the beta-function the smaller the waist of the beam, but the faster the beam size rises around the waist. It should be noted that the highest luminosity is not reached if the two waists of the beams are at the same location but if the beams are focused slightly before the actual centre of the collision. In Figure 108 the dependence of luminosity on waist position is shown for a number of different values of the vertical beta-function. The optimum is obtained by roughly focusing one RMS bunch length before the collision point. The maximum luminosity as a function of the beta-function is shown in Figure 108. One can conclude that the optimum vertical beta-function is about 0.2 mm, in which case the luminosity is 15% higher than for the SB2009 parameters.

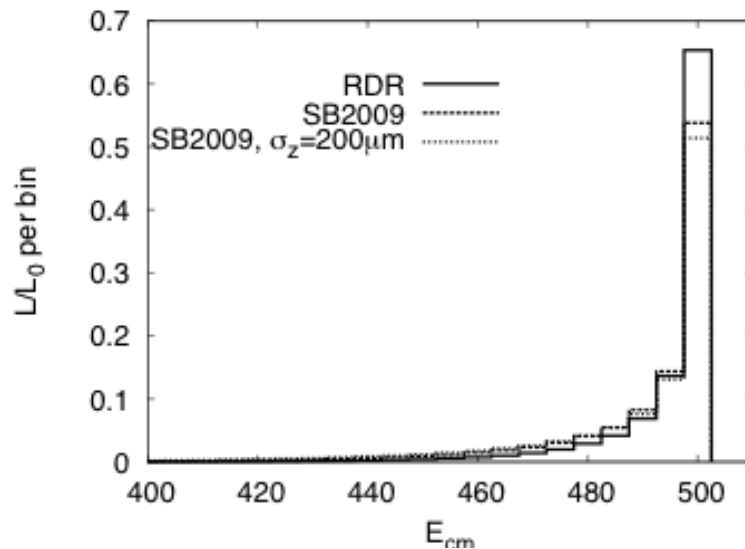


Figure 107: The luminosity spectrum for the RDR parameters and SB2009. The difference between the case with and without travelling focus is very small. Also a modified SB2009 set is shown in which the bunch length is reduced to 200 μm . The average energy loss of the beam particles is 2.6, 4.6 and 5.5%, respectively.

One option to further increase the luminosity is the use of the so-called travelling focus. In the normal focusing scheme all longitudinal slices of the beam are focused to at one longitudinal position. In the travelling focus scheme the focal point for the different slices is at different longitudinal positions. Usually the position to which a given slice is focused is chosen to coincide with the collision of that slices with a specific slices of the other beam. So each slice will have its smallest size in the very moment when it collides with this one specific slice of the other beam. The focusing beam-beam force will then keep the size of this slice small. Usually the focal point is $1.7 \sigma_z$ before the centre of the oncoming bunch. In case of a travelling focus, the optimum waist position is close to the centre of the collision. The maximum luminosity as function of beta is shown in Figure 108. The overall maximum is about 10% higher than without travelling focus.

One should note that the numbers from the Table 14 and this simulation are slightly different. The simulations presented here have been performed with very high statistics to limit the impact of random fluctuations.

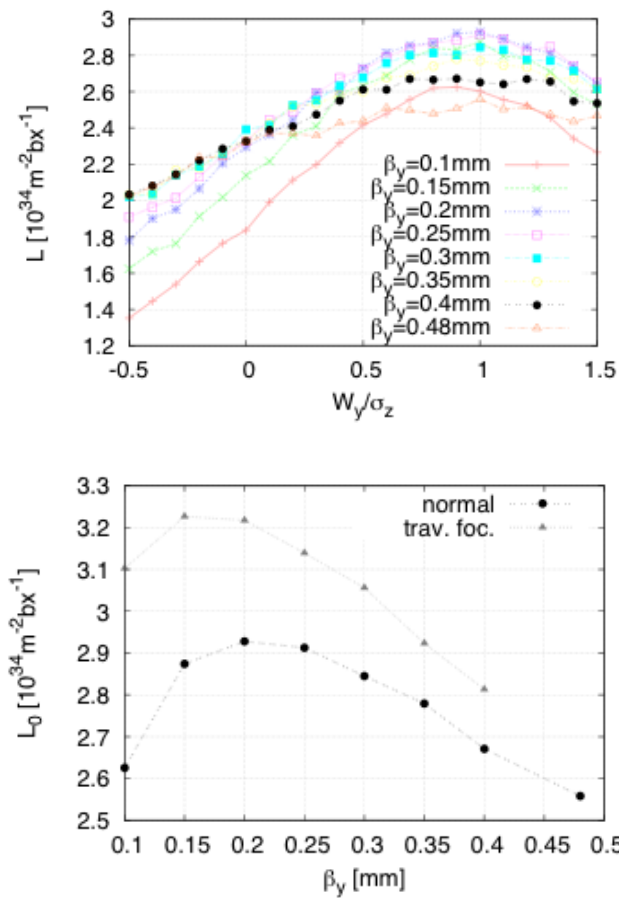


Figure 108: The luminosity per bunch crossing as a function of the longitudinal position of the vertical waist (top). The luminosity as a function of the vertical beta-function for the case with travelling focus and with no travelling focus (bottom).

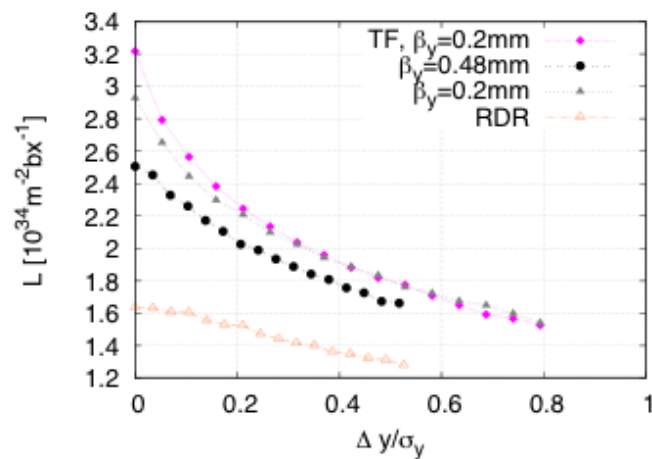


Figure 109: The luminosity as a function of the vertical beam-beam offset for the different parameter sets. The SB2009 parameters with travelling focus (TF) and without ($\beta_y = 0.48$ mm) are shown, together with the RDR nominal case. Also the luminosity for the SB2009 parameters with no travelling focus is shown for a reduced beta-function ($\beta_y = 0.2$ mm).

The price to pay for the higher specific luminosity is that the collision is less stable due to the larger disruption parameter. We can reformulate the luminosity as a function of bunch length and vertical disruption parameter [2]:

$$L \approx H_D D_y 1.74 \cdot 10^{34} \text{ cm}^{-2} \text{ s}^{-1} \frac{\mu\text{m}}{\sigma_z} \frac{P_{\text{beam}}}{\text{MW}} \propto \frac{D_y}{\sigma_z} N n_b f$$

From this it is easy to conclude that one either needs to decrease the bunch length or to increase the disruption parameter to achieve higher specific luminosity. In Figure 109 the luminosity of the beam-beam offset is shown for different cases. As can be seen, the luminosity drops faster if the specific luminosity is higher. Consequently, the beam-beam jitter will have a larger impact on luminosity, in particular the jitter from bunch to bunch, since it cannot be corrected using an intra-pulse feedback. The overall gain from the smaller beam size at the collision point can thus be reduced.

Also small offsets of the individual slices of the beams, e.g. due to wakefields or dispersion, can lead to large luminosity loss via the so-called banana effect [1]. But the beam emittance remains a good measure for the luminosity, if the collision offset and angle between the two beams is optimised [2]. This is illustrated in Figure 110 for the case of TESLA.

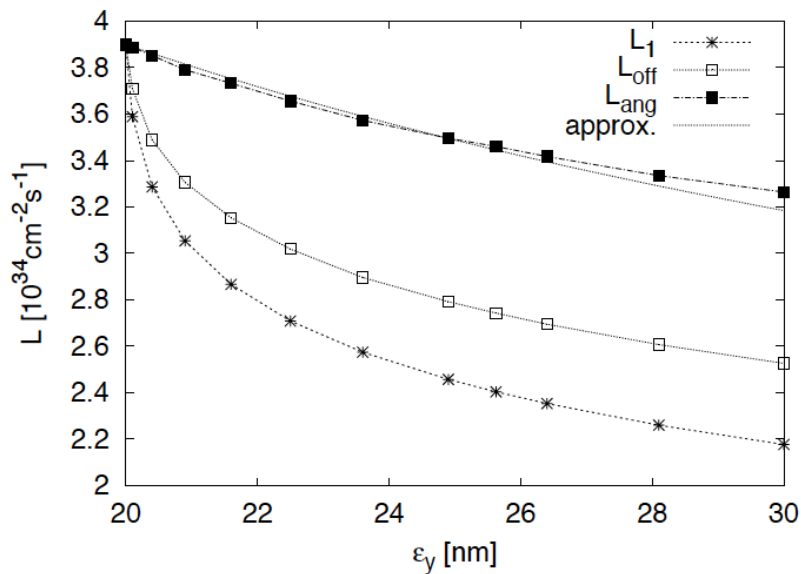


Figure 110: The luminosity as a function of the vertical beam emittance calculated for TESLA taken from [2]. The slice emittance is 20 nm and the total emittance is given by the combination of the slice emittance and a scattering of each slice with respect to the others. For the curve labeled L_1 only the mean offset and beam angle are corrected. For the curve L_{off} the offset has been optimized for luminosity and for L_{ang} also the beam angle has been optimized for luminosity. The comparison with the approximate formula $L \propto 1/\sqrt{\epsilon_y}$ shows that the emittance is a good measure for the luminosity even in case of strong disruption when full optimization can be performed.

In summary, it appears in principle possible to further push the specific luminosity of ILC. This will lead to a tightening of the tolerances in particular for dynamic effects. Failure to achieve the tighter specifications would reduce the luminosity gain to some extent. Hence further study will be needed on this very interesting and important subject

to come to a detailed conclusion. In particular a reduction of the bunch length could help to reduce the sensitivity to beam offsets.

3.15.3 CLIC Optimization at 3 TeV

We have performed a complete parameter optimisation for CLIC, see ref [4,5]. In this optimisation the beam-beam interaction played a central role and connected the choice of main linac accelerating structure to the damping ring and beam delivery system design.

CLIC operates in the regime of non-classical beamstrahlung. As a consequence the expression for the luminosity changes compared to the classical ILC case:

$$L = \frac{0.024}{\alpha^2} n_\gamma^{\frac{3}{2}} \frac{\sqrt{\gamma}}{\sqrt{\sigma_z r_e}} \frac{1}{\sigma_y} N n_b f_r$$

Table 15: CLIC parameters at different beam energies [4].

Parameter	Symbol	Value	Unit
Beam Delivery System + IP			
Total diagnostic section length	l_{coll}	2x 0.37	km
Total collimation system length	l_{coll}	2x 1.92	km
Total final Focus system length	l_{FF}	2x 0.46	km
Input transverse horizontal emittance	ε_x	660	nm rad
Input transverse vertical emittance	ε_y	20	nm rad
Nominal horizontal IP beta function	β_x^*	6.9	mm
Nominal vertical IP beta function	β_y^*	0.068	mm
Horizontal IP core beam size	σ_x^*	45	nm
Vertical IP core beam size	σ_y^*	0.9	nm
Bunch length	$\sigma_{s,\text{inj}}$	44	μm
Initial RMS Energy spread	$\sigma_{\Delta E/E}^*$	0.29	%
Total Energy spread		1	%
Crossing angle at IP	θ_C	20	mrad
Beamstrahlung mom. spread	δ_B	29	%
No. of photons / electron	n_γ	2.2	
No. of coherent pairs / bunch crossing	N_{coh}	38	10^7
No. of incoherent pairs / bunch crossing	N_{incoh}	0.03	10^7
Hadronic events / crossing	N_{hadron}	2.7	
Total luminosity	L_{pk}	6.0	$10^{34} \text{cm}^{-2} \text{s}^{-1}$
Luminosity (in 1% of energy)	$L_{99\%}$	2.0	$10^{34} \text{cm}^{-2} \text{s}^{-1}$

The number of photons needs to be limited in CLIC since we require that the luminosity spectrum is acceptable. The criterion used is to impose $L_{0.01}/L > 0.3$. The main parameters in this formula are determined by different CLIC sub-systems:

- The bunch charge and length are mainly a function of the linac design.
- The horizontal emittance is mainly a function of the damping ring performance, with some contributions from other systems.

- The vertical emittance depends on damping ring and the transport from the damping ring to the interaction point.
- The effective vertical and horizontal beta-functions are a function of the final focus system.

First, we will discuss the bunch charge limitation. The short-range longitudinal wakefield introduces an energy spread in the bunch, since the head of the bunch generates a field that decelerates the tail. We partly compensate this effect with the help of the accelerating RF field. This field is oscillating as a cosine in time. We let the bunch arrive shortly before the field reaches the maximum. This accelerates the tail slightly more than the head. This is obviously more efficient if we have a longer bunch and if we are further of the crest of the RF. Our target is to achieve less than 0.35% RMS energy spread at the end of the main linac by running at an average phase of 12° before the maximum field, to not compromise the accelerating field and the efficiency too much. For a given longitudinal wakefield, bunch charge and gradient one can now determine the bunch length that fulfils our constraints. This allows us to define $\sigma_z(N)$.

The transverse single bunch wakefield is now defining a unique value of N. In order to avoid beam break-up and in order maintain the vertical beam emittance during transport in the main linac, the transverse wakefield kick exerted by the head of the bunch on the tail needs to be limited. The limit depends on the lattice design, we use the design that we have previously optimised to allow the largest wakefield kicks. As a figure of merit to select the bunch charge we use $N W_T(\sigma_z(N)) = \text{const.}$

Using the luminosity formula, one can see that the horizontal beam size is a function of the bunch charge, if we want to obtain a certain luminosity spectrum. Usually the beam size would be expressed as $\sqrt{\epsilon_x \beta_x / \gamma}$, but at the CLIC energy the final focus system shows strong non-linearities and synchrotron radiation effects. Therefore full tracking of the beam is required.

The horizontal emittance is mainly dominated by the lattice design. Using strong wigglers one can hope to achieve the CLIC target of 500 nm in the horizontal plane, which should lead to 660 nm at the interaction point. Since the emittance depends to a large extent on collective effects, it will actually also depend on the bunch charge. The vertical emittance is determined by using optimised designs for the damping ring, the ring to main linac transport and the main linac. Realistic imperfections have been taken into account.

In a similar fashion the final focus system has been optimised to achieve the smallest possible spot size at the interaction point, as will be detailed below. The minimum horizontal beam size that is achievable has been found to be equivalent to a Gaussian with an RMS of about 40nm. The matching bunch charge that satisfies the criterion for the luminosity spectrum quality is about 4×10^9 particles. For smaller bunch charges the specific luminosity will suffer. Above this value the horizontal beam size needs to be increased above the minimum.

In the described fashion, the damping ring horizontal emittance and limitations from the final focus system design drive the accelerating structure choice for the CLIC main linac via the beam-beam interaction.

3.15.4 Final Focus Design Issues and ATF2

Achieving the CLIC IP beam sizes requires such a strong focusing, see Refs. [7,8], that its associated natural chromaticity surpasses that of any other existing project. To cancel this chromaticity without generating severe geometrical aberrations sextupoles, octupoles and decapoles are used and optimized as described in Ref. [8]. Consequently we should expect some limitations in the achievable IP beam sizes and also in the transverse density distribution at the IP. Basically, the residual geometrical aberrations plus the synchrotron radiation emitted at dipoles and quadrupoles deform the incoming Gaussian beam and modify the beam-beam interaction and its effects. In order to optimize the beam parameters it is critical to simultaneously consider the lattice transport and the beam-beam interaction.

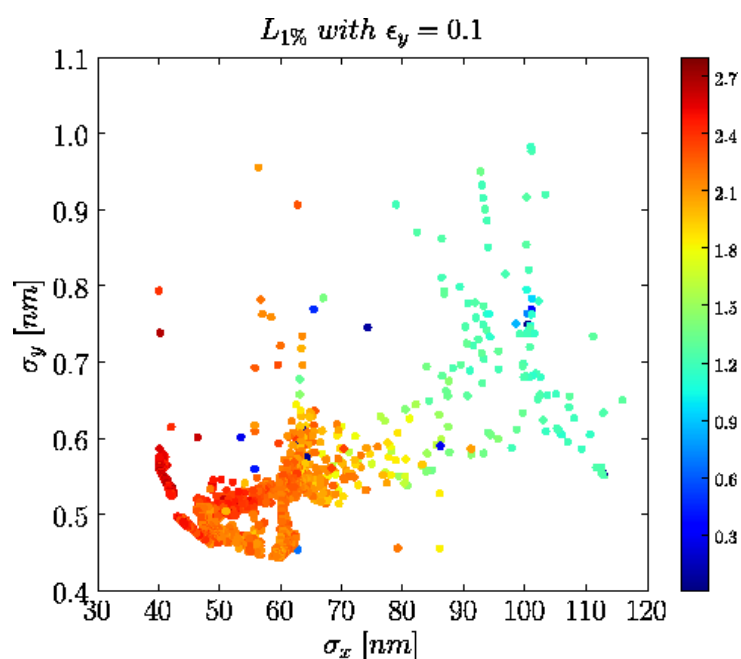


Figure 111: The luminosity in the 1% energy peak versus horizontal and vertical IP beam sizes during the Simplex optimization.

Figure 111 shows the luminosity in the 1% energy peak as function of the horizontal and vertical IP beam sizes as computed during the first stages of the FFS optimization procedure. More details of this optimization can be found in Ref. [9]. The last step of the optimization consisted in reducing the dispersion along the FFS to decrease the effects of synchrotron radiation. This clearly reduced the horizontal beam size at the IP, see Figure 112, and the total luminosity for the two bunch lengths under consideration (34 and 44 μm).

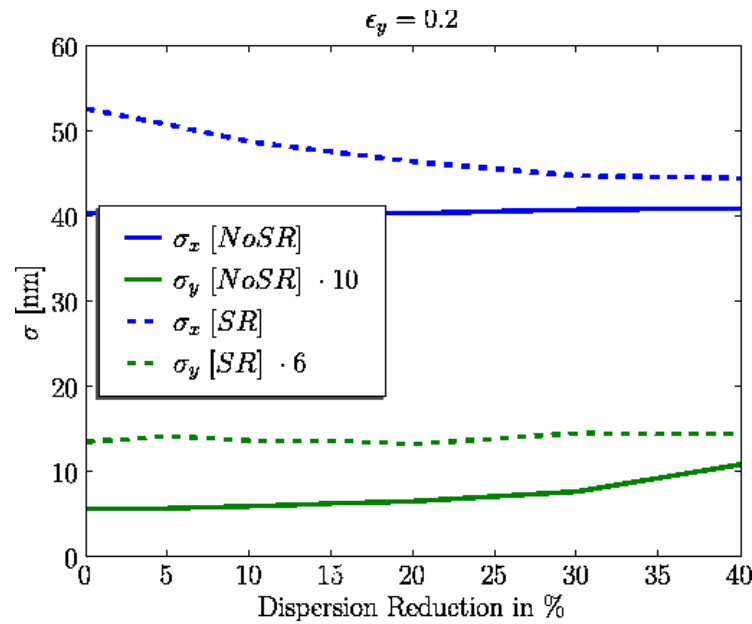


Figure 112: Horizontal and vertical IP beam sizes with and without synchrotron radiation as dispersion is being reduced in the FFS with the subsequent increase of the sextupole strength.

However it is remarkable that the luminosity in the 1% energy peak was not increased for the longer bunch with $\epsilon_y = 20$ nm, see Figure 113. This led to the conclusion that for this longer bunch and $\epsilon_y = 20$ nm the luminosity in the 1% energy peak has a maximum between RMS beam sizes of $\sigma_x = 40$ nm and $\sigma_y = 50$ nm. From previous beam-beam considerations using Gaussian beams in Ref. [10], this saturation is expected at around $\sigma_x = 30$ nm for a vertical emittance of 10 nm as shown in Figure 114.

It is reassuring that full lattice optimizations lead to results consistent with ideal beam-beam simulations. However during the lattice optimization, see Figure 111, the $\sigma_x = 30$ nm is clearly not accessible for the current CLIC FFS and the energy peak luminosity saturates for slightly larger horizontal beam sizes. This illustrates how the lattice transport can pose limitations and affect the beam-beam interaction. In practice the most serious challenge that the CLIC FFS will face is the realization of the small beam sizes in the presence of imperfections. This is discussed in the following.

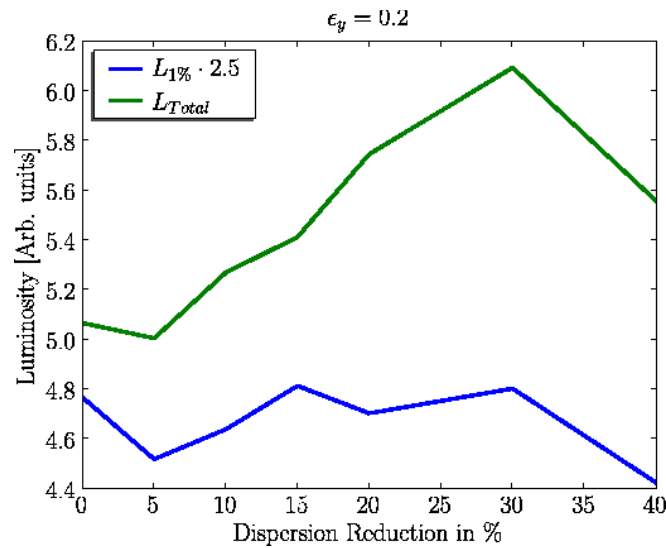


Figure 113: Total luminosity and luminosity in the 1% energy peak as dispersion is being reduced in the FFS with the subsequent increase of the sextupole strength. The horizontal beam size reduction increases the total luminosity but not the luminosity in the energy peak.

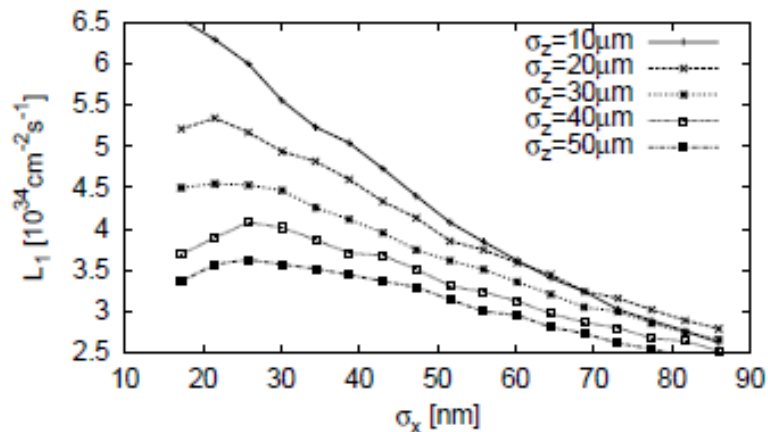


Figure 114: Luminosity in the 1% energy peak versus the horizontal IP spot size for various bunch lengths from Ref. [10]. The current CLIC bunch length is 44 μm . For this case a maximum of the luminosity is observed around 30 nm horizontal beam size.

3.15.4.1 Final Focus System Tuning

The CLIC FFS is extremely sensitive to imperfections. Few nanometres displacements of some elements lead to a luminosity loss in the percent level even after correcting the collision offset at the IP. The feasibility demonstration of the CLIC FFS via realistic simulations and experiments is critical for the CLIC study. For the experimental part an R&D proposal was submitted to ATF2 in KEK, see Ref. [11], where the ATF2 IP beta functions are reduced by a factor four to reach CLIC-like chromaticities. This proposal has been accepted as the natural continuation of ATF2 after it reaches its design goal of $\sigma_y = 37$ nm, probably by the end of 2010. The measured skew multipolar component of some ATF2 magnets is already posing limitations in the achievable beam sizes and alternative optics with relaxed horizontal parameters are under consideration, see Ref. [12].

Computer simulations should demonstrate that after introducing realistic errors in the FFS lattice there is a 90% probability that a tuning procedure would increase the luminosity to up to 90% of the design luminosity. Currently the CLIC FFS tuning simulations show 80% probability of reaching 80% of the luminosity. So far only the Simplex algorithm has proved successful using the luminosity as figure of merit and all the lattice parameters as variables. The high complexity and non-linearity of the CLIC FFS seriously limits the applicability of pre-designed tuning "knobs" and BPM-based alignment procedures. A large effort is presently being carried out to understand the limitations of the FFS tuning and develop improvements to reach the desired performance.

3.15.4.2 *Background Optimization*

In ILC it was demonstrated that an Anti-DiD magnetic configuration, see Ref. [13], can reduce the background by allowing the outgoing beams to travel closer to the magnetic field lines. A minor luminosity loss was observed. CLIC features higher energy beams and a larger crossing angle (20 mrad). An Anti-DiD magnetic configuration in the CLIC detector causes a 25% luminosity loss and therefore this has been discarded, Ref. [14].

3.15.5 Luminosity Operation at Lower than Nominal Energies

3.15.5.1 *ILC*

For the operation of ILC at lower than nominal energies, a set of basic parameters has been developed, see the SB2009 parameters in Table 14. Two solutions exist, one with and one without the travelling focus scheme. A specific problem of ILC is that the positron source is using the electron beam. If the energy of the electron beam falls to about 125 GeV the number of produced positrons is reduced. This leads to either a reduction of the positron bunch charge or to a mode of operation where every other electron pulse is accelerated to high energy to produce the positrons. The effective repetition rate is reduced in this case as only every second pulse can be used for luminosity production.

The luminosity reduction at lower energies is substantial. One reason is the scaling of the beam delivery system. It is assumed that the divergence has to be kept constant at all energies. As a consequence the horizontal beta-function has to increase at lower energies. But the two constraints from beam-beam interaction would allow a more favourable scaling. If one wants to maintain the same luminosity spectrum quality at lower energies, it would however be possible to decrease the beta-function in order to keep the horizontal beam size constant. If one aims at maintaining the same disruption in the collision to avoid tightening of tolerances, the beta-functions can be still kept constant. It appears not excluded that by exchanging the final doublet at lower energies one could gain enough aperture to allow the beta-function to remain constant. This would improve the low energy luminosity considerably.

3.15.5.2 *CLIC*

Recently, the Linear Collider Detector Study [24] has requested CLIC to provide operation modes at different energies for the 3 TeV design. In particular, they request a scenario in which the machine is first operated at full energy to discover new particles

and then at lower energies to perform threshold scans to further study the properties of these particles. The possibility to operate at lower energy has thus to be build into the design from the very beginning. It should be noted that a CLIC design with a centre-of-mass energy of 500 GeV also exists, but it will not be discussed here.

We decided that for these scenarios, the beam energy should remain constant until injection into the main linac. A number of options exist to reduce the beam energy at the end of the main linac. Firstly, one can extract the beam once it has reached the target energy and transport it in a simple line to the beam delivery system. This scheme would require extraction lines which compromise the linac fill factor. Secondly, one can reduce the gradient in the main linac to achieve the target final energy. This is the current baseline option. Thirdly, one can run the first part of the linac at full gradient and the end at zero acceleration or even decelerating to the target final energy. This scheme will prevent us from using any of the luminosity recovery ideas that can be applied to the second solution.

We assume that the beam delivery system magnets are simply scaled down in strength proportionally to the beam energy by modifying the magnet currents. This requires careful magnet design. The exceptions are the magnets of the final doublet, which would be replaced with magnets of appropriate strength as needed. It remains to be studied if the beam delivery system could be further optimised at lower energies with acceptable hardware modifications.

In the described scenario, the bunch charge has to be scaled proportionally to the gradient to preserve the same beam stability in the main linac and BDS. As a consequence we would like to reduce the horizontal beam size at the interaction point in order to optimise the luminosity. The unmodified beam delivery system layout prevents us from achieving the preferred beam size. As a result the luminosity per bunch crossing is drastically reduced at low energies, see Figure 115.

We developed a method to recover luminosity by using longer main beam pulses, i.e. by increasing the number of bunch crossings. A description of the procedure used is given in [3]. In Figure 115 the luminosity is shown as a function of the centre-of-mass energy. The steps at certain energies correspond to gradients that allow increasing the pulse length.

3.15.6 Beam-Beam Background

Beam-beam background has strong implications for the machine and detector design. The main important effects are the production of coherent electron-positron pairs, of incoherent pairs and of hadronic events. These processes have been studied since more than a decade and have been considered for previous project proposals. For the ILC detailed studies can be found in the reference design report [21]. For CLIC, studies have been performed recently for the new optimised parameters.

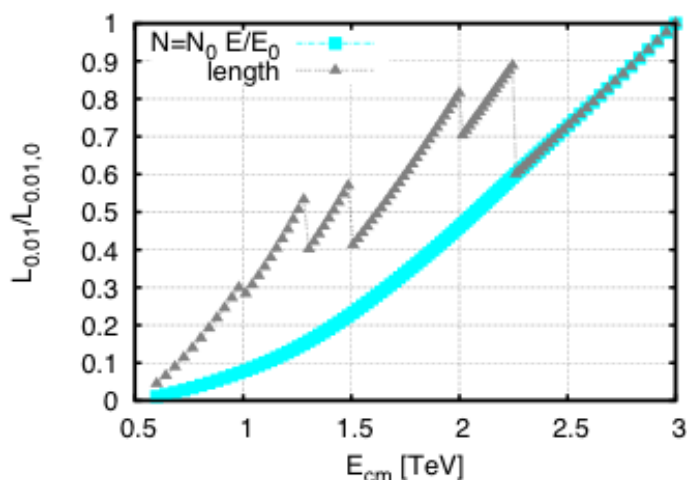


Figure 115: The luminosity within 1% of the target energy is shown as a function of the centre-of-mass energy, normalised to the value at nominal energy. The cyan curve corresponds to the luminosity per bunch crossing if we scale the bunch charge proportional to the energy. The triangles show the luminosity when the increases in pulse length, which are mentioned in the text, are implemented.

3.15.6.1 Coherent Pair Creation

Coherent pair creation can take place if a photon traverses a very strong electromagnetic field. The photon forms from time to time a virtual electron-positron pair loop, after which it usually continues as a photon. In a strong external field, the virtual pair however may extract enough energy to be put on the real plane. At 500 GeV center-of-mass energy, the critical energy of the beamstrahlung is much smaller than the beam energy and coherent pair creation plays a very minor role. At higher energies the critical energy of the beamstrahlung exceeds the beam energy substantially and coherent pair production becomes important. In case of CLIC about 4×10^8 coherent pairs are produced per bunch crossing, which is a significant number compared to the beam particles. While these particles are produced at small angles, they are deflected by the beam-beam forces. This is particularly important if the electron travels against the electron beam or the positron against the positron beam, since the beam are pushing the particle away from the beam axis. The coherent pairs dominate the aperture requirements for the spent beam. A crossing angle of 20mradian has been chosen in order to provide sufficient aperture to extract them from the detector and to also provide the necessary space reservation for the focusing quadrupoles.

Recently an effort has been launched to include the so-called trident cascade process in the beam-beam GUINEA-PIG [15]. This process is similar to the coherent pair production from beamstrahlung, except that the initial photon is a virtual photon in the electron or positron. The total number of pairs produced by this process is smaller than the coherent production from beamstrahlung in CLIC. But the energy spectrum is different which can lead to additional background in the detector forward region. Preliminary results for CLIC are shown in Figure 116.

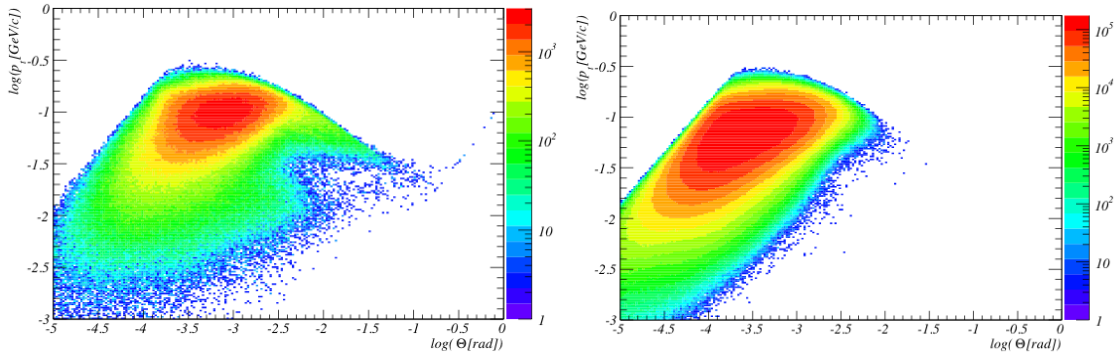


Figure 116: Angle vs. transverse momentum of the coherent pairs from virtual photons (right) and beamstrahlung (left). The plots are provided by Jakob Esberg [13].

3.15.6.2 *Incoherent Pair Creation*

The production of incoherent electron-positron pairs has strong implications on the vertex detector and forward region design. The relevant production processes are $\gamma\gamma \rightarrow e^+e^-$, $\gamma\gamma \rightarrow e + e^+e^-$, $ee \rightarrow ee + e^+e^-$, where the photons are from beamstrahlung. Some of the produced particles have larger angles, but most of them are produced with small angles. However, the beam-beam forces can significantly deflect these particles.

One has to avoid that these particles hit the inner layer of the vertex detector. This is ensured by the detector solenoid field, which will confine the particles to small distances from the beam axis and by choosing a sufficiently larger vertex detector radius. Based on the simulation results a radius of 30 mm has been chosen as a baseline. Further detailed studies are being performed to confirm this choice.

3.15.6.3 *Hadronic Background*

Hadrons can be produced by the collision of two photons, either virtual or real. The largest part of the cross section is not due to electro-weak interaction, e.g. two photons producing a quark-antiquark pair. Most of the events are due to the hadronic content of the photons interacting, i.e. one can imagine the photons to be equivalent to a spectrum of quarks and gluons. The events tend to be boosted into the forward region, and the total energy is smaller than for most of the interesting events, but they can still impact the experiments. The main effect is that the tracks from this background can be confused with tracks from actual physics events. The jet reconstruction algorithms can include them in the jets assigned to the physics event thus measuring jet masses, energies and angles incorrectly. In case of CLIC one finds about three of these events per bunch crossing, with a photon-photon centre-of-mass energy above 5 GeV. Since the time interval between two bunch crossings is only 0.5ns, the detector may integrate over several of them. There is a study group to analyse the impact of hadronic events on the quality of the physics analysis. In case of ILC the rate is much lower (0.15 per bunch crossing for RDR parameters and 0.35 for SB2009 parameters) and the distance is between bunches is much larger (370 ns and 740 ns, respectively), so the impact of hadronic events should be very much smaller.

3.15.6.4 *Luminosity Spectrum Reconstruction*

The ability to reconstruct the luminosity spectrum accurately is important at linear colliders. In particular, if the production threshold of a new particle is investigated the knowledge of the spectrum is primordial to be able to unfold the spectrum from the measured increase of the production rate as a function of the collider centre-of-mass energy. This is essential to measure the actual cross section of the particle production. It has been suggested to use low angle Bhabhas for this measurement [23]. One assumes that the two scattered particles have the same transverse momentum. By measuring the angle of the particles it is thus possible to determine the ratio of their energies. This information can be used to reconstruct the beam energy spectrum weighted with the luminosity. The strong beam-beam forces can however lead to deflection of the initial particles as well as the final ones. This can render the spectrum reconstruction difficult. Preliminary studies show that this effect can indeed be important and that measures to improve the spectrum reconstruction need to be investigated [20].

3.15.7 **Code Development and Benchmarking**

Due to the strong interaction between the two beams, strong-strong simulations are required. In these simulations the two beams are represented with a number of macroparticles. Currently two main codes exist to study beam-beam effects in linear colliders, CAIN [20] and GUINEA-PIG [19]. Recently GUINEA-PIG has been translated from C to C++ [14]. The new version has also been extended to be able to simulate depolarisation effects in the beam-beam collision [17].

As mentioned above, the reconstruction of the luminosity spectrum is an important issue for linear colliders. A proposed scheme for the spectrum reconstruction is based on the use of low angle Bhabhas [23] as explained above. One assumes that the scattered Bhabhas have the same transverse momentum. One concern for this method is that the initial state beam particles as well as the scattered Bhabhas are deflected by the strong fields of the beam, typically with an angle of up to a good fraction of a mradian. This can impact the accuracy of the luminosity spectrum reconstruction. GUINEA-PIG has been modified to be able to study this effect [20]. The results show that good control of the beam parameters is necessary to achieve results with a total error on the luminosity at the 10^{-3} level.

Careful benchmarking of the incoherent pair production routines in CAIN and GUINEA-PIG showed good agreement in total number of particles. But it also revealed a difference in the particles at large angles and transverse momentum. These particles form a background source for the vertex detector. The difference has been tracked back to a difference in the calculation of the production cross section. Comparison with the physics generator BDK [18] showed that the GUINEA-PIG results are more accurate. This confirms previous comparisons of GUINEA-PIG with the Vermaseren Monte-Carlo [thesis].

GUINEA-PIG has also been extended to be able to simulate the production of coherent pairs from virtual photons, the so-called trident cascade. First results are presented above.

3.15.8 References

1. R. Brinkmann, (DESY), O. Napoly, (DAPNIA, Saclay) , D. Schulte, (CERN). "Beam-beam instability driven by wake field effects in linear colliders". DESY-TESLA-2001-16, DESY-M-01-06K, CLIC-NOTE-505, CERN-CLIC-NOTE-505, CERN-OPEN-2002-007, PAC-2001-TPPH153, Feb 2001.
2. D. Schulte. "An Update of the Banana Effect", CLIC Note 560
3. D. Schulte et al. "CLIC Energy Scans", IPAC 2010
4. H. Braun et al. CLIC 2008 Parameters, CLC-Note 764, Oct 2008.
5. A. Grudiev, D. Schulte, Walter Wuensch (CERN), "Optimum frequency and gradient for the CLIC main linac accelerating structure", CERN-CLIC-NOTE-677, EUROTEV-REPORT-2006-0990
6. J. Clarke, B. Foster, M. Harrison, D. Schulte, A. Seryi, T. Tauchi, "Report from the GDE Physics Questions Committee", ILC-NOTE-2010-055.
7. P. Raimondi and A. Seryi, "Novel Final Focus Design for Future Linear Colliders", Phys. Rev. Lett. **86**, 3779-3782 (2001).
8. R. Tomas, "Non-linear Optimization of Beam Lines", Phys. Rev. ST Accel. Beams **9**, 081001 (2006).
9. R. Tomas and M. Jorgensen, "Optimizing the CLIC Beam Delivery System," CLIC-Note-735.
10. D. Schulte, "Luminosity Limitations at the Multi-TeV Linear Collider Energy Frontier", EPAC 2002.
11. D. Angal-Kalinin et al, "Exploring ultra-low β^* values in ATF2 -R&D Programme proposal", CARE/ELAN Document-2008-002.
12. R. Tomas et al, "ATF2 ultra-low IP betas proposal" PAC09, Vancouver, 2009.
13. A. Seryi, "IR optimization, DiD and anti-DiD", SLAC-PUB-11662 (2006).
14. B. Dalena et al, "Impact of the CLIC solenoid in the CLIC luminosity", Proceedings of IPAC 2010, Kyoto, Japan.
15. J. Esberg. To be published.
16. C. Rimbault, Ph. Bambade, K. Mönig, D. Schulte, "Study of Incoherent Pair Generation in GUINEA-PIG", EUROTeV-Report-2005-016.
17. C. Rimbault et al. "Implementation of Depolarization Due to Beam-Beam Effects in the Beam-Beam Interaction Simulation Tool GUINEA-PIG++" EUROTeV-Report-2008-066:
18. F.A. Berends, P.H. Daverveldt, and R. Kleiss, Comp. Phys. Common.**40**(1986)285
19. D. Schulte, "Study of Electronmagnetic and Hadronic Background in the Interaction Region of the TESLA Collider", TESLA- 97-08
20. C. Rimbault, Ph. Bambade, K. Mönig, D. Schulte, "Bias on Absolute Luminosity Measurements at the ILC from Beam-beam Space Charge Effects", EUROTeV-Report-2007-055.
21. International Linear Collider Reference Design Report, ILC-Report-2007-001.
22. P. Chen, G. Horton-Smith, T. Ohgaki, A. W. Weidemann and K. Yokoya, "Cain: Conglomerat D'abel Et D'interactions Nonlineaires", NIM A **355**, 107 (1995).
23. M. N. Frary, D. J. Miller, DESY-92-123A p379
24. <http://lcd.web.cern.ch/LCD/>
25. <http://www.linearcollider.org/GDE>

3.16 Beam-Beam Effects in Muon Colliders

Yuri I. Alexahin, Fermilab, P.O.Box 500, Batavia IL 60510
Mail to: alexahin@fnal.gov

3.16.1 Introduction

Muon Collider (MC) - proposed by G.I. Budker and A.N. Skrinsky more than 40 years ago – is now considered as the most exciting option for the energy frontier machine in the post-LHC era. It has a number of important advantages over e+e– colliders: better energy resolution, larger cross-section of scalar particles production etc. [1]. However, taking into account relatively high transverse emittance which can be obtained with ionization cooling, the bunch population should be as high as $\sim 2 \cdot 10^{12}$ in order to achieve competitive luminosities. This brings to the forefront the beam-beam effects, coherent instabilities and their interplay.

Table 16: Baseline muon collider parameters [2].

Parameter	Unit	Value
Beam energy	TeV	0.75
Repetition rate	Hz	15
Average luminosity / IP	$10^{34}/\text{cm}^2/\text{s}$	1.1
Number of IPs, N_{IP}	-	2
Circumference, C	km	2.73
β^*	cm	1 (0.5-2)
Momentum compaction, α_p	10^{-5}	-1.3
Normalized emittance, $\varepsilon_{\perp N}$	$\pi\text{-mm-mrad}$	25
Momentum spread	%	0.1
Bunch length, σ_s	cm	1
Number of muons / bunch	10^{12}	2
Beam-beam parameter / IP, ξ	-	0.09
RF voltage at 800 MHz	MV	16
Betatron tunes	-	20.56 / 16.58
Synchrotron tune	-	0.00057

3.16.2 Incoherent Beam-Beam Effect

An important feature of a muon collider necessary for achieving high luminosity is small beta-function at IP, $\beta^* \leq 1\text{cm}$, which is more typical for e+e– factories than for TeV-range circular machines. As a result the final focus quadrupoles excite a very strong chromatic beta-wave which should be suppressed with sextupoles as close to the origin as possible. The beam-beam interaction changes phase advances between the sextupoles across the IP making the problem more complicated: it must be taken into account already at the stage of lattice design.

A successful IR lattice design providing sufficiently large momentum acceptance and dynamic aperture of the whole ring with little sensitivity to the beam-beam effect was presented in [2]. Its basic parameters are cited in Table 16. The key to success was to arrange the optics so that the sextupoles correcting chromaticity in one plane were located at minima of beta-function in the other plane with phase advances from IP being multiples of π . In the result the beam-beam interaction reduces the beta-function values at the minima further suppressing spherical aberrations produced by these sextupoles.

3.16.2.1 *Dynamic Aperture*

The problem with dynamic aperture in a muon collider is somewhat alleviated by the limited number of turns the muons spend in the machine: their lifetime at 0.75 TeV is just 1700 turns. But they may be dumped even earlier – after about 1000 turns – to reduce heat deposition in magnets without significant impact on the integrated luminosity. This means that high order resonances will have little chance to show up.

A preliminary study of incoherent beam-beam effect was performed in the weak-strong approximation with the help of MAD8. The strong bunch was represented by 23 slices according to Zholents-Shatilov algorithm [3]. Figure 117 shows 1000 turns “diagonal” dynamic aperture obtained along the line $A_x=A_y$ with fixed values of the beam-beam parameter, the test particle momentum deviation and longitudinal position at the center of the bunch. More comprehensive studies using LIFETRAC code [3] are underway.

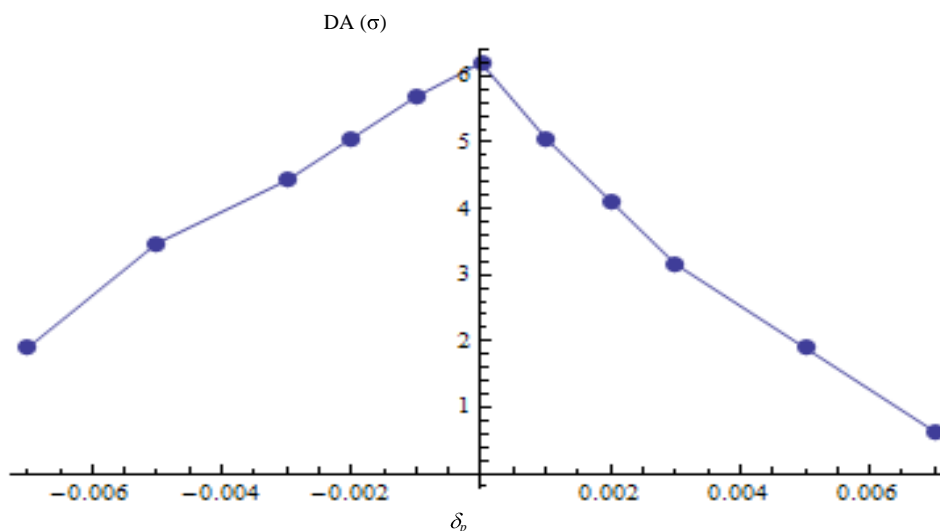


Figure 117: Dynamic aperture vs. constant momentum deviation in the presence of beam-beam interaction ($\xi = 0.1/\text{IP}$).

3.16.2.2 *Dynamic Beta Effect*

Conventional wisdom suggests choosing phase advances between IPs to be just above multiples of π . Then the beam-beam interaction reduces the beta-function values at IPs enhancing the luminosity – the phenomenon known in circular colliders as the “dynamic beta effect”.

However, this effect increases beta-functions at the IR quadrupole locations and may be detrimental in a TeV-range muon collider where the quadrupole aperture is restricted by high gradient requirements and the necessity of protection from the muon decay products [4]. From this point of view “neutral” phase advances – odd multiples of $\pi/2$ – are preferable. Then with 2 IPs we get half-integer tunes which are also beneficial for orbit stability and low detuning with amplitude in a bare lattice.

Still - as R. Palmer pointed out - there will be some luminosity enhancement by the beam-beam interaction due to a large length of the bunches ($\sigma_s \sim \beta^*$) which is akin to the “disruption” effect in linear colliders. Strong-strong simulation of this effect in linear approximation for the beam-beam force showed that at given parameters it almost completely compensates for the luminosity reduction due to the “hour-glass” effect [5].

With these considerations in mind, the current version of the MC lattice was chosen to have two identical super periods with phase advances between the IPs being $41 \times \pi/2$, $33 \times \pi/2$ in the two planes. But the requirements of coherent oscillations stability may necessitate a different choice of phase advances.

3.16.3 Coherent Beam-Beam Oscillations

The synchrotron tune in the muon collider is very low (see Table 16) as a consequence of a very small (by absolute value) momentum compaction factor needed to obtain sufficiently short bunches with moderate RF voltage. As the longitudinal motion is virtually frozen the beams are subject to a transverse BBU-like instability known in linear accelerators. Its rise-time in a single bunch may be as short as a few hundred turns [6]. A possibility was discussed of using RF quadrupoles to taper the tunes along the bunch and provide BNS damping [6].

The beam-beam interaction may render such a complication unnecessary: the instability – which is in essence a single-particle response to the wakefield generated by the head of the bunch – should be strongly suppressed by the beam-beam tune spread. For parameters of Table 16 the decoherence time of the initial (driving) perturbation is just $1/(N_{IP} \xi) = 5$ turns.

However, under conditions typical to a muon collider it may be more difficult to stabilize coherent beam-beam modes: in absence of a tune split between the two beams of approximately equal intensities there will be discrete spectral lines of π - and Σ -modes well separated from the incoherent tune spread [7]. The natural suppression mechanism by the synchrotron sidebands will not work due to a very small ratio of the synchrotron tune to the beam-beam parameter [7]. Numerical 3D simulations with realistic impedances are necessary to determine if the instability is strong enough to develop during limited lifespan of the muon beams and if it can be suppressed by chromaticity.

If there will be found a potential for instability, a remedy can be applied which was once considered for LHC: redistribution of phase advances between the superperiods [7]. In particular, a 180° phase advance difference between sectors IP1→IP2 and IP2→IP1 would completely suppress the coherent beam-beam modes. In our case the phase advances can be chosen as 20π , 17π in one half of the ring and 21π , 16π in the other half without changing the total tunes. However, such redistribution will create difficulties with dynamic beta increase in quadrupoles as discussed in the previous section and should be considered as the last resort.

3.16.4 References

1. S. Geer, "Muon Colliders and Neutrino Factories", *Ann. Rev. Nucl. Part. Sci.* 59 (2009) 347, <http://dx.doi.org/10.1146/annurev.nucl.010909.083736>
2. Y. Alexahin, E. Gianfelice-Wendt, A. Netepenko, "Conceptual Design of the Muon Collider Ring Lattice", *Proceedings of the 2010 International Particle Accelerator Conference*, Kyoto (2010).
3. D. Shatilov et al, "Lifetrac Code for the Weak-Strong Simulation of the Beam-Beam Effects in Tevatron", *Proceedings of the Particle Accelerator Conference*, Knoxville, TN, 2005, pp 4138-4140.
4. Y. Alexahin et al., "Muon Collider Interaction Region Design", *Proceedings of the 2010 International Particle Accelerator Conference*, Kyoto (2010).
5. A. Netepenko, "Muon Collider Ring Lattice Design", *Fermilab Beams-doc-3579-v1* (2010).
6. <http://www.cap.bnl.gov/mumu/pubs/snowmass96.html>
7. Y. Alexahin, "A Study of Coherent Beam-Beam Effect in the Framework of the Vlasov Perturbation Theory", *LHC Project Report 461* (2001); *NIMA* 480 pp.253-288 (2002).

4 Workshop and Conference Reports

4.1 Laser Applications for Future High-Energy and High-Intensity Accelerators

Ralph Assmann (CERN), Weiren Chou (Fermilab), Eric Esarey (LBNL),
 Dino Jaroszynski (U. of Strathclyde), Yun Liu (ORNL), Tor Raubenheimer (SLAC),
 Mike Seidel (PSI), Toshiki Tajima (LMU MPQ) and Kaoru Yokoya (KEK)
 Mail to: chou@fnal.gov

Note: This is a report from the Collider Working Group of the "Joint ICFA-ICUIL Workshop on High Power Laser Technology for Future Accelerators," April 8-10, 2010 GSI, Germany. A complete workshop report is in the works.

4.1.1 Introduction

The consensus in the world high-energy physics community is that the next large collider after the LHC will be a TeV-scale lepton collider. Options currently under study include the ILC (0.5-1 TeV), CLIC (up to 3 TeV) and the muon collider (up to 4 TeV), all using RF technology. On the other hand, the very high gradients (~ 10 GeV/m) possible with laser acceleration open up new avenues to reach even higher energy and more compact machines. At this workshop participants discussed and set forth a set of beam and laser parameters for a 1-10 TeV e^+e^- collider based on two different technologies – laser plasma acceleration (LPA) and direct laser acceleration (DLA). Because the effectiveness of a collider is judged by its luminosity, and the cross section for a process creating a large mass M varies as $1/M^2$, a high energy machine must also have high luminosity. The luminosity goal for a 10 TeV collider is 10^{36} $\text{cm}^{-2}\text{s}^{-1}$, a factor of 100 higher than for a 1 TeV machine. To reach this goal, the laser system must have high average power (~ 100 MW) and high repetition rate (kHz to MHz).

Moreover, the laser-based collider must have high wall-plug efficiency in order to keep power consumption at a reasonable level. To set this efficiency goal, the workshop compared the efficiency of a number of large accelerators, either in operation or in a design phase. The results are listed in Table 1. Our goal is 10% for an LPA.

Table 1: Comparison of wall-plug efficiency of various accelerators.

Accelerator	Beam	Beam energy (GeV)	Beam power (MW)	Efficiency AC to beam	Note on AC power
PSI Cyclotron	H ⁺	0.59	1.3	0.18	RF + magnets
SNS Linac	H ⁻	0.92	1.0	0.07	RF + cryo + cooling
TESLA (23.4 MV/m)	e ⁺ /e ⁻	250 × 2	23	0.24	RF + cryo + cooling
ILC (31.5 MV/m)	e ⁺ /e ⁻	250 × 2	21	0.16	RF + cryo + cooling
CLIC	e ⁺ /e ⁻	1500 × 2	29.4	0.09	RF + cooling
LPA	e ⁺ /e ⁻	500 × 2	8.4	0.10	Laser + plasma

It is difficult to set a reasonable goal for cost. Ideally, the cost of a collider based on laser technology should be significantly lower than colliders based on conventional RF technology in order to make this new technology attractive. Take the 0.5 TeV ILC as an example. The total estimated cost is about \$8B, of which about 1/3 is the RF cost. This gives roughly \$5M per GeV for RF. The laser cost of a LPA or DLA collider should be an order of magnitude lower in order to be competitive.

The workshop also studied the laser requirements for a 200 GeV $\gamma\gamma$ collider. This idea originated at BINP is based on the consideration that the cross section for Higgs production in a $\gamma\gamma$ collider is significantly larger than an e⁺e⁻ collider of the same energy. In 2008, it was proposed to the ICFA to build a 180 GeV $\gamma\gamma$ collider as the first stage of a full scale ILC in order to lower the construction cost and realize a more rapid start for the project. This proposal was not approved for a number of reasons: physics potential, cost saving potential, need for additional laser R&D. This workshop concluded that, as a matter of fact, the required laser systems for an ILC $\gamma\gamma$ collider may already be within reach of today's technology, whereas for a CLIC $\gamma\gamma$ collider the required laser technology could piggyback on the inertial fusion project LIFE at LLNL or the high power laser project ELI in Europe (see Sec. 1.4).

In addition to high-energy colliders, lasers also find application at another frontier – high-intensity accelerators. Lasers have been used in beam diagnostics for some time now, including beam profile monitor (“laser wire”) and beam polarization measurement. These require only low power lasers. A challenge, however, is to use a laser for stripping H⁻ particles during injection into a high-intensity proton machine, such as the SNS, J-PARC or Project X. In these MW-scale machines, the thin foils made of carbon or diamond that have been used for stripping would experience a severe heating problem and have limited lifetime. Experiments have demonstrated that a laser beam interacting with H⁻ particles can convert them to protons. However, to replace foils in real machine operation, the laser must have high average power (kW) and high repetition rate (hundreds of MHz). This workshop investigated the required laser parameters for the SNS and Project X.

4.1.2 1-10 TeV e^+e^- Colliders Based on Laser Plasma Acceleration

Advanced acceleration techniques are actively being pursued to expand the energy frontier of future colliders. Although the minimum energy of interest for the next lepton collider will be determined by high-energy physics experiments presently underway, it is anticipated that ≥ 1 TeV center-of-mass energy will be required. Laser-plasma accelerators are one promising technique for reducing the size and cost of future colliders, provided the needed laser technology is developed.

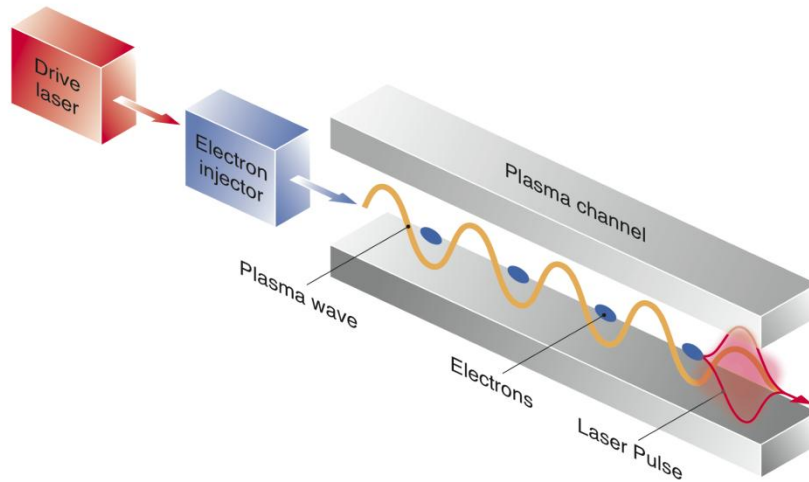


Figure 1: Laser-plasma acceleration: An intense laser pulse drives a plasma wave (wake) in a plasma channel, which also guides the laser pulse and prevents diffraction. Plasma background electrons that are injected with the proper phase can be accelerated and focused by the wake [1].

Laser-plasma accelerators (LPAs) are of great interest because of their ability to sustain extremely large acceleration gradients, thus resulting in compact accelerating structures [1-3]. Laser-plasma acceleration is realized by using a short-pulse, high-intensity laser to ponderomotively drive a large electron plasma wave (or wakefield) in an underdense plasma (see Fig. 1). The electron plasma wave has relativistic phase velocity, approximately the group velocity of the laser, and can support large electric fields in the direction of propagation of the laser. When the laser pulse is approximately resonant (duration on the order of the plasma period) and the laser intensity is relativistic (with normalized laser vector potential $a_0 = eA/m_e c^2 \sim 1$), the magnitude of the accelerating field is on the order of $E_0[\text{V/m}] = 96(n_0[\text{cm}^{-3}])^{1/2}$, and the wavelength of the accelerating field is on the order of the plasma wavelength $\lambda_p[\mu\text{m}] = 3.3 \times 10^{10}(n_0[\text{cm}^{-3}])^{-1/2}$, where n_0 is the ambient electron number density. For example, $E_0 \approx 30$ GeV/m (approximately three orders of magnitude beyond conventional RF technology) and $\lambda_p \approx 100$ μm for $n_0 = 10^{17} \text{ cm}^{-3}$. Rapid progress in laser-plasma accelerator research, and in particular the demonstration of high-quality GeV electron beams over cm-scale plasmas at Lawrence Berkeley National Laboratory [4] has increased interest in laser-plasma acceleration as a path toward a compact TeV-class linear collider [5]. A conceptual diagram of a LPA-based collider is shown in Fig. 2.

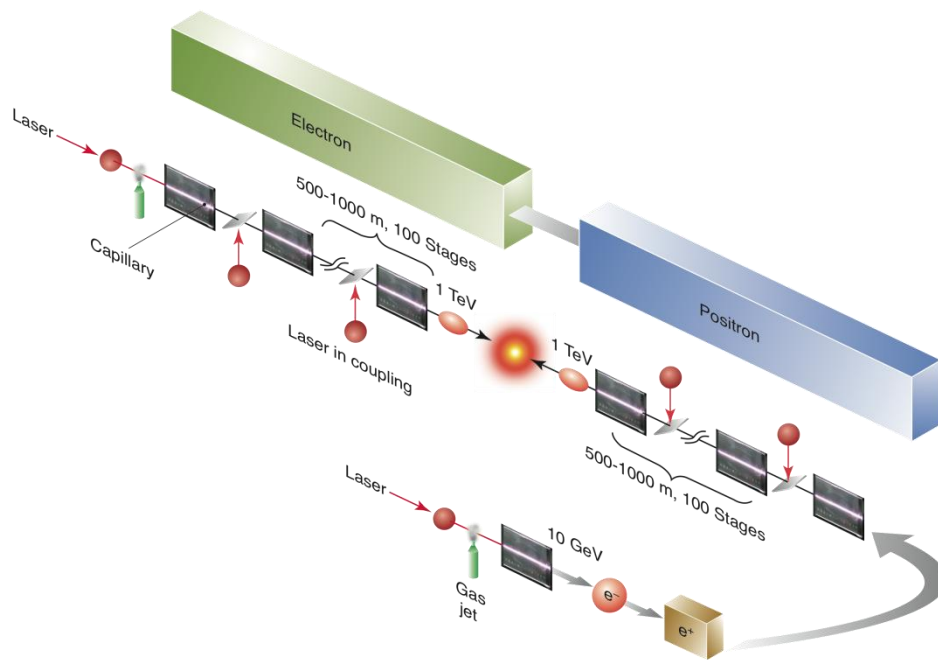


Figure 2: Concept for a LPA-based electron-positron collider. Both the electron and positron arms start with a plasma-based injection-acceleration module where controlled injection techniques are applied to produce a high quality ~ 10 GeV electron beam. Electrons are then accelerated to 1 TeV using 100 laser-plasma modules, each consisting of a 1-m long preformed plasma channel (10^{17} cm^{-3}) driven by a 30 J laser pulse giving a 10 GeV energy gain. A fresh laser pulse is injected into each module. Similarly, positrons are produced from a 10 GeV electron beam through pair creation and then trapped and accelerated in a LPA module to ~ 10 GeV. Subsequent LPA modules would accelerate positrons to 1 TeV. A luminosity of $10^{34} \text{ cm}^{-2} \text{ s}^{-1}$ requires 4×10^9 particles/bunch at a 13 kHz repetition rate [1].

In the standard laser wakefield acceleration configuration, the electron plasma wave is driven by a nearly resonant laser (pulse duration on the order of the plasma period) propagating in a neutral, underdense ($\lambda_p \gg \lambda$, where λ is the laser wavelength) plasma. There are several regimes of plasma acceleration that can be accessed with a laser driver. Two regimes that have attracted attention for collider applications are the quasi-linear regime [3] and the bubble [6] (or blow-out [7]) regime. The quasi-linear regime is accessible for parameters such that $\pi^2 r_L^2 / \lambda_p^2 \gg a_0^2 / 2\gamma_L$, where a_0^2 can be written as a function of the laser intensity I_0 : $a_0^2 = 7.3 \times 10^{-19} (\lambda [\mu\text{m}])^2 I_0 [\text{W}/\text{cm}^2]$ (linear polarization), $\gamma_L = (1 + a_0^2/2)^{1/2}$, and r_L is the laser spot size. The amplitude of the accelerating field of the plasma wave in the quasi-linear regime is $E_z \approx 0.76(a_0^2/2\gamma_L)E_0$. This regime is characterized by regular plasma wave buckets and nearly-symmetric regions of acceleration-deacceleration and focusing-defocusing (see Fig. 3). In the quasi-linear regime, the accelerating and focusing phase regions for electrons and positrons are symmetric since the wakefield is approximately sinusoidal.

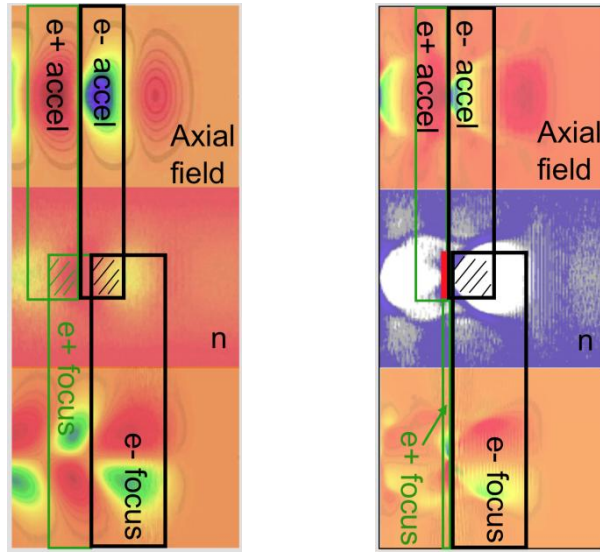


Figure 3: Wakes generated in the quasi-linear (left) and bubble (right) regimes by a laser pulse with $a_0=1$ (left) and $a_0=4$ (right). Top figures are axial electric field, central figures are density, and bottom figures are transverse electric fields. The black boxes indicate the accelerating/focusing regions for electrons, and the green boxes are for positrons (courtesy C.G.R. Geddes *et al.*, LBNL).

The bubble regime of LPA occurs for laser-plasma parameters such that $\pi^2 r_L^2 / \lambda_p^2 \ll a_0^2 / 2\gamma_L$. This regime is characterized by complete removal of plasma electrons and creation of an ion cavity (see Fig. 3). The bubble regime has several attractive features for acceleration of electron beams. Inside the moving ion cavity, the focusing forces for electrons are linear (and attractive) and uniform for all phases and the accelerating field is independent of transverse position with respect to the cavity axis. The major drawback of accessing the highly-nonlinear bubble regime is that acceleration of positrons is problematic because the entire ion cavity is defocusing for positrons, and a positron beam will be scattered transversely. There does exist a small phase region immediately behind the bubble where positrons could be accelerated and focused; however, here some of the attractive properties of the bubble regime (e.g., uniform accelerating and constant linear focusing) are lost.

The amount of charge that can be accelerated in a plasma wave is determined by the plasma density and the size of the accelerating field. The maximum charge that can be loaded is given by the number of charged particles required to cancel the laser excited wake (beam loading limit). A collider will operate with asymmetric shaped particle bunches such that bunches can be loaded with charge near the beam loading limit without a large wake-induced energy spread. The maximum number of loaded charged particles into a small ($\ll \lambda_p = 2\pi/k_p$) segment is approximately $N = n_0 k_p^{-3} (E_z/E_0)$.

In general, the energy gain in a single laser-plasma accelerator stage may be limited by laser diffraction effects, dephasing of the electrons with respect to the accelerating field phase velocity (approximately the laser driver group velocity), and laser energy depletion into the plasma wave. Laser diffraction effects can be mitigated by use of a plasma channel (transverse plasma density tailoring), guiding the laser over many Rayleigh ranges. Dephasing can be mitigated by plasma density tapering (longitudinal plasma density tailoring), which can maintain the position of the electron beam at a given phase of the plasma wave. Ultimately, the single-stage energy gain is determined

by laser energy depletion. The energy depletion length scales as $L_d \sim \lambda_p^3/\lambda^2 \propto n_0^{-3/2}$ and the energy gain in a single stage scales with plasma density as $W_{\text{stage}} \approx E_z L_d \propto n_0^{-1}$.

After a single laser-plasma accelerating stage, the laser energy is depleted and a new laser pulse must be coupled into the plasma for further acceleration. This coupling distance is critical to determining the overall accelerator length (set by the average, or geometric, gradient of the main linac) and the optimal plasma density at which to operate. One major advantage of laser-driven plasma acceleration is the potential for a short coupling distance between stages, and, therefore, the possibility of a high average (geometric) accelerating gradient and a relatively short main linac length. Although conventional laser optics might require meters of space to focus intense lasers into subsequent LPA stages, plasma mirrors show great promise as optics to direct high-intensity laser pulses, requiring only tens of cm to couple a drive laser into a plasma accelerator stage. A plasma mirror uses overdense plasma creation by the intense laser on a renewable surface (e.g., metallic tape or liquid jet) to reflect the laser beam. Reducing the main linac length requires the coupling length between stages to be on the order of the length of a single plasma acceleration stage.

The beam-beam interaction at the interaction point (IP) of a collider produces radiation (beamstrahlung) that generates background for the detectors and increases the beam energy spread (resulting in loss of measurement precision). The beam-beam interaction is characterized by the Lorentz-invariant beamstrahlung parameter Υ (mean field strength in the beam rest frame normalized to the Schwinger critical field). The current generation of linear collider designs based on conventional technology operate in the classical beamstrahlung regime $\Upsilon \ll 1$. Next generation linear colliders (≥ 1 TeV) will most likely operate in the quantum beamstrahlung regime with $\Upsilon \gg 1$. In the quantum beamstrahlung regime, the average number of emitted photons per electron scales as $n_\gamma \propto \Upsilon^{2/3}$ and the relative energy spread induced scales as $\Delta E_\gamma \propto \Upsilon^{2/3}$. Assuming that the center of mass energy, luminosity, beam power, and beam sizes are fixed, $n_\gamma \propto (N\sigma_z)^{1/3}$ and $\Delta E_\gamma \propto (N\sigma_z)^{1/3}$, where σ_z is the particle bunch length [5]. In this regime, beamstrahlung is reduced by using shorter bunches and smaller charge per bunch. Laser-plasma accelerators are intrinsically sources of short (fs) electron bunches, due to shortness of the plasma wavelength λ_p .

Tables 2A and 2B show estimates of parameters for electron-positron colliders for three cases: a 1 TeV CoM collider with a plasma density of $n_0 = 10^{17} \text{ cm}^{-3}$, a 10 TeV CoM collider with a plasma density of $n_0 = 10^{17} \text{ cm}^{-3}$ (Scenario I in Table 2), and a 10 TeV CoM collider with a plasma density of $n_0 = 10^{18} \text{ cm}^{-3}$ (Scenario II in Table 2). In all these cases a laser wavelength of $\lambda = 1 \text{ }\mu\text{m}$ and an intensity $3 \times 10^{18} \text{ W/cm}^2$ ($a_0 = 1.5$) is assumed. The laser-plasma accelerator parameters are based on scaling laws for the quasi-linear regime obtained from simulation codes. A mild plasma density taper is assumed. The length of one linac is on the order of 0.1 km for the 1 TeV, $n_0 = 10^{17} \text{ cm}^{-3}$ case and of the order 1 km for the 10 TeV, $n_0 = 10^{17} \text{ cm}^{-3}$ case. The conversion efficiencies assumed are 50% for laser to plasma wave and 40% for plasma wave to beam (laser to beam is 20%). A high laser wall plug efficiency of 50% is also assumed, giving an overall wall plug to beam efficiency of 10%. Notice that the laser energy per stage per bunch is on the order of tens of J (for $n_0 = 10^{17} \text{ cm}^{-3}$) and the required rep-rates are of the order of tens of kHz (for $n_0 = 10^{17} \text{ cm}^{-3}$), clearly indicating the need for the development of laser systems with high average power (hundreds of kW) and high peak

power (hundreds of TW). The higher rep-rate (170 kHz) and higher total wall power (3.4 GW) required for the higher plasma density case ($n_0 = 10^{18} \text{ cm}^{-3}$) is less favourable than the $n_0 = 10^{17} \text{ cm}^{-3}$ case.

A process that extracts the energy of the remaining wakefields in the plasma has been suggested [8]. Inserting circuitry in the plasma as a passive feedback system extracts the wakefield energy, converts this energy into electric energy, and feeds it into an external circuit. The conversion efficiency is on the order of unity. Thus, it would enhance the coupling efficiency of the laser pulse to the wakefield energy by at least a factor of 2 (or even more).

Table 2A: Beam parameters of 1 TeV and 10 TeV e^+e^- colliders based on LPA technology.

Case	1 TeV	10 TeV (Scenario I)	10 TeV (Scenario II)
Energy per beam (TeV)	0.5	5	5
Luminosity ($10^{34} \text{ cm}^{-2} \text{ s}^{-1}$)	1.2	71.4	71.4
Electrons per bunch ($\times 10^9$)	4	4	1.3
Bunch repetition rate (kHz)	13	17	170
Horizontal emittance $\gamma\epsilon_x$ (nm-rad)	700	200	200
Vertical emittance $\gamma\epsilon_y$ (nm-rad)	700	200	200
β^* (mm)	0.2	0.2	0.2
Horizontal beam size at IP σ_x^* (nm)	12	2	2
Vertical beam size at IP σ_y^* (nm)	12	2	2
Luminosity enhancement factor	1.04	1.35	1.2
Bunch length σ_z (μm)	1	1	1
Beamstrahlung parameter Υ	148	8980	2800
Beamstrahlung photons per electron n_γ	1.68	3.67	2.4
Beamstrahlung energy loss δ_E (%)	30.4	48	32
Accelerating gradient (GV/m)	10	10	10
Average beam power (MW)	4.2	54	170
Wall plug to beam efficiency (%)	10	10	10
One linac length (km)	0.1	1.0	0.3

Table 2B: Laser and plasma parameters of 1-10 TeV e^+e^- colliders based on LPA technology.

Case	1 TeV	10 TeV (Scenario I)	10 TeV (Scenario II)
Wavelength (μm)	1	1	1
Pulse energy/stage (J)	32	32	1
Pulse length (fs)	56	56	18
Repetition rate (kHz)	13	17	170
Peak power (TW)	240	240	24
Average laser power/stage (MW)	0.42	0.54	0.17
Energy gain/stage (GeV)	10	10	1
Stage length [LPA + in-coupling] (m)	2	2	0.06
Number of stages (one linac)	50	500	5000
Total laser power (MW)	42	540	1700
Total wall power (MW)	84	1080	3400
Laser to beam efficiency (%) [laser to wake 50% + wake to beam 40%]	20	20	20
Wall plug to laser efficiency (%)	50	50	50
Laser spot rms radius (μm)	69	69	22
Laser intensity (W/cm^2)	3×10^{18}	3×10^{18}	3×10^{18}
Laser strength parameter a_0	1.5	1.5	1.5
Plasma density (cm^{-3}), with tapering	10^{17}	10^{17}	10^{18}
Plasma wavelength (μm)	105	105	33

4.1.3 10 TeV e^+e^- Colliders Based on Direct Laser Acceleration

The Direct Laser Acceleration (DLA) research effort focuses on development of high-gradient dielectric-loaded vacuum accelerator structures driven with high-repetition rate tabletop near-infrared lasers. The concept is to use dielectric structures to couple very-high laser fields to a particle beam much in the way that microwave structures are used to couple RF fields to a beam except that the wavelength and dimensions are reduced by a factor of 10,000 (from cm to μm). The dielectric structure confines a speed-of-light optical mode that is driven by a laser and will accelerate synchronous charged particles as shown in Figure 4. In contrast to plasma-coupling schemes, structure-based acceleration offers strong coupling to the particle beam, and is fundamentally a linear acceleration process. Consequently, laser pulse energies in the $<1 \mu\text{J}/\text{pulse}$ range are needed to generate GeV/m-class gradients, the process has no minimum laser energy threshold, and efficient energy transfer between laser and particle beam is possible [9]. Lasers with the required peak and average power, and $>30\%$ wall-plug efficiency are commercially available. The technology to integrate much of the accelerator infrastructure onto a single silicon or silica substrate (an “accelerator chip”) exists today and is being advanced rapidly by industry. The program leverages the private sector’s multi-billion dollar investments in semiconductor and telecommunication technology to produce an entirely new accelerator technology.

The primary challenges for this technology are the requirement of exquisite phase control of multiple lasers and the reduction in the dimensions from microwave-scales to

near-IR that lead to very small machine apertures. Since carrier-phase envelope methods were proposed in 1999, significant progress in optical phase stabilization of ultrashort lasers has occurred, leading to microwave-reference frequency combs for optical metrology, and to the efficient, coherent combination of the outputs of multiple lasers [10]. The small apertures require constructing the accelerator structures with micron-scale dimensions. Three styles of structures are being considered: photon band-gap fibers [11], a 3-D band-gap ‘woodpile’ structure [12], and a grating structure [13]. The small dimensions also require small bunch charge and small emittances which is also naturally required by optimum beam loading and beam transport considerations. As optimum beam loading bunch charges are on the order of 10 fC, the pulse repetition rate must be dramatically raised to provide sufficient beam power to attain adequate luminosity. Fortunately, repetition rates in the tens of megahertz range are natural for fiber lasers and allow for bunch-by-bunch feedback systems that will be necessary to maintain beam control.

Beam transport through the small aperture requires very small normalized emittances. In a manner similar to RF accelerators, microscale periodic focusing elements will play an important role for beam containment in the structure vacuum channel. Simple beam transport considerations have led us to a possible FODO lattice for beam transport in a PBG fiber accelerator. Focusing elements of 2 cm length, 1 mm bore, and a gradient of ~ 500 T/m spaced ~ 2 m apart would allow for transport of a beam with an emittance of $\sim 10^{-10}$ m-rad through a $\sim 1.5 \lambda$ aperture typical for these near-field structures. While 0.1 pm is a very small normalized emittance, it corresponds to a phase space density of $N/\varepsilon = 4 \times 10^{14}$ e/m, well below the 6×10^{15} e/m densities routinely achieved today from photo-injector sources [14].

Early laser acceleration experiments were performed on the Stanford University campus (Figure 5), and in 2007 the same collaboration moved to SLAC with the development of the E163 test facility in the NLCTA. Recent successes include demonstration of attosecond bunch train formation [15] and the first demonstration of the staging of two laser accelerator sections driven at optical wavelengths [16]. The future program will explore the technical limits to laser acceleration, including gradient, acceptance and emittance preservation, and apply semiconductor and fiber-optic manufacturing techniques to demonstrate an entirely new class of structures. Tables 3A and 3B list parameters for a 10 TeV CoM DLA collider. It is important to note that the intrinsically small bunch charge leads to cleaner beam collisions than any other approach considered thus far and may make the DLA technique the only reasonable choice at such very high energy-scales.

Table 3A: Beam parameters of a 10 TeV e^+e^- collider based on DLA technology.

Energy per beam (TeV)	5
Luminosity ($10^{34} \text{ cm}^{-2}\text{s}^{-1}$)	105
Electrons per bunch ($\times 10^9$)	0.002
Bunch repetition rate (kHz)	25000
Horizontal emittance $\gamma\epsilon_x$ (nm-rad)	0.1
Vertical emittance $\gamma\epsilon_y$ (nm-rad)	0.1
Horizontal beam size at IP σ_x^* (nm)	0.064
Vertical beam size at IP σ_y^* (nm)	0.064
Bunch length σ_z (μm)	335
Beamstrahlung parameter Υ	0.377
Beamstrahlung photons per electron n_γ	0.52
Beamstrahlung energy loss δ_E (%)	4.37
Accelerating gradient (GV/m)	0.5
Average beam power (MW)	39
Wall plug to beam efficiency (%)	10
One linac length (km)	10

Table 3B: Laser parameters of a 10 TeV e^+e^- collider based on DLA technology.

Wavelength (μm)	8.0
Pulse energy/stage (nJ)	240
Pulse length (μm)	1740
Repetition rate (kHz)	25,000
Peak power (kW)	17
Average laser power/stage (kW)	10
Energy gain/stage (GeV)	1.3
Stage length [LPA + in-coupling] (m)	2.6
Number of stages (one linac)	3900
Total laser power (MW)	156
Total wall power (MW)	390
Wall plug to laser efficiency (%)	40
Laser spot rms radius (μm)	16
Laser intensity (W/cm^2)	6.4×10^9
Laser strength parameter a_0	1.2×10^{-3}

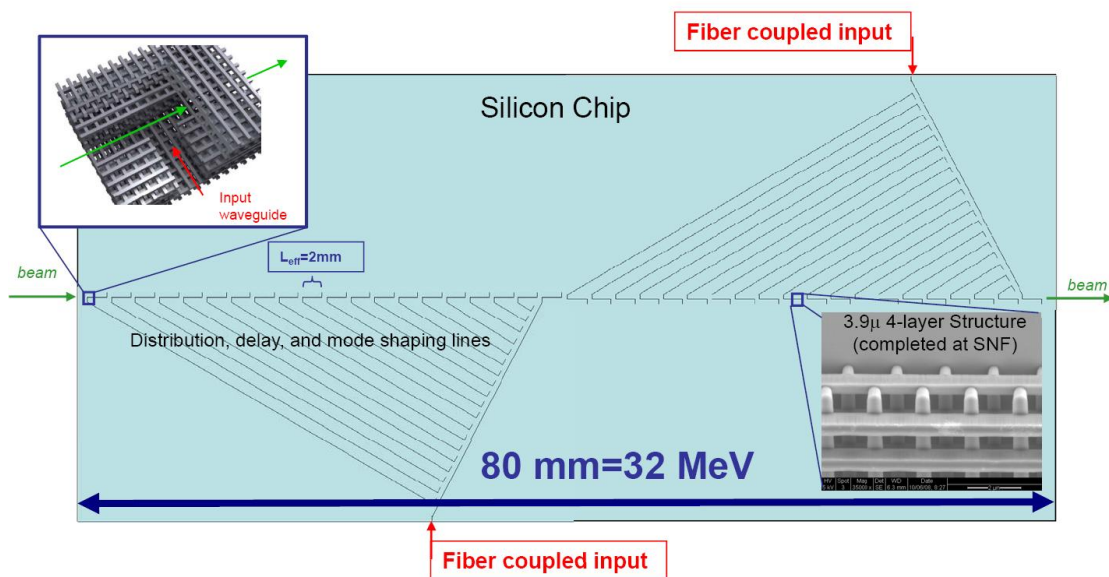


Figure 4: Cartoon showing an integrated silicon woodpile accelerator structure composed of 40 woodpile accelerating structures powered from two fiber lasers. At known damage fluences for 2 mm light, 32 MeV energy gain in 8 cm is expected. Cutaway of coupler region (inset, upper left, courtesy B. Cowan, Tech-X), and SEM image of fabricated silicon woodpile lattice (inset, lower right, courtesy C. McGuinness, Stanford).

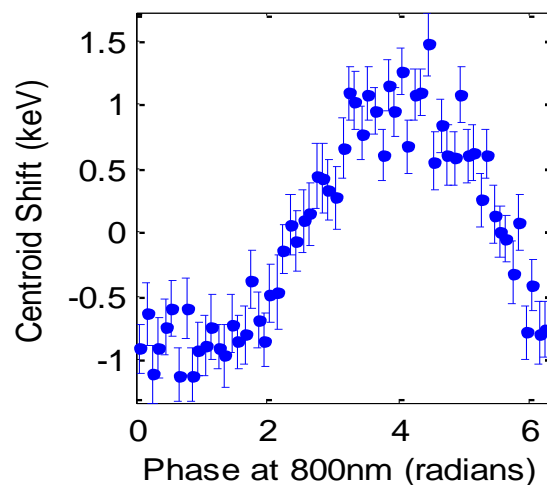


Figure 5: Experimental observation of optical acceleration of optically bunched electrons. The sinusoidal variation of energy of all ~ 350 optical bunches with the phase of the accelerator is plainly visible. Bunches are prepared by the IFEL process, and accelerated by the inverse transition radiation process. Maximum observed gradient 6 MeV/m is due to low coupling efficiency of ITR process; near-field structures are expected to yield a factor of ~ 100 better gradient.

4.1.4 200 GeV $\gamma\gamma$ Colliders

An electron-electron linear collider can be converted to a photon-photon collider by converting the electron beams into photon beams by irradiating laser beams just before the collision point as shown in Figure 6.

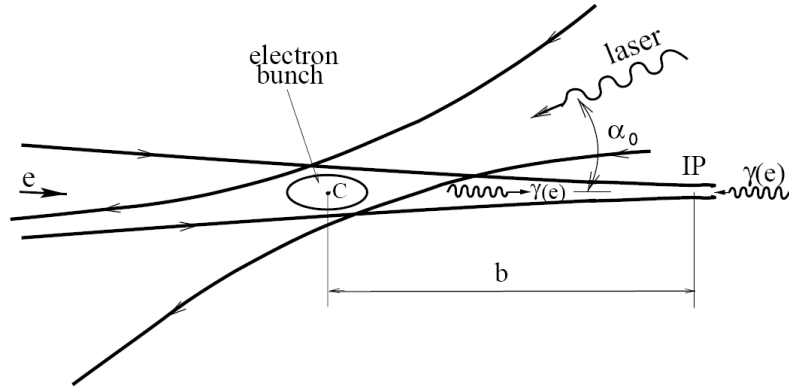


Figure 6: Illustration of the principle of a $\gamma\gamma$ collider.

This scheme opens the possibility for investigating different physics from the collider than when it is operating with charged particle beams. The wave length λ_L of the laser should be as short as possible for creating high energy photons from a given electron energy. However, it must satisfy

$$\lambda_L [\mu\text{m}] > \sim 4 E_e [\text{TeV}]$$

where E_e is the electron energy, because, otherwise, the created high-energy photons would be lost by electron-positron pair creation in the same laser beam. To obtain a narrow photon energy spectrum the laser beam should be circularly polarized (and electrons longitudinally polarized). Linear polarization may sometimes be needed depending on the physics processes being studied.

Since the transverse electron beam size at the conversion point is much smaller than the laser spot size, the probability of conversion is almost entirely determined by the laser parameters and is independent of the electron parameters as long as the electrons go through the entire length of the laser pulse. For almost all the electrons to be converted into photons, the required flash energy of the laser pulse is approximately given by

$$A = \omega_L * \sigma_C / S_L$$

where ω_L is the laser photon energy, σ_C the cross section of Compton scattering, and S_L the effective cross section of the laser beam. S_L cannot be too small due to the Rayleigh length requirement. Thus, in any case A is about a few Joules. On the other hand, the required pulse structure of the laser beam, which must match the electron beam, strongly depends on the collider design. In particular, a superconducting collider (e.g. ILC) and a normal-conducting collider (e.g., CLIC) demand very different pulse structures. The pulse structure can be characterized by a few parameters: n_b the number of bunches in a train, t_b the interval between bunches, $n_b * t_b$ the train length, and f_{rep} the repetition frequency of the trains. The train length is $O(\text{ms})$ for superconducting colliders but is $O(\mu\text{s})$ or less for a normal-conducting collider.

Table 4 shows examples of the required laser parameters for low-energy (Low-mass Higgs region) $\gamma\gamma$ colliders based on the ILC and CLIC parameters. The parameters for

the ILC is based on those given by V. Telnov [17] slightly modified according to the present ILC parameters [18]. The parameters for CLIC are based on the proposal CLICHÉ [19] with the updated parameters of CLIC [20]. V. Telnov made important correction to some of the CLIC parameters as well as provided the laser parameters. [21] (For the ILC a possible use of FEL is proposed [22] but this is irrelevant in the present context.)

All of these parameters are subject to change depending on the project evolution as well as on the optimization of the interaction region. Owing to the long bunch train (980 μ s) and large bunch spacing (370 ns) for the ILC it is possible to use an optical cavity for accumulating the laser power (the multiplication factor Q in the table) so that the requirements for the laser are greatly relaxed at the cost of very high precision optical system [23]. This type of optical cavities is similar to that currently under construction for a Compton x-ray source at KEK [24].

For the CLIC it would be difficult to employ an optical cavity because the bunch train is short (177 ns) and the bunch spacing small (0.5 ns). However, the required laser system is similar to a single laser beam line of the Laser Inertial Fusion Energy (LIFE) project at LLNL in the US. This laser beam line has an output energy of >10 kJ per pulse at a repetition rate >10 Hz, or an average laser power >100 kW. (LIFE project would need a total of 192 lines.) The amplifier is capable to deliver a pulse of 177 ns. A modified front end can readily split a continuous pulse to 354 short pulses of 5 J each. Given appropriate funding, LLNL could put together a 10 kJ module that is diode pumped within 3 years [25]. The main difference between LIFE and CLIC is the repetition rate (10 Hz vs. 50 Hz). This problem could be solved by replacing Nd:glass by ceramic Nd:YAG, which would allow the repetition rate to be increased to >50 Hz. Technology similar to this has also been proposed for the Extreme Light Infrastructure (ELI) project in Europe [26].

Table 4: Beam and laser parameters of $\gamma\gamma$ colliders.

Electron Beam Parameters	ILC	CLIC
Energy per electron beam (GeV)	100	100
Max energy of photons (GeV)	60 (75)	60
$\gamma\gamma$ luminosity at the high energy peak ($10^{34} \text{ cm}^{-2} \text{ s}^{-1}$)	0.13	0.19
Electrons per bunch ($\times 10^{10}$)	2	0.68
Number of bunches in a train (n_b)	2640	354
Distance between bunches (t_b , ns)	370	0.5
Length of the train ($n_b \cdot t_b$, μs)	980	0.177
Repetition frequency (f_{rep} , Hz)	5	50
Electron bunch length σ_z (μm)	300	44
Normalized emittance $\varepsilon_{x/y}$ (mm-mrad)	10/0.035	1.4/0.050
Beta-function at IP $\beta_{x/y}$ (mm)	4/0.3	2/0.02
Beam size $\sigma_{x/y}$ (nm)	450/7.3	120/2.3
Distance between conversion point and IP (mm)	~ 1.5	~ 0.5
Crossing angle (mrad)	25	25
Laser Parameters		
Wavelength (μm)	1 (0.5)	1
Rayleigh range (mm), f#	$\sim 0.5, 20$	$\sim 0.4, 18$
Laser pulse energy (J)	$\sim 10/Q$	5
Pulse length (r.m.s., ps)	~ 1.5	~ 1
Peak power (TW)	$\sim 2.5/Q$	2
Average power (kW)	150/Q	90
Laser power in a train (MW)	25/Q	10000
Cavity enhancement factor	$Q \sim 300$	1

Notes on Table 4: (by V. Telnov)

- 1) Distance between the Compton conversion point (CP) and the interaction point (IP) is $b = \gamma\sigma_y$.
- 2) Thickness of the laser target is equal to 1.2 collision lengths.
- 3) Luminosity in the high energy peak means $L_{\gamma\gamma}(W > 0.8W_{\text{max}})$
- 4) For the ILC, the numbers are given for $\lambda = 1 \mu\text{m}$. Those in () are for $\lambda = 0.5 \mu\text{m}$.
- 5) For the ILC, $\lambda = 1 \mu\text{m}$ is OK and $\lambda = 0.5 \mu\text{m}$ may be possible. But for CLIC only $\lambda = 1 \mu\text{m}$ is allowed because the disruption angle is 1.5 times larger. [The disruption angle is proportional to $(N/\sigma_z)^{1/2}$.]
- 6) "Undulator" parameter $\xi^2 = 0.15$ (0.2) was used for $\lambda = 1$ (0.5) μm , corresponding to reduction of W_{max} by 5%.

4.1.5 Laser Stripping of H^- Particles in High-Intensity Proton Accelerators

4.1.5.1 Laser Stripping of H^- Particles for SNS

The Spallation Neutron Source (SNS) utilizes charge-exchange injection to "stack" a high-intensity proton beam in the accumulator ring for short-pulse neutron production. In this process, a 1 ms long H^- beam pulse is transported to a carbon stripping foil located at the injection point of the ring. The electrons are stripped and the resulting proton is merged with previously accumulated beam. This injection scheme is central to the operation of many facilities, including the SNS, J-PARC, ISIS and PSR.

As the beam power of the SNS is increased from the 1.44 MW design to more than 3 MW as envisioned in the SNS Power Upgrade project, the stripping foils become radioactive and produce uncontrolled beam loss, which is one of the main factors limiting beam power in high intensity proton rings.

A “foil-less” charge exchange injection method was first proposed in the 1980s by using a field dissociation process. This scheme requires an impractically large laser power, which is indeed the central difficulty involved in ionizing neutral hydrogen. Recently, ORNL scientists came up with a three-step scheme for laser stripping.

An H^- ion has two electrons. The first electron is loosely bound with a binding energy of 0.7 eV, whereas the second one is tightly bound with a binding energy of 13.6 eV. The ORNL 3-step scheme works as follows: First, H^- ions are converted to H^0 by stripping off the first electron in a magnetic field; then H^0 atoms are excited from the ground state ($n = 1$) to the upper levels ($n \geq 3$) by a laser, and the excited states H^{0*} are converted to H^+ by stripping the second electron in a second magnetic field.

In a proof-of-principle experiment, a third harmonic beam from a Q-switched laser was used for stripping. The laser generates a 30 Hz, 6 ns pulses with a peak power of ~ 10 MW at 355 nm. The stripping efficiency reached 90%. The positive result has encouraged us to proceed in developing a real scheme for SNS stripping. Such a system will need to reach an efficiency of 98%, similar to that of conventional foils.

A simple multiplication of 10 MW laser peak power, used in the first experiments, and the duty factor of the SNS beam (6%) yields an average laser power of 0.6 MW at 355 nm to strip the entire ion beam. Obviously, this power is too large to make the device practical. Therefore, a number of approaches have been investigated to mitigate the requirement of peak/average laser power.

1) Optimization of H^- beam parameters

An appropriate dispersion derivative of the H^- beam will be designed to eliminate the Doppler broadening of the absorption line width and therefore to reduce the required frequency sweep for the laser beam. The vertical size as well as the horizontal angular spread of the H^- beam will be minimized. The optimization of the H^- beam parameters will reduce required peak power of the laser to the 1 MW level. Reduction of the bunch length of the ion beam can further reduce the average laser power requirement.

2) Macropulse laser system

At SNS, the H^- beam consists of approximately 50-ps long micropulses separated by ~ 2.5 ns and gated into mini-pulses 650 ns long. The period of minipulses, or a turn, is determined by the SNS accumulation ring beam path length (~ 1 μs) and the beam energy. The minipulses are bunched into macropulses with a length of 1 ms and a repetition rate of 60 Hz. In order to achieve high efficiency laser stripping, the laser pulses need to overlap with each ion beam micropulse at the interaction point. The ideal (minimum laser power requirement) condition would be that the laser pulses have an identical temporal structure as the H^- beam. A prototype of such a macropulse laser system has been developed in collaboration with Continuum Inc. It includes a mode-locked seed laser, a pulse picker, multi-stage solid-state amplifiers, and harmonic generation crystals to convert infrared beam to UV light. The

challenge of the macropulse laser system is the high repetition rate and over 1 ms macropulse duration.

3) Beam recycling optical resonator

The photon-hydrogen interaction results in a negligible loss to the laser beam power; it is expected that the average power of the laser can be significantly reduced by recycling the laser beam with an optical resonator. Different cavity configurations including Fabry-Perot, ring cavity, or cavity with built-in harmonic generation crystals need to be investigated. Optical resonator technology is well developed for low-power, infrared, and often continuous laser beams. However, for the SNS the resonator needs to work on a high intensity UV laser beam. In addition, since the photon-hydrogen interaction has to occur inside the resonator, the optics need to operate within a high vacuum and its control electronics need to survive in an environment with high radiation dose. These constraints pose severe technical challenges in the development of the optical resonator.

Table 5A lists the parameters of the SNS H^- beam and Table 5B summarizes the required laser parameters with and without the beam recycling optical resonator.

Table 5A: SNS H^- beam parameters.

Beam energy (GeV)	1.0 (upgrade: 1.3)
Beam power (MW)	1.4 (upgrade: 3.0)
Beam macropulse length (ms)	1.0
Beam micropulse length (ps)	50
Peak macropulse H^- current (mA)	38
Ring accumulation time (turn)	1060
Ring bunch intensity	1.6×10^{14}
Vertical size (mm)	0.6
Vertical emittance (mm-mrad)	0.225π
Horizontal size (mm)	3
Vertical emittance (mm-mrad)	0.225π

Table 5B: Required laser parameters for SNS laser stripping.

Method	Macropulse laser	Macropulse laser w/ 20x resonator
Laser wavelength (nm)	355	355
Micropulse length (ps)	50	50
Micropulse energy (μJ)	50	2.5
Micropulse repetition rate (MHz)	402.5	402.5
Macropulse length (ms)	1	1
Macropulse energy (J)	20	1
Macropulse repetition rate (Hz)	60	60
Average power (W)	1200	60
Temporal profile	Flat	Flat
Contrast	N/A	N/A
Efficiency	Normal solid-state lasers	Normal solid-state lasers
Polarization	100/1	100/1
Cost	Multi \$M	Multi \$M
Laser beam quality	$M^2 < 1.2$	$M^2 < 1.2$
Pulse stability	1%	1%
Laser pointing stability (μrad)	1	1
Laser availability	24/7	24/7

4.1.5.2 Laser Stripping of H^- Particles for Project

Project X would convert H^- particles to protons at 8 GeV. This has the advantage of using a laser of longer wavelength because the photon energy would be increased by the relativistic γ factor ($\gamma = 9.526$) due to the Doppler shift. The beam parameters are listed in Table 6 and the beam pulse structure is shown in Figure 7.

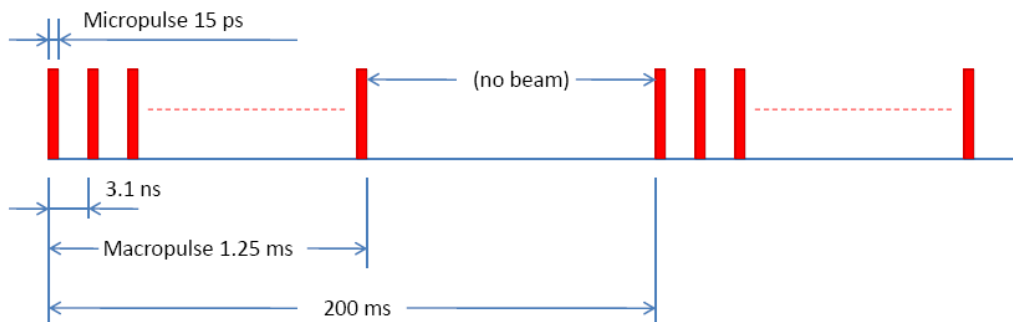
**Figure 7:** H^- pulse structure of Project X.

Table 6: Project X H⁻ beam parameters.

Kinetic energy (GeV)	8
Relativistic γ	9.526
Micropulse length (ps)	15 ps
Micropulse frequency (MHz)	325
Micropulse period (ns)	3.1
Macropulse length (ms)	1.25
Macropulse current (mA)	20
Macropulse frequency (Hz)	5
No. H ⁻ per micropulse	4×10^8
No. micropulses per macropulse	4×10^5
No. H ⁻ per macropulse	1.6×10^{14}
No. H ⁻ per second	8×10^{14}
Vertical beam size (mm)	1.5
Horizontal beam size (mm)	1.5
Beam power (MW)	1

4.1.5.2.1 Direct Laser Ionization

The photoionization of the ground state of the hydrogen atom H(1s) has been studied extensively in the past half century. For low intensity radiation there are exact expressions of this process in terms of the cross section obtained from the perturbation theory [27]. In this approximation, the incident photon flux density is much smaller than 1 atomic unit (a.u.) and the pulse duration is much longer than an optical cycle. However, this approximation is no longer valid when intense laser pulses are employed, since the peak electric fields can be comparable with or larger than 1 a.u. and the pulse may last only a few optical cycles or even a fraction of a cycle. Therefore, perturbative methods are not applicable and numerical methods for solving the time-dependent Schrödinger equation (TDSE) are required.

Ionization of hydrogen atoms by intense laser pulses is a complex subject that is still not fully understood [28-30]. Although many theoretical approaches have been proposed, they typically break down at high laser intensities or neglect important aspects of the laser-atom interaction such as long-range Coulomb interaction or realistic pulse shapes. On the other hand, numerical solutions of the TDSE provide accurate predictions, but are extremely computationally intensive and converge slowly at high intensities. Current results show that no simple relationship links ionization rate to pulse duration, frequency and intensity, due to competing ionization mechanisms, evolving energy levels, resonances and stabilization.

Calculations performed for 24.8 nm (50 eV), 2.5 fs (30 periods) pulses suggest that intensities beyond 10^{17} W/cm² are required for efficient (> 90%) ionization of hydrogen atoms [31]. From an experimental standpoint, few absolute measurements of the ionization yield are available. An experiment performed with 600 fs, 248 nm laser pulses measured ~0.001% ionization for intensities of the order of 10^{14} W/cm² [32].

4.1.5.2.1 Three-Step Stripping

Electrons in hydrogen atoms exposed to intense laser radiation can be excited to higher states. For the Project X parameters, the $n = 2$ transition can be triggered when the hydrogen beam interacts with a 1024 nm laser beam at an angle of ~ 96 degree. A laser peak power of ~ 3.5 MW is required for 90% stripping.

It may be possible to reduce the required laser energy by decreasing the incidence angle (Figure 8). However, this approach can only be investigated by performing detailed simulations of the response of hydrogen atoms to the laser field.

Counter-propagating geometry would require a laser at around $1.8 \mu\text{m}$, which could be achieved using an OPA. However, detailed calculations would be required to establish the powers required and the role of Stark Shifting, etc.

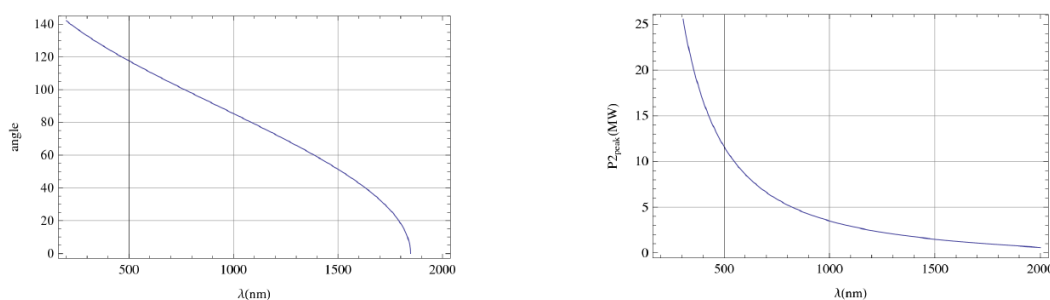


Figure 8: Wavelength vs. angle and power vs. wavelength required for ionization of hydrogen atoms.

4.1.6 Acknowledgements

Carl Schroeder and Wim Leemans (LBNL) contributed to the writing of Section 1.2. Valery Telnov (BINP), Chris Barty (LLNL) and Wolfgang Sandner (MBI) made important comments in Section 1.4. Enrico Brunetti (U. of Strathclyde) contributed to Section 1.5.2.

4.1.7 References

1. W.P. Leemans and E. Esarey, *Physics Today* **62**, 44 (2009).
2. T. Tajima and J.M. Dawson, *Phys. Rev. Lett.* **43**, 267 (1979).
3. E. Esarey, C.B., Schroeder, W.P. Leemans, *Rev. Modern Phys.* **81**, 1229 (2009).
4. W.P. Leemans *et al.*, *Nature Physics* **2**, 696 (2006).
5. C.B. Schroeder *et al.*, in Proc 2008 Advanced Accelerator Concepts Workshop, edited by C. B. Schroeder, E. Esarey, and W. Leemans, AIP Conf. Proc. **1086** (Amer. Inst. Phys., NY, 2009), p. 208.
6. A. Pukhov and J. Meyer-ter-Vehn, *Appl. Phys.* **B 74**, 355 (2002).
7. W. Lu *et al.*, *Phys. Rev. ST Accel. Beams* **10**, 061301 (2007).
8. T. Tajima and A. Chao, private communication.
9. R. H. Siemann, “Energy efficiency of laser driven, structure based accelerators”, *Phys. Rev. ST Accel. Beams* **7**, 061303, (2004); see also N. Na, *et al.*, “Energy efficiency of an intracavity coupled, laser-driven linear accelerator pumped by an external laser”, *Phys. Rev. ST Accel. Beams* **8**, 031301, (2005).

10. W. Liang, A. Yarovy, A. Kewitsch, G. Rakuljic, “Coherent combination of semiconductor lasers using optical phase-lock loops”, *Opt. Lett.*, **32** (4), p.370, (2007).
11. X. E. Lin, “Photonic band gap accelerator”, *Phys. Rev. ST Accel. Beams* **4**, 051301, (2001).
12. B. Cowan, “Three-dimensional dielectric photonic crystal structure for laser-driven acceleration”, *Phys. Rev. ST Accel. Beams* **11**, 011301, (2008); see also C. McGuinness, *et al.*, “Accelerating electrons with lasers and photonic crystals”, *J. Modern Optics*, **56** (18&19), p.2142ff, (2009).
13. T. Plettner, *et al.*, “Proposed few optical cycle laser driven particle accelerator structure”, *Phys. Rev. ST Accel. Beams* **9**, 111301, (2006); see also T. Plettner, R.L. Byer, “Proposed dielectric-based microstructure laser-driven undulator,” *Phys. Rev. ST Accel. Beams* **11**, 030704 (2008).
14. E. Colby *et al.*, “An electron source for a laser accelerator”, in *Proc. 2003 Part. Accel. Conf.*, p.2101-2103, (2003).
15. C. M. S. Sears *et al.*, “Production and characterization of attosecond bunch trains”, *Phys. Rev. ST Accel. Beams*, **11**, 061301, (2008).
16. C. M. S. Sears *et al.*, “Phase stable net acceleration of electrons from a two-stage optical accelerator”, *Phys. Rev. ST Accel. Beams*, **11**, 101301, (2008).
17. Private communication.
18. RDR, <http://www.linearcollider.org/about/Publications/Reference-Design-Report>
19. D. Asner *et al.*, “Higgs physics with a $\gamma\gamma$ collider based on CLIC 1”, *Eur. Phys. J. C* **28**, 27–44 (2003)
20. R. Tomas, “Overview of the Compact Linear Collider”, *Phys. Rev. ST Accel. Beams* **13**, 014801 (2010). Two parameter sets for $E_{CM} = 0.5$ and 3 TeV are given. Here, the former is used.
21. Private communication.
22. For example, E. Saldin *et al.*, Proc. PAC2009, Vancouver, BC, Canada, WE6PFP083.
23. For example, G. Klemz *et al.*, “Design study of an optical cavity for a future photon collider at ILC”, *Nucl. Instr. Meth.* **A564**, 212 (2006).
24. J. Urakawa, “Development of a compact x-ray source based on Compton scattering using 1.3 GHz superconducting RF accelerating linac and a new laser storage cavity”, submitted to *Nucl. Instr. Meth. A*.
25. C. Barty, private communication.
26. W. Sandner, private communication.
27. H. A. Bethe and E. E. Salpeter, *Quantum Mechanics of One- and Two-Electron Atoms*, pp 295-322, Springer-Verlag (1957).
28. A. N. Grum-Grzhimailo *et al.*, *Phys. Rev. A* **81**, 043408 (2010).
29. S. Borbély *et al.*, *Phys. Rev. A* **77**, 033412 (2008).
30. S. Geltman, *J. Phys. B: At. Mol. Opt. Phys.* **33**, 1967 (2000).
31. J. Bauer *et al.*, *J. Phys. B: At. Mol. Opt. Phys.* **34**, 2245 (2001).
32. G. A. Kyrala and T. D. Nichols, *Phys. Rev. A* **44**, R1450–R1453 (1991).

5 Recent Doctoral Theses

5.1 ATF2 Optics System Optimization and Experiment Study

Sha Bai

IHEP, 19B YuquanLu, Shijingshan District, Beijing, 100049, China

Mail to: baisha@ihep.ac.cn

Graduation Date: 1 July 2010

Supervisor: Prof. J. Gao

Abstract:

ATF2 is a test facility for ILC and CLIC type final focus systems based on local chromaticity correction. It makes use of the low emittance beam extracted from the ATF damping ring, and aims to reach a final beam size of 37nm at the optical focal point (hereafter referred to as IP, interaction point, by analogy to the linear collider collision point) after correcting for the effects of inaccuracies in magnet strengths and alignment. To reach such a goal in order to get such small beam size at IP, this dissertation firstly presents optimization work of the ATF2 optical system, and get a vertical beam size which is smaller than the designed one. Meanwhile, introduces analysis of several orthogonal multi-knobs to correct for inaccuracies in magnet strengths and alignment, manipulation of the vertical beam size at IP with multi-knobs. Finally, with the measured beam size and dispersion at IP, two twiss parameters estimation methods were developed. The substantial works of these researches can be summarized as follows:

- 1) Study the ATF2 optical system and the principle of novel local chromaticity correction; take advantage of its telescopic system optical building to match the IP β function in order to adjust the beam size. At the same time, analyze the optical aberration and introduce two correction methods, after beam tracking, a smaller beam size than designed value is got. In the ATF2 initial commissioning, suitable optical modes with variable β function at IP are produced, which benefit the newly installed diagnostic instruments (Shintake, wire scanners, cavity BPMs etc...) and for the initial alignment of magnets with beam.
- 2) In the presence of every kind of inaccuracies of magnets strength and alignments, a detailed analysis of coupling, dispersion, waist scans and β function correction multi-knobs are introduced, and a vertical beam size which is very close to the linear beam size is obtained based on a simulation study.
- 3) During the initial commissioning, several kinds of beam diagnostic instruments with different resolutions are installed at different IP location. And the dispersion and beam size were measured from them. Two analysis methods were given to get the twiss parameters and emittance while the minimum vertical beam size can't be resolved; some results obtained were rather close to expectations, like the horizontal emittance, so as to provide valuable experience for the ATF2 future commissioning.

5.2 Simulation and Experimental Research on Laser Wakefield Electron Accelerators

Da Zhang Li

IHEP, 19B YuquanLu, Shijingshan District, Beijing, 100049, China

Mail to: lidz@ihep.ac.cn

Graduation Date: 25 June 2010

Supervisors: Prof. J. Gao, Prof. X.-W. Zhu

Abstract:

One of the most important advanced acceleration concepts is laser plasma acceleration. The amplitude of the accelerating electric fields generated from plasma-based accelerator may beyond 100 GV/m, which is more than 1000 times higher than traditional radio frequency accelerating structures. LWFA (Laser WakeField Accelerators) based on ultra-short and ultra-intense laser pulses are very attractive for its size and costs comparing with traditional accelerators which is usually several kilometers long with billions of dollars' budgets. With the rapid development of laser technique, beams with shorter pulse length and higher power intensity are generated from new facilities all over the world, which makes it possible to produce energetic particles and radiations by laser-plasma interactions. In this thesis, we focus on the simulation and experimental studies of laser wakefield electron accelerations. Theoretical analysis of laser plasma acceleration are taken to find out how can we use typical 100TW laser facilities producing quasi-energetic high energy electron bunches and how can we optimize the bunch qualities. This thesis consists of 3 parts:

In part I (Chapter 2), firstly we study how to compile a plasma particle-in-cell (PIC) simulation code via reading the multi-dimensional PIC code KLAP (Kinetic LAsER Plasma) which is developed by Prof. Sheng Zheng-Ming et al. at IOP. And then we introduce 2 more efficient PIC algorithms, ponderomotive guiding center and quasi-static approximation. At the last of Chapter 2, we give a brief introduction of the PIC codes we used in this thesis: OOPIC and VORPAL. We mainly talk about the advantages of these two codes and how to create input files for these two programs.

In the second part of this thesis (Chapter 3 and Chapter 4), we carry on theoretical and simulation analysis on 3 main questions in laser wakefield accelerations: how can we use an ultra-short and ultra-intense laser pulse to generate large amplitude wakefields in plasmas stably? How can we inject enough electrons into the wakefield? How can we enlarge the effective accelerating length of laser pulses and plasmas? Beginning with fundamental theoretical equations, we deduce the expression of the wakefield in bubble regime step by step. And then we study the mechanisms of the self-injection of the background plasma electrons and clarify the thresholds of self-injections. In section 3.4, based on typical 100TW laser facilities, we do some simulations by OOPIC and VORPAL. We fix the laser parameters and do explicit plasma density scanning as in a real LWFA experiment. According to the simulation results, we find that the threshold of wavebreaking in 2-D condition is much lower than 1-D theoretical result, $E_{wb,2D} \approx 0.29E_{wb,1D}$. Once wavebreaking occurs, background electrons can be self-injected into the wake and accelerated by the longitudinal electric fields. In addition, we give a qualitative conclusion on the relationship between plasma

density and energy spread of the captured electron bunch $\Delta\bar{E}_{abs} / \Delta E_{gain} \propto n_e^{3/2}$ under the assumption of a simple sheath model which is presented by Doctor Lu Wei in UCLA.

In order to solve the problems during self-injections, we show theoretical and simulation results of density ramping injection (DRI) methods. It is shown that the number of the captured electrons by DRI is 10 times larger than in normal self-injected process and the energy and absolute energy spread of the bunch doesn't change a lot. We can further optimize the bunch qualities through changing the ramp length or the difference between high density region and low density region. In Section 4.3 and 4.4, we discuss how to expand the effective acceleration length in LWFA. According to theoretical analysis, relativistic self-guiding and preformed plasma channel can guide the laser pulse and enlarge the diffraction length of laser beams. Relativistic self-guiding is not effective enough to short pulse ($c\tau < L$), while preformed plasma channel method is effective to all kind of pulse length. We use a parabolic preformed plasma channel in our simulation and find out this kind of plasma distribution can guide laser very well comparing to self-guiding effect.

In the third part of this thesis (Chapter 5 and Chapter 6), we show our experimental research on LWFA. In Chapter 5, we first introduce the aim and setup of the joint LWFA experiment at CAEP, Mianyang. Secondly, according to the results, we present our analysis of the optical guiding effects of the capillary to the ultrashort and ultraintense laser pulse. This is the first time that the laser pulses with more than 100TW power can be guided perfectly by capillaries. Then we discuss the reasons for not observing the high energy electrons in our experiment by analyzing the discharge current curves. At the last of Chapter 5, we show some experimental study results on gas-filled capillary machining. In Chapter 6 we introduce a laser-cluster experiment we did in IOP last year, and show some preliminary results. In this experiment, we get X-rays with more than 10^{11} photons from the interaction of ultrashort and ultrahigh laser pulses and inert gas clusters.

5.3 Researches on Electron Injection and Plasma Density Diagnostics in Laser Plasma Wakefield Acceleration

An He

Jieshiping 15-2405, Shijing Mountant, Beijing, China

Mail to: hean1978@hotmail.com

Graduation Date: 24 June 2010

Supervisors: Prof. J. Gao, Prof. X.-W. Zhu

Abstract:

Laser-plasma Wakefield Accelerators (LWFA) can have much higher accelerating gradient than that of the traditional RF cavity, normal or super-conduction, powered accelerators. It relies on the fact that the plasma wave can carry an accelerating electric field as high as 100 GV/m, while the traditional RF cavity powered accelerators are usually limited about 100 MV/m. This high accelerating field means a significant reduction of the size of an accelerator. As the beam energy requirement in High Energy Physics (HEP) goes higher and higher, unfortunately the cost and scale of such a traditional accelerator also increase. Therefore, LWFA with about a thousand times

higher accelerating gradient has been a promising candidate for a table-top accelerator. In the mean time, the applications of these LWFA in proton therapy, nucleus medicine, nuclear fusion, material science and structural biology are also growing fast. All these make LWFA research as a frontier topic more and more attractive to scientists specialized in plasma physics, lasers and accelerator physics. My dissertation is focused on the simulations of the electron injection processes in LWFA, and the diagnostics of plasma density in capillary in LWFA experiments. This dissertation is composed of three parts:

The first part (Chapter 2) summaries the physics mechanism of LWFA, the concepts and the formulae those are scattered in many frontier research papers. It also introduces some hot research topics that are still attractive and need more brilliant ideas.

The second part (Chapter 3 to Chapter 4) studies two electron injection methods, the external electron injection and the optical injection in detail.

In Chapter 3, the external electron injection that the electron bunch is injected into plasma before laser pulse is studied in detail. Through 1-D theory we have found that the longitudinal bunch length can be compressed by a factor of two orders of magnitude (from a few hundred micrometers to a few micrometers). Through the research on beam loading of the injecting bunch, we have found that for a bunch of $\sigma_{rms} = 60\mu m$ when the condition of $n_{b0}/n_p < 0.01$ is met, the beam loading can be ignore. With the 1-D simulations of particle-in-cell (PIC-VORPAL) code, we obtain a $311MeV$, $1pC$ electron bunch with 1.8% energy spread, $2.75\mu m$ bunch length. With simulations we have found that in 1-D this injection method can effectively accelerate bunch in 3-4 cm accelerating distance. The effects of bunch's initial energy, bunch longitudinal length, the laser pulse intensity on the injection are analyzed.

In Chapter 4, the colliding pulse injection (CPI) is studied in detail. The dynamics of electrons in CPI system is analyzed. The feasibility of CPI method is proved. With 2-D simulation by OOPIC, the injection, trapping and accelerating processes are presented and analyzed. The choice of the optimal initial parameters is found and presented. The transverse betatron oscillation of the electron bunches in wakefield is confirmed by simulation. With 1-D simulation by VORPAL, the inhabitation of beatwave on the plasma wakefield is confirmed. Through both theory and PIC simulation, the effects of the colliding pulse's polarizations on CPI are analyzed. These effects include the electron heating, the wakefield inhibition and the injected charges in both PP (parallel polarization) and CP (crossed polarization) cases.

The third part (Chapter 5) analyzes the scattering character of the capillary waveguide which is the key component of LWFA experiments. For the first time, a method to measure the plasma density in the capillary by using X-ray computerized tomography and interference phase-shift technique is proposed. Many simulations and min-experiments have been done and the whole processes are demonstrated by simulation. The feasibility of our scheme is proved. The fully formed detecting system is designed and the parameters of key optics are analyzed. A Mach-Zehnder interferometer prototype is set up. The overview of the experiment by proposed new method is then presented.

6 Forthcoming Beam Dynamics Events

6.1 ICFA Advanced Beam Dynamics Mini-Workshop: X-Band RF Structures, Beam Dynamics and Sources (XB10)

This workshop, referred to as XB10 will take place at the Cockcroft Institute (UK), from Tuesday 30th November through Friday 3rd December, 2010. (<http://www.cockcroft.ac.uk/events/XB10/index.htm>).

The workshop will address RF issues pertinent to X-band accelerating structures in linear colliders and light sources and will also include medical and industrial linacs. RF sources are also included in this workshop, together with aspects of RF fields in structures and cavities, wakefields, RF couplers and beam dynamics issues. The workshop will also embrace both active and passive overmoded and quasi-optical components. Accelerating structures, novel and high power RF sources, light sources and drive beams will be amongst the areas of interest. A series of invited plenary talks will be given, in addition to contributed topics. This will also include breakdown issues pertinent to high gradient structures, but the focus of the workshop will be on RF and impedance issues both from both a theoretical and experimental perspective, with a view to capitalise on potential synergies between national laboratory facilities, smaller scale university groups and industrial organisations. A satellite workshop will also be conducted on medical and industrial X-band linacs. The workshop builds on the highly successful XB08 workshop (<http://www.cockcroft.ac.uk/events/X-Band/index.htm>). Delegates will be given the opportunity to submit papers for publication in the ICFA mini-workshop proceedings. Tours of the on-site ALICE and EMMA facilities at Daresbury will also be available.

Program Committee: Drs. R. M. Jones (chair), W. Wuensch, S. Tantawi, T. Higo, D. Schulte, Profs. S. Chattopadhyay, R. Carter.

Contact

XB10 Chair, R.M. Jones, Roger.Jones@manchester.ac.uk

FInstP, CSci, CPhys, SMIEEE School of Physics and Astronomy
The University of Manchester, UK

7 Announcements of the Beam Dynamics Panel

7.1 ICFA Beam Dynamics Newsletter

7.1.1 Aim of the Newsletter

The ICFA Beam Dynamics Newsletter is intended as a channel for describing unsolved problems and highlighting important ongoing works, and not as a substitute for journal articles and conference proceedings that usually describe completed work. It is published by the ICFA Beam Dynamics Panel, one of whose missions is to encourage international collaboration in beam dynamics.

Normally it is published every April, August and December. The deadlines are 15 March, 15 July and 15 November, respectively.

Categories of Articles

The categories of articles in the newsletter are the following:

1. Announcements from the panel.
2. Reports of beam dynamics activity of a group.
3. Reports on workshops, meetings and other events related to beam dynamics.
4. Announcements of future beam dynamics-related international workshops and meetings.
5. Those who want to use newsletter to announce their workshops are welcome to do so. Articles should typically fit within half a page and include descriptions of the subject, date, place, Web site and other contact information.
6. Review of beam dynamics problems: This is a place to bring attention to unsolved problems and should not be used to report completed work. Clear and short highlights on the problem are encouraged.
7. Letters to the editor: a forum open to everyone. Anybody can express his/her opinion on the beam dynamics and related activities, by sending it to one of the editors. The editors reserve the right to reject contributions they judge to be inappropriate, although they have rarely had cause to do so.

The editors may request an article following a recommendation by panel members. However anyone who wishes to submit an article is strongly encouraged to contact any Beam Dynamics Panel member before starting to write.

7.1.2 How to Prepare a Manuscript

Before starting to write, authors should download the template in Microsoft Word format from the Beam Dynamics Panel web site:

<http://www-bd.fnal.gov/icfabd/news.html>

It will be much easier to guarantee acceptance of the article if the template is used and the instructions included in it are respected. The template and instructions are expected to evolve with time so please make sure always to use the latest versions.

The final Microsoft Word file should be sent to one of the editors, preferably the issue editor, by email.

The editors regret that LaTeX files can no longer be accepted: a majority of contributors now prefer Word and we simply do not have the resources to make the conversions that would be needed. Contributions received in LaTeX will now be returned to the authors for re-formatting.

In cases where an article is composed entirely of straightforward prose (no equations, figures, tables, special symbols, etc.) contributions received in the form of plain text files may be accepted at the discretion of the issue editor.

Each article should include the title, authors' names, affiliations and e-mail addresses.

7.1.3 Distribution

A complete archive of issues of this newsletter from 1995 to the latest issue is available at

<http://icfa-usa.jlab.org/archive/newsletter.shtml>.

This is now intended as the primary method of distribution of the newsletter.

Readers are encouraged to sign-up for electronic mailing list to ensure that they will hear immediately when a new issue is published.

The Panel's Web site provides access to the Newsletters, information about future and past workshops, and other information useful to accelerator physicists. There are links to pages of information of local interest for each of the three ICFA areas.

Printed copies of the ICFA Beam Dynamics Newsletters are also distributed (generally some time after the Web edition appears) through the following distributors:

Weiren Chou	chou@fnal.gov	North and South Americas
Rainer Wanzenberg	rainer.wanzenberg@desy.de	Europe ⁺⁺ and Africa
Susumu Kamada	susumu.kamada@kek.jp	Asia ^{**} and Pacific

⁺⁺ Including former Soviet Union.

^{**} For Mainland China, Jiu-Qing Wang (wangjq@mail.ihep.ac.cn) takes care of the distribution with Ms. Su Ping, Secretariat of PASC, P.O. Box 918, Beijing 100039, China.

To keep costs down (remember that the Panel has no budget of its own) readers are encouraged to use the Web as much as possible. In particular, if you receive a paper copy that you no longer require, please inform the appropriate distributor.

7.1.4 Regular Correspondents

The Beam Dynamics Newsletter particularly encourages contributions from smaller institutions and countries where the accelerator physics community is small. Since it is impossible for the editors and panel members to survey all beam dynamics activity worldwide, we have some Regular Correspondents. They are expected to find interesting activities and appropriate persons to report them and/or report them by themselves. We hope that we will have a "compact and complete" list covering all over the world eventually. The present Regular Correspondents are as follows:

Liu Lin	Liu@lnls.br	LNLS, Brazil
Sameen Ahmed Khan	Rohelakan@yahoo.com	SCOT, Oman
Jacob Rodnizki	Jacob.Rodnizki@gmail.com	Soreq NRC, Israel
Rohan Dowd	Rohan.Dowd@synchrotron.org.au	Australian Synchrotron

We are calling for more volunteers as Regular Correspondents.

7.2 ICFA Beam Dynamics Panel Members

Name	eMail	Institution
Rick Baartman	baartman@lin12.triumf.ca	TRIUMF, 4004 Wesbrook Mall, Vancouver, BC, V6T 2A3, Canada
Marica Biagini	marica.biagini@lnf.infn.it	LNF-INFN, Via E. Fermi 40, Frascati 00044, Italy
Yunhai Cai	yunhai@slac.stanford.edu	SLAC, 2575 Sand Hill Road, MS 26, Menlo Park, CA 94025, U.S.A.
Swapn Chattopadhyay	swapan@cockcroft.ac.uk	The Cockcroft Institute, Daresbury, Warrington WA4 4AD, U.K.
Weiren Chou (Chair)	chou@fnal.gov	Fermilab, P.O. Box 500, Batavia, IL 60510, U.S.A.
Wolfram Fischer	wfischer@bnl.gov	Brookhaven National Laboratory, Bldg. 911B, Upton, NY 11973, U.S.A.
Yoshihiro Funakoshi	yoshihiro.funakoshi@kek.jp	KEK, 1-1 Oho, Tsukuba-shi, Ibaraki-ken, 305-0801, Japan
Miguel Furman	mafurman@lbl.gov	Center for Beam Physics, LBL, 1 Cyclotron Road, Berkeley, CA 94720-8211, U.S.A.
Jie Gao	gaoj@ihep.ac.cn	Institute for High Energy Physics, P.O. Box 918, Beijing 100049, China
Ajay Ghodke	ghodke@cat.ernet.in	RRCAT, ADL Bldg. Indore, Madhya Pradesh, 452 013, India
Ingo Hofmann	i.hofmann@gsi.de	High Current Beam Physics, GSI Darmstadt, Planckstr. 1, 64291 Darmstadt, Germany
Sergei Ivanov	ivanov_s@mx.ihep.su	Institute for High Energy Physics, Protvino, Moscow Region, 142281 Russia
Kwang-Je Kim	kwangje@aps.anl.gov	Argonne Nat'l Lab, Advanced Photon Source, 9700 S. Cass Avenue, Argonne, IL 60439, U.S.A.
In Soo Ko	isko@postech.ac.kr	Pohang Accelerator Lab, San 31, Hyoja-Dong, Pohang 790-784, South Korea
Alessandra Lombardi	alessandra.lombardi@cern.ch	CERN, CH-1211, Geneva 23, Switzerland
Yoshiharu Mori	mori@kl.rii.kyoto-u.ac.jp	Research Reactor Inst., Kyoto Univ. Kumatori, Osaka, 590-0494, Japan
Mark Palmer	mark.palmer@cornell.edu	Wilson Laboratory, Cornell University, Ithaca, NY 14853-8001, USA
Chris Prior	c.r.prior@rl.ac.uk	ASTeC Intense Beams Group, STFC RAL, Chilton, Didcot, Oxon OX11 0QX, U.K.
Yuri Shatunov	yu.m.shatunov@inp.nsk.su	Acad. Lavrentiev, prospect 11, 630090 Novosibirsk, Russia
Junji Urakawa	junji.urakawa@kek.jp	KEK, 1-1 Oho, Tsukuba-shi, Ibaraki-ken, 305-0801, Japan
Jiu-Qing Wang	wangjq@mail.ihep.av.cn	Institute for High Energy Physics, P.O. Box 918, 9-1, Beijing 100049, China
Rainer Wanzenberg	rainer.wanzenberg@desy.de	DESY, Notkestrasse 85, 22603 Hamburg, Germany

*The views expressed in this newsletter do not necessarily coincide with those of the editors.
The individual authors are responsible for their text.*